



ANALYSIS, IMPLEMENTATION AND INVESTIGATION
OF A WIRELESS IN-MOLD SENSOR FOR
INJECTION MOLDING

by

FLORIAN MÜLLER

A Dissertation
in Candidacy for the Degree of
Doktor der montanistischen Wissenschaften

Montanuniversitaet Leoben
Department Polymer Engineering and Science

Chair of Polymer Processing
Head: Univ.-Prof. Dipl.-Ing. Dr.mont. Clemens Holzer

Supervision: Prof. Dr. Clemens Holzer
Prof. Dr. Paul O'Leary

January 2014

I hereby declare on oath that I did this dissertation
in hand by myself using only the literature cited at
the end of this thesis

Florian Müller
Leoben, January 2014

Abstract

Injection molding is a highly dynamic process with the need to be controlled if highly accurate technical parts are to be repeatedly produced on a mass production scale. The need to control the process evokes the necessity for sensors enabling detection of the current process conditions.

This work presents the analysis, implementation and investigation of a wireless in-mold sensor, called the *acoustic-emission* sensor. The sensor makes use of structure-borne sound as transmission medium eliminating the need of undesirable wiring connecting the sensor head to the exterior surface of the mold. The sensor detects the melt front location at (multiple) predetermined positions. A movable pin, e.g. an ejector pin, is accelerated through the melt pressure within the passing melt front and the pin impacts on a resonant structure. The structure is excited and oscillates at its resonant frequency and distributes the oscillations in form of structure-borne sound within the whole metal mass of the mold. An accelerometer on the outside surface of the mold enables the detection and further recognition of the resonant structure oscillation. Consequently the temporal position of the melt front can be measured at predetermined positions. Simultaneous detection at multiple locations is possible. This is achieved by designing individual resonators to have distinct resonant characteristic.

Signal processing is used to separate the sounds emanating from the resonators. In addition to two classical approaches a new linear algebraic approach is introduced, the *frequency pattern recognition method*. The new algebraic enables a least squares approximation for the instant of time when the resonator was excited, i.e., when the melt front reached the sensor. The new method uses discrete orthogonal polynomials and constrained basis functions. Additionally, the method yields the complete covariance propagation, from which an uncertainty can be computed via the inverse student-t distribution. In this manner, the time of excitement and a confidence interval can be determined. This is of special interest in instrumentation.

Experimental results verify the good performance of the acoustic-emission sensor concept when implemented in an injection mold. In comparison to conventional in-mold sensors the acoustic-emission sensor shows at least identical results in terms of response time which is a very important value

for melt front position detection.

The acoustic-emission sensor was tested in combination with the frequency pattern recognition method in a long term test showing reliable automatic melt front detection with single or multiple implemented resonators.

Kurzfassung

Spritzgießen ist ein hochdynamischer Prozess, mit dem durch den Einsatz von Regelungstechnik hoch präzise reproduzierbare technische Spritzgussbauteile in Serienfertigung hergestellt werden. Für die Regelung des Prozesses sind Eingangsgrößen notwendig, die den Zustand des Prozesses über Sensoren detektieren.

Diese Arbeit befasst sich mit der Auswertung, Implementierung und Untersuchung eines kabellosen Werkzeugsensors. Der als *Schallsensor* bezeichnete Sensor verwendet Körperschall als Übertragungsmedium. Dadurch entfällt die Notwendigkeit, Sensorkabel innerhalb des Spritzgusswerkzeuges zu verlegen, wodurch signifikante Vorteile entstehen.

Der Schallsensor kann an (mehreren) vorher definierten und modifizierten Stellen im Werkzeug den Zeitpunkt der vorbeiströmenden Schmelzefront detektieren. Ein beweglicher Stift, z.B. ein Auswerferstift, wird durch den in der Schmelze vorherrschenden Druck beschleunigt, bis er auf einem Resonanzkörper auftrifft. Die Struktur des Resonanzkörpers wird in Schwingung versetzt und überträgt diese in den Metallkörper des Werkzeuges. Ein an der Außenfläche angebrachter Beschleunigungssensor zeichnet die Schwingungen auf und ermöglicht die Erkennung. Dadurch kann die zeitliche Position der Schmelzefront an den vordefinierten Stellen gemessen werden. Durch Verwendung unterschiedlich geformter Resonanzkörper ist eine gleichzeitige Erkennung und Unterscheidung an mehreren Positionen möglich.

Zur Unterscheidung der aufgezeichneten Schwingungen wird Signalverarbeitung verwendet. Zusätzlich zu zwei klassischen Signalverarbeitungsverfahren wurde ein neuer Ansatz entwickelt unter Verwendung linearer Algebra, *Frequenz-Muster Methode* genannt. Die neue Methode ermöglicht unter Anwendung der Methode der kleinsten Fehler-Quadrate eine Approximation für die Erkennung des Zeitpunktes, an dem die Resonanzstruktur angeregt wurde. Die Signalverarbeitung verwendet diskrete orthogonale Polynome sowie Basis-Funktionen mit implementierten Randbedingungen. Zusätzlich ermöglicht die neue Methode die Berechnung der Kovarianz-Fortpflanzung, wodurch die Unsicherheit mit Hilfe der invertierten Student-t-Verteilung berechnet werden kann. Somit kann der Zeitpunkt der vorbeifließenden Schmelze mit einem Vertrauensintervall bestimmt werden, dass

besonders im Bereich der Messtechnik wichtig ist.

Experimentelle Ergebnisse beweisen die gute Funktionalität des neuen Sensorkonzeptes. Dabei wird das Sensorsystem konventioneller Sensorik gegenübergestellt und verglichen. Im Allgemeinen weist das neue Sensor-konzept mindestens gleich gute Messwerte im Bereich der Ansprechzeit auf wie herkömmliche Werkzeug-Sensorik. Die Ansprechzeit ist dabei eine der wichtigsten Größen im Bereich der Schmelzfrontdetektion.

Der Schallsensor wurde mit dem neu entwickelten Auswerteverfahren *Frequenz-Muster Methode* in einem Langzeitversuch getestet und zeigte zuverlässige automatische Schmelzfront Erkennung mit einem beziehungsweise mehreren implementierten Resonatoren.

Acknowledgments

This doctoral thesis was carried out in the Research Studios Austria (RSA) project PolySens as well as in the project PolyRegion. RSA was a funding program run by the Austrian Federal Ministry of Economy, Family and Youth. The project PolyRegion was funded by the European Territorial Cooperation.

I would like to thank Prof. Dr. Clemens Holzer, Professor of the Chair of Polymer Processing at the Montanuniversitaet Leoben, for giving me the chance to do research and compose this doctoral thesis. Further I like to thank him for his support and critical review of the work to ensure the quality of the thesis.

A special thank goes to Prof. Dr. Paul O’Leary, Professor of the Chair of Automation at the Montanuniversitaet Leoben, for supervising this work and for supporting me during my research work. He always helped with occurring problems and gave useful hints to solve them. I would also like to thank him for pushing me further and for all the knowledge, not only in the field of mathematics, I learned from him.

A great thank goes to Dr. Christian Kukla and Ass. Prof. Dr. Thomas Lucyshyn who arranged the project PolySens and PolyRegion. They also helped developing the idea presented in this doctoral thesis and helped in countless discussions to find solutions for the upcoming problems.

Furthermore I like to thank Ass. Prof. Dr. Gerhard Rath, researcher at the Chair of Automation at the Montanuniversitaet Leoben, for giving me ongoing support during the whole doctoral thesis. He always had a good advice to guide the work in the right direction. In the same breath I like to thank Ing. Gerold Probst. He supported me in the construction of the electric components, in designing several evaluation programs and always

had a helping hand during the measurements.

A major thanks goes to my colleagues at the Chair of Polymer Processing as well as the colleagues at the Chair of Chemistry of Polymeric Materials in Leoben. Their support made my work joyful and they always had an open ear for fruitful discussions while having a cup of coffee.

Finally I like to thank my family and friends and especially Anna for continuous mental support and supporting my schemes.

Florian Müller,
Leoben, January 2014

Contents

| | | |
|----------|--|-----------|
| 1 | Introduction and Motivation | 1 |
| 1.1 | Economical Motivation | 3 |
| 1.1.1 | Injection Molding | 3 |
| 1.1.2 | Injection Molding Process Control | 6 |
| 1.1.2.1 | Process Window | 10 |
| 1.1.2.2 | In-Mold Sensors: An Economic Review | 12 |
| 1.2 | In-Mold Sensing Technology | 15 |
| 1.2.1 | Common In-Mold Sensor Types and their Usage | 16 |
| 1.2.2 | Wireless In-Mold Sensor Types | 24 |
| 2 | Acoustic-Emission Sensor | 31 |
| 2.1 | Principle of Operation | 31 |
| 2.2 | Measurable Process Variables | 33 |
| 2.3 | Test Mold Setup for Acoustic-Emission Sensor | 36 |
| 2.4 | Ejector Pin Design of Acoustic-Emission Sensor in a Series Tool | 38 |
| 3 | Theoretical Framework | 47 |
| 3.1 | Melt Pressure | 48 |
| 3.2 | Pin Movement | 49 |
| 3.3 | Resonant Structure Modeling | 53 |
| 3.4 | Elastic Waves | 56 |
| 3.5 | Transducer | 58 |
| 3.6 | Signal Processing | 60 |
| 3.6.1 | Envelope Detection | 61 |
| 3.6.2 | Filter Signal Processing | 65 |
| 3.6.3 | Statistical Signal Processing | 71 |

| | | |
|----------|--|------------|
| 3.6.4 | Frequency Pattern Recognition Method | 76 |
| 3.6.4.1 | Spectral Leakage | 79 |
| 3.6.4.2 | Polynomial Approach for Spectral Leakage | 84 |
| 3.6.4.3 | Signature Identification | 88 |
| 3.6.4.4 | Signature Matching | 89 |
| 3.6.4.5 | Computational Complexity | 92 |
| 3.6.4.6 | Covariance Propagation and Confidence Interval | 93 |
| 3.6.4.7 | Decision Process | 95 |
| 4 | Experiments and Results | 97 |
| 4.1 | Cavity Wall Temperature Response Characteristic | 98 |
| 4.2 | Proof of Concept Measurements | 106 |
| 4.2.1 | One Implemented Acoustic Actuator | 109 |
| 4.2.2 | No Implemented Acoustic Actuator | 111 |
| 4.2.3 | Two Implemented Acoustic Actuators | 112 |
| 4.2.4 | Two Implemented Acoustic Actuators - Increased Injection Rate | 117 |
| 4.3 | Acoustic-Emission Sensor Performance Evaluation | 120 |
| 4.3.1 | Pressure Influence Investigation | 126 |
| 4.3.2 | Spring Influence Investigation | 133 |
| 4.3.3 | Pin Mass Investigation | 135 |
| 4.3.4 | Pin Movement Simulation | 136 |
| 4.4 | Resonator Frequency Response Analysis | 137 |
| 4.4.1 | Resonant Structure Design | 138 |
| 4.4.2 | Acoustic Spectrum Analysis | 140 |
| 4.5 | Signal Processing | 146 |
| 4.5.1 | Signal Envelope Detection Method | 147 |
| 4.5.2 | Band-Pass Filter Method | 151 |
| 4.5.3 | Frequency Pattern Recognition Method | 155 |
| 4.5.3.1 | Experimental Signature Identification | 156 |
| 4.5.3.2 | Experimental Signature Matching | 158 |
| 4.6 | Long Term Evaluation of Acoustic-Emission Sensor | 165 |
| 4.6.1 | One Installed Acoustic Actuator | 166 |
| 4.6.2 | Two Installed Acoustic Actuators | 169 |
| 5 | Conclusion and Outlook | 176 |
| | Abbreviations | 179 |
| | Bibliography | 181 |

Chapter 1

Introduction and Motivation

In polymer processing injection molding is the most important manufacturing process for the mass production of technical parts in polymer materials. With its variety of influencing factors it is a highly dynamic process which needs to be controlled for constant product quality. Manufacturers of injection molding machines improved machinery control strategies [2, 64, 100] over the last few decades towards high repeatability with the target of producing high quality parts with zero defects. However, for consistent production of zero defect parts solely controlling the machine is not sufficient. Information has to be obtained from the inside of the mold if satisfactory control is to be achieved. This process information is more correlated to part quality since it is recorded at the point where product quality arises - the cavity. Therefore a need for in-mold sensors is given for monitoring the current state, which is used as input variable for closed-loop control strategies.

Several types of in-mold sensors are commercially available [1, 92, 97, 122, 180]. Especially cavity wall temperature sensors and in-mold pressure sensors are common but just marginally implemented [11, 31, 71, 97, 98]. In literature it is estimated that less than 5 % of the molds in Germany [11] and below 1 % of the molds worldwide are instrumented [71]. This directly leads to the question why so few molds are instrumented nowadays although requirements for plastic parts are continuously rising while costs need to be reduced. In this thesis an economical review of in-mold sensors is given trying to answer this question.

The commercially available temperature sensors are not only used for melt temperature respectively contact temperature sensing but are also used for melt front detection [9, 99]. This binary-like switch behavior at the moment the melt front passes the sensor head enables a melt front dependent control of the switch-over point which is crucial for part quality [1, 92, 180]. Further-

more, the signal can be used for balancing of multi-cavity molds equipped with hot runner systems or independently controllable valve gates [8, 41]. The cavity pressure is a good estimator for part quality [42, 83, 118, 123, 197]. Monitoring the time-dependent pressure characteristic yields the possibility of automatically detecting faulty parts [36, 92]. Additional control strategies exist for adapting the cavity pressure achieving a more consistent part quality [56, 57].

Further sensor types, such as flow front detectors [27, 193] or in-situ morphology analyzing systems [79, 147] are mentioned and investigated in literature but unfortunately never appeared on the open market.

A disadvantage of all commercially available in-mold sensors is the necessity for wiring to provide energy and to communicate data. As a result, a significant effort in the construction phase of a new mold has to be invested to find space for the required wire ducts. Since wires are sensitive to clamping special attention is needed during maintenance work. If one can eliminate the need of wires for in-mold sensors implementation would be become significantly easier.

In this thesis a wireless in-mold sensor approach, named the *acoustic-emission sensor*, is presented. The acoustic-emission sensor consists solely of mechanical components within mold. These mechanical components, in form of an assembly called an *acoustic actuator*, are designed to generate a distinctive sound triggered by the passing melt front. This behavior is achieved by a sprung movable pin which protrudes inside the cavity. When the melt front overflows this pin it is accelerated by the increasing melt pressure until it impinges on a resonant structure generating a distinctive sound. The sound is transmitted through the metal mass of the mold as structure-borne sound and can be recorded by an accelerometer mounted at any outside surface of the mold obviating any wires from the inside of the mold. If several different acoustic actuators are implemented in one mold separation can be achieved by designing different resonant structures with unique frequency responses. Each one with its unique frequency response behavior can be detected, using just one mounted accelerometer, making it simple and cheap to equip molds with a plurality of sensors.

In the thesis the acoustic-emission sensor concept is presented in detail describing the theoretical background and measurable process parameters. Besides preliminary proof of concept measurements different influencing parameters are investigated, e.g. injection rate, viscosity and spring rate, whereby the movement of the pin is described by a mathematical model as well as using finite element method (FEM) to investigate the impact of these in-

fluencing parameters. Additional measurements were performed to estimate the long term performance of the acoustic-emission sensor and its error rate. For automated detection of the system different signal processing strategies were tested, each with a different level of information extraction and calculation effort. Two of the algorithms are well known; the envelope detection method as well as a classical filter method. The third algorithm is especially designed for the acoustic-emission sensor. The so called *frequency pattern recognition algorithm* is designed to detect the short term frequency patterns from the oscillating resonators and separate them using frequency signatures. The main target is the independent recognition of different resonant structures solely having one accelerometer. The algorithm is implemented using simple and efficient linear-algebraic matrix computation. This enables not only calculating the resulting coefficients but also their variances which is of special interest in instrumentation. Moreover, the algorithm utilizes a recently published method for windowing using orthogonal Gram polynomial basis functions of low degree.

The introduced measurement concept is patent pending.

1.1 Economical Motivation

Plastics are one of the most important materials in the 21st century [184]. In Fig. 1.1 the development of the world plastics production as well as the European plastics production are shown for comparison over a large time span. It is seen, from the early beginning of polymers an ongoing increase of the yearly output is happening, except for the duration of economic crisis. In the year 2010 about 280 mega tones of plastics were produced worldwide [148].

1.1.1 Injection Molding

Injection molding is the most important process to produce complex technical plastic parts [2, 31, 92, 97, 180]. The process has developed over the last 50 years to a high output, fully automated, precise finished goods production process. In Fig. 1.2 a typical injection molding cycle is shown. During the injection phase the melted polymer is injected into the cavity via the nozzle of the plastification unit. At the same time the mold is clamped together with the clamping force building up a sealed chamber in the mold, called cavity. The filling of the cavity is volume rate controlled meaning that the movement of the plastification screw is velocity controlled. Having a backflow barrier installed at the screw tip the melted polymer is forced to flow into the cavity. At the switch-over point, which is the transition from the injection phase

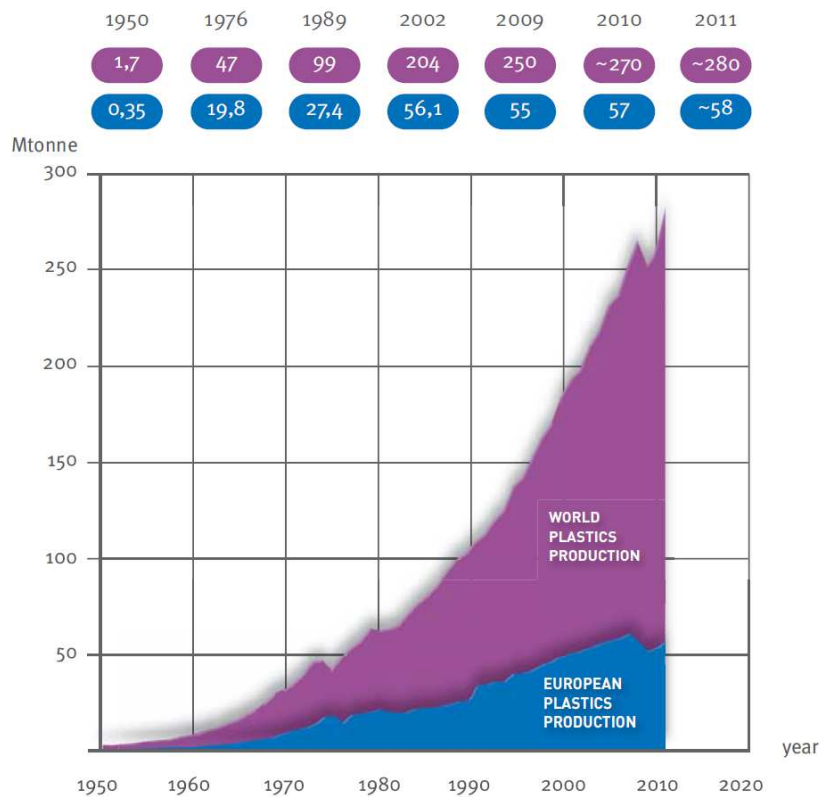


Figure 1.1: Worldwide and European plastic output from 1950 to 2010. The data includes Thermoplastics, Polyurethanes, Thermosets, Elastomers, Adhesives, Coatings and Sealants as well as PP-Fibers. Not included PET-, PA- and Polyacryl-Fibers [148].

to the pressure holding phase, the velocity controlled filling is switched to pressure controlled filling/holding. The task of the pressure holding phase is to compensate shrinkage of the polymer which is a result of the solidification process. Holding pressure is consequently an essential phase for the resulting part quality.

The mold respectively the cavity gives the melted polymer its shape and also dissipates the heat out of the polymer part. It is desired to cool the part homogeneously to minimize warpage. This is achieved by positioning sufficient cooling channels underneath the cavity surface in a way to obtain a homogeneous cavity surface temperature. During the solidification time the plastification screw starts rotating and moving backwards. The back-flow barrier is a mechanical part and is opened through the first backwards movement of the screw as a result of inertia forces. The rotation of the screw melts the polymer and the melt is positioned in front of the back flow barrier

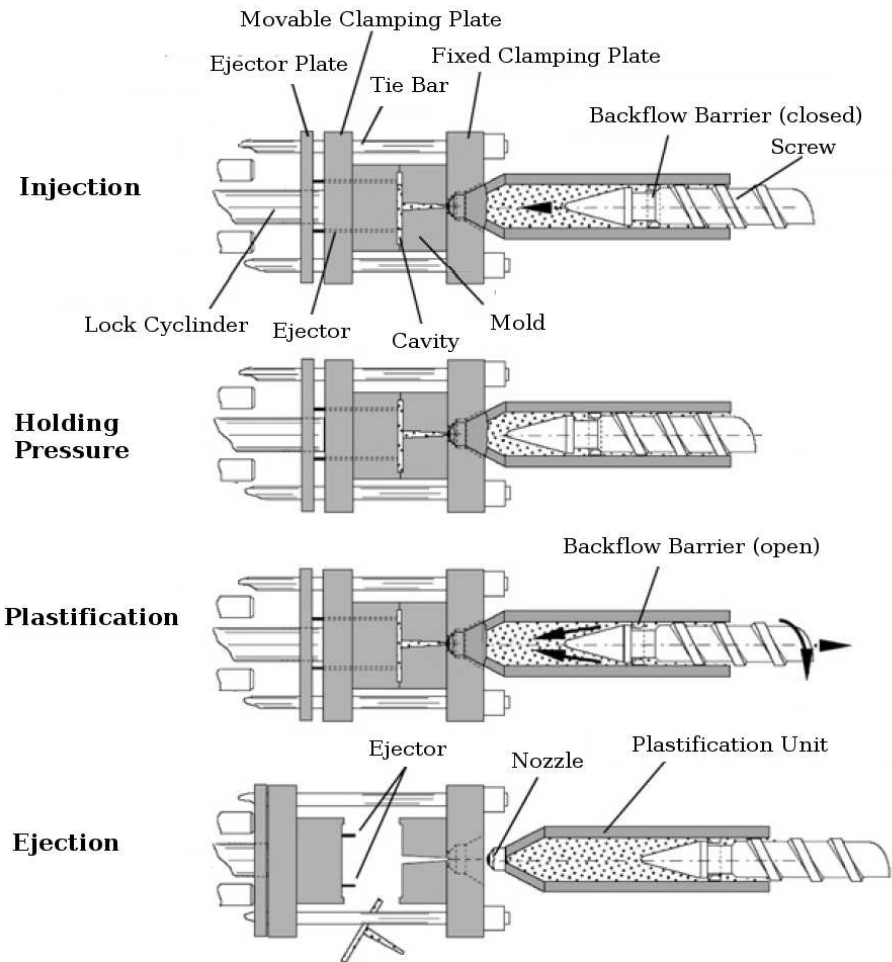


Figure 1.2: Typical injection molding cycle in reference to [164].

waiting to be injected in the following cycle. The melting process is mainly driven by friction forces as well as barrel heating.

As soon as the ejection temperature of the polymer is reached the mold is separated and the produced part is ejected using ejector pins. An option is to pull back the plastification unit during solidification time (after plastification is finished or during plastification if a needle valve gate is used) and ejection phase to reduce heat transport from the hot plastification unit into the cold mold. After ejection of the part the mold is closed and the plastification unit is connected to the mold again to reach the origin of the injection molding cycle.

Injection molding is a process designed for high output. Especially since

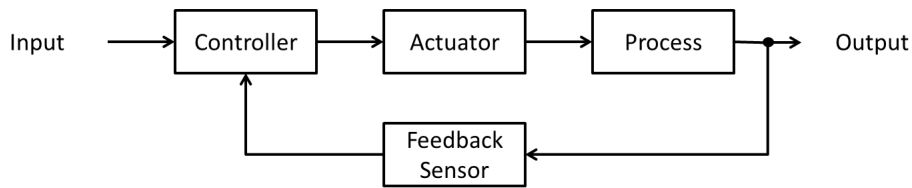


Figure 1.3: Feedback control system in reference to [72].

the 1990s a higher increase of the annual manufacturing productivity rate is recognized. The annual increase¹ between 1950 and 1990 is about 0.8% per year and since then a higher rate of 1.5% is recognized [97]. A similar trend is shown in Fig. 1.1 for the European market with a breakpoint around 1990. In Kazmer [97] three main reasons for this increase are listed comprising *improved manufacturing system design*, the *reduction of number of employees* as well as a *higher level of automation*. For automating systems it is important to obtain information from the current process state and feed this information back to the control system. This enables correcting occurring system disturbances and therefore reproducing identical cycles again and again. Only when continuously controlled process control is used part quality can be ensured reducing faulty manufactured parts.

In Fig. 1.3 a typical feedback control system is shown [72]. An input parameter, also called set parameter, is compared in the controller to the output parameter, e.g. detected by a sensor. The difference of the set point to the currently measured process state is taken as the input for the controller which governs the actuator. With manipulating the actuator the process can be regulated towards the desired set point. To be closer to the part quality it is important to measure process values near the location where part quality arises - within the cavity. Consequently, in-mold sensors are required to obtain this information.

1.1.2 Injection Molding Process Control

Injection molding is a highly dynamic process which needs continuous process control for compensating varying parameters [31, 97, 194]. The injection molding process mainly happens in the melt state of the polymer. This consequently yields the desire to precisely control the melt temperature for consistent product quality, e.g. [66, 94, 110, 115]. Furthermore, the melted

¹The data is from the United States manufacturing market and is taken from Kazmer [97].

plastic needs to be deformed into the desired shape. Therefore a pressure or force has to be applied on the melted plastic. Finally, a heat transfer is necessary to solidify and maintain the part in the desired shape [1,92,97,180]. As it can be seen, it is mainly all about temperatures and pressures which need to be controlled to form constant product quality.

For machinery control a variety of sensors with the ability to detect different measurement parameters are necessary to realize closed-loop control, e.g. measuring the melt temperature or injection rate. Thereby a lot of effort went into designing robust control systems for the injection molding machine improving response and repeatability [2,64,100]. This development results from the fact, that for many years the machine was the center of interest in research, e.g. [31,66,93,94,98,115]. From an economic point of view this is comprehensible. Every investment in the machine can be used for all clamped molds on this particular machine whereas an investment in one single mold is just usable for this particular mold. Consequently, an investment in the machine has a higher return on investment in short term consideration since it can be used for every mold available.

In [98] Kazmer et al. point out that the vast majority of product machinery still uses conventional sensors for closed-loop control, regulating the process via machine set-points. In doing so, typically manufacturers use this machine-centric approach with the set control limits hoping that their setup is *good enough* [98]. However, there is a good possibility that the part quality may wander outside the set quality limits, due to a number of unpredictable reasons, which include ‘variation in material properties (particularly when reground resins are used), change in the ambient environment (e.g., humidity or temperature in the shop), and machine characteristics (particularly those using hydraulic power)’ [31]. So, the in-situ states of the polymer in the mold are neither accurately observed nor properly controlled, leading to suboptimal processes, low yields, environmental waste and finally costs² [98]. In addition Kazmer et al. claim, that *there is an urgent need for more advanced and intelligent in-mold sensors that can provide comprehensive, real-time state feedback of the process internal to the mold where the product is formed*. In Chen et al. [31] it is mentioned that *the lack of online quality feedback of part quality is one of the two major challenges for the implementation of real-time quality control*.

In [194] Wang et al. propose a system to classify the measurable variables for injection molding. The system provides three levels: The first level contains machine variables. This set of variables can normally be well and indepen-

²The costs arise as a result of faulty parts and consequently higher processing times since the parts have to be redone.

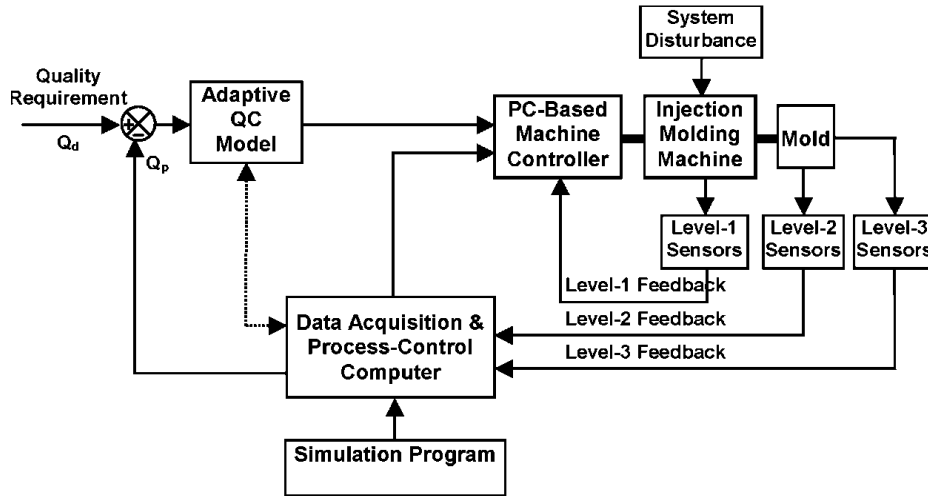


Figure 1.4: Multi-level control system architecture describing the three level system of process control in injection molding [194].

cently controlled for instance by proportional–integral–derivative (PID) controllers. As an example for level one variables the temperature of the barrel (divided into different zones) or the pressure during packing/holding phase is mentioned. The second level of measurable variables are process variables which are dependent. They depend not only on the process conditions, but also on the material, the machine and the mold configuration used. Level two variables are for instance melt-temperature, melt pressure or melt front advancement. The responses of the process are quality criteria, classified as level three variables. Part weight, shrinkage and warpage or optical defects are members of the level three variables. The control of these variables is the ultimate focus of a control system.

Using this classification system the acoustic-emission sensor is a level two sensor, dedicated to deliver the current process condition from the inside of the mold.

In Fig. 1.4 a possible control architecture for such a three level system is shown. It consists of one feed-forward loop and three feed-back loops. Initial process conditions are obtained using numerical simulations. The results of the numerical simulation as well as the obtained level-2 and level-3 measurement values are process within the process-control computer. In addition an adaptive quality control model is used to alter the machine process parameters to modify the process and compensate system disturbances and receive the desired part quality. All the measurement values are directly obtained within the mold using level-2 and level-3 sensors. Machine parameters are monitored too and are process within the machine controller [194].

For control of the injection molding process a proper control model is needed. A controller evaluates the detected sensor information and manipulates an actuator which influences the process. Over the last decades several different control strategies have been developed, all with the target to make the process more reliable and repeatable. In Chen et al. [31] a review over the development is given and summarized in the following paragraph.

In general the molding machine control (level one) is developed better compared to the process control (level two) or quality control (level three). Besides conventional PID controllers, which sometimes cannot guarantee high standard machine performance, additional advanced control technologies were developed, e.g. [19, 33, 34, 77]. Since process variables (level two) are more closely related to quality variables (level three) it is rational to control the process variables instead of the machine parameters [83]. Control strategies using process parameters as the input go back to the 1980s where Agrawal et al. [2] suggested introducing 'plastic variables'. These variables are controlled to achieve desirable and consistent part quality. The plastic variables describe the true condition of the plastic within the mold.

Melt pressure has an essential role in determining the part quality since it is dependent on many different other process variables. The pressure can be measured at different locations with different accuracy, e.g. within the mold, within the plastification barrel in front of the screw tip or by measuring the hydraulic pressure or energy consumption of the electric drive. Process control strategies which use the melt pressure as the input information were investigated to enhance part quality. In excerpts three control strategies are mentioned, i.e. the self-tuning regulator by Gao et al. [56], model predictive control by Dubay [42] or artificial neural network (ANN) for describing the relationship between cavity pressure and machine parameters by Woll et al. [198, 199]. There are other important process variables, such as the melt temperature, for which additional control strategies were developed. Again ANN strategies combined with physical models were investigated by Zhao and Gao [206] for controlling the melt temperature. Further algorithms, like generalized predictive control (GPC), were successfully tested for controlling the melt temperature [43, 151]. Collins [36] developed a multivariable control system, manipulating a set of machine parameters to take the complex process dynamics into account. Other ways of controlling process variables have been investigated, e.g. monitoring mold separation, which is an easy to access estimator for the cavity pressure. The mold separation is a reliable indicator for part weight and thickness [2, 18].

As it can be seen there are a lot of strategies to use the recorded process data. The problem is there are just few of them commercially available. Chen et

al. [31] consequently insist on developing quality sensors and control-oriented process and quality models to enhance part quality in production.

1.1.2.1 Process Window

Level two variables are expanded, compared to the level one variables, by the process, the material and the mold. When starting up a new mold, a molding engineer is setting up the injection molding machine based on the information from the material supplier, the mold designer and to a great extent on his experience. In a time consuming trial and error procedure the processing parameters are found to match the demanded properties of the produced part. Now it is possible to produce good quality parts but there is a chance of leaving the quality part processing window due to unpredictable reasons which include variation in material properties, environmental changes, e.g. humidity or temperature, machine characteristics or mold configuration [31]. All the listed influencing parameters have a different impact on part quality with a complex interaction between the variables [150, 157]. One method to display the correlations is to plot a process window. The following section about process windows is summarized out of Kazmer [97].

In Fig. 1.5 a process window in dependence of two different process parameters³, x_1 and x_2 , is shown. For each quality attribute, y_i , with i an index for each attribute, a lower and an upper specification limit (LSL_j and USL_j respectively) is set,

$$LSL_i < y_i < USL_i. \quad (1.1)$$

In case of an undefined limit, the boundary is just set with $\pm\infty$, e.g. for maximum cost of the part no lower specification is necessary. However, there are additional limitations. For instance, the ram velocity has a specific range limiting the process parameter x_i . Each of the process conditions, x_i , is constrained by lower and upper process limits, LPL_i and UPL_i ,

$$LPL_i < x_i < UPL_i. \quad (1.2)$$

The specification limits as well as the process limits define the *nominal process window*. In general it can be stated that each additional active limitation reduces the region of the process window. However, there are not active constraints, too. In Fig. 1.5 the process limitation $x_1 > UPL_1$ or the specification limit $y_1 < LSL_1$ is a non-active limitation, indicated by a dashed line.

³In principle it is possible to describe a process window in dependence of all n process parameters. However, for easier visibility and comprehension it is solely shown for two parameters.

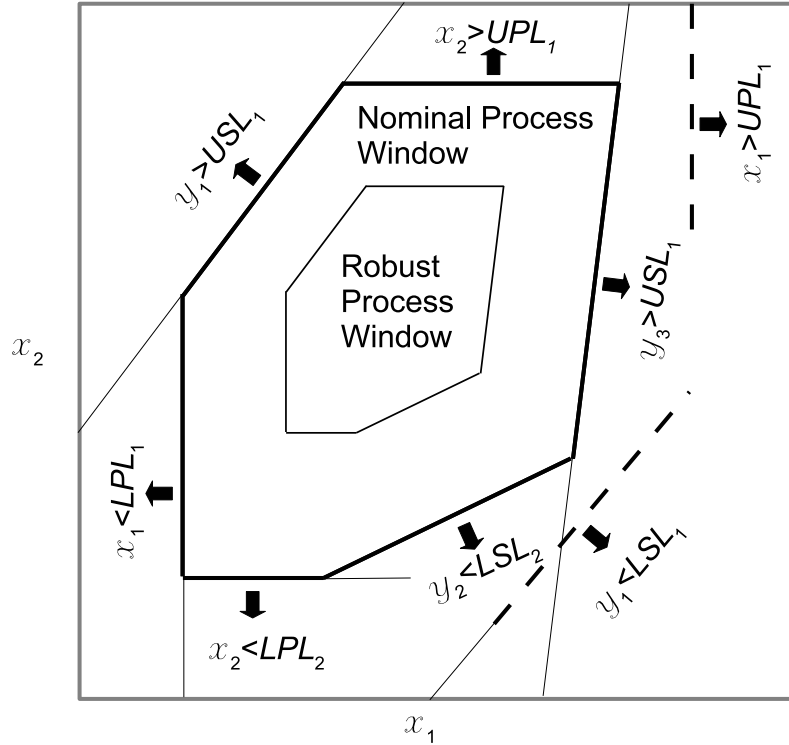


Figure 1.5: Process window for two different process parameters x_1 and x_2 limited by lower and upper quality specification attributes ($LSL_j < y_j < USL_j$) as well as lower and upper process limitations ($LPL_i < x_i < UPL_i$). In reference to Kazmer [97].

These constraints are said to be *dominated* by the other tighter constraints $y_2 > LSL_2$ and $y_3 < USL_1$.

For each pair of process conditions intersecting inside the nominal process window a part with the desired quality attributes should be producible. In fact, all intersecting points near the boundary may have poor results. The reason is that there is variation in the process states x_i as well as uncertainty in the process models y_i . Consequently a smaller and more robust process window has to be established for which the process is insensitive for variation. In Kazmer [97] two methods are proposed for finding such a robust process window, first the Monte Carlo analysis and second the constraint based reasoning.

An important aspect is the influence arising from the processed material, i.e. batch-to-batch variation. The batch-to-batch variation depends on the type of material processed. In Angelova et al. [3] it is written that for synthetic

polymers (such which originate from oil) the variation is small. When processing bio-polymers the batch-to-batch variation is significantly higher due to their 'bio-preparation' in living organisms, e.g., plants or crustaceans. The second aspect is the environment in the production shop. Changes in the shop, e.g. humidity and shop temperature [157], influence the cavity surface temperature leading to different process conditions. This can cause large problems during the manufacturing of high quality parts and consequently shop climate needs to be considered in the planning phase [68]. Since machines are developed towards a high repeatability with closed-loop feedback controls trying to avoid a drift in the machine performance [64, 100], the listed influences are small when using new highly developed injection molding machines. However, not every influencing parameter can be compensated by having a high cycle-to-cycle repeatability of the machine to achieve high quality parts, e.g. the influence of the material batch-to-batch variation or mold influencing parameters. As a result, the current process conditions have to be recorded and evaluated to influence the set points of the machine to compensate variations for achieving constant part quality.

1.1.2.2 In-Mold Sensors: An Economic Review

In the mold the final part quality is shaped and therefore needs special attention. It is very important for prediction and closed loop control of the process to measure the in-mold conditions and not to use process parameters gained at any other location than the cavity, e.g. nozzle pressure or screw position [35, 88, 195].

For producing high quality parts a special knowledge about the surface temperature of the mold is necessary. In literature it is stated that the mold temperature respectively cavity surface temperature is a critical parameter on the final quality of the part, e.g. [111, 118, 122, 144, 162, 177, 200]. Another important aspect is the pressure loss and the pressure propagation in the cavity which is highly dependent on a variety of other variables, e.g. melt viscosity or melt temperature. Therefore melt pressure⁴ is often measured as a vital aspect for parts with tight tolerances or as part quality estimator [42, 83, 118, 123, 197].

Since the mold surface temperature and the cavity pressure are the most important process variables sensors have been developed to sense these two parameters and are commercially available in a wide range [9, 71, 90, 97, 99].

⁴Melt pressure can be sensed at different locations with different accuracy, e.g. using cavity pressure sensor, a pressure sensor within the plastification barrel in front of the screw tip or by measuring machine hydraulic pressure or energy consumption at electrical machines.

However, Groleau [71,97] mentioned that in the year 2002 less than 1% of the injection molding processes in the United States have been instrumented with in-mold sensors and these sensors are mainly temperature couples or pressure transducers⁵. In an interview [11] with Mr. Behrens, the head of platform 'spritzguss-schulung.de', he claims that solely 5% of the molds in Germany⁶ are instrumented with in-mold sensors and a rethinking in terms of a holistic view of the process is necessary. In the year 2013 Kazmer guessed⁷ that the number of instrumented molds worldwide, including India and China, is below 1%. Although both numbers are just guessed from experience they show how little attention the instrumentation of the process gets. Hence, there must be several reasons for companies to avoid installing in-mold sensors and not to use the advantages of the recorded data.

All the commercial available in-mold sensors require wires for data transmission and power supply [113]. Consequently, wire ducts from the sensor head to the outside of the mold are required. Increasing complexity of the molds exacerbate finding sufficient space for these wire ducts, especially when trying to minimize the mold structure modification to reduce total costs of the mold [61]. In addition, a conflict between components such as ejector pins, cooling lines or sliders is present when implementing sensors [97,121]. This conflict reduces the chance of implementing sensors since the listed mold components are crucial for producing high quality parts, too.

Another important reason for not implementing in-mold sensors are costs. Particularly, when a multi-cavity mold needs to be equipped with in-mold sensors in every cavity, e.g. cavity wall temperature sensors and/or cavity pressure sensors per cavity, the total costs of the sensor equipment can exceed the 10% total cost level of the mold. As an extreme example in an interview with Martin Mitterer from the company Boida, St. Ulrich in Austria, it is claimed, that if a 32-fold multi-cavity mold would be equipped with in-mold pressure sensors in each cavity the costs for the sensors would exceed the total costs of the mold [131].

To estimate mold construction and mold production costs predictive calculation models were developed, i.e. by Kazmer [96]. The calculation model is

⁵The number was actually presented in a keynote speech by Groleau, president of RJG Inc, leader in injection molding training, technology and resources. However, there is no written publication including this number besides the citation in Kazmer [97].

⁶The reference is from the year 2012 so most probably the number is from the year before.

⁷Personal communication, February 22, 2013.

a top-down approach of which one aspect is devoted to sensors⁸. The total costs are calculated as,

$$C_{total_mold} = C_{cavities} + C_{mold_base} + C_{customization}, \quad (1.3)$$

whereby the factor $C_{cavities}$ consists mainly of the material costs, the machining and the finishing costs. The factor C_{mold_base} consists mainly of the mold mass multiplied by the price of the used metal and a fixed offset value. $C_{customization}$ is a sum of the following aspects,

$$\begin{aligned} C_{customization} = & C_{cavities} \sum_i f_{cavity_customizing}^i \\ & + C_{mold_base} \sum_i f_{mold_customizing}^i, \end{aligned} \quad (1.4)$$

whereby the coefficient $f_{cavity_customizing}^i$ corresponds to the factors governing the costs of customizing the cavity inserts. The coefficients $f_{mold_customizing}^i$ correspond to the factors governing the costs of modifying the mold base. The variable i represents the effort for each subsystem of the mold, i.g. feed-system, cooling system, ejector system, structural system and miscellaneous. The coefficients $f_{cavity_customizing}$ and $f_{mold_customizing}$ are listed for a wide field of modifications in [96]. Tab. 1.1 shows an excerpt for getting an impression of what different modifications cost. The costs for implementation of an in-mold sensor are shown, too. The factor for adapting the cavity to implement an in-mold sensor is $f_{cavity_customizing} = 0.05$ and the factor for the mold is $f_{mold_customizing} = 0.1$. These values are quite similar to those of implementing a round ejector pin.

In Rawabdeh and Petersen [158] it is mentioned that construction effort costs the same as the costs of the sensor itself. Hence, the effort to implement a sensor within a mold has a significant financial impact and needs to be considered.

A third reason why industry does not implement in-mold sensors is the dependence of the process on the sensor reliability. Especially, when the sensors are used for controlling a strong dependence on long-life functionality with high reliability exists, e.g. detection of the switch-over point. If one of the sensors fails at least one half of the mold has to be disassembled in a time consuming task because production cannot be continued without the signal of the sensor. Consequently, life expectancy as well as their reliability

⁸In this approach only the construction effort for the mold and the mold production costs are considered and not the costs of the sensor equipment as such.

Table 1.1: Cost coefficients for various parts of mold and cavity taken from [96].

| Modification | $f_{cavity_customizing}^i$ | $f_{mold_customizing}^i$ |
|------------------------------------|-----------------------------|---------------------------|
| Round ejector pin | 0.1 | 0.1 |
| Actuated core pull | 0.4 | 0.5 |
| Two plate cold runner system | 0.05 | 0.1 |
| Hot runner system with valve gates | 0.5 | 4.0 |
| Mold temperature sensors | 0.05 | 0.1 |
| Mold pressure sensors | 0.05 | 0.1 |

are a crucial topic for in-mold sensors. In Kazmer [97] it is stated that the overall lifetime of a sensor varies greatly in dependence of design and the conditions at which the sensor is operated. Due to the cyclic load, mechanical parts may fatigue across many pressure and thermal cycles. When the sensor is directly exposed to the melt abrasion and corrosion are common, too. When the sensor has an active circuit within the sensor head, high temperatures as they occur in injection molding reduce life time. In Sato et al. [165] it is claimed, that a capacitor may have an expected mean time to failure (MTTF) of 20000 hours at a temperature of $20^{\circ}C$. However, the MTTF reduces dramatically to 2000 hours when operated at $85^{\circ}C$. Consequently, it is desirable to have non active circuits under cyclic mechanical and thermal load to improve life expectancy of the sensor.

1.2 In-Mold Sensing Technology

Obtaining measurement data from the inside of the mold is investigated for many decades now. Unfortunately, only a few measurement concepts reached the status of being commercially available. In this chapter both types of sensors are discussed in detail, commercial available and only in literature mentioned sensing concepts.

1.2.1 Common In-Mold Sensor Types and their Usage

On a commercially available basis there mainly two big players in Europe who offer in-mold sensors for injection molding: Kistler Instrumente AG, Winterthur, Switzerland, and Priamus System Technologies AG, Schaffhausen, Switzerland. Both companies offer a wide range of cavity wall temperature sensors with varying head diameters as well as cavity pressure sensors again with varying head diameters. There is another company, called FOS Messtechnik GmbH, Schacht-Audorf, Germany, offering cavity wall temperature sensors and cavity pressure sensors, too. Additional specialized sensors are provided using infra-red (IR)-radiation for temperature measuring, like the FOS type MTS 408 - IR - STS.

Kistler and FOS additionally offer combined sensors where at least two physical values can be measured in one housing. Kistler offers combined temperature and pressure sensors, like the Kistler 6188AA. FOS has combined pressure and IR sensors, like the MTPS 408.

In injection molding machines there are two additional manufacturer for sensors dedicated for melt state sensing. Both manufacturers have specialized sensors for detecting melt temperature and pressure in the region of the nozzle as well as in hot runner systems: Dynisco Europe GmbH, Heilbronn, Germany, and Gefran SPA, Provaglio d'Iseo, Italy. As it can be seen the main focus is definitely on temperature and pressure instrumentation of the polymer melt at different stages of the injection molding process.

Besides their obvious ability to measure the cavity temperature or cavity pressure these sensors can be used for gaining additional information. Cavity wall temperature sensors are perfectly suited for melt front position detection, respectively detecting the temporal moment the melt front passes the sensor head.

In injection molding there are some cases where it is of special interest to know the temporal point the melt front passes a location. The conventional method of molding a part is divided in two phases, the volumetric filling phase and the pressure holding phase [1, 92, 103, 160, 180]. At the switch-over point⁹ the cavity is typically filled up to about 98%. In Sheth et al. [172] and Bader [7] a more detailed discussion on positioning of in-mold sensors for switch-over point detection is given. To detect this point several different methods are known whereof seven different are presented and compared in Kazmer et al. [99]. Two of the presented methods use in-mold sensors, i.e.,

⁹The point the machine is switched from volumetric filling to pressure packing/holding.

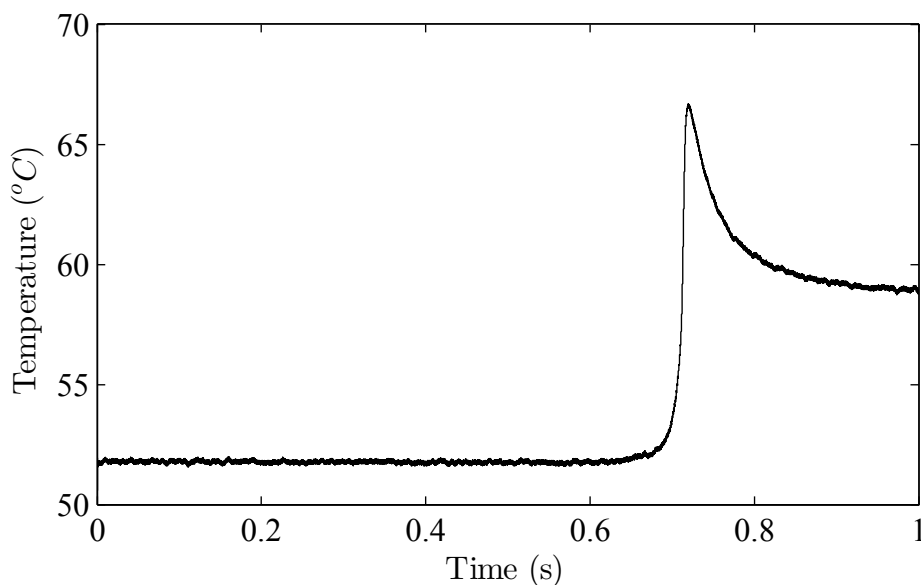


Figure 1.6: Cavity temperature sensor signal monitored over the time of an injection molding cycle. At 0.7s the temperature signal increases indicating the moment of passing melt front.

in-mold pressure sensors and cavity wall temperature sensors. In this manner a cavity temperature sensor is not used for actual temperature sensing but only for recognizing a steep increase in the detected temperature originating from the hot melt [9, 99].

Kazmer et al. [99] report that the response time of type N thermocouples with a head diameter of 1 mm is 0.01 s, respectively 10 ms. In chapter *Cavity Wall Temperature Response Characteristic*, page 98, response time measurements for type N thermocouples with a head diameter of 0.6 mm were performed achieving faster response times than those reported by Kazmer. Due to their fast response time thermocouples are perfectly suitable for switch-over point detection if positioned correctly [7, 99]. As soon as the hot melt front reaches the cavity temperature sensor its signal respectively the temperature at the sensor head rises steeply. In Fig. 1.6 this behavior can be seen for one cycle. At 0.7 s the temperature signal increases steeply indicating the moment of passing melt front.

Cavity pressure sensors are suitable for detection of the switch-over point, too, as they record a significant increase in the cavity pressure level as soon as the melt front reaches the part flow path end, e.g. [1, 84, 86, 92, 172, 180]. The other five methods for switch-over point detection presented in Kazmer et al. [99] use machinery variables to calculate/measure the 98 % volumetric

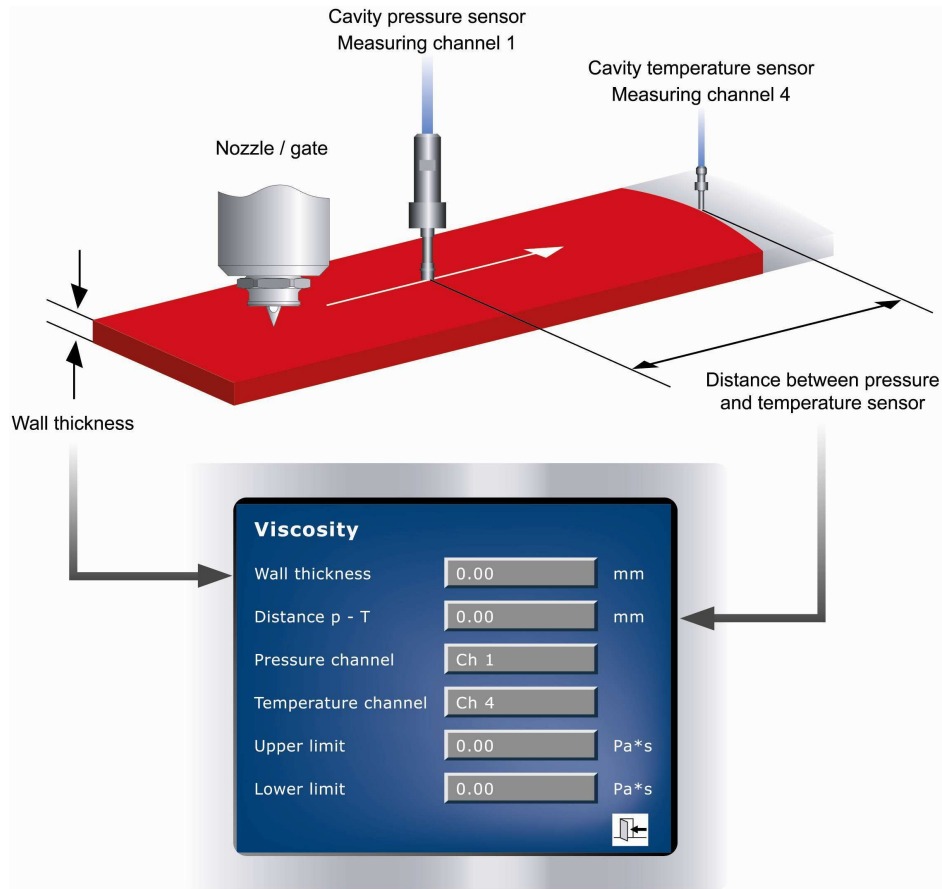


Figure 1.7: Viscosity measurement device from Priamus System Technologies. An in-mold pressure sensor as well as a cavity temperature sensor are combined for measuring process parameters to calculate the viscosity via Eq. 1.6 [155].

filling point, respectively the switch-over point. However, in several publications it is insisted to use in-mold sensors for the detection of the switch-over point because it is crucial for continuous high part quality to switch-over at the precise point to avoid over- or under-filling [36, 99, 100]. Panchal and Kazmer [143] presented a method for in-situ shrinkage measurement using a pressure sensor. They examined the strain recovery of an initially loaded pressure sensor delivering results about the polymer shrinkage behavior. Priamus System Technologies [155] uses the combination of a cavity temperature sensor and a pressure sensor for calculating the viscosity in a constant flow channel. In Fig. 1.7 the measurement setup is shown. A cavity pressure sensor as well as a temperature sensor are positioned in a known distance

ΔL . When the melt front reaches the pressure sensor a timer is started. As soon as the melt front reaches the cavity temperature sensor the timer is stopped, resulting in the time difference Δt . Consequently the melt front velocity can be calculated as,

$$v_x = \frac{\Delta L}{\Delta t}. \quad (1.5)$$

The pressure drop over the length is calculated under the assumption that the melt front pressure is constant at ambient pressure¹⁰. Hence, the current value of the pressure sensor minus the constant value is considered as the pressure drop value dp/dL . Finally, the cavity height H has to be known. With all the values known the average viscosity η can be calculated as,

$$\eta = \frac{H^2}{12v_x} \frac{dp}{dL}. \quad (1.6)$$

It has to be mentioned that the system delivers valid absolute viscosity values only if the cavity height as well as the width, which is important for melt front velocity, is constant over the measurement length ΔL . Since cavity shapes rarely fulfill these geometrical requirements the system is only able to measure relative viscosity changes but not the absolute viscosity level if the flow channel geometry is varying over the measurement length. However, a good field of application for this system is to use it in runners with constant diameter.

Another type of in-mold sensors are infra-red (IR) sensors. IR sensors have been known in injection molding for up to 40 years [12, 50, 98, 104, 116, 140] but are avoided often due to their expense, fragility and calibration difficulties [133]. The IR sensor detects the radiation sent off by the melt and is correlated to a temperature. Besides sensing the temperature of an emitting object a big advantage of IR sensors is their ability of detecting the passing melt front instantaneously. It is reported that fast response times of up to 1 to $10^{-2} \mu s$ were measured [91, 98, 114]. However, when used for temperature sensing the problem is that a weighted average of the temperature from an unknown measuring volume is detected which is dependent on the absorption coefficient of the polymer [55, 132]. In the worst case, even the opposite cavity wall temperature is detected resulting in zero information about the polymer state.

¹⁰Although it is unknown which pressure value is used in the system by Priamus, the melt front pressure is mostly considered with ambient pressure. However, this is just valid if the air in the cavity chamber is not compressed and does not act on the melt front. Consequently, optimal venting of the cavity is required.

Another field of application for IR sensors is continuous quality control. Near infrared spectroscopy is mainly used in extrusion [62,196] but was also applied for injection molding. Dumitrescu et al. [44] investigated the usage of near infrared spectroscopy to detect online color concentration and batch moisture for different polymers. Ghita et al. [63] used near infrared spectroscopy to detect variations in injection speed and melt temperature as well as color concentration.

Up to now, the presented sensor types are more or less commercially available from distributors. In literature many more approaches for process instrumentation are published from which an excerpt is presented as examples of what is measurable with laboratory measurement equipment. For the best of the author's knowledge none of the presented systems is or was commercially available (in Europe) respectively is used in a significant manner.

The idea of using structure-borne sound in injection molding is not new but much less common than pressure or temperature sensors. In Ujma et al. [191] a tool is presented to monitor an injection mold via structure-borne sound and detect maintenance intervals by sensing unusual sound by wear. Additionally, it is claimed to detect crack initiation during running production. A similar system is described in a patent by Haidlmair Holding GmbH, Austria, [168].

In Seuthe [169] a method is presented using ultrasonic structure-borne sound for monitoring and optimizing the injection molding cycle by recording the resonance spectrum of the mold during or after the production cycle. By generating one or more reference models every occurring change of the current recorded spectrum to the reference model can be recognized and may be referenced to a process change. Beside general occurring injection molding failures no specific failures are listed which could be recognized by the system. Only special attention is given on mold attrition which is detectable by the system. In another publication by Seuthe [170] a method is presented to investigate a part produced by injection molding. The part is excited with an energy impulse and its frequency response is measured. Using a reference spectrum enables the detection of differences within the part.

In Thomas et al. [186] a similar system is described where ultrasonic sound is introduced into the injection mold and the continuous resonant frequency spectrum is recorded monitoring any change in characteristic parameters. Characteristic parameters mentioned are injection rate, start of packing phase or stop point of injection or packing phase.

The listed cites are all patent specifications and consequently no measurement results are presented. Hence, it cannot be estimated how well the

presented ideas work in production.

Measurement methods using ultrasonic scanning across the mold cavity are used for different applications. The ability of the ultrasound to interrogate noninvasively, nondestructively and rapidly enables it for the detection of parameters concerning the surface and internal regions of the material [109, 193]. In injection molding the filling behavior of the cavity is of special interest. By using ultrasonic scanning methods it is possible to determine the melt front [193], the orientation of the polymer [45], fiber orientation in the polymer melt [10,78] or even perform in-situ measurements of shrinkage [124]. In He et al. [79] principle correlations and effects of process variables to the ultrasonic velocity and attenuation were investigated, e.g. temperature and pressure as well as changes in the morphology of the polymer. Another field of application of ultrasound transducers is the improvement of upcoming weld lines during injection molding by an oscillation unit influencing the morphology at the weld line interface [112]. An additional advantage of ultrasonic measurement is the possibility to examine the polymer in the melt phase as well as during solidification and even in the frozen state achieving continuous measurement data [109,147].

A different measurement system for detecting the melt front progress in the cavity is presented by Chen et al. [27, 29]. A capacitive transducer is implemented in the mold enabling the measurements of the melt front position in real-time. Due to the measurement principle just flat parts can be monitored by the system. This limitation results from the fact that a flat plate capacitor has to be formed. In Fig. 1.8 the capacitive transducer (CT) output signal over time is plotted. In this case the CT value stands for the flow front enhancement. In the plot measurements for different constant filling velocities are shown indicating the functionality of this sensor system. In addition, the melt front velocity can be derived from the melt front position mathematically via calculating the derivative.

In Kazmer et al. [98] and Asadizanjani et al. [5,58] a feasibility analysis of an in-mold multivariate sensor is published. In just one housing the sensor should be able to detect not only melt temperature and melt pressure but also melt velocity, melt viscosity and cavity temperature. To measure these values of the melt at least an IR sensor and a pressure transducer have to be implemented in the housing. Additionally, a thermocouple or a resistance temperature detector is incorporated in the application specific integrated circuit (ASIC) to compensate local temperature. One possible design of the multivariate sensor is shown in Fig. 1.9. The sensor is protected by a housing in which a lens is implemented enabling the transmission of the

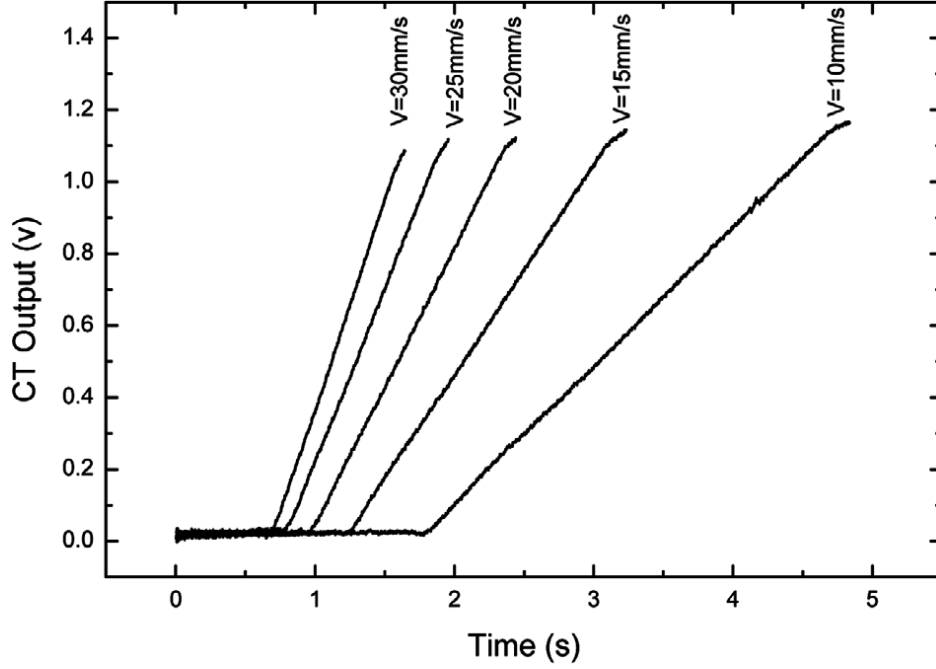


Figure 1.8: Capacitive transducer (CT) output signal, which represents the melt front enhancement, is plotted over time for different constant filling velocities [27].

IR irradiation. Below the lens a piezostack is located to obtain the current pressure level. The ASIC is implemented inside of the sensor to provide local signal processing of the data, reduction of the signal to noise ratio and provide process data in digital format.

From the different implemented sensor types it is obvious that the melt temperature can be obtained by the IR sensor and that the current pressure level can be obtained by the generated voltage of the compressed piezostack. A more detailed look is necessary to understand how the melt velocity and viscosity is estimated. In Fig. 1.10 *Right* the overflow behavior of the sensor head with the footprint area S_0 is shown. In each time step dt the melt front advances a distance dx . In dependence of the distance dx a different inclination of the IR sensor signal can be observed as shown in Fig. 1.10 *Left*. This velocity dependent behavior is a result of the amount of radiation which is sensed by the pyrometer. This dependence can mathematically be described via,

$$\frac{dT}{dt} = \frac{2r}{S_0} T_0 v_x \sqrt{1 - \left(1 - \frac{x}{r}\right)^2}, \quad (1.7)$$

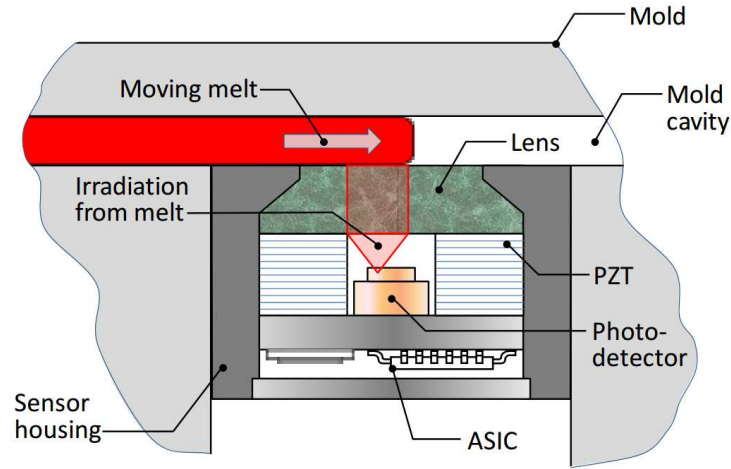


Figure 1.9: Possible design of the multivariate sensor housing the different sensor methods including IR sensor and pressure transducer [98].

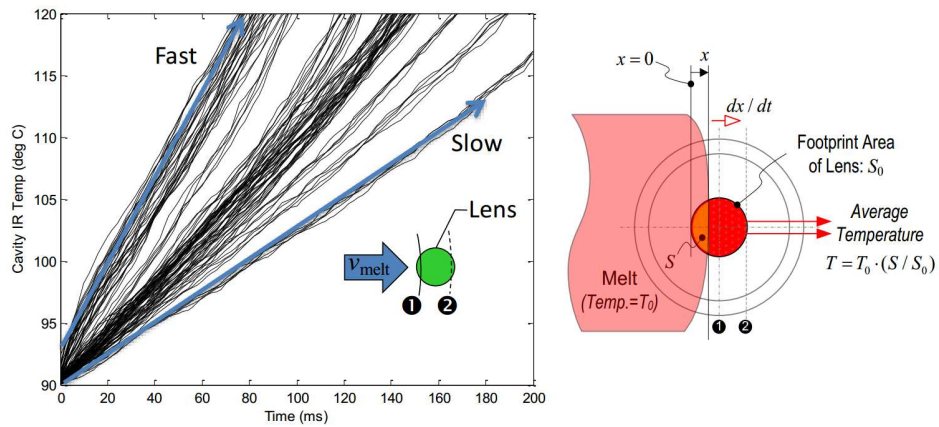


Figure 1.10: *Left:* Melt front velocity dependent response time of the IR sensor; *Right:* Principle idea of measuring the melt front velocity in dependence of IR response time [98].

with x as the melt front position, T_0 the melt temperature and v_x the melt front velocity. The radius r corresponds to the surface described by the footprint area S_0 of the lens. The equation can be rearranged to obtain the velocity as,

$$v_x = \frac{S_0}{T_0 2r} \left(\frac{dT}{dt} \right)_{max} . \quad (1.8)$$

When having the current melt front velocity v_x the melt viscosity η can be calculated via,

$$\eta = \frac{H^2}{12 v_x} \frac{dp}{dt}, \quad (1.9)$$

with H the cavity height, and dp/dt the temporal pressure gradient. The measurement concept was verified via experimental measurements by Pacher et al. [141].

Besides the hardware sensors there is also a field of research developing virtual sensors based on mathematical models. These models provide current information about the melt state in the mold using machine data as boundary conditions. First proposals without experimental data go back to 1996 presented by Speight et al. [174]. First experimental data verifying a virtual sensor was shown by Chen and Gao in 2000 [28]. In Lin et al. and Cheng et al. [32, 107] further research work is presented giving a detailed overview about the mathematical approach used for calculating the desired process values. Although several assumptions for easier calculation are made, e.g. isothermal filling phase and incompressible melt beyond the barrel, good results were achieved. A problem which is not mentioned in the publications is that precise material data are most essential for calculating process parameters [173] like melt front behavior.

Coming back to hardware sensors, all the presented sensors are tied to wires. Neglecting energizing and data transmitting wires would yield significant advantages for mold construction and mold handling during operation. Few researchers started presenting concepts in literature for wireless in-mold sensors which some are picked out and are presented in the following section.

1.2.2 Wireless In-Mold Sensor Types

In the last years with different approaches it was tried to detach in-mold sensors from the energizing and data transmitting wires. Wires within a mold are limiting in a plurality of ways. Often, it is hard to find space for wire ducts, since no intersection with ejector pins or cooling lines is possible. In addition, sliders are an area where hardly any sensor can be installed since the wires are always in danger of being ripped off. To reduce the required space of the wires they are as thin as possible resulting in small bending radii. The small dimensions, however, make them easily damageable. Consequently wireless sensors are desirable for injection molds.

When thinking of wireless sensors one of the first questions that arises is how to power the sensor and secondly how to transmit the obtained data.

Methods using a power storage, e.g. batteries, suffer from the fact that molds are used for continuous mass production over months or years in 24/7 shift operation. It is shown that current power storage cannot provide the necessary amount of energy for continuous sensor operation [4, 17, 51, 149]. In addition, batteries are not well suited when operated above temperatures of 150 °C [178] and batteries would occupy valuable space within the mold. The data transmission of the recorded signal yields some challenges, too. In Flammini et al. [51] the usage of radio-frequency (RF) for installing a wireless sensor network collecting temperature data from a processing machine was successfully investigated. However, no data was collected from the mold as such since additional challenges occur when using RF for transmitting data from the inside of a steel/aluminum mold. In Fan et al. [48] it is stated that the steel/aluminum, which is commonly used for building molds, is shielding RF signals. Consequently, the data communication is limited. In different application fields the usage of surface acoustic wave (SAW) is often used when wires cannot be used for the transmission of data. In Bulst et al. [20] a review of current sensors using SAW is presented. In Stevens et al. [178] a wireless temperature sensor network system making use of SAW for a switch-box temperature detection is presented. However, this kind of application is not tested/published for the field of injection molding yet.

In the year 2002 Zhang, Theurer, Gao and Kazmer [205] started developing a novel concept of a wireless self energized in-mold sensor yielding the possibility to detect the in-mold pressure wirelessly. Since 2002 a plurality of publications by different researchers of the working group were written extending the capabilities of this sensor system. Since it is the only comparable measurement system for injection molding to the system presented in this thesis a detailed look on the wireless sensor system is given. The following presented information was taken from several different publications including [5, 48, 58, 59, 61, 98, 185, 203–205].

In Fig. 1.11 *a*) two wired sensors are implemented in a mold. It can be seen that structural modifications of the mold are necessary for the data transmitting and supplying wires. In Fig. 1.11 *b*) the wireless approach is shown. The implementation effort is significantly lower for placing three sensors in the mold. Ultrasound, a mechanical electromagnetic wave, is used for transmitting the data. Ultrasound can propagate through the metal without limitation of an electromagnetic shielding effect [205]. For ultrasound generation a certain amount of energy is necessary which is converted from melt pressure to electrical energy. A piezoceramic element is compressed generating the necessary amount of energy [185]. The amount of energy is proportional to the melt pressure which is simultaneously measured. A secondary piezo-

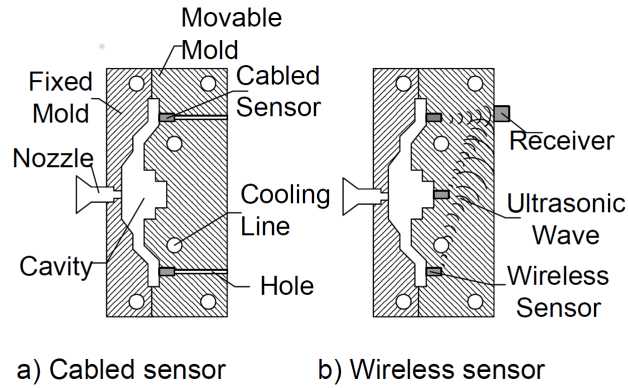


Figure 1.11: Schematics of a wired sensor *a)* and a wireless sensor *b)* installed in a mold [205].

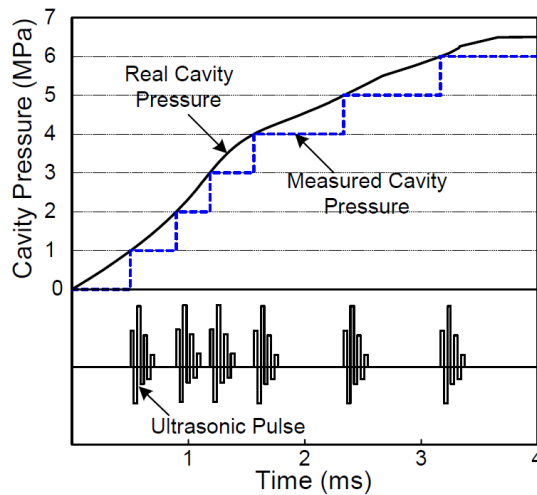


Figure 1.12: *Top:* Digitalization of the analog pressure curve into multiples of the threshold value; *Bottom:* For each pressure level a pulse is generated [204].

ceramic element starts vibrating and emits the measured pressure level in form of ultrasound. For energy minimization the detected pressure level is discretized and emitted in pulses. The discretization process result can be seen in Fig. 1.12 *Top*. The analog pressure curve is approximated by a step function whereby each step is a multiple of a predefined threshold. If the next step value is reached a pulse is emitted (see Fig. 1.12 *Bottom*). The

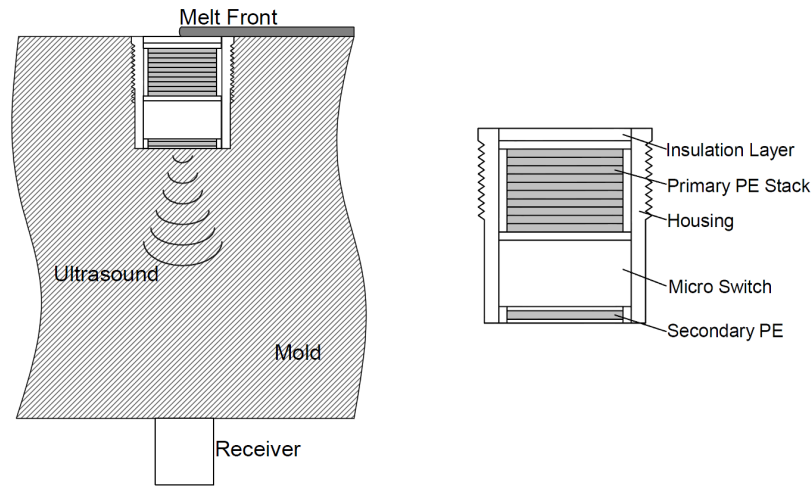


Figure 1.13: *Left:* Schematic setup of a mold with implemented wireless sensor. Energy is acquired from the passing melt front to transmit the obtained measurement values via ultrasound to a receiver mounted on the outside surface of the mold; *Right:* Design setup of the self energized wireless in-mold sensor consisting of two piezoelectric stacks (one for energy acquisition as well as pressure sensing, the second for ultrasound generation) and a micro-switch which digitalizes the analog pressure curve into pulses [205].

pulses are continuously recorded by a receiver mounted outside on the mold surface.

Fig. 1.13 shows the design of the wireless in-mold sensor, consisting of three main components [205]:

1. the primary piezoelectric stack for energy extraction as well as pressure measurement;
2. a micro-switch for digitizing the analog pressure curve into multiples of a preset threshold as well as charging the secondary piezoelectric stack and
3. a secondary piezoelectric stack for ultrasound generation.

When incorporating a multiple number of wireless sensors it is necessary to choose different carrier frequencies for identification of the source (Multiple-Transmitter-Single-Receiver configuration). The carrier frequency is set by varying the dimensions of the secondary piezoelectric stack. It is important to

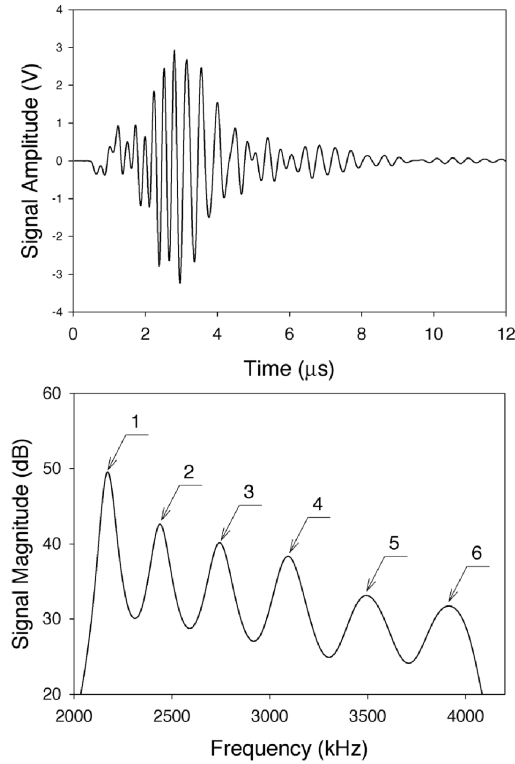


Figure 1.14: *Top:* Time domain signal of six pulses transmitted at the same time; *Bottom:* Frequency domain of the *Top* signal. All six pulses can be separated in the frequency domain [203].

choose dimensions which result in non-overlapping frequency bands to detect the individual transmitter [204]. In Fig. 1.14 *Top* a time domain signal of six simultaneously generated pulses from six different ultrasonic transmitters is shown. In Fig. 1.14 *Bottom* the signal is shown in the frequency domain. As it can be seen all six pulses can be separated in terms of the center frequency and thereby be separately detected [203].

In the year 2008 the sensor concept was extended for additional sensing of the melt temperature. The data is transmitted in terms of shifting the carrier frequency of the pulse in dependence of the sensed melt temperature. In Fig. 1.15 *Top* a simulated spectrum of the carrier frequency shift in dependence of the sensed temperature can be seen. With increasing temperature the carrier middle frequency is shifted to higher frequencies. In Fig. 1.15 *Bottom* correlation of the temperature change to frequency dependence is plotted for experimental data. With the system it is possible to detect tem-

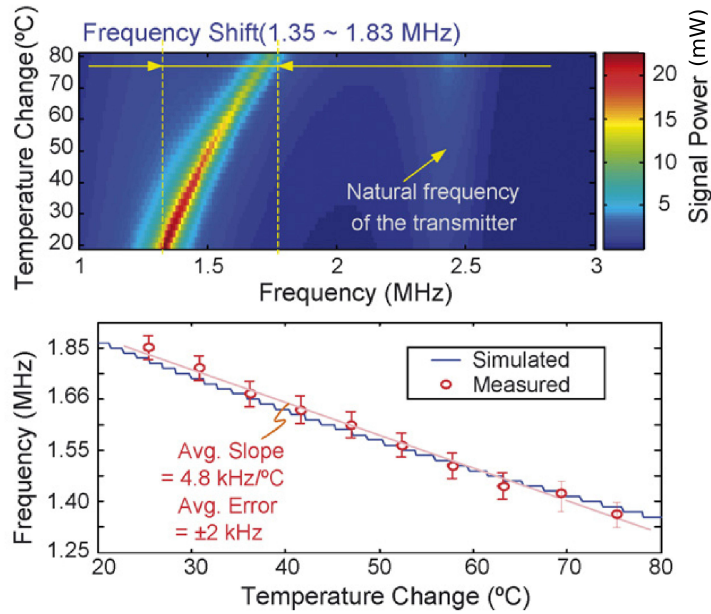


Figure 1.15: *Top:* Spectrum of the simulated frequency shift in dependence of the measured melt temperature; *Bottom:* Experimental data of the measured carrier frequency shift. In Reference to [59].

peratures in the range from 20 to 80 °C. Thereby the center of the carrier frequency is shifted from 1.35 to 1.83 MHz [48, 59].

In Fan et al. [48] first measurements of the wireless dual-parameter sensor within a mold are presented. In Fig. 1.16 *Top* the comparison of a commercially available wired in-mold pressure sensor with the recorded data of the wireless dual-parameter is shown. In Fig. 1.16 *Bottom* the comparison of the temperature data from a commercially available and the dual-parameter sensor is shown. For both quantities, the pressure and the temperature, a good match is achieved indicating the successful proof of the ultrasonic wireless measuring concept [48, 61].

The next consequent step is to fuse the already presented multivariate sensor with the wireless transmission technology published by the same research group. A patent describing this step was published recently by the inventors [60].

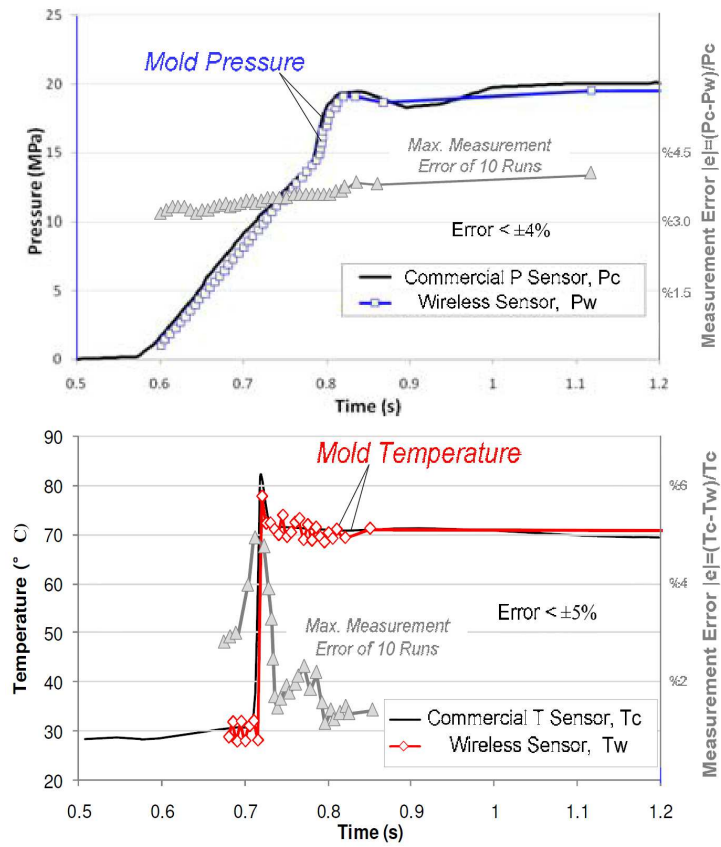


Figure 1.16: *Top:* Comparison of a commercial wired pressure sensor with wireless dual-parameter sensor; *Bottom:* Comparison of a commercial wired temperature sensor with wireless dual parameter sensor [48].

Chapter 2

Acoustic-Emission Sensor

In this chapter the focus is put on the mechanical components of the acoustic-emission sensor and their principle of operation. A section is dedicated to the possible measurable process values which can be obtained from the sensor. In addition, the used test mold and its setup is described. The mold is specially equipped enabling the investigation of different influence parameters on the sensor behavior. Finally, a concept is presented how the acoustic-emission sensor could be implemented in a series tool using the widely used ejector pins.

2.1 Principle of Operation

The acoustic-emission sensor is a wireless in-mold sensor for injection molding. The measurement principle is based on introducing a distinctive sound into the metal mass of the mold, triggered by a passing melt front. Structure-borne sound in the bandwidth of audible frequencies and slightly above serves as the data transmitting medium. In this manner, the acoustic-emission sensor has no need for wiring within the mold, yielding tremendous advantages over the whole lifetime cycle of a mold. Inside the mold solely mechanical parts are required assembled to form the *acoustic actuator* shown in Fig. 2.1. The shown acoustic actuator is only used for test purpose in this manner and its functionality is adapted for the usage in a series mold (confer Chapter 2.4, on page 38). The acoustic actuator consists of a sprung movable pin (*A*) protruding slightly into the cavity's chamber. The distance the movable pin protrudes into the cavity is equal to its movement distance. Hence, no other surface defect than a normal ejector mark is expected on the part surface. The correct position of the movable pin is ensured by a spring (*B*) pushing the pin into the upper position. As a result, the pin is always in

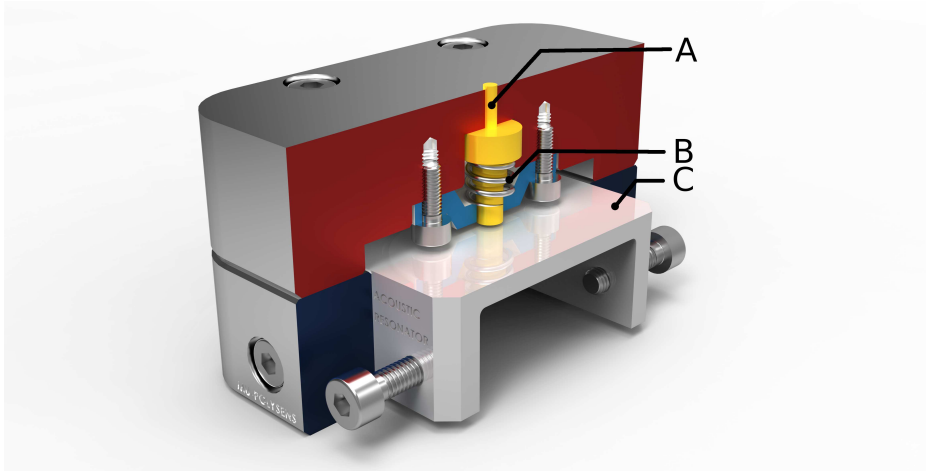


Figure 2.1: Rendered section view of the acoustic actuator which is installed in the test mold. The actuator consists of a sprung movable pin (*A*) which is pushed by a spring (*B*) in the cavity. The movable pin is accelerated by the melt front towards the resonant body (*C*) on which it impinges generating a structure-borne sound with a unique frequency pattern depending on the resonator's shape.

the initial upper position at the beginning of an injection molding cycle enhancing process reliability. The pin is accelerated by the melt pressure until it impacts on the resonator body (*C*). The resonator body is mounted by four screws in the housing frame of the acoustic actuator and can easily be changed. The shape of this resonator defines the eigen-frequencies of the structure with which it will oscillate after excitement. This oscillation is distributed into the metal mass of the mold via structure-borne sound and can be recorded by an accelerometer mounted on the outside surface of the mold. The assembled acoustic actuator is installed within the provided chambers incorporated in the test mold by four screws enabling good transmission of the structure-borne sound into the mold.

Measurement of melt front at multiple locations is possible. This is achieved by designing individual resonant structures all with distinctive resonance characteristic. Consequently, on excitement, the structures oscillate with their eigen-frequency distributing the sound into the metal mass of the mold. After recording of the sound separation of the resonators is possible using signal processing.

At this point it has to be mentioned that the acoustic actuator shown in Fig. 2.1 is larger than actually necessary. It was designed in this size to

enable simple exchangeability of the components and to have maximum of flexibility during the research work.

2.2 Measurable Process Variables

In reference to the already introduced classification system for in-mold sensors the acoustic-emission sensor is a level two sensor. It is capable to detect process parameters, especially melt front position with temporal resolution. If multiple resonators are located within the mold a matrix like measurement grid is available. Hence, not only the time-dependent flow front advancement is calculable but also additional information.

The measurable process parameters depend mainly on the number of installed acoustic actuators. When one actuator is placed in the cavity a single result is achieved. After applying signal processing the temporal point of resonator excitement t_i , for the resonator with index i , is known. In addition, the install location x_i of the actuator is known. In this manner, the signal can be used for instance for switch-over point detection which is of special interest in injection molding.

When placing a multiple number of acoustic actuators in the mold a different level of measurable process parameters is available. It has to be differentiated if the mold has just a single cavity or multiple cavities and if the acoustic actuators are installed all in one cavity, one in each cavity or multiple in each cavity. In the following listing the possible configurations are discussed with focus on the measurable process variables:

a) plural acoustic actuators in one cavity: With multiple implemented acoustic actuators in one cavity a matrix measurement of the melt front can be performed. In Fig. 2.2 a schematic with three actuators is shown. With the foreknowledge of the locations x_i and the temporal resolution of the melt front position t_i resulting from signal processing, an average melt front velocity \bar{v}_{mf} can be calculated by the equation,

$$\bar{v}_{mf} = \frac{|\mathbf{x}_1 - \mathbf{x}_2|}{|t_1 - t_2|} = \frac{\Delta x}{\Delta t} \quad (2.1)$$

with,

Δx represents the shortest flow path,

Δt time needed for the shortest flow path.

The melt front velocity is a key variable in the filling phase, because a uniform melt front propagation can minimize non-uniformity of the

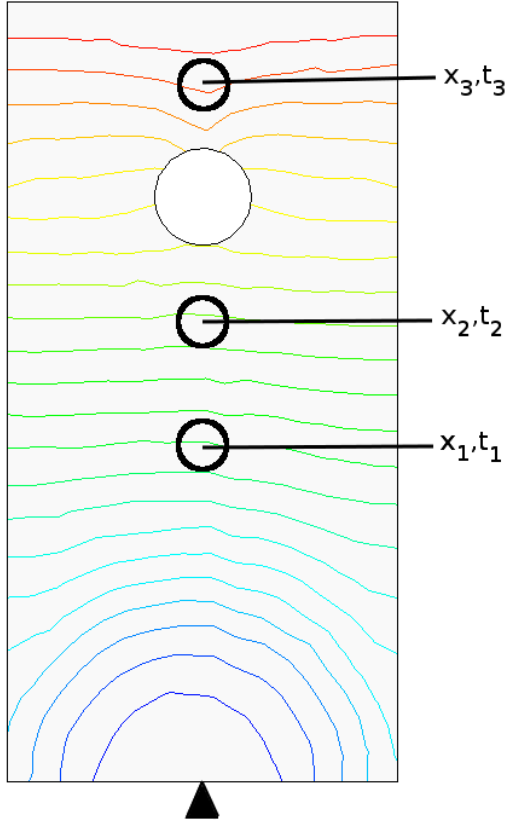


Figure 2.2: Schematic of average melt front advancement sensing with multiple incorporated acoustic actuators. The location x_i of the three movable pins is known and the temporal moments of melt front passing t_i is measured.

molded parts [30,175]. Although the injection velocity can be controlled precisely by the machine [190,201,202] profiling of the injection velocity remains still a challenge [30].

An additional process value of special interest is the viscosity η of the polymer. In Malkin and Isayev [117] it is shown, that if having a melt velocity v_x and additionally a melt pressure drop dp the viscosity η can be calculated via,

$$\eta = \frac{H^2}{12 v_x} \frac{dp}{dx}, \quad (2.2)$$

where H is the constant thickness of the cavity; thereby a Newto-

nian fluid ($\tau = \eta\dot{\gamma}$) is assumed for simplicity¹. However, the acoustic-emission sensor is not capable of detecting an absolute pressure drop dp/dx . Hence, only changes in the melt front velocity can be estimated, but no link to the absolute viscosity can be established, but a relative change can be measured under the assumption of having all other process parameters constant.

Another field of application is in sequential injection molding (SIM). Here, the time the melt front reaches a certain flow length is of interest particular [92, 176]. This point indicates the moment to open the next nozzle and enable a new flow path for the melt. With the method of SIM large parts with reduced weld lines and lower injection pressure can be produced, e.g. bumpers for automotive engineering [14].

b) plural acoustic actuators in multi cavity mold: If the mold is equipped with a plurality of cavities the implementation of acoustic actuators can be used for automatic sprue balancing, e.g. using a hot runner system. Each cavity is provided with one acoustic actuator, each located at the same flow path position. The time until the melt front reaches the acoustic actuator in each cavity is measured. The time differences are used as an input parameter for closed loop control. The controller tries to minimize the time difference by adapting a controlling element. Different systems using different controlling elements are presented in literature, e.g. valve controlling or temperature control of runner elements [41, 52, 85]. The system can be combined for the complete filling detection of each cavity [8].

In addition, all the benefits from implementing acoustic actuators in a single cavity (option *a*) can be combined with multi-cavity implementation (option *b*).

Summarizing the possibilities the new acoustic-emission sensor offers: In principle it is possible to detect the melt front. Thereby the obtained information from the sensor system is identical to those gained by cavity wall temperature sensors or cavity pressure sensors used for melt front detection. Major advantages arise with installing multiple acoustic actuators in the cavity since the implementation effort is nearly independent of the number of acoustic actuators. This advantage is mainly attributable to the wireless sensor concept.

¹Thermoplastic materials do have a shear thinning behavior in general which needs to be considered to measure the correct viscosity value, e.g. power-law model or Carreau viscosity model.

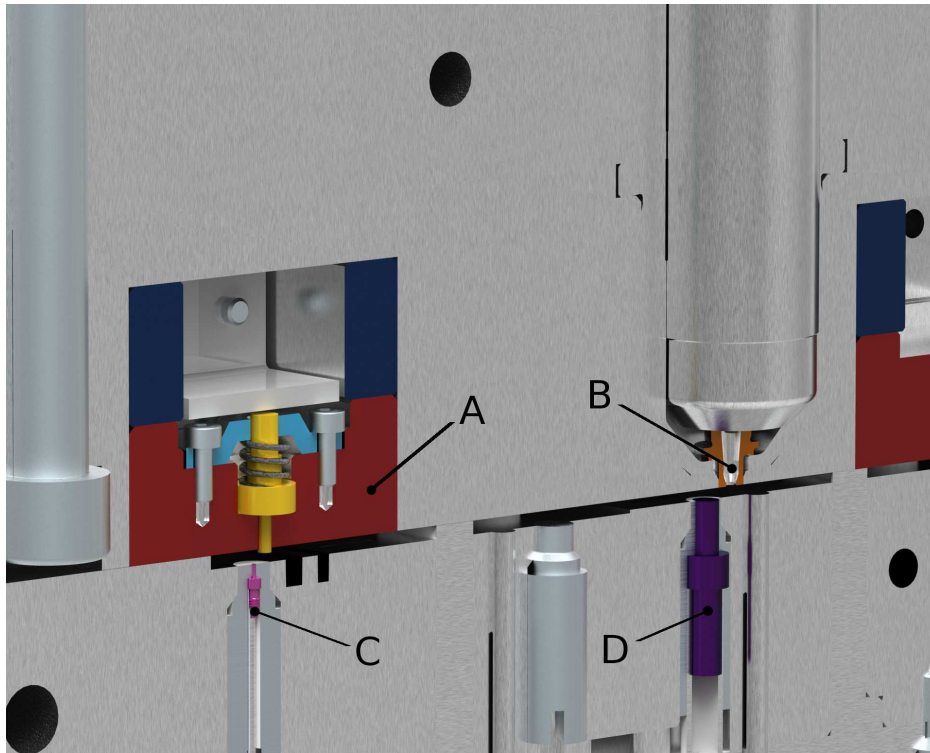


Figure 2.3: Rendered section view of the test mold with all implemented in-mold sensors. The acoustic actuator is positioned near the flow path end (A). The cavity is gated by a hot runner system equipped with a nozzle system (B). On the opposite cavity side a temperature sensor (C) and an in-mold pressure sensor (D) is installed.

2.3 Test Mold Setup for Acoustic-Emission Sensor

The test mold was designed to support investigation of the sensor and the factors influencing the achieved performance. To this end the acoustic actuators and their implementation space have been made larger than essentially necessary. In this manner components can be exchanged with less effort. For performance evaluation of the acoustic-emission sensor the mold should yield the possibility to locate common in-mold sensors, such as cavity temperature or pressure sensors, at the same flow length position as the acoustic actuator is positioned ensuring the same measuring conditions for both sys-

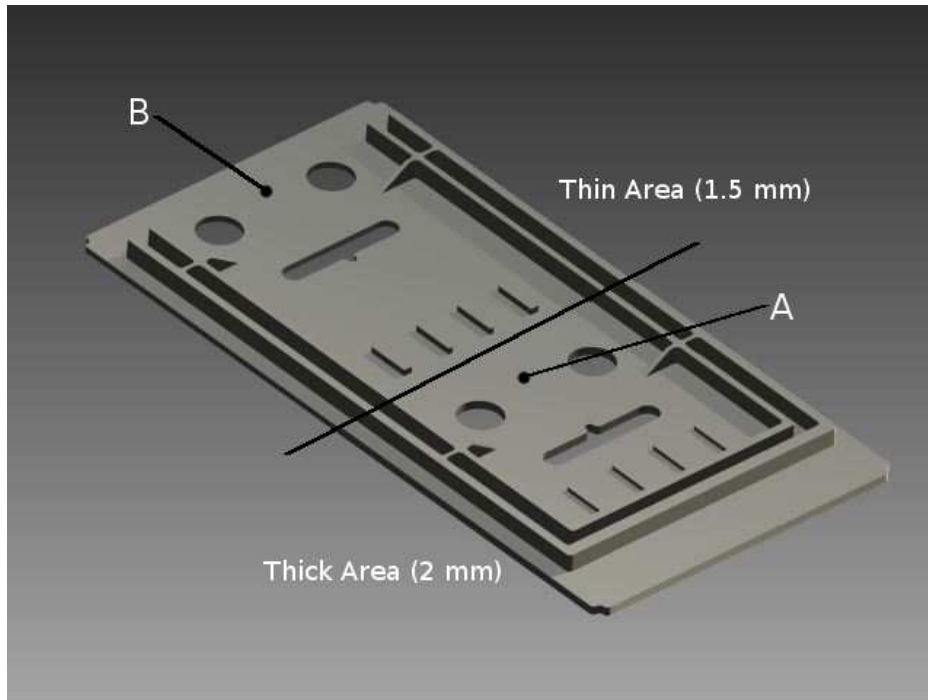


Figure 2.4: Rendered image of the produced part which has two dissimilar thick areas (1.5 mm and 2.0 mm). On the top side of the part additional features are placed as a two row u-shaped rib. The part has additional wholes influencing the flow path.

tems. This enables comparison of well established measurement systems with the new concept.

The test mold (shown in Fig. 2.3 as a rendered section view) is a two cavity mold with identical parts, which are gated by a hot runner system equipped with gate nozzles (*B*). Each gate can be independently controlled by an electromagnetic actuator [41]. The figure shows the mold with one installed acoustic actuator. The acoustic actuator is located near the flow path end (*A*). On its direct opposite cavity wall side a drilled hole is located enabling the implementation of several different in-mold sensors (the sensors are integrated via adapters to fit in the hole). In the shown figure a cavity wall temperature sensor (4009b) from Priamus System Technologies AG, Switzerland, with a head diameter of 0.6 mm is located (*C*). The second in-mold sensor incorporated in the cavity (*D*) is a pressure sensor (6157) by Kistler Holding AG, Switzerland. Through the adapter design interchangeability of the sensors is possible.

The produced part in the mold is a rectangularly shaped flat part with outer

dimensions of 160 mm by 80 mm whereby two different wall thicknesses are realized. One area of 80 mm by 80 mm is 1.5 mm thick and the other area is 2 mm thick. On the bottom side of the part a flat plane is realized and on the top side two rows of ribs are placed in a u-shape form. The part has additional features in the shape of holes. These holes influence the flow path of the melt. The part is shown as a rendered image in Fig. 2.4. The gate (A) is located on the flat bottom side in the thicker part area. Position B labels the location of the installed acoustic actuator which is near the flow path end of the part.

Another requirement for the test mold was the possibility to 'deactivate' the acoustic actuators. Therefore the housing with the pin can be replaced by a blanked insert keeping the resonator silent while the melt front passes. This setup was especially important for the proof of concept measurements described in Chapter 4.2, on page 106.

2.4 Ejector Pin Design of Acoustic-Emission Sensor in a Series Tool

The design of a separate insert for generating a distinctive sound is not practical for a series tool. The components used for investigation were designed larger than essentially necessary which in turn is the biggest disadvantage because valuable space near the cavity surface is used. Consequently, for series molds a different solution is desirable moving most of the components away from the cavity surface.

An essential component of each mold are the ejector pins conventionally used for part demolding. In a series mold ejector pins are fixed inside the ejector plate and are only guided on a short length l_g near the cavity surface. By moving the ejector plate the pin is moved and the part is ejected from the cavity. A schematic is shown in Fig. 2.5.

By adapting ejector pins, they can be used as the movable pin for the acoustic-emission sensor and can fulfill the task of the movable pin. In Fig. 2.6 a schematic of the functionality is given. In the left sketch of Fig. 2.6 the acoustic actuator is reduced to its minimal configuration²,

²Note that this configuration is functionally not reliable since it cannot be ensured that the pin is in initial position at the beginning of an injection molding cycle.

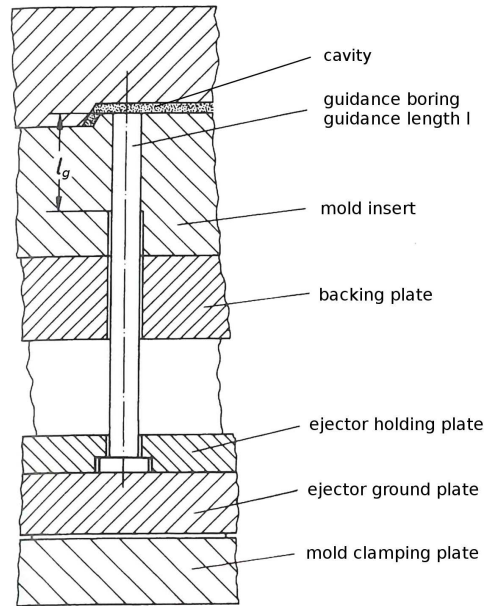


Figure 2.5: Principle of implementation of an ejector pin inside a conventional mold. The pin is clamped between ejector ground plate and ejector holding plate. In addition the pin is guided in the guidance boring on a length l . In reference to [122, 125].

consisting only of:

- A, ejector plate serving as a resonator and
- B, movable ejector pin.

To achieve identical functionality as with the acoustic actuator used for the measurements in this thesis a conventional ejector pin is shortened at its clamping position enabling an axial movement. To remain a high quality surface its length is adapted for the desired pin movement distance. For separation of multiple acoustic actuators there is a need to implement individual resonant structures. The structure gets excited by the impact through the accelerated ejector pin. The best place to locate the structures is in the ejector ground plate just below the movable ejector pin. In a conventional mold the ejector ground plate is a metal plate where only the ejector rod is mounted and the rest of the plate offers space for additional implementation. However, to ensure mechanical stability of the modification some considerations have to be made. Another aspect is to enable reliable functionality of the system while remaining fully mechanical in its components.

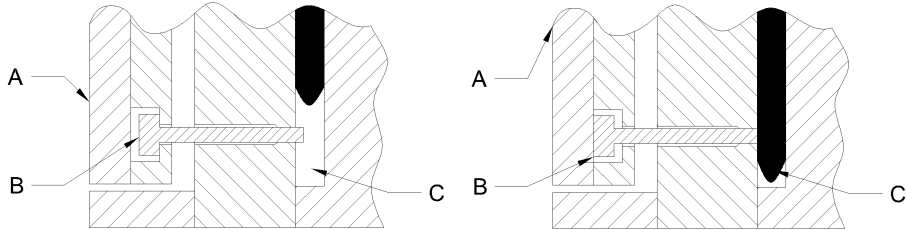


Figure 2.6: *Left:* Acoustic actuator in initial position; *Right:* Acoustic actuator in activated position. The system is reduced to minimal configuration comprising a resonant structure in form of the ejector ground plate (*A*) and a movable ejector pin (*B*). In addition the in-fluxing polymer (*C*) is shown.

Due to shrinkage of the polymer part a certain demolding force F_R is necessary³. While demolding is in process a contact stress between ejector pin and part surface can be calculated as,

$$\sigma_D = \frac{F_R}{\sum_i A_{E,i}}, \quad (2.3)$$

with $A_{E,i}$ the surface of ejector pin i . In case of a round ejector pin $A_E = d_E^2 \pi / 4$, with d_E the diameter of the pin. The diameter d_E is selected in dependence of the demolding force and the number of implemented ejector pins. It is desired to prevent the part from having surface failure or having strong ejector marks. During the cooling phase the polymer is increasing its stiffness and can endure a certain stress without suffering ejector marks. Consequently, having a large ejector area decreases local stress and enables an earlier demolding without having ejector marks.

The increase of the ejector pin causes some disadvantages. In the worst case, during the pressure holding phase, a hydrostatic melt pressure level in the whole cavity can occur for some time. Actual injection molding machines can inject melt with up to⁴ $p_{melt} = 2500$ bar. This pressure can in worst case act during the pressure holding phase on the pin surface evoking forces that are guided into the ejector ground plate. Normally the ejector ground plate is designed with sufficient thickness to endure these forces. As a result of the modifications to implement the functional parts of the acoustic actuator, the

³The shrinkage evokes a normal force F_N which is proportional to the friction force F_R via the friction coefficient μ . In Burgsteiner [22] an investigation on the demolding process with special focus on measuring the friction coefficient μ is given in detail.

⁴The value is mainly dependent on the screw diameter.

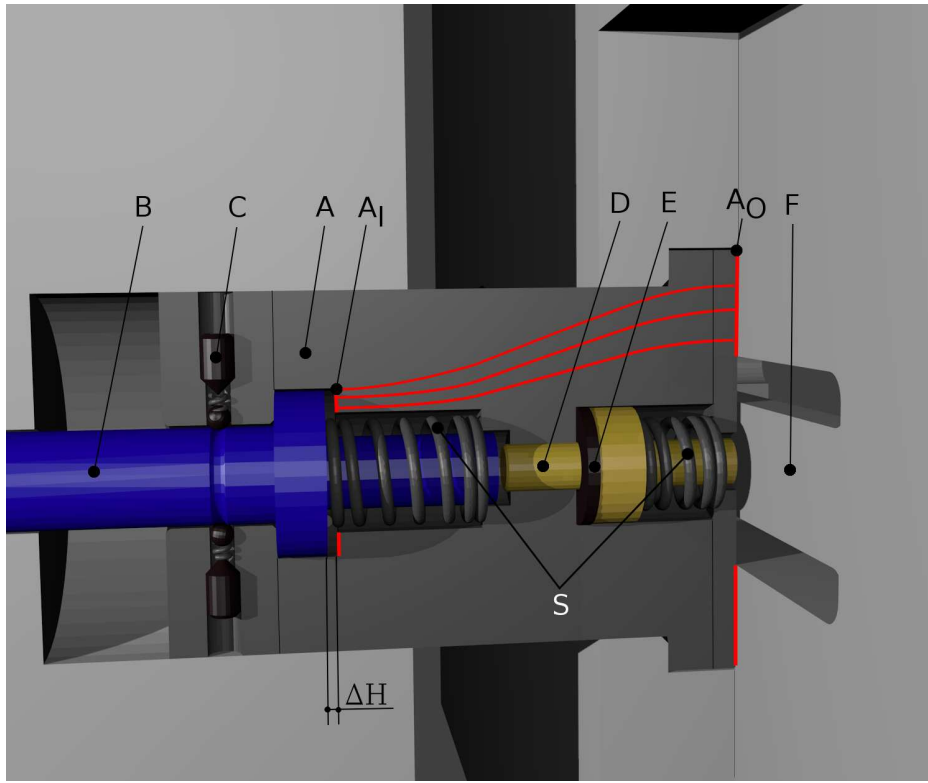


Figure 2.7: Rendered section view of a possible design of the acoustic actuator in a series tool. The housing (A) comprises two separated pins, the main ejector pin (B) and the acoustic actuator pin (D). The ejector pin is supported by a big spring as well as spring system (C) holding it in initial position. The acoustic actuator pin impacts on the resonant body (F) which is implemented in the ejector ground plate. To reduce bouncing the acoustic actuator pin is damped using a rubber-like plate (E). During pressure holding phase the force acting on the ejector pin is guided over the surface A_I inside the housing (indicated by the red lines as the force flux) and over the surface A_O inside the ejector ground plate. Both movable pins are supported by springs (S) to ensure correct initial position.

resonant structure is directly positioned below the ejector pin. The resonant plate is thin which makes it mechanically weak and as a result the plate will most probably bend under the acting forces, leading to large ejector marks, or in worst case break. Consequently, it is desired to guide the acting forces around the resonant plate.

In addition, it is expected that the ejector pin mass has a significant impact on the sensor's response time performance. Hence, the pin should have the lowest possible mass for high response measurement system. Moreover, it is desired to have an infinitesimally small contact time between the pin and the resonator, i.e. a contact similar to a Dirac-impulse. This is a result of the spectrum of a Dirac-impulse which is constant over all frequencies with constant amplitude, also known as white noise [73]. This enables that the resonator is excited at all its eigen-frequencies yielding easier separation. As a result, a small mass would support having a short contact time. However, buckling is an issue if the pin diameter is carried out to small. As it can be seen, there are several influencing factors all pointing in a different design direction.

In Fig. 2.7 a rendered section of a possible construction design is shown using an ejector pin as the movable pin for the acoustic-emission sensor. The main targets during construction are, whereby the first point is a functional requirement and the others are mechanical ones:

1. enabling a short impact time of the movable pin, so that the resonant structure is excited at all its eigen-frequencies;
2. decoupling of the force, so that it does not act directly on the resonant structure;
3. enabling sufficient stability of the components during pressure holding phase, and
4. ensure usability of the ejector pin for part demolding.

To resolve requirement 1., the system was split up into two separate pins, a main ejector pin (B) and an acoustic actuator pin (D). Both are implemented in a housing (A) holding up all the necessary components and giving structural stability. To enable assembling of all parts the housing consists of three turned parts mounted together by screws. The main ejector pin is supported by a large spring (S), ensuring correct initial position as well as automatically pushing the pin in the initial position after demolding. In the initial position the main ejector pin protrudes within the cavity. The distance depends on the mass of the system and should be long enough to generate a good signal to noise ratio to enhance sound detection. The main ejector pin is supported by an additional spring system (C). A spring pushes against a ball which rests in a flute incorporated in the main ejector pin. Via this system it is possible to set up the necessary melt pressure acting on the pin until the movement begins. In the moment the melt pressure level

exceeds the spring force of system C the balls are pushed out of the flute and do not interact anymore with the movement of the ejector pin⁵. This system also acts as a guidance supporting the pin movement. After demolding of the part, the large spring (S) pushes the ejector pin back and both spring supported balls hold the main ejector pin again via the incorporated flute. After the ejector pin is accelerated it impacts on the acoustic actuator pin (D) and forwards its energy on the small pin. After energy transfer the ejector pin impacts on the red indicated surface A_I at which the force is guided through the housing in the ejector ground plate. To decouple the two pins, the distance between the ejector pin and the acoustic actuator pin has to be smaller than the distance ΔH . Otherwise the pins would interact after energy transfer. The small pin impacts later on the resonant body (F) which is implemented in the ejector ground plate⁶. Since the acoustic actuator pin is very small a short impact time can be achieved enabling an impact behavior similar to a Dirac-impulse. In addition, the acoustic actuator pin is supported by a spring (S) ensuring correct initial position after impact. To reduce bouncing of the acoustic actuator pin during back movement a rubber-like plate (E) with high damping characteristics is located between the pin and the surface. Due to the properties of the rubber-like plate energy is dissipated and the bouncing is highly damped. In best case, the damping is high enough that no bouncing of the acoustic pin occurs at all. Both movable pins are supported by a spring (S) to ensure a correct initial position of the pins after ejection of the part.

During the pressure holding phase high forces are transferred into the housing (A) by the ejector pin. In injection molding pressure levels of up to $p_{melt} = 2500$ bar can theoretically be reached⁷. The ejector pin is pushing against the surface indicated by A_I . At this surface a force is introduced into the part which is indicated by the red lines describing the force flux. At the surface A_O the force is transmitted into the ejector ground plate. To ensure stability of the system the housing has to be investigated if it can endure the maximum occurring forces.

In consideration of a pressure level of $p_{melt} = 2500$ bar a force F ,

⁵Since the ball can rotate inside the drill hole, friction between the ball and moving pin will be small and will not affect pin movement.

⁶In this section view the resonant structure is part of the ground plate but could also be implemented as an insert in the ground plate enabling simple exchange.

⁷This high level will not be reached during conventional injection molding. However, when setting up a wrong switch-over point and not having implemented a maximum pressure level many machines are able to pressurize the melt with $p_{melt} = 2500$ bar. In worst case a hydrostatic pressure propagation is present yielding the need to design the mechanism to endure this pressure level.

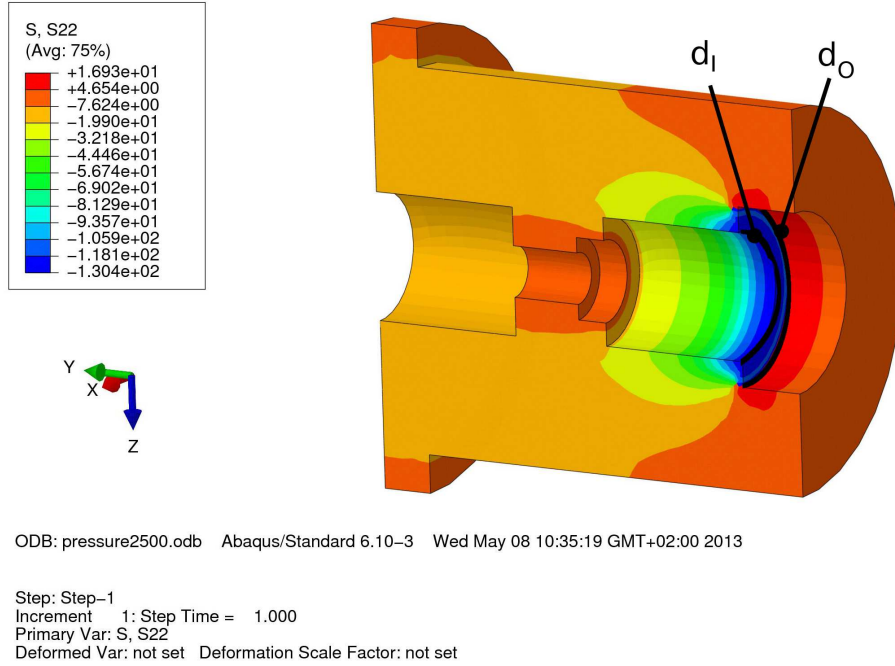


Figure 2.8: Local stress calculation result of the housing during pressure holding phase. A maximum compression stress of $\sigma = -130$ MPa is present which has to be endured by the steel.

$$F = p_{melt}A_E, \quad (2.4)$$

is inside the ejector pin, where A_E is the surface of the ejector pin projecting inside the cavity at which the melt pressure acts. The pressure or stress σ acting on the housing can be calculated as,

$$\sigma = \frac{4F}{(d_O^2 - d_I^2)\pi}, \quad (2.5)$$

with d_O and d_I the outer and inner diameter of the contact area between ejector pin and housing. The stress σ was used as a boundary condition to calculate the local stress distribution within the housing using FEM software. Statically simulations were performed using Abaqus CAE 6.10 from Dassault Systemes, United States. At the surface A_I the stress σ was applied whereas the surface A_O was fixed concerning movement and rotation. A typical elastic steel was set up having a Young's modulus $E = 210$ GPa and a Poisson ratio of $\nu = 0.3$. The density was set to $\rho = 7.3$ gcm⁻³. In Fig. 2.8 the local

stresses in main direction⁸ 22, which is in reference to the y-coordinate, are shown as a section view. As it is expected the highest stress appears as compressive stress indicated by blue color. The highest noticed value is $\sigma_{max} = -130$ MPa. If using a steel St 50-2 (standard DIN 17100), which has a yield strength of $R_{eH} = 295$ MPa [53], a margin of safety S can be calculated as,

$$S = \frac{R_{eH}}{|\sigma_{max}|} = 2.3. \quad (2.6)$$

For statically consideration the safety factor is sufficient. However, additional considerations concerning dynamic load as a result of cyclic impact have to be made.

During the demolding process the force direction is reversed. A force is guided into the ejector ground plate from which it is transferred into the housing. Via the contact surface between the housing and the ejector pin the force is guided into the main ejector pin, which acts on the part during demolding. Finally, the ejector pin diameter has to be investigated towards buckling under the present cavity pressure. Since the pin is guided in the top region and is mounted on its bottom this refers to Euler buckling condition case three, resulting in $\beta = 0.699$ influencing the effective length $l_k = l\beta$ of the ejector pin. Thereby l is the pin length and was investigated in three steps, $l_1 = 10$ cm, $l_2 = 15$ cm and $l_3 = 20$ cm. The critical buckling force is calculated via,

$$F_l = \frac{\pi^2 EI}{l_k^2}, \quad (2.7)$$

with E the Young's modulus and I the area moment of inertia which is calculated for a circularly shaped rod as,

$$I = \frac{\pi d^4}{64}, \quad (2.8)$$

with d the diameter of the rod. The buckling force F_l is compared against the present force resulting from the pressure acting on the pin. The current force F_c in dependence of the pin diameter is calculated as,

$$F_c = \frac{4p_{melt}}{\pi d^2}. \quad (2.9)$$

As long as $F_c < F_{lk}$ no instability occurs. In Fig. 2.9 the results are shown for three different rod lengths in dependence of the rod diameter. In case of

⁸Direction 22 refers to the y coordinate and is the typical notation in Abaqus.

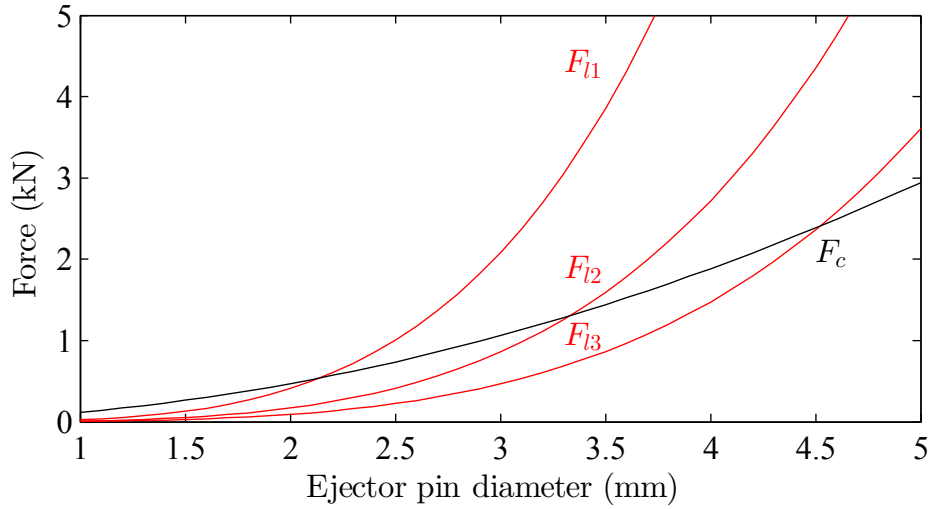


Figure 2.9: Buckling force F_{lk} for three different rod lengths l_1 , l_2 and l_3 in dependence of rod diameter. Actual present force F_c inside the rod is calculated under the assumption of p_{melt} and for stability reasons $F_c < F_{lk}$.

the shortest rod l_1 at least a rod diameter of 2.2 mm is necessary to ensure stability. For the longer rod distances greater diameters are needed. For l_2 at least 3.4 mm and for l_3 at least 4.5 mm are needed to preserve stability of the rod under maximum melt pressure.

To sum up, a possible design of the acoustic actuator for a series tool was presented. For implementation design aspects have to be considered to ensure long time reliability and mechanical stability. Due to the fact that a low mass of the system increases sensor performance contrary requirements come into conflict. One major aspect that cannot be neglected is the high pressure level that may be present during pressure holding phase yielding the potential to destroy the acoustic actuator or any component coupled to the system. As a result, sufficient diameters are needed to remain mechanical stability at the expense of performance.

Chapter 3

Theoretical Framework

This chapter is constructed in the same chronology as the melt front detection happens during injection molding. In Fig. 3.1 the process chart is visualized. Origin is the melt pressure from the in-fluxing melt which acts on the movable pin. This pressure accelerates the pin until it impacts and excites the resonant structure. The oscillation of the structure is distributed into the metal mass of the mold as an elastic wave. A mounted accelerometer converts the elastic wave into a voltage using the piezoelectric effect. Finally, signal processing for recognition of resonator activation event is discussed. It has to be mentioned that this framework is written with particular focus on the field of usage of the acoustic-emission sensor – injection molding. Furthermore, a short information about used nomenclature is given: vectors are indicated by boldface lowercase letters, e.g. \mathbf{y} , and matrices are indicated by boldface capital letters, e.g. \mathbf{H} . Additionally, it has to be noted that the notation $y[n]$ is equally used to the vector representation \mathbf{y} .

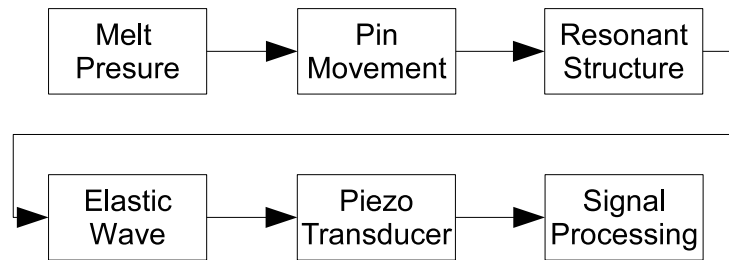


Figure 3.1: Process chart of melt front detection using the acoustic-emission sensor.

3.1 Melt Pressure

Injection molding is a molding process driven by pressure and temperature. For the acoustic-emission sensor the pressure p is essential since it acts on the movable pin accelerating it. The pressure within the melt is a result of the viscosity η of the material, which is the resistance of the material against the deformation applied to it in form of a force or stress.

The pressure difference Δp along a path ΔL within the melt can be calculated (in reference to Pahl et al. [142]) for a rectangular chamber by rearranging the equation,

$$\dot{V} = \frac{1}{\eta_N} \frac{\Delta p}{\Delta L} \frac{H^3 B}{12}, \quad (3.1)$$

to the pressure difference Δp ,

$$\Delta p = \frac{12}{H^3 B} \dot{V} \eta_N \Delta L, \quad (3.2)$$

with ΔL as the melt front advancement, H and B the height and width (with the assumption $L \gg B \gg H$) and \dot{V} the volume flow rate. The viscosity η , i.e. η_N , the Newtonian viscosity [130], is a measure of the fluid which describes the resistance to gradual deformation by shear stress or tensile stress. It is defined for a Newtonian fluid as,

$$\tau = \eta \dot{\gamma}, \quad (3.3)$$

with τ the shear stress and $\dot{\gamma}$ the shear rate. At this point it has to be mentioned that thermoplastic polymers are in general not Newtonian fluids but have a shear thinning behavior which can be described for example by the Carreau-model¹ [24–26],

$$\eta = \frac{\eta_0}{[1 + (t_1 \dot{\gamma})^2]^{\frac{1-n}{2}}} \quad (3.4)$$

with η_0 the zero-shear viscosity, t_1 a time constant, n a parameter describing the slope in the power-law region and $\dot{\gamma}$ the shear rate.

For simplicity of the formula the pressure is calculated using Newton's law. Integrating Eq. 3.2 leads to,

$$p = \frac{12}{H^3 B} \dot{V} \Delta L \eta_N + p_0, \quad (3.5)$$

¹Furthermore, the viscosity is dependent on the acting temperature (higher temperature leads to lower viscosity) and pressure (higher pressure leads to higher viscosity).

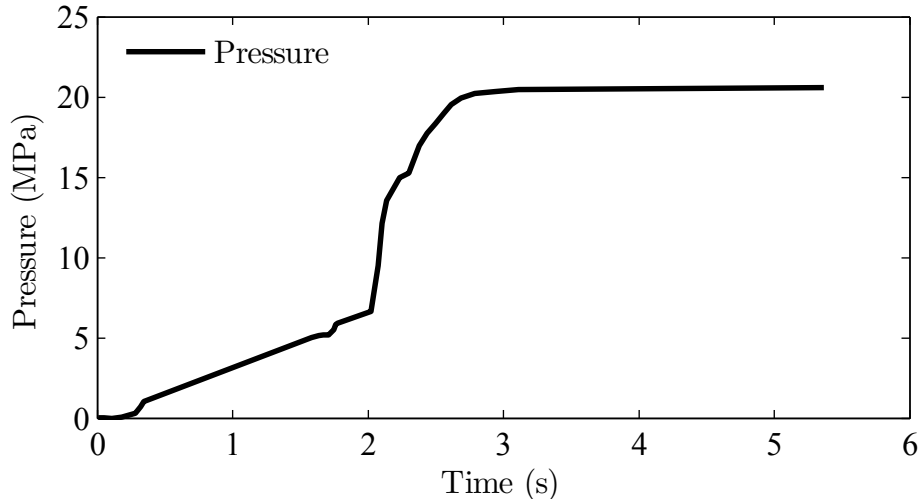


Figure 3.2: Typical cavity pressure for injection molding during filling and packing phase³. In reference to [57].

with p_0 the pressure at the melt front (in most cases ambient pressure). If monitoring the cavity pressure at a stationary point, i.e. the position of the movable pin, the pressure acting on the pin can be calculated² using Eq. 3.5. With ongoing melt front advancement ΔL the pressure increases linearly. Gao et al. [57] have shown experimental results for the pressure control during the cooling phase of a rectangular plate. The filling phase is also monitored by a pressure transducer placed close to the sprue. The result of the time-dependent pressure history is shown in Fig. 3.2. During the filling phase which happens until approximately 2s, a linear pressure increase behavior can be seen, as it is described via Eq. 3.5.

3.2 Pin Movement

With having the melt pressure p which acts on the pin, the time-dependent movement of the pin can be calculated. This is for two reasons of interest. First, by knowing the time the pin needs until it impacts on the resonant structure, a so called *response time*, can be calculated. The response time is essential to estimate overall sensor performance. It is expected that pin

²Under the assumption of having constant cavity geometry and constant viscosity; constant viscosity is only achieved when the volume flow rate is constant and isothermal conditions are present.

³In the publication the measurement location is not mentioned but from the shown result it is believed that the cavity pressure sensor is located near the gate.

movement time is the limiting time of the whole measurement chain. Second, an impact velocity and/or impact energy can be calculated which is important for the amplitude of excitement of the resonant structure.

The sensor system is described using Newton's law of motion⁴. The sum of all forces F_i has to be equal the mass m times the acceleration \ddot{x} of the system. This can be written as,

$$\sum_i F_i = m\ddot{x}. \quad (3.6)$$

In case of the acoustic-emission sensor an unidirectional movable pin, accelerated by an increasing melt pressure acting on the constant pin area, as well as a spring, have to be described. For that purpose some assumptions and simplifications have to be made to enable solving the governing equation, i.e. frictionless movement, neglect of gravitation and venting conditions of the cavity. The describing differential equation of the sensor system is,

$$m\ddot{x}(t) = F(t) - kx(t), \quad (3.7)$$

with m the mass of the pin, k the spring rate, $x(t)$ the time-dependent position as well as its second temporal⁵ derivative $\ddot{x}(t)$, the acceleration. $F(t)$ is the time-dependent force acting on the pin area.

The solution of the differential equation is the sum of the complementary solution $x_c(t)$ and the particular solution $x_p(t)$,

$$x(t) = x_c(t) + x_p(t). \quad (3.8)$$

For the complementary solution the homogenous differential equation has to be solved,

$$m \frac{d^2 x(t)}{dt^2} + kx(t) = 0. \quad (3.9)$$

It is assumed that the solution is proportional to $x(t) = e^{\lambda t}$, for some constant λ . Substituting this into Eq. 3.9 yields,

$$m \frac{d^2 e^{\lambda t}}{dt^2} + ke^{\lambda t} = 0. \quad (3.10)$$

The term $\frac{d^2 e^{\lambda t}}{dt^2}$ is substituted by $\lambda^2 e^{\lambda t}$ resulting in,

$$m\lambda^2 e^{\lambda t} + ke^{\lambda t} = (m\lambda^2 + k)e^{\lambda t} = 0. \quad (3.11)$$

⁴The form $F = ma$ was actually formulated by Leonard Euler in the year 1750 [46].

⁵The form \dot{x} is identical to $\frac{dx}{dt}$. Consequently \ddot{x} is the same as $\frac{d^2x}{dt^2}$.

The roots for Eq. 3.11 have to be found. The term $e^{\lambda t} \neq 0$ for any λ , hence, $m\lambda^2 + k$ has to hold the roots. The roots are,

$$\lambda_{1,2} = \pm j \sqrt{\frac{k}{m}}, \quad (3.12)$$

with $j = \sqrt{-1}$. As a result, two solutions x_1 and x_2 are found as,

$$x_1(t) = C_1 e^{-j \frac{\sqrt{kt}}{\sqrt{m}}}, x_2(t) = C_2 e^{j \frac{\sqrt{kt}}{\sqrt{m}}}, \quad (3.13)$$

with C_1 and C_2 an arbitrary constant. This yields the general solution as,

$$x(t) = x_1(t) + x_2(t) = \frac{C_1}{e^{j \frac{\sqrt{kt}}{\sqrt{m}}}} + C_2 e^{j \frac{\sqrt{kt}}{\sqrt{m}}}. \quad (3.14)$$

The general solution can be further simplified by using Euler's identity,

$$e^{\alpha + j\beta} = e^{\alpha} \cos(\beta) + j e^{\alpha} \sin(\beta), \quad (3.15)$$

resulting in,

$$x(t) = C_1 \left(\cos \left(t \sqrt{\frac{k}{m}} \right) - j \sin \left(t \sqrt{\frac{k}{m}} \right) \right) + C_2 \left(\cos \left(t \sqrt{\frac{k}{m}} \right) + j \sin \left(t \sqrt{\frac{k}{m}} \right) \right). \quad (3.16)$$

Regrouping Eq. 3.16 and redefining the constants $(C_1 + C_2) \triangleq C_3$ and $i(-C_1 + C_2) \triangleq C_4$ yields,

$$x(t) = C_3 \cos \left(t \sqrt{\frac{k}{m}} \right) + C_4 \sin \left(t \sqrt{\frac{k}{m}} \right). \quad (3.17)$$

The particular solution will be of the form $x_p(t) = a$, with a constant a . The second derivative $\ddot{x}_p(t) = \frac{d^2 a}{dt^2} = 0$. Substituting this into the differential equation yields,

$$m \frac{d^2 x_p(t)}{dt^2} + k x_p(t) = F, \quad (3.18)$$

$$m \cdot 0 + k a = F.$$

Consequently, the constant is calculated as $a = F/k = x_p(t)$. Finally, the general solution is found as,

$$x(t) = x_c(t) + x_p(t) = C_3 \cos \left(t\sqrt{\frac{k}{m}} \right) + C_4 \sin \left(t\sqrt{\frac{k}{m}} \right) + \frac{F}{k}. \quad (3.19)$$

The two constants C_3 and C_4 are still unknown but can be solved by introducing two boundary conditions. At time zero the distance and the velocity equals zero. This can be written as,

$$\begin{aligned} x(0) &= 0, \\ \dot{x}(0) &= 0. \end{aligned} \quad (3.20)$$

Substituting $x(0) = 0$ into Eq. 3.19 yields,

$$x(0) = C_3 \cos \left(0\sqrt{\frac{k}{m}} \right) + C_4 \sin \left(0\sqrt{\frac{k}{m}} \right) + \frac{F}{k} = 0, \quad (3.21)$$

and by definition $\cos(0) \triangleq 1$, and $\sin(0) \triangleq 0$ which simplifies Eq. 3.21. From Eq. 3.21 C_3 is found as $-\frac{F}{k}$. To find the second constant Eq. 3.19 has to be derived with respect to t , yielding,

$$\frac{dx(0)}{dt} = \frac{F}{k} \sqrt{\frac{k}{m}} \sin \left(0\sqrt{\frac{k}{m}} \right) + C_4 \sqrt{\frac{k}{m}} \cos \left(0\sqrt{\frac{k}{m}} \right) = 0. \quad (3.22)$$

Now, C_4 is calculated to be zero. Having solved both constants, $C_3 = -F/k$ and $C_4 = 0$, Eq. 3.19 can be written as,

$$x(t) = \frac{F}{k} - \frac{F}{k} \cos \left(t\sqrt{\frac{k}{m}} \right) = \frac{F - F \cos \left(t\sqrt{\frac{k}{m}} \right)}{k}. \quad (3.23)$$

Finally, the force is time-dependent resulting in the equation,

$$x(t) = \frac{F(t) - F(t) \cos \left(t\sqrt{\frac{k}{m}} \right)}{k}. \quad (3.24)$$

For completeness the time-dependent velocity of the pin movement is computed to be,

$$\dot{x}(t) = \frac{F}{k} \sqrt{\frac{k}{m}} \sin \left(t\sqrt{\frac{k}{m}} \right). \quad (3.25)$$

With Eq. 3.24 the influence of the time-dependent force $F(t)$ and thus the pressure $p(t)$, the spring ratio k and the pin mass m can be investigated. The relationship between the force and the pressure is given via,

$$p(t) = F(t)A = F(t)r^2\pi, \quad (3.26)$$

with A the pin surface⁶ on which the pressure acts and r the pin radius defining the surface A .

Using Eq. 3.25 the velocity of the movable pin at impact can be calculated. This is of special interest if one wants to calculate the energy which is forwarded at impact from the pin on the resonant structure. For a good signal to noise ratio a big amplitude of the oscillation is desired which is achieved by high impact velocities and consequently high kinetic energy T . The kinetic energy is calculated as [188],

$$T = \frac{m\dot{x}^2}{2}. \quad (3.27)$$

3.3 Resonant Structure Modeling

A principle part of the acoustic-emission sensor system is the resonant structure. The structure is excited with its resonant frequency by the impact of the movable pin. For separation of multiple implemented resonant structures it is desirable to design structures with different frequency response. In this chapter a short summary on the mathematical description of resonance behavior of structures is given.

Assuming a physical system, i.e. a resonant structure, engineers are often interested in the structural behavior of the system on special frequencies in advance which is described by obtaining its eigen-vector. By knowing the eigen-vectors as well as the physical properties of the material, e.g. Young's modulus E or Poisson's ratio ν , structural optimizations can be performed. The studies were initiated by Helmholtz [82] and Rayleigh [159] back in the 19th century. Since then methods have been developed for the analysis of physical structures and for efficient solving of eigen-value problems [105]. The mathematical description of the behavior of a linear mechanical system to a harmonic excitation can be expressed by a second order ordinary differ-

⁶For simplification the pin surface area A is considered as constant and not dependent on melt front advancement. In addition, the pressure gradient at the melt front is neglected. Both assumptions are possible due to the small pin diameter and fast melt front advancement.

ential equation [47]. It is assumed that principal orientations are decoupled and can be expressed as a single-degree-of-freedom (SDOF) equivalent via,

$$m\ddot{x}(t) + c\dot{x}(t) + kx(t) = f(t), \quad (3.28)$$

where m is the modal mass, c is the modal damping coefficient, k is the modal stiffness and f is the excitation. Thereby $x(t)$ is the time-dependent position with its first and second derivative with respect to time, i.e. $\dot{x}(t)$ and $\ddot{x}(t)$. Using the Laplace transform on this equation, assuming zero initial conditions and harmonic excitations, leads to the frequency response function,

$$\frac{X}{F} = \frac{1}{m(j\omega)^2 + c(j\omega) + k} = \frac{1/m}{(j\omega - \lambda_1)(j\omega - \lambda_1^*)}, \quad (3.29)$$

where X and F are the response and the excitation, ω is the frequency and $j = \sqrt{-1}$. Assuming a single-mode underdamped system ($c < 2\sqrt{km}$) the complex conjugate poles, which are the solution of the equation, are,

$$\{\lambda_r, \lambda_r^*\} = -\frac{c}{2m} \pm \sqrt{\frac{c^2}{4m^2} - \frac{k}{m}} = -\zeta_r\omega_r \pm j\omega_r\sqrt{1 - \zeta_r^2}, \quad (3.30)$$

with,

$$\omega_r^2 \triangleq \frac{k}{m} \quad \text{and} \quad \zeta_r \triangleq \frac{c}{2m\omega_r} = \frac{c}{2m\sqrt{k/m}}, \quad (3.31)$$

where ω_r is the natural frequency and ζ_r is the critical damping ratio. Since most systems are more complex, more efficient methods are needed for the estimation of the natural frequency response. In Lee and Jung [105] a summary over some common methods for solving the symmetric eigen-value problem associated with linear vibration are described besides presenting a novel approach. The system to solve is defined as,

$$\mathbf{K}\phi_j = \lambda_j\mathbf{M}\phi_j, \quad (3.32)$$

where \mathbf{K} and \mathbf{M} are the stiffness and mass matrices of order n . ϕ_j represents the j^{th} mode shape and λ_j the square of the j^{th} natural frequency. With normalized eigen-vector,

$$\phi_j^T\mathbf{M}\phi_j = 1, \quad (3.33)$$

and differentiation with respect to a design parameter the derivative of the eigen-value is given as,

$$(\mathbf{K} - \lambda_j \mathbf{M})\phi'_j = -(\mathbf{K}' - \lambda_j \mathbf{M}')\phi_j + \lambda'_j \mathbf{M}\phi_j. \quad (3.34)$$

Premultiplying by ϕ_j^T leads to the eigen-value derivative,

$$\lambda'_j = \phi_j^T (\mathbf{K}' - \lambda_j \mathbf{M}') \phi_j, \quad (3.35)$$

where $\lambda'_j \triangleq \partial \lambda_j / \partial p$, $\mathbf{K}' \triangleq \partial \mathbf{K} / \partial p$ and $\mathbf{M}' \triangleq \partial \mathbf{M} / \partial p$, and p is a design parameter. In Eq. 3.35 the eigen-value derivative ϕ'_j cannot be directly estimated since the matrix $\mathbf{K} - \lambda_j \mathbf{M}$ is singular. To find the eigen-vector derivative several methods are proposed, e.g. Rudisill and Chu [161] and Nelson [129] which are efficient methods. Nowadays many software packages offer the possibility to calculate the eigen-values, respectively the response frequencies, of a structural system of arbitrary design by discretizing the system into a finite number of regions, e.g. Abaqus FEA by Dassault Systems, France, or Inventor by Autodesk, United States.

The resonators used for the acoustic-emission sensor are plate shaped. Many researchers have investigated the resonance behavior of this shape and Leissa has published a book [106] summarizing many of the found results up to 1969. The general governing equation of the motion for transverse displacement for a homogenous plate is described in Möser [126] as,

$$\frac{\partial w^4}{\partial x^4} + 2 \frac{\partial^4 w}{\partial x^2 \partial y^2} + \frac{\partial^4 w}{\partial y^4} - \frac{m''}{D} \omega^2 w = \frac{j\omega p}{D} \quad (3.36)$$

with $m'' = \rho h$ as the mass per unit area with ρ the density and h the plate thickness, w the transverse displacement, p is an external force and D the flexural rigidity which is defined as,

$$D = \frac{Eh^3}{12(1 - \nu^2)}, \quad (3.37)$$

with E as the Young's modulus and ν the Poisson's ratio. It can be seen that the oscillation is clearly material dependent. Since Eq. 3.36 is in general form, boundary conditions have to be applied for special cases.

In the publication of Leissa [106] a multitude of different boundary conditions for plate resonators with the outer dimensions $a \times b \times h$ are described. For the acoustic-emission sensor system a two side clamped plate resonator was used. It is labeled C-F-C-F (C . . . clamped, F . . . free) and the frequency parameters λ and λ^* are defined as,

$$\lambda = \omega a^2 \sqrt{\rho/D} \quad \text{and} \quad \lambda^* = \omega b^2 \sqrt{\rho/D}, \quad (3.38)$$

with $\omega = 2\pi f$, ρ the density per unit area and D the flexural rigidity described in Eq. 3.37. The frequency parameters λ and λ^* are listed in tabular form for different mode shapes and a/b ratios for the C-F-C-F plate [106, p.75, Tab. 4.40] which enables the calculation of the frequencies as,

$$f = \frac{\lambda}{2\pi a^2} \sqrt{\frac{D}{\rho}}, \quad f^* = \frac{\lambda^*}{2\pi b^2} \sqrt{\frac{D}{\rho}}. \quad (3.39)$$

For the acoustic-emission sensor system it is desired to have resonator structures with different frequency response. From Eq. 3.37 and Eq. 3.38 it can be seen that changing the resonator dimensions will result in different resonant frequencies. Since space is always an issue, the height h is the parameter which should be adapted at first. When varying the height h it is important to consider limiting factors like a lower boundary due to mechanical stability and an upper boundary so that the resonator is not too stiff and will hardly oscillate.

3.4 Elastic Waves

Acoustic is the generation, the transmission and the reception of sound in form of mechanical oscillation and wave process in elastic materials (gases, fluids and solids) [101].

The oscillations of the resonant structure are distributed through the solid metal mass of the mold and are consequently structure-borne sound. Solid materials have the possibility to propagate longitudinal and transverse waves (see Fig. 3.3), in contrast to fluids and gases, in which waves only propagate as longitudinal waves. Hence, transverse waves are special to solid materials which is a result of their possibility to transfer tangential stress, also called shear stress [38]. Longitudinal waves are defined as a wave where particle displacement coincides with the direction of wave propagation. For transverse waves the propagation direction is orthogonal to the direction of displacement [38]. For both waves a minimal distance between two points with identical phase can be found, called wavelength λ . In Fig. 3.3 the principle of a longitudinal and transverse wave is shown. In addition, the model of an elastic body is shown. The elastic body can be shown as a model of nodes representing atoms or molecules and connecting springs. If the body is deformed the energy is stored within the springs and as soon as the force is omitted the body deforms into the initial shape.

Acoustic sound waves are always linked to their propagation medium. Both the velocity of sound and damping of amplitude are dependent on the type

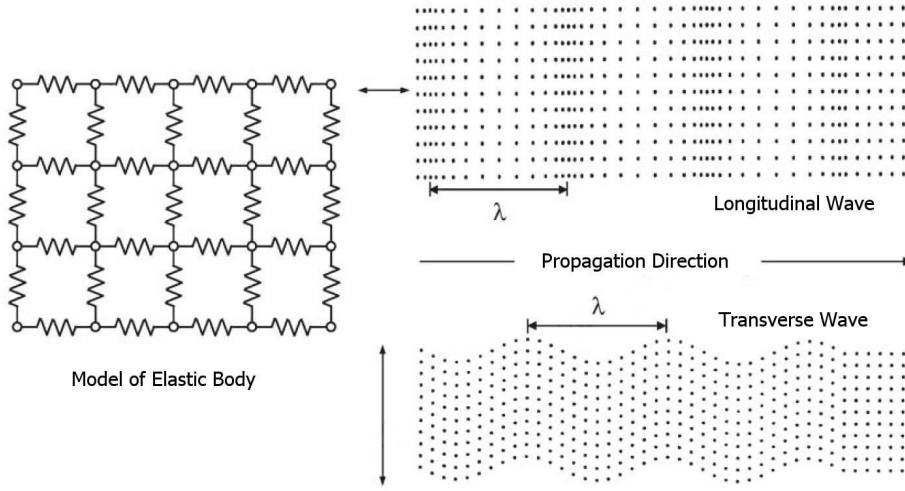


Figure 3.3: Model of an elastic body as well as principle oscillation of a longitudinal and transverse wave, with λ the wave length [109].

of material [109]. During structure-borne sound propagation the particles of the material are displaced on basis of physical regularities and fulfill an oscillation around the neutral position. Through a mechanical coupling (see model of elastic body in Fig. 3.3) neighboring particles are displaced as well, but with a temporal shift. The result is an onward total movement [109]. The following section is taken from Cremer [38]. The displacement ξ of the particle to its neutral position in a direction, e.g. x -direction, can be described as a strain ϵ ,

$$\epsilon_x = \frac{\partial \xi}{\partial x}. \quad (3.40)$$

This strain results in a stress σ or stress change in comparison to the neutral position. The proportional factor between stress and strain is in the sense of the Hook's law the longitudinal stiffness factor D ,

$$\sigma_x = D\epsilon_x = D \frac{\partial \xi}{\partial x}. \quad (3.41)$$

In addition, the stress is dependent on the position in the material. Hence, a mass element of length dx and a density ρ has an accelerated stress difference which is denoted as,

$$\left(\sigma_x + \frac{\partial \sigma_x}{\partial x} dx \right) - \sigma_x = \rho dx \frac{\partial^2 \xi}{\partial t^2}. \quad (3.42)$$

When introducing the velocity ν_x , Eq. 3.42 can be re-written as,

$$D \frac{\partial \nu_x}{\partial x} = \frac{\partial \sigma_x}{\partial t}. \quad (3.43)$$

As it can be seen the values are linked in time and space. Differencing Eq. 3.43 by time and space leads to the general wave equation,

$$D \frac{\partial^2}{\partial x^2} (\sigma_x, \nu_x) = \frac{\partial^2}{\partial t^2} (\sigma_x, \nu_x), \quad (3.44)$$

in x -direction.

The molds used for injection molding are mainly build from steel. The sound propagation in steel is approximately 5000 m s^{-1} [81]. Imagining a very big mold with a travel distance of the sound from the source to the outside surface of the mold of 1 m, the time for sound propagation is about 0.2 ms, which is very short. Consequently, sound propagation will have no significant impact on the sensor performance at all.

3.5 Transducer

The task of the transducer is to convert mechanical strain into electricity [87]. Mechanical strain is the result of occurring vibrations. It can be measured as the displacement $x(t)$, the velocity $v(t)$ or the acceleration $a(t)$ [74]. These parameters are related to each other through differentiation and integration,

$$a(t) = \frac{dv(t)}{dt} = \frac{d^2x(t)}{dt^2}. \quad (3.45)$$

For the conversion of the mechanical stress to a proportional electricity a piezoelectric accelerometer attached to the metal mass of the mold is used. The sensor is based on the *direct piezoelectric effect*. This effect is mainly found in crystals and some complex ceramics [87]. If pressure is applied to the material it is deformed and a change in the magnitude of the polarization occurs, which results in a small voltage across the sample [87]. The change in polarization leads from the fact that the center of gravity of the positive and negative charge are elastic deformed building microscopic dipoles within the unit cell and leading to a measurable voltage over the sum of the unit cells.

A seismic mass is connected to the piezo element for accelerometer sensors. If the seismic mass is displaced by an external force a proportional charge can be measured. Using Newton's law of motion lets one calculate the corresponding acceleration. In Fig. 3.4 a typical mechanical setup of an accelerometer in compression mode is shown. The compression mode accelerometer uses

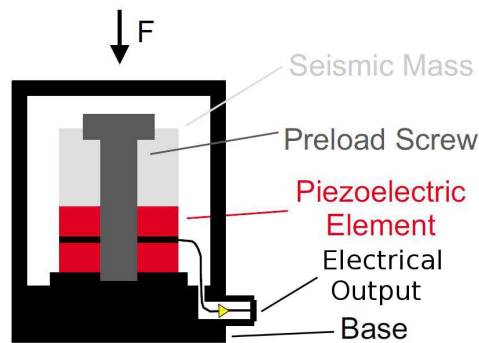


Figure 3.4: Accelerometer in compression mode for sensing structure-borne sound [74].

the longitudinal piezoelectric effect. Here, the piezoelectric element is sandwiched between the seismic mass and the base with an elastic preloaded screw. When the sensor is accelerated, the piezoelectric element is squeezed and creates an electrical output. The frequency response of piezoelectric accelerometers is determined by the low frequency limit and the resonance frequency. In the usable frequency range, which is specified by the manufacturer, the frequency response is linear within the accuracy tolerances [74]. Mounting of the accelerometer is also an important aspect for sensing the vibrations. In Haase [74] four mounting possibilities are listed:

1. stud mounting;
2. adhesive mounting;
3. magnetical mounting and
4. hand-held probe tips.

The used mounting of the sensor has a significant influence since the resonance frequency of the mounted sensor depends also on the stiffness of the contact between the sensor and the measurement object [74,102]. In Fig. 3.5 it can be seen that stud mounting has the widest frequency response because it provides the stiffest coupling. Adhesive mounting, however, is a more flexible mounting possibility. If the glue is used in thin layers and the curing is stiff, adhesive mounting is almost equivalent to stud mounting [74].

For a more temporary mounting of the sensor a ferromagnetic coupling or a hand-held probe tip is possible. Both methods result in a lower frequency response of the sensor and should only be used for e.g.g finding the best mounting location.

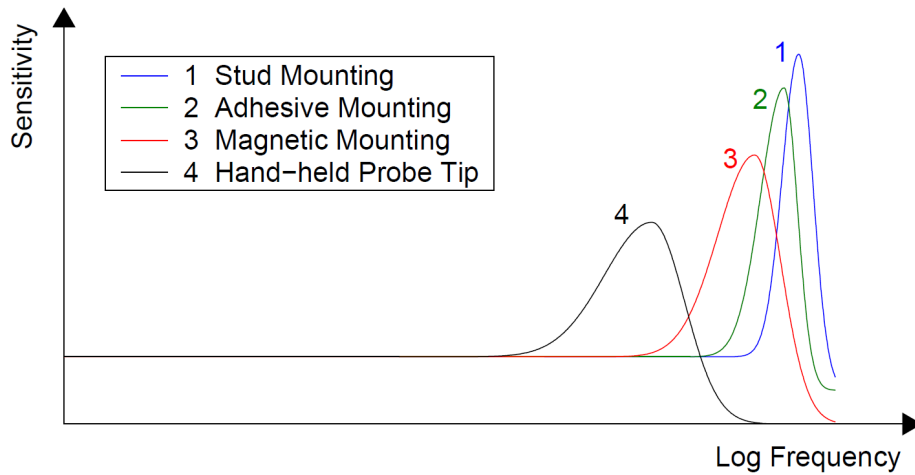


Figure 3.5: Resonance frequency of an accelerometer in dependency of mounting situation [74].

3.6 Signal Processing

At the beginning of the detection chain a piezoelectric accelerometer generates a continuous signal $y_P(t)$. The signal $y_P(t)$ is amplified and afterward digitized by an analog-to-digital converter (ADC). This leads from $y_P(t) \rightarrow y_P[n]$, with $n \in \mathbb{N}^+$, the discrete sample number. The target of the following signal processing is to implement optimal event detectors, optimal in terms of signal to noise ratio. The target of all the presented methods is to detect and analyze the recorded sound with special focus on the distinctive generated sound by the acoustic resonators.

Three different signal processing methods are presented:

1. envelope method;
2. filter signal processing and
3. frequency pattern recognition method.

The simplest method applied is the *envelope method*. This method was used to perform the signal processing on a programmable logic controller (PLC). A PLC has consecutive limited time slots in which the complete calculation per task cycle has to be finished to ensure real-time processing. The envelope method reduces the amount of data to simplify the decision process. As a result of this data reduction solely the impact event can be detected and the separation of multiple events is not possible.

The second method presented uses a classical filter approach with bandpass filters to detect and separate multiple resonator signals. Thereby the knowledge of the oscillation behavior of the resonator is used for the filter design process.

For the third approach at first statistical signal processing is introduced for the reduction of calculation effort. The third approach, called *frequency pattern recognition method*, uses a new, numerically very efficient algebraic approach. Polynomial windowing is combined with a discrete Fourier transform to implement a signature matching algorithm. Therefore each resonator response behavior is stored in a signature matrix. During runtime the signatures are searched in the data stream $y_P[n]$. In addition to calculating the matching coefficients, which represent the amount of presence of a resonant structure, the calculation of the variances with consideration of the covariance of the coefficients is straightforward. This enables the calculation of a confidence interval which is an important aspect for instrumentation.

3.6.1 Envelope Detection

The first method applied for the detection of an activated acoustic actuator is a simple signal processing method called *envelope detection* [120]. The method was used to enable the impact detection on hardware with limited calculation power, e.g. a PLC. The advantage of using a PLC is the ability of real time calculation. Each running task on the PLC has fixed time slots and is called periodically in which the calculations have to be finished. In Fig. 3.6 an example with two different task classes and an additional timer class is shown. Cycle#1 has a cycle time of 10 ms and Cycle#2 has a cycle time of 30 ms. The additional timer is called every 5 ms. As it can be seen, the central processing unit (CPU) processing time is scheduled between the tasks in a way that each task has sufficient calculation time. This can only be achieved by interrupting one cycle, process another and come back to the interrupted cycle to proceed calculations. If one time slot is exceeded the PLC goes into an error handling mode [15]. This fact has an even higher impact if the sampling rate of the recorded data is high in comparison to the fastest task class of the PLC since the chance is high that the available calculation time is not sufficient. This case was present for the acoustic-emission sensor since the impact sound is solely of short duration and consequently a high sampling rate is necessary. Due to these restrictions an efficient low calculation cost algorithm was used - the *envelope detector* - which consists of two steps,

1. calculating the envelope and
2. the decision process for acoustic actuator activation detection.

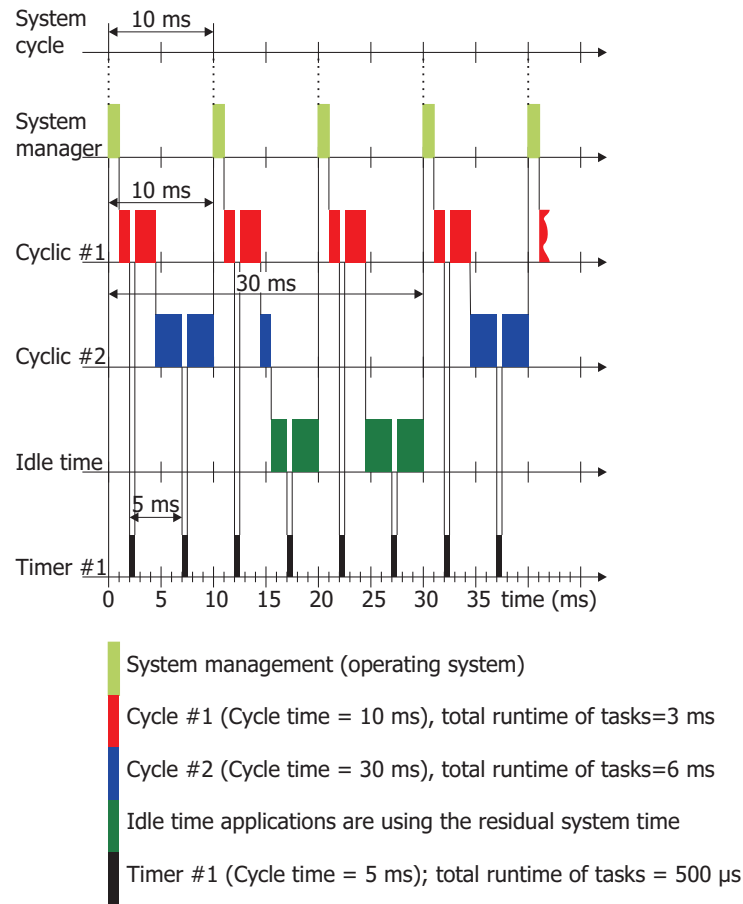


Figure 3.6: Task diagram of a PLC from Bernecker+Rainer Industrie Ges.m.b.H, Austria. Two different task classes *Cycle#1* and *Cycle#2* are shown, one with 10 ms cycle time, the other with 30 ms calculation time. In addition, a timer cycle is implemented in this example. In reference to [13].

At first, from the oscillating signal the envelope is calculated with the property of instantaneous increase and slow decaying behavior. This process conserves the amplitude of the signal for a longer period since the signal does not die away immediately. In Fig. 3.7 a test signal is shown as a black line. The signal was synthesized with a frequency sampling rate of $f_s = 44.1$ kHz. The red line represents its calculated envelope using Algorithm 3.1. The variable y_E , which holds the actual value of the envelope, is set to 0 at the beginning. Additionally, two constants, the frequency sampling rate f_s as well as the decay characteristic τ have to be defined. The function `CALCENVELOPE()` is called in strict time slots and processes the stored values of the recorded

Require: y_P ▷ Transducer signal
Require: $y_E = 0$ ▷ Envelope signal
Require: τ ▷ Define decay characteristic
Require: f_s ▷ Define sampling rate

1: **function** CALCENVELOPE(y_P, y_E) ▷ Gets called at f_s -rate
2: **if** $y_P > y_E$ **then**
3: $y_E \leftarrow y_P$
4: **end if**
5: $y_E \leftarrow y_E - f_s * y_E / \tau$
6: **return** y_E ▷ Stored for decision process
7: **end function**

Algorithm 3.1: Pseudo-code for the calculation of the envelope of the acoustic signal.

signal y_P ⁷. Next, the actual signal y_P is compared to the current calculated envelope y_E . If the actual signal is greater than the envelope signal it gets replaced by it. Additionally, for each cycle a certain amount is subtracted from y_E , defined by the characteristic value τ . The signal y_E is used for the decision process.

For the test signal shown in Fig. 3.7 τ is set⁸ to 0.98 to show the decaying behavior in a clear manner. At 2 ms the original signal is sharply damped. However, the envelope stays on a higher level for a longer period of time although the signal y_P is already decayed. The instantaneous response characteristic can at best be observed at around 0.5 ms. The envelope follows the sharp rise of the original signal instantaneously.

When having calculated the envelope a decision process is needed which decides if an acoustic actuator activation is present or not. For increased

⁷This process is in dependence of the sampling rate f_s and the maximum task class of the PLC. If the sampling rate is below the task class no buffer is needed and the sampling rate is defined by the task class cycle time itself. However, if the sampling rate exceeds the highest task class a buffer has to be introduced (some modules of the PLC offer hardware buffering).

⁸The value was found by experience.

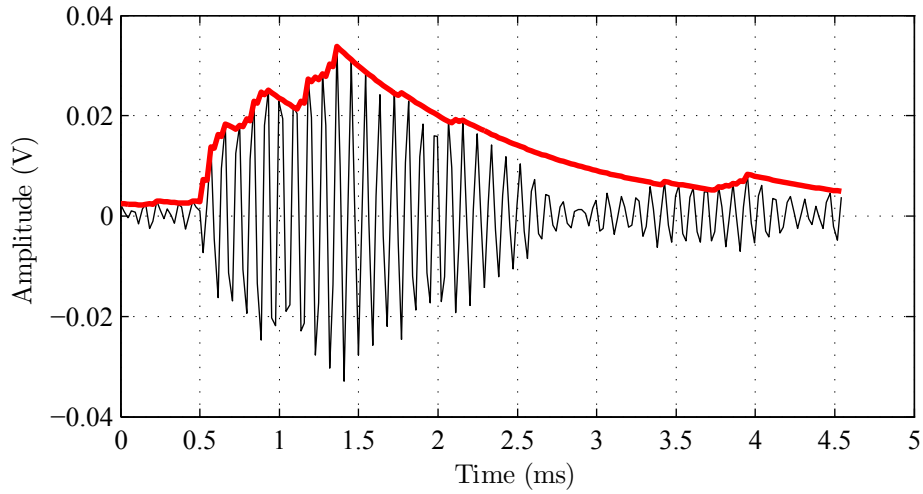


Figure 3.7: Calculation of the envelope curve y_E for easier detection of the acoustic actuator activation.

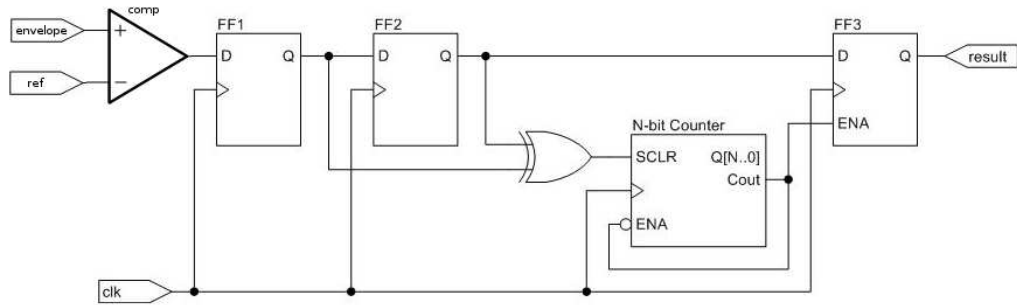


Figure 3.8: Schematic logic circuit originally for button debouncing in reference to [40]. This hardware setup can be implemented in the PLC in software yielding high flexibility in terms of adapting.

fail-safe performance three criteria were set up and have to be fulfilled for a positive detection:

1. the signal has to appear in a certain window after start of the process, i.e. injection molding;
2. the peak has to reach a certain amplitude level and
3. the peak has to stay above this level for a certain duration.

Knowing the cavity's shape and its volume as well as the injection rate and additionally the implementation location of the acoustic actuator, an estimated window for the signal appearance can be determined. This window

ensures that not any other upcoming intense sound, e.g. the opening sound of the valve gate nozzle, are falsely detected as an activated acoustic actuator. The second and the third criteria are both linked to the amplitude of the envelope. First, a certain amplitude level has to be reached after which a timer starts measuring the duration of the overshoot. If the envelope stays long enough above the detection amplitude, an activation of an acoustic actuator is deemed to have occurred.

The requirements to detect the duration of the overshoot are similar to those of a debouncing filter, e.g. when triggering a button⁹. In Fig. 3.8 the logic circuit of a debouncing circuit is shown which was implemented in the PLC in software. The circuit is synchronized by a clock (*clk*). At first the envelope signal is compared (*comp*) to a reference value. The reference value is holding the amplitude value which has to be overshoot by the calculated envelope signal y_E . The envelope is stored as a logic level - when higher as the detection level a 1 is stored otherwise 0 - in two flip-flops (*FF1* and *FF2*). Consequently, the last two states of the envelope are stored in the flip-flops. When the state of the envelope stays long enough at the same state the flip-flop *FF3* is enabled by the connector *ENA*, and the result is true. The time the envelope has to stay above the reference value is realized by a N-bit counter which starts counting in the moment *FF1* and *FF2* have the same state. If the envelope changes its state during the counting the N-bit counter is cleared and reset by a XOR gate (see XOR truth table in Tab. 3.1) indicating that the envelope was not long enough above the detection level. The *result* is again a logic level indicating the state of the acoustic actuator.

Table 3.1: XOR truth table for two input variables *A* and *B* [187].

| Input | | Output |
|-------|---|--------|
| A | B | |
| 0 | 0 | 0 |
| 1 | 0 | 1 |
| 0 | 1 | 1 |
| 1 | 1 | 0 |

3.6.2 Filter Signal Processing

Filter signal processing is a method for manipulating an input signal in a manner such that undesired components in the output signal are modified or

⁹The debouncing is necessary to ensure just one button pressing event is sensed instead of recognizing falsely multiple.



Figure 3.9: Block diagram of a filter manipulating an input signal $x[n]$ to the output signal $y[n]$, which is modified in a way that unwanted components of the input signal are attenuated [74].

removed. Filters are used in a wide application field in analog or digital signal processing [89, 139, 187]. However, the focus in this chapter is on digital signal processing and especially on techniques used for the acoustic-emission sensor. The content of this section was mainly inspired by Haase, who wrote a PhD thesis on vibrational analysis in steel rolling [74], and Zhuang, who investigated filter techniques for the evaluation of the acoustic-emission sensor [207], as well as Oppenheim and Schaffer, who wrote a fundamental book about discrete-time signal processing [139].

The idea of filtering is to have an input signal $x[n]$, with n the discrete sample number, manipulate it in a manner such that unwanted portions or frequency components are attenuated, and provide a new output signal $y[n]$, as it is shown in Fig. 3.9. Since the filter is implemented as a digital filter in terms of software it is highly flexible and can easily be adapted for the actual requirements.

Digital filters are a subclass of linear time-invariant systems (LTIs). In Oppenheim and Schaffer [139] the class of LTI is defined by the principle of superposition,

$$\mathsf{T}\{a x_1[n] + b x_2[n]\} = a \mathsf{T}\{x_1[n]\} + b \mathsf{T}\{x_2[n]\}, \quad (3.46)$$

where $x_1[n]$ and $x_2[n]$ are the respective inputs, a and b are arbitrary constants and T is a mapping operator, mapping between the input and output signal $y[n] = \mathsf{T}\{x[n]\}$.

In general a signal $x(t)$ from an analog source, e.g. a sensor, is acquired using an analog-to-digital converter (ADC). The signal is sampled with the sampling frequency $f_s = 1/T$, with T the sampling interval. As a result, discrete samples $x[n]$ are obtained. For describing the sampling process the unit-strength impulse $\delta(n - m)$ has to be introduced as,

$$\delta(n - m) = \begin{cases} 1 & \text{for } n = m \\ 0 & \text{for } n \neq m \end{cases}. \quad (3.47)$$

The unit-strength impulse train, $\delta_T(n)$, can be viewed as the superposition of a set of shifted discrete-time unit-strength impulses and is expressed as,

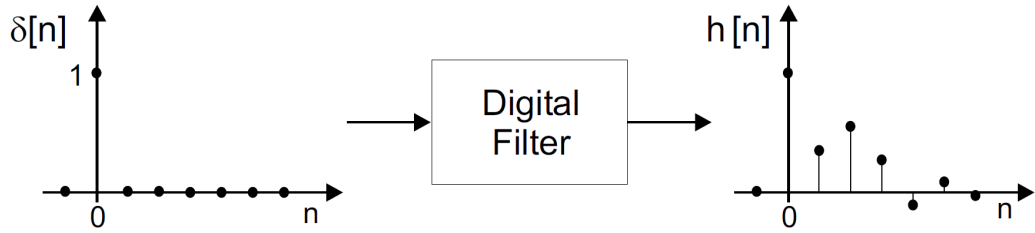


Figure 3.10: *Left:* Dirac impulse at sample $n = 0$; *Right:* Impulse response $h[n]$ of the digital filter [74].

$$\delta_T(n) = \delta(n + \infty T) + \dots + \delta(n + 2T) + \delta(n + T) + \delta(n) + \delta(n - T) + \delta(n - 2T) + \dots + \delta(n - \infty T) \quad (3.48)$$

Eq. 3.48 can be written as the sum over all samples k as a function of time n ,

$$\delta_T(n) = \sum_{k=-\infty}^{\infty} \delta(n - kT), \quad (3.49)$$

where $\delta(n - kT)$ denotes a delayed unit-strength impulse occurring at $n = kT$, and $\delta(n + kT)$ denotes an advanced unit-strength impulse occurring at $n = -kT$. Hence, the ideal sampled signal is given by,

$$x[n] = x(n) \times \delta_T(n) = x(n) \sum_{k=-\infty}^{\infty} \delta(n - kT). \quad (3.50)$$

If the principle of superposition (Eq. 3.46) is combined with the representation of a sequence as a sum of delayed impulses (Eq. 3.50), it can be denoted that a linear system can completely be characterized by its impulse response $h_k[n]$ to an input $\delta[n - k]$ for $n = k$ (see Fig. 3.10). For the system output $y[n]$ it follows under the assumption of the time invariance property,

$$y[n] = \sum_{k=-\infty}^{\infty} x[k]h_k[n - k] \quad \text{for all } n. \quad (3.51)$$

From Eq. 3.51 it can be seen, that the system is completely described by the impulse response. Consequently, filters can be described by their impulse response $h[n]$. This is a fundamental property of stationary linear differential systems and the basis for solving ordinary differential equations (ODEs). The sum in Eq. 3.51 is also denoted as the *convolution* of $x[n]$ and $h[n]$, i.e.,

$$y[n] = x[n] * h[n]. \quad (3.52)$$

Another way of representing linear filters is the *difference equation*, noted as,

$$y[n] = \sum_{k=1}^M a_k y[n-k] + \sum_{k=0}^N b_k x[n-k]. \quad (3.53)$$

Eq. 3.53 can be shown as a direct realization of the difference equation in form of a noncanonic block diagram referred to as the *direct form I*. An implementation with minimum number of delay elements, e.g. $y[n-k]$ with $n \neq k$, is referred to as a *canonic direct form* implementation or *direct form II* [139].

The filter characteristic is described by the filter coefficients a_k and b_k . The current output sample $y[n]$ is calculated by the previous N input samples $x[n-k]$ as well as the previous M output samples $y[n-k]$. If all a_k are zero the filter is known as non-recursive or finite-impulse response (FIR) filter. In case of $M \neq 0$ the filter is called recursive or infinite-impulse response (IIR) filter. For a FIR filter the recursive term of Eq. 3.53 can be neglected which yields the fact that the coefficients b_n are in fact the filter response $h[n]$ for $n = 0, 1, \dots, N$.

The representation of the filter by its impulse response or the difference equation describes the characteristic in the time domain; however, it is often desired to describe filtering behavior in the frequency domain using the *frequency response*. The frequency response is related to the impulse response of a digital filter through the Fourier transform,

$$H(\nu) = \mathfrak{F}\{h[n]\}, \quad (3.54)$$

with ν the frequency. As a transfer function the *z-transform* is introduced which is identical to the Fourier transform when evaluated on the unit circle in the complex plane. The z-transform operator $\mathcal{Z}\{\cdot\}$ is defined as [139],

$$\mathcal{Z}\{x[n]\} = \sum_{n=-\infty}^{\infty} x[n]z^{-n} = X(z), \quad (3.55)$$

with $z = re^{j\omega}$. Applying the z-transform on the impulse response leads to,

$$H(z) = \mathcal{Z}\{h[n]\}. \quad (3.56)$$

In reference to Eq. 3.52, where the time-dependent output was described by the convolution sum of the impulse response and the input signal, the equivalent notation in the frequency domain is,

$$Y(z) = \mathcal{Z}\{x[n] * h[n]\} = X(z) H(z). \quad (3.57)$$

The spectrum of the output signal $Y(z)$ is described by the multiplication of the spectrum of the input signal $X(z)$ and the frequency response $H(z)$ of the filter.

The four most common filters are: *low-pass filter*, *high-pass filter*, *band-stop filter* and *band-pass filter*. The low-pass filter enables frequency components up to a critical frequency ν_c to pass the filter. The output signal contains consequently just the low frequency portions of the input signal. The opposite filter type is the high-pass filter. All frequency components up to a critical frequency ν_c are attenuated so that just high frequency components of the input signal are present in the output signal. The band-pass filter lets frequencies pass which are in a certain range. The opposite filter - the band-stop filter - attenuates frequencies in a certain range. In Fig. 3.11 the frequency response of these four filter types are represented in ideal form. In literature, often just low-pass filters are discussed since a low-pass filter can be algebraically transformed into each of the other three filter types [108,139]. However, it is not possible to design filter response characteristics with such sharp rectangular¹⁰ behavior as shown in Fig. 3.11 because of the time frequency duality. As a result, different approaches try to approximate the ideal frequency response characteristic which leads to design tolerances. In Fig. 3.12 the tolerance scheme for a low-pass filter frequency response (dashed line) is shown. The frequency response is divided into three sections, the *pass-band*, the *transition-band* and the *stop-band*. The transition-band begins at the frequency ν_p , which is the end of the pass-band, too. The stop-band begins at the frequency ν_s . In addition, tolerances for the gain have to be determined. The pass-band gain tolerance is between 0 db and $-\delta_p$ and the stop-band tolerance gain is below $-\delta_s$.

There are several methods known to design a filter, all leading to different properties of the filter, e.g. Butterworth-Filter, Chebyshev-Filter or Elliptical-Filter. These filter design techniques are discussed in detail for instance in Oppenheim and Schaffer [139].

¹⁰This is a consequence of the Fourier transformation for a rectangular signal which leads to the *sinc* function [74].

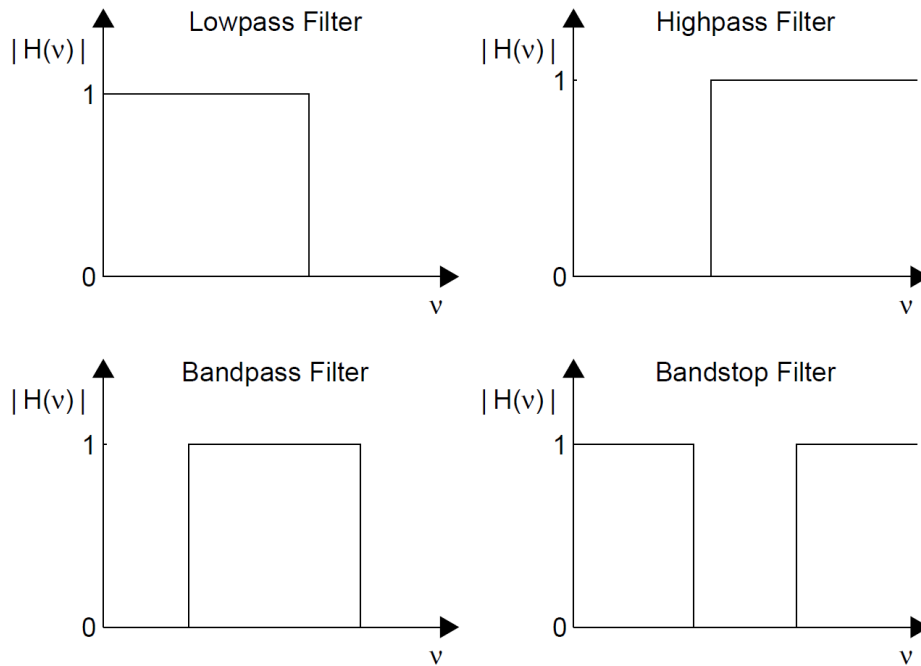


Figure 3.11: Frequency response $|H(\nu)|$ in dependence of the frequency ν of the four general filter types [74].

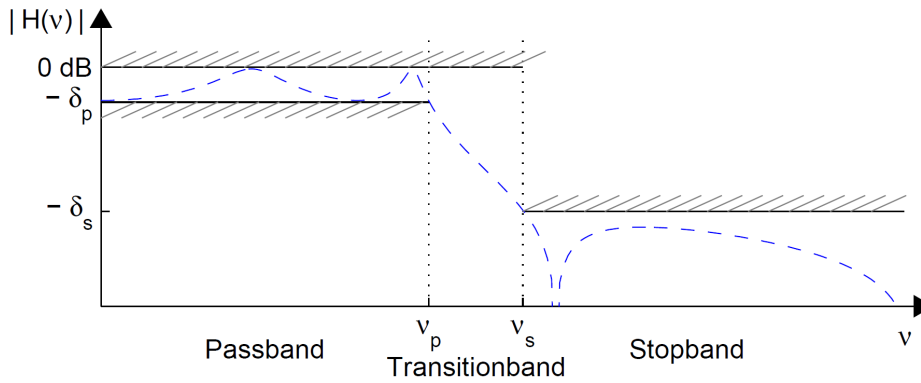


Figure 3.12: Tolerance scheme of the frequency response $|H(\nu)|$ (dashed line) of a low-pass filter. The frequency response is divided in three regions, the pass-band ($0 < \nu < \nu_p$), the transition-band ($\nu_p < \nu < \nu_s$) and the stop-band ($\nu_s < \nu < f_s/2$) whereas tolerances for the gain have to be determined (δ_p and δ_s) [74, 139].

3.6.3 Statistical Signal Processing

The aim of statistical signal processing in the present manner is to find statistical relevant portions of the recorded signal $y_P[n]$ to reduce calculation effort on the region of interest. When recording data with high frequency sampling rates f_s a large amount of data is generated. Assuming a recording time of 1.5 s and sampling frequency of $f_s = 120$ kHz, a signal data set $y_P[n]$ of the size 180000 x 1 is generated. When performing signal processing, i.e. filter signal processing or frequency pattern matching, for finding the event of the activated acoustic actuator in the complete data set $y_P[n]$, the algorithm would not be efficient and consequently time consuming.

To overcome this inefficiency, the signal $y_{Po}[n]$ is analyzed towards statistically significant portions on which the signal processing is performed afterwards. Since additional distinctive sound is generated due to the impact of the movable pin on the resonant structure a short but sharp deflection is expected in the recorded signal. The deflection can also be narrowed down to a short time frame at which the melt front passes the acoustic actuator. Throughout the rest of the time solely large levels of noise are expected in the recorded signal. This foreknowledge can be used to set up the statistical signal processing algorithm to reduce the overall amount of data for signal processing.

The advantage of statistical analysis in comparison to spectral analysis or model-dependent probability can be found in its numerical efficiency, consequently calculation complexity is low [74]. A more detailed explanation of statistical signal processing and its methods can be found for instance in [70, 74, 95, 119].

The first order moment is called the *mean* value of a data set and is indicated by \bar{y}_P . It is calculated via,

$$\bar{y}_P \triangleq \frac{1}{N} \sum_{i=1}^N y[i]. \quad (3.58)$$

The second order moment is the *variance* σ^2 . There are two ways of calculating the variance depending on working with a distribution of scores taken from a sample or population. The reason is that for samples the mean value is not known and has to be estimated from the taken samples. As a result it will defer from the population mean. To consider this underestimation the denominator is defined as $N - 1$ giving a bigger variance [192]. Hence, this equation is called *sample variance* and is given by,

$$\sigma^2 \triangleq \frac{1}{N-1} \sum_{i=1}^N (y[i] - \bar{y}_P)^2. \quad (3.59)$$

The sum of squares yield a maximum likelihood predictor for a Gaussian distributed signal. In general the sample variance is Student-t distributed with $f = N - 1$ degrees of freedom. However, if the sample size N is large it can be approximated with the standard normal distribution [16]. To obtain the *standard deviation* the positive square root of the variance has to be calculated, i.e. $\sigma \triangleq \sqrt{\sigma^2}$.

The advantage of the standard deviation is that it holds the same unit as the recorded data set yielding the ability to give a range around the mean value ($\bar{y}_P \pm \sigma$) where 68 % of all recorded data points will lie within, when the samples are normal distributed. In the range of $\bar{y}_P \pm 2\sigma$ approximately 95 % of all values will lie within [74, 163].

There are two more moments of degree three and four. The momentum of third degree is named *skewness* μ_3 and one of its definitions is,

$$\mu_3 \triangleq \frac{1}{N\sigma^3} \sum_{i=1}^N (y[i] - \bar{y}_P)^3, \quad (3.60)$$

whereby dividing by σ^3 normalizes the skewness making it dimensionless.

The skewness is a dimensionless number and gives additional information about the shape of the distribution (especially asymmetry). Since it is a momentum of odd degree the sign is retained yielding the possibility of positive and negative values for the skewness. A skewness around zero indicates a perfectly symmetrical distribution [6, 74].

The fourth momentum is named *kurtosis* μ_4 . The kurtosis is conventionally defined as,

$$\mu_4 \triangleq \left[\frac{1}{N\sigma^4} \sum_{i=1}^N (y_i - \bar{y})^4 \right] - 3. \quad (3.61)$$

Like the skewness, the kurtosis is defined as a dimensionless value by dividing with the normalizing term σ^4 . The kurtosis gives additional information about the shape of the distribution. The value of the kurtosis describes the peakedness of a distribution relative to a normal distribution. The term -3 ensures a zero value of the kurtosis for a normal distribution. Negative values indicate a flat distribution and positive values indicate a peaked distribution [6, 74].

Two example distributions and their effect on the value of the skewness and the kurtosis are shown in Fig. 3.13. On the left side a typical unsymmetrical

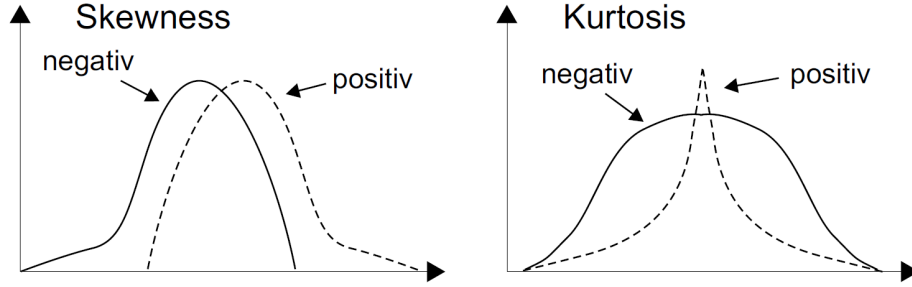


Figure 3.13: *Left:* Schematic representation of two unsymmetrical distributions with tails pointing in positive and negative direction. This is leading to a positive and negative skewness; *Right:* Schematic representation of a significantly different form of a normal distribution indicated by positive and negative values of the kurtosis [74].

distribution for a positive and a negative value of the skewness is shown. The positive or negative value of the skewness results from the unsymmetrical tail pointing once towards to positive and once to negative values. On the right side two distributions which significantly differ from a normal distribution are shown.

Having recorded a data set with a large number of data points the small region of interest needs to be identified. For the complete data set $y_P[n]$ with N components a mean value \bar{y} can be estimated using Eq. 3.58. This mean value is further used for local variation and a local skewness calculation for each data point i via,

$$\begin{aligned} \sigma^2[i] &= (y_P[i] - \bar{y}_P)^2, \quad \forall i \in \mathbb{N} : i = 1, 2, \dots, N, \\ \mu_3[i] &= \left| \frac{(y_P[i] - \bar{y}_P)^3}{N\sigma^2[i]} \right|, \quad \forall i \in \mathbb{N} : i = 1, 2, \dots, N. \end{aligned} \quad (3.62)$$

Both data sets, σ^2 and μ_3 , are further processed to split the recorded signal \mathbf{y}_P in statistically significant portions. Therefore the distributions of the local variance and skewness is estimated by the categorical distribution. Bins in form of k identically spaced categories are introduced. Each data point of the variance and the skewness are assigned to one bin generating a distribution of the whole data set. The best way of representing such a distribution in a graphical manner is the histogram [156]. The distribution is normalized for further processing. For simplicity the probability calculation is only shown for the variance and is identically calculated for the skewness. The data

point x is introduced which represents one value of the data set $\sigma^2[i]$. The same procedure is applied to the skewness. A cumulative sum of the bins is calculated estimating the cumulative distribution function [23], i.e.,

$$F_X(x) \triangleq P(X \leq x) = P_X((-\infty, x]), \quad (3.63)$$

for a real-valued random variable X with the property of F ,

$$\lim_{x \rightarrow -\infty} F(x) = 0, \quad \lim_{x \rightarrow +\infty} F(x) = 1. \quad (3.64)$$

Now a value between $[0, 1]$ from \mathbb{R} can be set for X which gives a certain value for x . This value can be searched in the data set $\sigma^2[i]$ giving a point of significant statistical importance. By setting up a range around this point a data set can be extracted which is analyzed towards the appearance of the signature pattern.

A demonstration signal $y[n]$ is introduced consisting mainly of large levels of white Gaussian noise. The signal duration is 10 s and has $N = 1000$ samples. At the sample $n_1 = 500$ (or at 5 s) a deflection is generated which is described via,

$$d[n] = 5e^{-0.5(n-n_1)}, \quad 500 \leq n \leq 700, \quad (3.65)$$

and is added to the noise. Using $y[n]$ the descriptive statistic method is applied to find the statistical important portion.

In Fig. 3.14 *Top-Left* the signal is shown and as it can be seen the deflection is hard to locate just from viewing at the signal $y[n]$. Using Eq. 3.62 a local variance $\sigma^2[n]$ and a local skewness $\mu_3[n]$ is calculated for all samples N shown in Fig. 3.14 *Top-Middle* and *Top-Right*. From just inspecting both signals it is clear that locating the deflection around 5 s has a better signal to noise ratio, especially the variance. Both signals, $\sigma^2[n]$ and $\mu_3[n]$, present a large spike at 5 s lifting of the ground noise level and enabling simpler identification. These spikes are a result of the large difference of the deflection to the mean values as well as its unsymmetrical shape. In Fig. 3.14 *Middle* the histograms of the local variance and skewness are shown. For easier recognition just $k = 15$ bins were chosen showing the distribution of the values of $\sigma^2[n]$ and $\mu_3[n]$. Both distributions consist of mainly small components caused by the white Gaussian noise. Just little larger components are contained in the signal which are attributable to the damped deflection. In Fig. 3.14 *Bottom* the normalized cumulative distribution are shown for the variance and the skewness (see Eq. 3.63). Finally, a value for X is chosen, i.e. $X = 0.999$. Due to the normalization process at least one bin is above the value X . Since the bins correspond to the value of the variance or the skewness, all temporal

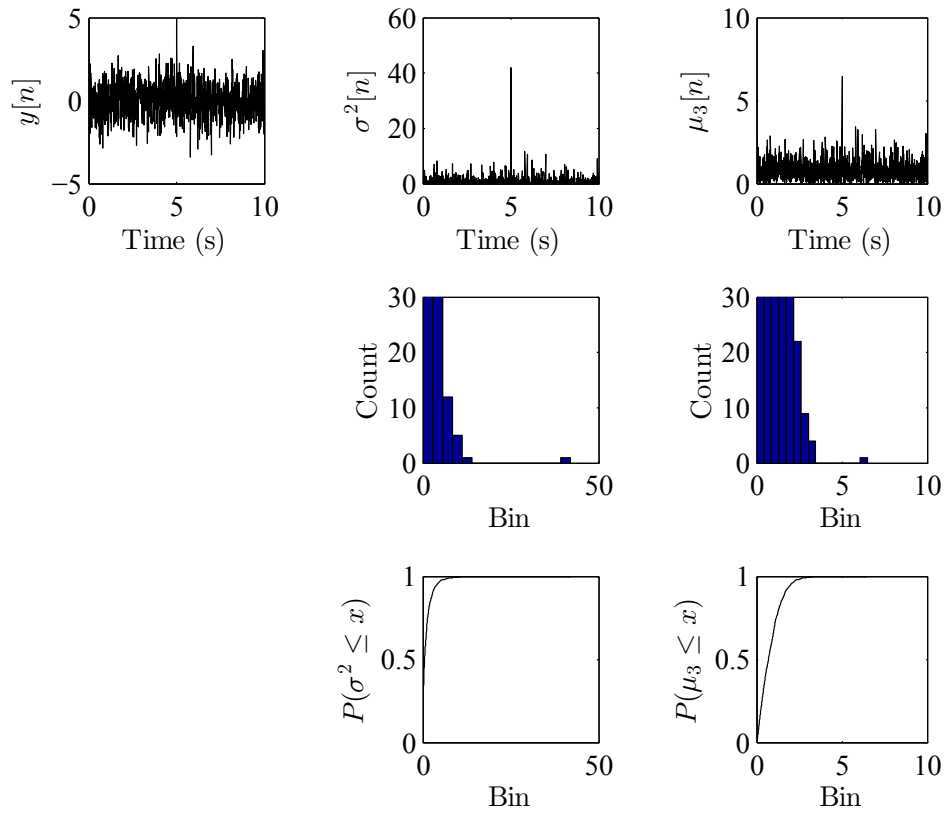


Figure 3.14: *Top-Left:* Demonstration signal $y[n]$ consisting of mainly white Gaussian noise with a deflection at 5s which should be found using descriptive statistic; *Top-Middle:* Local variance $\sigma^2[n]$ indicating the deflection at 5s; *Top-Right:* Local skewness $\mu_3[n]$ indicating the deflection at 5s; *Middle-Left:* Histogram of the local variance which mainly consists of noise indicated by large amount of small components; *Middle-Right:* Histogram of the local skewness which mainly consists of noise indicated by large amount of small components; *Bottom-Left:* Cumulative distribution function of the local variance; *Bottom-Right:* Cumulative distribution function of the local skewness.

moments can be searched in the signal for which the variance or skewness value is exceeded. Consequently a statistically significant region is identified. This example is very simple due its small number of samples. When processing larger signals which differ in shape to each other the presented method

has significant advantages in finding statistical important regions with small computational complexity.

3.6.4 Frequency Pattern Recognition Method

The frequency pattern recognition algorithm was developed to combine advantages of both techniques previously presented, i.e., fast computation and separation of signals from different resonant structures by frequency analysis [127]. The signal detector should be optimal in terms of noise performance and in detecting the characteristic oscillations of the installed resonators. Due to the complex mechanical form of the mold the signals from the acoustic actuators are not fully independent to each other as a result of internal reflections within the mold. Consequently, classical correlation detectors will not function optimally [49].

To avoid this problem, a novel algebraic approach for signature recognition is implemented. This method is numerically efficient while maintaining the advantage of full spectrum pattern matching. In addition, this method yields the covariance propagation which enables calculating a confidence interval for the found correlation coefficients.

The method mainly consists of two steps:

1. *Signature identification*, i.e. identifying the optimal frequency domain signatures for each resonator. This task is performed prior to the measurement. The resultant signatures are stored and used for signature matching. This step can be considered as a calibration of the system;
2. *Signature matching*, which enables the calculation of the correlation coefficient for each resonator. This calculation is formulated as a linear matrix algebraic computation and is numerically efficient. The covariance propagation for the linear operator can be computed straightforward.

In most common literature on digital signal processing, e.g. [139, 152], the computation of the discrete Fourier transform (DFT) is formulated as,

$$s[k] = \sum_{n=0}^{N-1} y[n] e^{-j2\pi nk/N} = \sum_{n=0}^{N-1} y[n] W_N^{kn}, \quad k = 0, 1, \dots, N-1, \quad (3.66)$$

whereby $y[n]$ is the n^{th} sample of the input signal. N is the total number of available samples and k defines the discrete frequency $f_k = (2\pi nk/N)f_s$

with respect to the sampling frequency f_s . In Equation 3.66 $s[k]$ may be a complex number since the Euler identity is defined as,

$$W_N^{kn} = e^{-j2\pi nk/N} = \cos(2\pi kn/N) - j \sin(2\pi kn/N), \quad (3.67)$$

with $j = \sqrt{-1}$. When having N input samples there are N components in the discrete Fourier spectrum $s[k]$. Computing the DFT is most commonly implemented using the fast Fourier transform (FFT) algorithm. Thereby the property of symmetry and periodicity of W_N^{kn} is exploited to increase speed dramatically. There are many algorithms for calculating the FFT like Cooley-Turkey algorithm [37] or Good-Thomas algorithm [67]. Heideman, Johnson and Burrus have shown in [80] (1985) that the basic ideas of the FFT algorithm of Cooley and Turkey can be traced back to Gauss, as early as 1805. The DFT and FFT are functionally identical, the FFT is simply a numerically more efficient method of performing the computation. The computation of the DFT can also be formulated as a matrix operation. The discrete Fourier basis function $f(k)$,

$$f(k) \triangleq e^{-j2\pi nk/N}, \quad (3.68)$$

can be concatenated forming the columns of a matrix \mathbf{F} , such that,

$$\mathbf{F} \triangleq [f(0), f(1), \dots, f(N-1)]. \quad (3.69)$$

In MATLAB¹¹ a command for generating the DFT is provided, $\mathbf{F} = \text{dftmtx}(N)^T$. The operator \cdot^T indicates the transpose operation. However, \mathbf{F} is scaled by \sqrt{N} and the matrix norm will be $|\mathbf{F}| = \sqrt{N}$. To obtain a basis function set with a 2-norm of 1, i.e. $|\mathbf{F}| = 1$, the diagonal has to be divided by \sqrt{N} .

In Fig. 3.15 *Top* the continuous signal $\cos(\omega t)$ and in Fig. 3.15 *Bottom* $\sin(\omega t)$ are shown as solid black lines in the interval $[0, 2\pi]$ for three different angular frequencies $\omega = 2\pi f$, with f the frequency.

The DFT is an approximation of the true (i.e., mathematical), analytically defined Fourier transform (FT) in a synthetic (digital) environment [171]. In-between the nodes no information is available since it is neglected during the sampling process. Coming from the Euler identity (Eq. 3.67) the real part of W_N^{kn} has to correspond to $\cos(2\pi kn/N)$ wave as it is shown in Fig. 3.15. The nodal values of \mathbf{F} are indicated by red crosses. \mathbf{F} was calculated with

¹¹MATLAB, from The MathWorks Inc, United States, stands for Matrix Laboratory. MATLAB is a high-level language and interactive environment that enables performing computationally intensive tasks faster than with traditional programming languages such as C, C++, and Fortran [183].

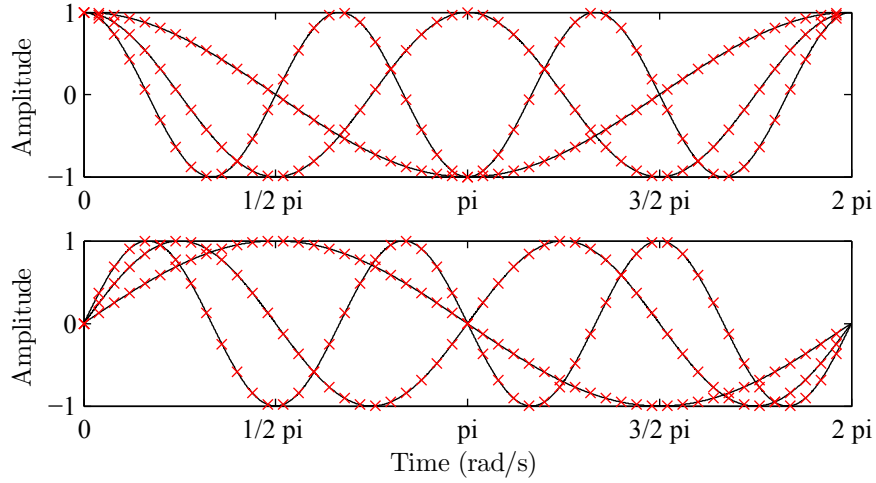


Figure 3.15: *Top:* The solid black line shows the continuous signal of $\cos(\omega t)$ in the interval $t = [0, 2\pi]$ with three different angular frequencies $\omega = 2\pi f$, with f as the frequency. The crosses represent the real part of \mathbf{F} , i.e. $\Re(\mathbf{F})$, which was generated at $N = 50$ nodes; *Bottom:* The solid line represents $\sin(\omega t)$ with the imaginary part of \mathbf{F} , i.e. $\Im(\mathbf{F})$, plotted as red crosses. For both continuous signals the discrete Fourier transform matrix \mathbf{F} leads to identical results at all 50 nodes.

$N = 50$. The imaginary part of W_N^{kn} is approximated by the imaginary nodes of \mathbf{F} , $\Im(\mathbf{F})$. In both cases the continuous signal is well approximated at the available nodes as shown in Fig. 3.15.

Having defined the Fourier basis function set it is possible to calculate the full spectrum \mathbf{s} of the signal \mathbf{y} with respect to the basis function set \mathbf{F} as,

$$\mathbf{s} = \mathbf{F}\mathbf{y}. \quad (3.70)$$

Calculating the spectrum in this manner is significantly less efficient than computing an FFT if all spectral components are required. However, as shall be seen, given the need for only a low number of signatures the method offers significant advantages, both with respect to numerical efficiency and also in estimating the covariance propagation. When calculating the spectrum of the data set \mathbf{y} some considerations about spectral leakage and Gibbs error have to be made. These are discussed in the next section.

3.6.4.1 Spectral Leakage

When calculating the spectrum \mathbf{s} as it is stated in Eq. 3.70 some attention must be paid to spectral leakage. A detailed explanation of the following section is given in Harker and O’Leary [76].

In Eq. 3.50 it was shown how a continuous signal $x(n)$ is sampled to obtain a discrete-time signal $x[n]$. During this process signal modification occurs due to the specified frequency sampling rate f_s which eliminates the information between two samples. As a result of the Nyquist criteria, solely frequencies below $f_s/2$ can be recognized. All higher frequencies are mirrored to lower frequencies. This phenomenon is called *aliasing*. To prevent aliasing an appropriate filter, i.e. a low-pass filter, is used before sampling the data [181]. The resulting spectrum from Eq. 3.70 is periodic in multiples of the frequency sampling rate f_s . This is a result of the definition of the Fourier transformation. The spectrum $X(e^{j\omega})$ can be written in terms of magnitude $|X(e^{j\omega})|$ and phase $\angle X(e^{j\omega})$, i.e.,

$$X(e^{j\omega}) = |X(e^{j\omega})|e^{j\angle X(e^{j\omega})}. \quad (3.71)$$

The phase, however, is not uniquely defined since any integer multiple of 2π may be added without modifying the phase [139].

A demonstration signal $y[n]$ is introduced to illustrate the effect of spectral leakage as well as different methods of handling the effect, i.e. classical solutions as well as a new algebraic approach using polynomials. For simplicity of notation $y[n]$ denotes the same signal as \mathbf{y} , for all discrete time signals. For signal processing, normally, just a portion of the recorded data is taken, $y_N[n] = y[k : k + N - 1]$, starting at sample k having a length of N samples. Up to now, no modification has been performed to the recorded data set. The demonstration data set $y[n]$ is synthesized by,

$$y[n] = A_1 \sin(2\pi f_1 n) + A_2 \sin(2\pi f_2 n) + A_3 \sin(2\pi f_3 n) + \epsilon(n), \quad (3.72)$$

at the samples $n = 1, 2, \dots, N$. The values for the amplitude A_i and frequency f_i are listed in Tab. 3.2. The $\epsilon(n)$ noise term is generated by a random distribution of values in the interval $[0:1]$ multiplied with a factor $\sigma = 0.02$. The signal was synthesized with a frequency sampling rate $f_s = 2048$ Hz and a duration of $N = 2048$ samples which corresponds to 1 s recording time. The resulting signal $y[n]$ is plotted as a bold black line in Fig. 3.16.

Table 3.2: Values for the amplitude A_i and frequency f_i for the demonstration signal $y[n]$ defined via Eq. 3.72

| i | A_i (V) | f_i (Hz) |
|-----|-----------|-------------------------|
| 1 | 1.1 | 0 (direct current (DC)) |
| 2 | 1.1 | 12 |
| 3 | 1.1 | 14.5 |

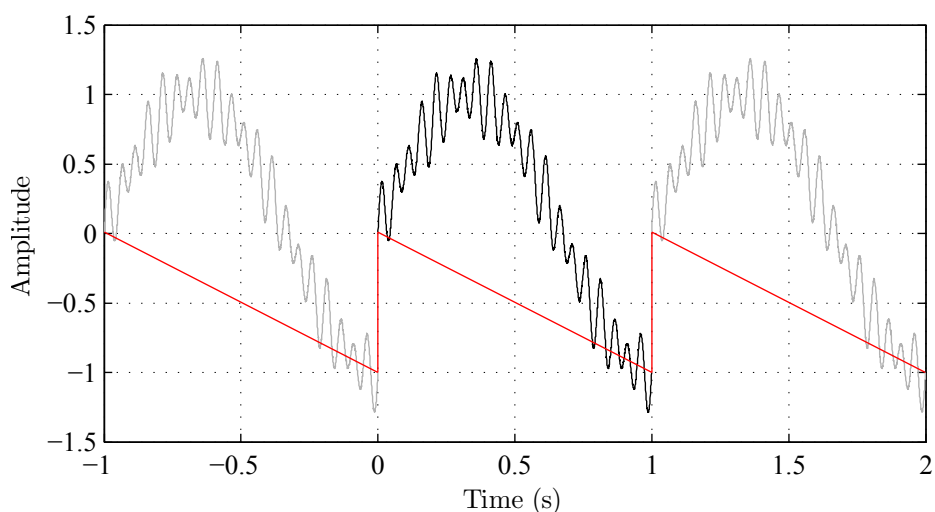


Figure 3.16: Time domain signal $y[n]$ with duration of 1 s (solid black line). Due to a subharmonic low frequency portion the signal has a discontinuity when being replaced at multiples of its length indicated by a pale line. The discontinuity can be approximated by a sawtooth (red line) which will influence the spectrum by superposition.

The signal consists of a low frequency subharmonic portion as well as two higher harmonic frequencies. The goal is to identify the two harmonic frequency portions. The subharmonic portion can be seen as a drift of a sensor which perturbed the signal and affects the spectrum in an undesired manner. As already shown in Eq. 3.71 the phase can be multiplied by any integer multiple of 2π . As a result of the duality property of the DFT the time domain signal can be seen as multiples of its measurement period T . This is shown in Fig. 3.16 by the gray line signal which is just the original signal $y[n]$ by integer multiples of T . However, if aperiodic portions are present in the signal a discontinuity appears at the beginning and at the end of the signal indicated by the sawtooth (red line). Since the aperiodic portion of the signal

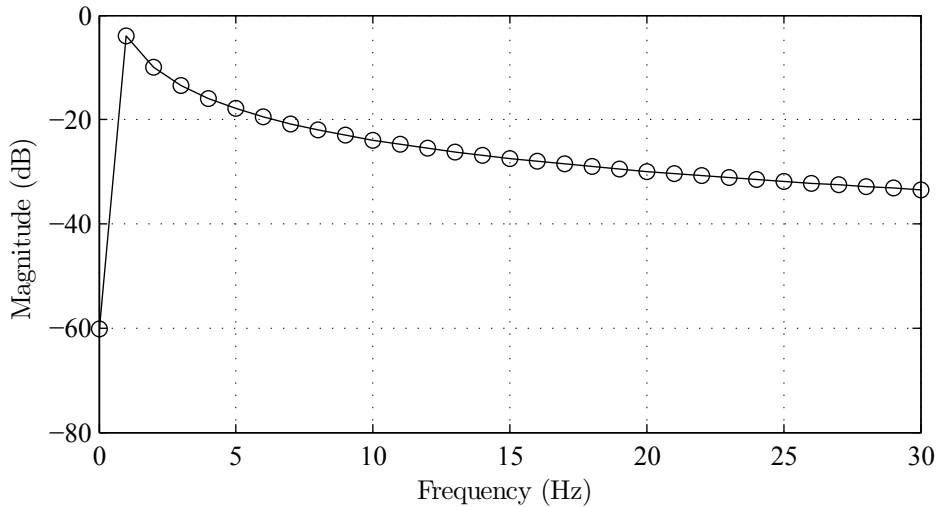


Figure 3.17: Magnitude spectrum of a single sawtooth signal. The sawtooth comprises components over the complete frequency spectrum with decreasing magnitude.

is not an integer multiple of the fundamental frequency $f_m = 1/T$ and has significant energy it will be present in the spectrum \mathbf{s} . This is called *spectral leakage*. The resulting spectrum of the signal $y[n]$ is a superposition of the spectrum of the sawtooth as well as the spectrum from the actual signal. The magnitude spectrum of a simple sawtooth is shown in Fig. 3.17. It can be seen that a sawtooth shaped signal yields components over all frequencies with decreasing magnitude. Consequently, this behavior will affect also the periodic frequency components.

To overcome spectral leakage windows respectively windowing was introduced, e.g. [139]. Common windows are typically symmetric, resulting in a generalized linear phase, with approximately zero value and zero derivative at both ends of the window and with the same length of the signal itself. By pre-multiplying the observed signal with the window it is hoped to force the signal into a position that no discontinuity appears at the beginning and at the end of the signal. Thereby, the spectrum of the sawtooth should be minimized or at best completely vanished. The multiplication of the window ω is performed element wise¹², i.e.,

$$\mathbf{y}_\omega = \mathbf{y} \circ \omega. \quad (3.73)$$

Classical windows are the Hanning-, Blackman- or Kaiser-window. Here

¹²The symbol \circ is called Hadamard product which represents the element for element multiplication of two vectors or matrices.

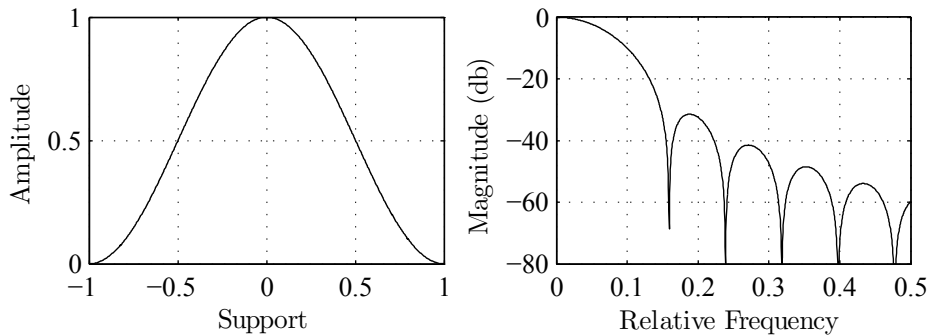


Figure 3.18: *Left:* Time domain shape of the Hanning window with approximately zero value and zero derivative at both ends of the window; *Right:* Frequency response of the Hanning window.

the Hanning window is used to demonstrate its effect on the demonstration signal. The Hanning window is described via the equation,

$$\omega = 0.5 + 0.5 \cos(\phi), \quad (3.74)$$

whereby ϕ is sampled at N evenly spaced points in the range $0 \leq \phi_i \leq 2\pi(N-1)/N$. In Fig. 3.18 the time domain shape over a normalized support length as well as the frequency response of the Hanning window is shown. By applying the Hanning window on the demonstration signal the signal \mathbf{y}_ω is obtained which has now the form as shown in Fig. 3.19. The discontinuity disappeared at both signal ends which enables smooth transition between the recurringly placed signal.

The magnitude spectrum of the demonstration signal $y[n]$ is computed using Eq. 3.70 and is shown in Fig. 3.20 *Top*. It can clearly be observed that the spectrum is a superposition of the spectrum from the sawtooth (compare Fig. 3.17) and the spectrum of the sinusoidal frequency components. The two peaks at 15 and 20 Hz indicate the components f_2 and f_3 , which are the components to be identified.

In Fig. 3.20 *Bottom* the magnitude spectrum of the signal modified by a Hanning window is shown. Both peaks are more clearly visible and have a better signal to noise ratio. However, both frequencies are spread over both neighboring frequencies. This is a result of the applied Hanning window. The sawtooth spectrum is still present especially at low frequencies.

A significant disadvantage of the window method is that the original signal cannot be reconstructed. This is a result of the zero values of the window at both ends. Reconstructing the signal to the time domain, however, would be of special interest for frequency domain filters.

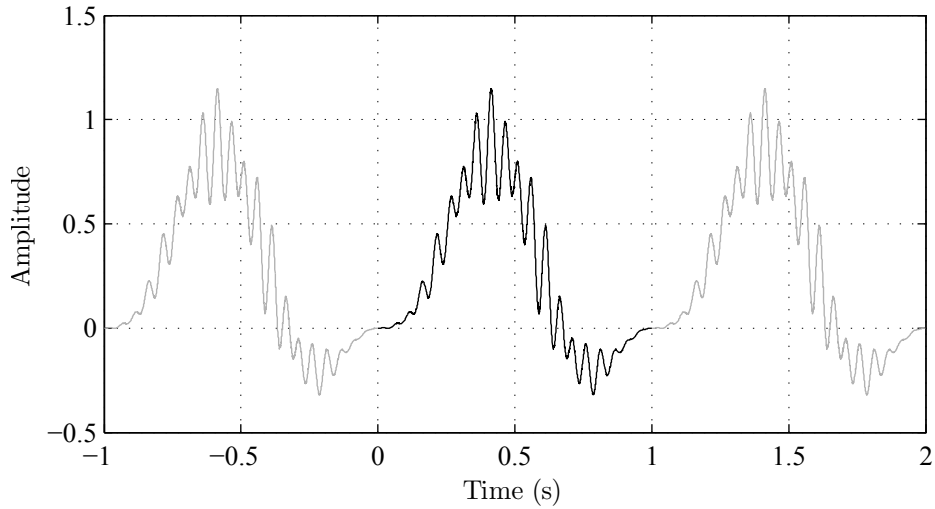


Figure 3.19: Demonstration signal modified by a Hanning window. The obtained signal \mathbf{y}_ω can be recurrently placed next to each other without discontinuity. The aim of the signal modification is to reduce spectral leakage.

For completeness the back-transformation of the spectrum \mathbf{s} into the time domain is shown. The signal can be mapped in any of the domains without a loss of information, i.e.,

$$\hat{\mathbf{y}} = \mathbf{F}^T \mathbf{s} = \mathbf{F}^T \mathbf{F} \mathbf{y} = \mathbf{y} \quad \text{with} \quad \mathbf{s} = \mathbf{F} \mathbf{y} \quad \text{and} \quad \mathbf{F}^T \mathbf{F} = \mathbf{I}. \quad (3.75)$$

However, $\mathbf{F}^T \mathbf{F} = \mathbf{I}$ only holds if \mathbf{F} is a complete orthonormal basis function set.

Windowing is the classical approach to deal with spectral leakage. Recently, a new approach to reduce spectral leakage was published using polynomial basis functions [136]. The method has significant advantages since it is a linear operator in matrix form which simplifies the calculation and enables the estimation of the covariance propagation. A short summary of the most important steps of the mathematical derivation is described in the following section which is taken from the more detailed publications by O’Leary and Harker [76, 136, 137].

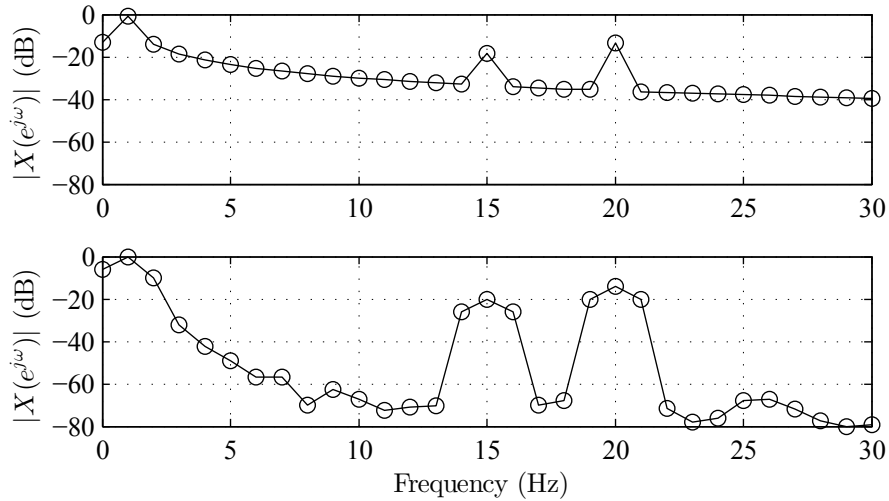


Figure 3.20: *Top:* Magnitude spectrum of the unmodified signal \mathbf{y} . Both frequencies can be identified although the spectrum is superimposed by the one of the sawtooth; *Bottom:* Magnitude spectrum of the signal modified by a Hanning window. Both frequencies can be identified more clearly in terms of signal to noise ratio. However their frequencies are spread onto both neighboring frequencies. The spectrum of the sawtooth is more attenuated but still present.

3.6.4.2 Polynomial Approach for Spectral Leakage

The columns of the Vandermonde matrix \mathbf{V} are concatenated from polynomials up to order n and the matrix is defined as,

$$\mathbf{V} \triangleq [\mathbf{x}^0, \mathbf{x}^1, \dots, \mathbf{x}^{n-1}] = \begin{bmatrix} x_1^0 & x_1^1 & \dots & x_1^{n-1} \\ x_2^0 & x_2^1 & \dots & x_2^{n-1} \\ \vdots & \vdots & \ddots & \vdots \\ x_m^0 & x_m^1 & \dots & x_m^{n-1} \end{bmatrix}, \quad (3.76)$$

on the support 1 to m . In theory \mathbf{V} is complete for $m = n$ with full rank, i.e. $\text{rank}(\mathbf{V}) = n$, spanning the full space \mathfrak{R}^n . However, this does not hold when computed at discrete points and for higher degrees since the matrix becomes poorly conditioned and is degenerate.

As early as 1883 Gram [69] introduced an orthogonal basis set, named the Gram basis. However, the synthesis via the recurrence relationship introduces serious errors which limit the degree of usable polynomial [135]. Later, Schmidt [167] introduced a process on basis of Gram's publication to orthog-

onalize an arbitrary basis set which is not inherently orthogonal, named the Gram-Schmidt orthogonalization. Unfortunately, the process turns out to be numerically unstable [65]. Recently, a stable process for the synthetization of an orthonormal polynomial Gram basis set with comparable computational accuracy with Fourier basis was introduced by O'Leary and Harker [134]. The process is based on a Lanczos method with complete reorthogonalization. Consider a matrix \mathbf{G} which is concatenated from columns \mathbf{g}_i , i.e.,

$$\mathbf{G} = [\mathbf{g}_0, \mathbf{g}_1, \dots, \mathbf{g}_{n-1}], \quad (3.77)$$

whereby the i^{th} column corresponds to the i^{th} basis function \mathbf{g}_i . The basis set is defined to be complete and of full rank. In addition, the basis is designed to be orthogonal satisfying the inner product,

$$\langle \mathbf{g}_i, \mathbf{g}_j \rangle = \delta_{ij}, \quad (3.78)$$

with δ_{ij} the Kronecker delta. Furthermore, the basis is defined to have a 2-norm of 1, resulting in an orthonormal basis set. In terms of matrix notation this can be summarized as,

$$\mathbf{G}^T \mathbf{G} = \mathbf{G} \mathbf{G}^T = \mathbf{I}, \quad (3.79)$$

with \cdot^T the transpose operator and \mathbf{I} the identity matrix.

From the requirements defined a synthetization algorithm for \mathbf{G} can be derived. The first two bases \mathbf{g}_0 and \mathbf{g}_1 are generated as,

$$\mathbf{g}_0 = \frac{1}{\sqrt{n}}, \quad \mathbf{g}_1 = \frac{x - \bar{1}\bar{x}}{|x - \bar{1}\bar{x}|}, \quad (3.80)$$

with \bar{x} the mean value of the nodes. All higher basis are derived via the recurrence relation,

$$\mathbf{g}_i = \alpha \{ \mathbf{I} - \mathbf{G}_{i-1} \mathbf{G}_{i-1}^T \} (\mathbf{g}_{i-1} \circ \mathbf{g}_1) \quad \text{for } 1 < i < n - 1, \quad (3.81)$$

with α a factor to ensure 2-norm of 1 of the generated basis \mathbf{g}_i ,

$$\alpha = \frac{1}{| \{ \mathbf{I} - \mathbf{G}_{i-1} \mathbf{G}_{i-1}^T \} (\mathbf{g}_{i-1} \circ \mathbf{g}_1) |}. \quad (3.82)$$

Now having an orthonormal polynomial basis set an arbitrary signal \mathbf{y} can be represented or approximated by a function $\hat{\mathbf{y}}$ which is a series of basis functions¹²,

$$\hat{\mathbf{y}} = \mathbf{G} \mathbf{a}, \quad (3.83)$$

with \mathbf{a} the spectrum of $\hat{\mathbf{y}}$ with respect to the basis function \mathbf{G} .

If the basis function \mathbf{G} is truncated the function $\hat{\mathbf{y}}$ is an approximation of the signal \mathbf{y} . The aim is to find the values of \mathbf{a} to minimize the error between the approximation and the signal in a least square sense¹².

The error vector \mathbf{e} is given by¹²,

$$\mathbf{e} = \mathbf{y} - \hat{\mathbf{y}} = \mathbf{y} - \mathbf{G}\mathbf{a}. \quad (3.84)$$

The functional to be minimized E is the square of the 2-norm of \mathbf{e} , i.e.¹²,

$$E = \mathbf{e}^T \mathbf{e} = \{\mathbf{y} - \mathbf{G}\mathbf{a}\}^T \{\mathbf{y} - \mathbf{G}\mathbf{a}\}. \quad (3.85)$$

The extrema is calculated when evaluating the derivative of E with respect to \mathbf{a} and setting it to zero, i.e.,

$$\frac{dE}{d\mathbf{a}} = -2\mathbf{G}^T \mathbf{y} + 2\mathbf{G}^T \mathbf{G}\mathbf{a} = 0, \quad (3.86)$$

and solving for \mathbf{a} ,

$$\mathbf{a} = (\mathbf{G}^T \mathbf{G})^{-1} \mathbf{G}^T \mathbf{y} = \mathbf{G}^+ \mathbf{y}. \quad (3.87)$$

The matrix \mathbf{G}^+ is the Moore-Penrose pseudo inverse [65]. Using Eq. 3.79 simplifies Eq. 3.87 to,

$$\mathbf{a} = \mathbf{G}^T \mathbf{y}. \quad (3.88)$$

The signal approximation can now be written as,

$$\hat{\mathbf{y}} = \mathbf{G}\mathbf{a} = \mathbf{G}\mathbf{G}^T \mathbf{y}, \quad (3.89)$$

with $\mathbf{P} \triangleq \mathbf{G}\mathbf{G}^T$ the projection onto the basis function. As long as a complete basis function set is used, $\mathbf{G}\mathbf{G}^T = \mathbf{I}$ and the approximation $\hat{\mathbf{y}}$ is identical to the signal \mathbf{y} itself.

Multiplying the projection $\mathbf{P}_d \triangleq \mathbf{G}_d \mathbf{G}_d^T$ of a truncated basis function set up to degree d onto the signal \mathbf{y} generates a signal \mathbf{y}_g which is associated with the low frequency components in a least square approximation,

$$\mathbf{y}_g = \mathbf{P}_d \mathbf{y}. \quad (3.90)$$

¹²Harker M., O'Leary P. Polynomials for the Reduction of Spectral Leakage and Gibbs Error in FFT Based Signal Processing, not published. Personal communication 2013.

Subtracting \mathbf{y}_g from the original signal \mathbf{y} results in the reduced signal \mathbf{y}_r in which the correlations associated with the low frequency components are removed, i.e.,

$$\mathbf{y}_r = \mathbf{y} - \mathbf{y}_g = \{\mathbf{I} - \mathbf{G}_d \mathbf{G}_d^T\} \mathbf{y} = \mathbf{P}_d^\perp \mathbf{y}, \quad (3.91)$$

with $\mathbf{P}^\perp \triangleq \{\mathbf{I} - \mathbf{G}_d \mathbf{G}_d^T\}$, called the orthogonal complement of a truncated basis function, with d the maximum degree used.

This method has additional significant advantages since it does not add computational complexity during calculation of the spectrum as shall be seen. When generating a complete Fourier basis set \mathbf{F} the transformation of the reduced signal \mathbf{y}_r in the frequency domain can be computed as,

$$\mathbf{s}_r = \mathbf{F} \mathbf{y}_r = \mathbf{F} \{\mathbf{I} - \mathbf{G}_d \mathbf{G}_d^T\} \mathbf{y} = \mathbf{H} \mathbf{y}, \quad (3.92)$$

with $\mathbf{H} \triangleq \mathbf{F} \{\mathbf{I} - \mathbf{G}_d \mathbf{G}_d^T\}$. This computation is a residualization process by the approximation onto the low degree polynomial basis. This two stage computation, the residualization followed by a DFT, is numerically more efficient. The computation of the transformation matrix \mathbf{H} can be performed prior and has consequently no additional computational complexity during runtime.

Applying the described method for polynomial windowing on the test signal introduced in Eq. 3.72 offers two possibilities:

1. using a global least square approximation or
2. using a local Gram polynomial approximation.

Using method 1. results in the spectrum shown in Fig. 3.21 *Top*. The signal is modified especially at lower frequency components in comparison to the calculation of the spectrum without a window. The frequencies to be identified, f_2 and f_3 , have a comparable signal to noise ratio as they had for the spectrum of the unmodified signal (compare Fig. 3.20).

The local approximation can be performed using a global operator \mathbf{S} which performs local polynomial approximation on a support length l_s (see O'Leary and Harker [135] for details on the global operator). Eq. 3.92 is modified to calculate the spectrum of \mathbf{y} to,

$$\mathbf{s}_r = \mathbf{F} \{\mathbf{I} - \mathbf{S} \mathbf{S}^T\} \mathbf{y}. \quad (3.93)$$

When the magnitude spectrum of $y[n]$ is calculated using method 2. the result shown in Fig. 3.21 *Bottom* is received. The spectrum is clearly different to all the calculated ones before. All the unwanted frequency components,

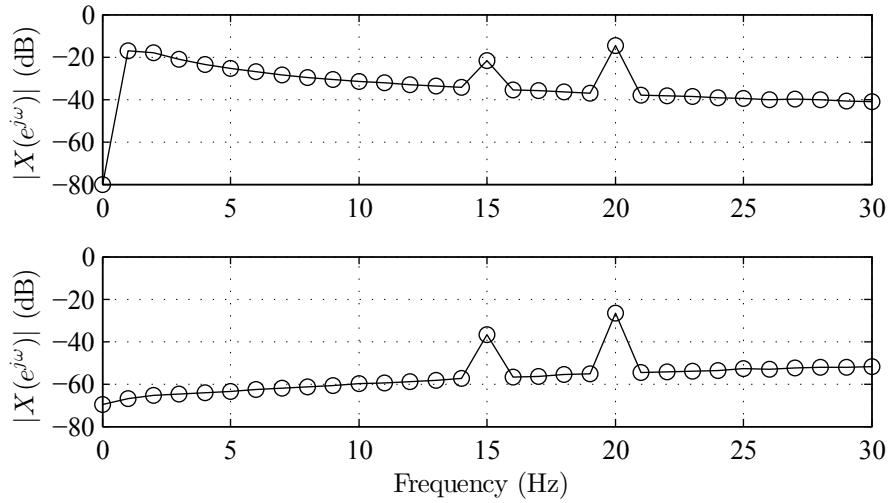


Figure 3.21: *Top:* Magnitude spectrum of signal modified by orthogonal complement of a low degree Gram basis. Both peaks can be identified at their synthesis frequency with similar signal to noise ratio to the unmodified signal. The spectrum at low frequencies is more attenuated than the unmodified signal; *Bottom:* Magnitude spectrum of signal modified by local polynomial approximation of low degree. Both peaks can be clearly identified at a better signal to noise ratio than the unmodified signal. In addition the spectrum of the sawtooth is completely removed from the spectrum.

besides the two frequencies f_2 and f_3 , which are desired to be identified, are attenuated. As a result, the signal to noise ratio to identify f_2 and f_3 is enhanced in comparison to all the other spectra shown while having no frequency spreading.

3.6.4.3 Signature Identification

The signature identification can be seen as the calibration of the frequency recognition method. During signature identification each resonator i is activated artificially and its oscillation behavior is recorded. It has advantages to perform the signature measurements in a silent environment to have a better quality of the recorded signatures¹³. The time domain signal from the accelerometer is recorded and the corresponding spectrum is calculated,

¹³It is also possible to perform measurements during runtime and define the recorded signal as the signature. Thereby the noise of the machine is stored in the signature, too.

$$\mathbf{s}_i = \mathbf{H}\mathbf{y}_P, \quad (3.94)$$

with $\mathbf{H} \triangleq \mathbf{F}\{\mathbf{I} - \mathbf{G}_d\mathbf{G}_d^T\}$. The procedure is repeated for each implemented resonator yielding a set of spectra for n resonators. However, these spectra are not fully independent to each other. This is a result of the complex mechanical shape of the resonator as well as the mold which leads to internal reflections. Orthogonal signatures $\hat{\mathbf{s}}_i$ are achieved by projecting the signatures on their orthogonal compliment. For n resonators the orthogonalization process can be written as,

$$\hat{\mathbf{s}}_i = \left\{ \mathbf{I} - \left(\sum_k \mathbf{s}_k \mathbf{s}_k^T \right) \right\} \mathbf{s}_i \quad \forall k \in [1, \dots, n], k \neq i. \quad (3.95)$$

For the most measurements two resonators were implemented in the mold. To support understanding of the orthogonalization process Eq. 3.95 is explicitly written for two resonators,

$$\begin{aligned} \hat{\mathbf{s}}_1 &= \mathbf{s}_1 - \mathbf{s}_2 \mathbf{s}_2^T \mathbf{s}_1 = \{\mathbf{I} - \mathbf{s}_2 \mathbf{s}_2^T\} \mathbf{s}_1, \\ \hat{\mathbf{s}}_2 &= \mathbf{s}_2 - \mathbf{s}_1 \mathbf{s}_1^T \mathbf{s}_2 = \{\mathbf{I} - \mathbf{s}_1 \mathbf{s}_1^T\} \mathbf{s}_2. \end{aligned} \quad (3.96)$$

The n orthogonal signatures $\hat{\mathbf{s}}_i$ can be used for the signature matching process. Therefore a matrix¹⁴ \mathbf{S} is built storing the n signatures. The complex signatures are concatenated to build the columns of the matrix \mathbf{S} and are divided by their 2-norm,

$$\mathbf{S} = \left[\frac{\hat{\mathbf{s}}_1}{|\hat{\mathbf{s}}_1|}, \dots, \frac{\hat{\mathbf{s}}_n}{|\hat{\mathbf{s}}_n|} \right]. \quad (3.97)$$

In this manner the matrix \mathbf{S} has a unitary norm and consequently \mathbf{S}^+ , the Moore - Penrose pseudoinvers, will have an unitary norm, too.

3.6.4.4 Signature Matching

The impact of the movable pin on the acoustic resonator can be mathematically approximated by a dirac pulse. Consequently the signatures correspond to the frequency response of the resonator. Given measurements of the resonator response, i.e. $\hat{\mathbf{s}}_i$, with additional noise, the task is to solve the inverse problem to receive the maximum Likelihood predictor for the coefficient \mathbf{c} . The inverse problem is formulated as,

¹⁴The signature matrix \mathbf{S} must not be mixed up with the local polynomial approximation operator from Eq. 3.93.

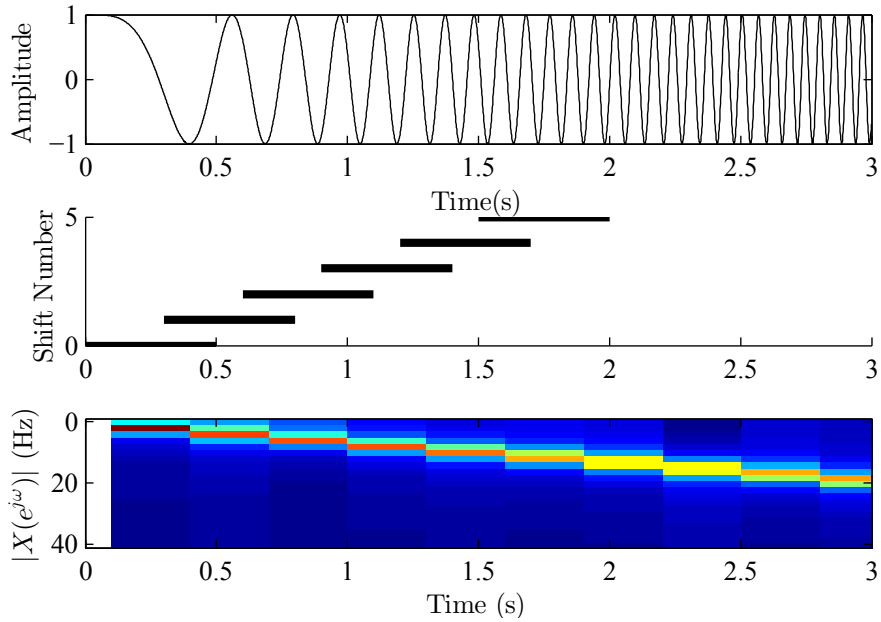


Figure 3.22: *Top:* Chirp signal in time domain with a duration of 3 s and a sampling frequency $f_s = 1000$ Hz; *Middle:* Representation of the STFT in terms of bars indicating the portion of the signal used for transformation in the frequency domain; *Bottom:* Frequency representation of the chirp signal, showing the varying frequency over time which could not be shown by using a DFT. The spectrum is presented centered for each window.

$$\min_c \| \mathbf{s}_t - \mathbf{S}c \| . \quad (3.98)$$

Hereby \mathbf{s}_t denotes the temporal varying spectrum of the signal \mathbf{y} . This is necessary since the DFT is mainly for stationary signals. A DFT cannot calculate the temporal moment a frequency appears in the time domain signal. For the acoustic-emission sensor it is a requirement to find the temporal moment in the data stream \mathbf{y} at which the oscillation of one of the resonators appeared. However, it is possible to define a STFT where just a portion of the signal is transformed into the frequency domain preserving a temporal component. For each calculation step a new portion of the signal is chosen. This can be realized using a rectangular window with length l which is shifted by a number of p samples through the data stream \mathbf{y} . In Listing 3.1 the MATLAB code for calculating the STFT is shown. To support under-

Listing 3.1: Fragment code for calculating a STFT using MATLAB.

```
1 p    % Number of samples the window is shifted
2 l    % Number of samples for window width
3 sig  % recorded signal
4
5 sigL = length(sig);
6 F = dftmtx(sigL) ;
7
8 i = 0;
9 while(i*p+l < sigL)
10     spec(:,i+1) = abs(F * sig((i*p+1:i*p+l+1) ));
11     i = i + 1;
12 end
```

standing a test signal is set up and the STFT is calculated. The signal is described via,

$$\mathbf{y} = \cos(\alpha \mathbf{x}^2), \quad (3.99)$$

with $\alpha = 20$. The signal is also called chirp signal. It has the characteristic to continuously change frequency over time as it can be seen in time domain representation in Fig. 3.22 *Top*. The signal was synthesized with a sampling frequency $f_s = 1000$ Hz. For calculation of the STFT, in reference to Listing 3.1, $l = 500$ and $p = 300$. In Fig. 3.22 *Middle* the STFT is shown in terms of bars indicating the cutout portions \mathbf{y}_t , the temporal varying signal. For each step of the STFT the window is shifted by p adding new data points as well as dropping the same amount of points out of \mathbf{y}_t . For \mathbf{y}_t the magnitude spectrum is calculated which is shown in Fig. 3.22 *Bottom*. Using the local transformation enables the observation of the moving frequency whereas using a global operator this frequency sweep would not have been visible. Thereby the spectrum has a resolution of $l/2$ data points spread over a frequency range of $f_s/2$. The calculation of the spectrum is performed each p/f_s seconds. Note, that it takes at least l/f_s seconds to perform the computation of the first spectrum. In Fig. 3.22 the spectrum is centered on the window length yielding an empty spectrum for the first $l/(2f_s)$ seconds. The target is to minimize the function defined in Eq. 3.98. The error vector \mathbf{e} is defined as,

$$\mathbf{e} = \mathbf{s}_t - \mathbf{S}\mathbf{c}. \quad (3.100)$$

The functional to be minimized E is the square of the 2-norm of the error vector \mathbf{e} ,

$$E = \mathbf{e}^T \mathbf{e}. \quad (3.101)$$

For a least square approximation the extrema of E with respect to the coefficient \mathbf{c} is calculated which results in reference to Eq. 3.87 in,

$$\mathbf{c} = (\mathbf{S}^T \mathbf{S})^{-1} \mathbf{S}^T \mathbf{s}_t = \mathbf{S}^+ \mathbf{s}_t, \quad (3.102)$$

with \mathbf{S}^+ the Moore-Penrose pseudoinverse [65]. In Eq. 3.102 the spectrum \mathbf{s}_t can be replaced by $\mathbf{H}\mathbf{y}$, which leads to,

$$\mathbf{c} = \mathbf{S}^+ \mathbf{H}\mathbf{y}_t = \mathbf{L}\mathbf{y}_t, \quad (3.103)$$

defining \mathbf{L} as,

$$\mathbf{L} \triangleq \mathbf{S}^+ \mathbf{H} = \mathbf{S}^+ \mathbf{F} \{ \mathbf{I} - \mathbf{G}_d \mathbf{G}_d^T \}. \quad (3.104)$$

When calculating the coefficient vector \mathbf{c} , actually a matrix is calculated storing the coefficient vector for each resonator i in the columns, i.e.,

$$\mathbf{c} = [\mathbf{c}_1, \dots, \mathbf{c}_n], \quad (3.105)$$

for all n resonators.

The correlation coefficient will indicate how much of a signature is detected in the current portion of the signal \mathbf{y}_t .

3.6.4.5 Computational Complexity

It was stated that calculating the spectrum using a DFT is numerically inefficient. The transformation matrix \mathbf{F} is of square form $l \times l$, when being complete. Consequently, calculating the spectrum is the multiplication of a square matrix times a vector. In Bürgisser et al. [21] the numerical work for multiplying two rectangular matrices ($\mathbf{A} \in \mathbb{R}^{n \times l}$ by $\mathbf{B} \in \mathbb{R}^{l \times m}$) is stated to be of order¹⁵ $\mathcal{O}(mnl)$.

Typical values used for the acoustic-emission sensor are $l = 600$. Consequently, the temporal snippet of the signal \mathbf{y} , \mathbf{y}_t is of length 600. As a result, 360000 computations are necessary to calculate the full spectrum of \mathbf{y}_t .

Using the frequency pattern recognition method the operator \mathbf{L} is multiplied with the signal \mathbf{y}_t . \mathbf{L} is of the rectangular form $n \times l$ with n the number of resonators ($n \ll l$). In this thesis a maximum of $n = 2$ resonator was used

¹⁵It has to be noted that there are more efficient methods two multiply two matrices, e.g. Strassen algorithm [179].

and hence only 1200 calculations were necessary to receive one value of the coefficient vector \mathbf{c} . Consequently the computational effort is significantly reduced in comparison to calculating the full spectrum at first.

3.6.4.6 Covariance Propagation and Confidence Interval

In general the recorded signal \mathbf{y} will be perturbed by noise. An important question is how this noise on the input signal will influence respectively propagate into the solution \mathbf{c} . In Brandt [16] the covariance Λ for a vector is defined as,

$$\Lambda_c \triangleq \{\mathbf{c} - E(\mathbf{c})\}\{\mathbf{c} - E(\mathbf{c})\}^T. \quad (3.106)$$

Substituting the relationship $\mathbf{c} = \mathbf{L}\mathbf{y}$, yields,

$$\Lambda_c = \{\mathbf{L}\mathbf{y} - \mathbf{L}E(\mathbf{y})\}\{\mathbf{L}\mathbf{y} - \mathbf{L}E(\mathbf{y})\}^T. \quad (3.107)$$

The operator \mathbf{L} can be factored out to the left and right,

$$\Lambda_c = \mathbf{L}\{\mathbf{y} - E(\mathbf{y})\}\{\mathbf{y} - E(\mathbf{y})\}^T\mathbf{L}^T. \quad (3.108)$$

By definition $\Lambda_y = \{\mathbf{y} - E(\mathbf{y})\}\{\mathbf{y} - E(\mathbf{y})\}^T$, consequently,

$$\Lambda_c = \mathbf{L}\Lambda_y\mathbf{L}^T. \quad (3.109)$$

For independent and identically distributed (i.i.d.) Gaussian noise,

$$\Lambda_y = \sigma^2\mathbf{I}, \quad (3.110)$$

and substituting into Eq. 3.109,

$$\Lambda_c = \sigma^2\mathbf{L}\mathbf{L}^T. \quad (3.111)$$

Having the covariance matrix Λ_c a 3σ confidence interval can be calculated. The 3σ interval comprises the solution within a probability¹⁶ 99.73%. In this section the covariance matrix will solely be discussed for the case of having $n = 2$ resonators. However, the calculation of the covariance matrix as well as the confidence interval is also possible for higher numbers of n .

The covariance matrix has a squared symmetrical form, i.e.,

$$\Lambda_c = \begin{bmatrix} \mathcal{C}_{11} & \mathcal{C}_{12} \\ \mathcal{C}_{21} & \mathcal{C}_{22} \end{bmatrix} = \begin{bmatrix} \sigma_{xx}^2 & \sigma_{xy}^2 \\ \sigma_{yx}^2 & \sigma_{yy}^2 \end{bmatrix}, \quad (3.112)$$

¹⁶Since the sample size is large the Student-t distribution can be approximated with the standard normal distribution [16].

with $\sigma_{ij}^2 = \sigma_{ji}^2$, for $i \neq j$. The covariance matrix describes the form of a general ellipse [75]. From this ellipse the two tangents on the most outer points of the ellipse are searched. The form of the ellipse is scaled by χ^2 , the confidence envelope or the squared Mahalanobis distance.

The equation of an ellipse with a confidence scaling factor χ^2 is described via¹⁷,

$$E(x, y, \chi) = [x \ y \ \chi] \begin{bmatrix} \Lambda^{-1} & 0 \\ 0 & -\chi^2 \end{bmatrix} \begin{bmatrix} x \\ y \\ 1 \end{bmatrix} = 0 \quad (3.113)$$

Considering a covariance matrix of the form,

$$\Lambda_c = \begin{bmatrix} 1 & 0.5 \\ 0.5 & 1 \end{bmatrix}, \quad (3.114)$$

and a $\chi^2 = 3\sigma$ which will have the elliptical form shown in Fig. 3.23. The covariance value \mathcal{C}_{12} and \mathcal{C}_{21} rotates the ellipse out of its normal position. Having $\mathcal{C}_{12} = \mathcal{C}_{21} = 0$ would lead to an ellipse in normal position. \mathcal{C}_{11} and \mathcal{C}_{22} define the main axes lengths of the ellipse. In addition, the χ^2 value scales the ellipse. The target is to find both axis parallel tangents to the ellipse which describe the width of the confidence interval. Therefore the point on the ellipse with zero derivative in each axis direction has to be computed. The solution can be found in [152].

For the x-direction the confidence interval with respect to χ^2 can be calculated as,

$$r_1 = 2 \frac{\sqrt{(4\sigma_{xx}\sigma_{yy} - \sigma_{yx}^2 - 2\sigma_{xy}\sigma_{yx} - \sigma_{xy}^2)\sigma_{xx}(\sigma_{xx}\sigma_{yy} - \sigma_{xy}\sigma_{yx})}\chi}{-\sigma_{yx}^2 + (-2\sigma_{yx} - \sigma_{xy})\sigma_{xy} + 4\sigma_{xx}\sigma_{yy}}, \quad (3.115)$$

and in y-direction,

$$r_2 = 2 \frac{\sqrt{(4\sigma_{xx}\sigma_{yy} - \sigma_{yx}^2 - 2\sigma_{xy}\sigma_{yx} - \sigma_{xy}^2)\sigma_{yy}(\sigma_{xx}\sigma_{yy} - \sigma_{xy}\sigma_{yx})}\chi}{-\sigma_{yx}^2 + (-2\sigma_{yx} - \sigma_{xy})\sigma_{xy} + 4\sigma_{xx}\sigma_{yy}}. \quad (3.116)$$

Finally, Eq. 3.115 and Eq. 3.116 can be simplified with $\sigma_{xy} = \sigma_{yx}$ (covariance matrix is symmetric) yielding,

¹⁷Personal communication, Paul O'Leary, *Algebraic-Geometric Methods for the Derivation of Direct Polynomials in the Mahalanobis and Euclidean Distances*, 2012; not published yet.

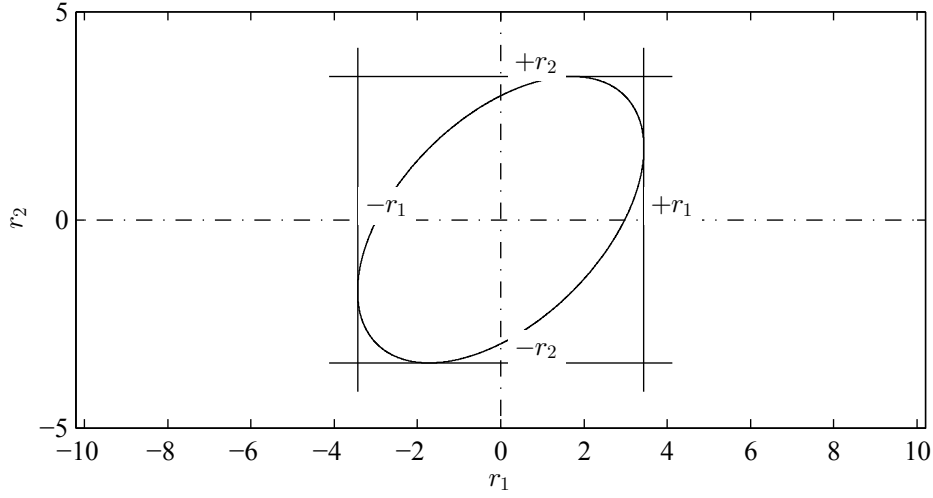


Figure 3.23: Resulting ellipse described by covariance matrix Λ_c with a scaling value $\chi^2 = 3\sigma$. The axis parallel tangents to the ellipse are searched and can be calculated via Eq. 3.115 and Eq. 3.116.

$$r_1 = 2 \frac{\sqrt{(4\sigma_{xx}\sigma_{yy} - 4\sigma_{yx}^2)\sigma_{xx}(\sigma_{xx}\sigma_{yy} - \sigma_{yx}^2)}\chi}{4\sigma_{xx}\sigma_{yy} - 4\sigma_{yx}^2}, \quad (3.117)$$

and,

$$r_2 = 2 \frac{\sqrt{(4\sigma_{xx}\sigma_{yy} - 4\sigma_{yx}^2)\sigma_{yy}(\sigma_{xx}\sigma_{yy} - \sigma_{yx}^2)}\chi}{4\sigma_{xx}\sigma_{yy} - 4\sigma_{yx}^2}. \quad (3.118)$$

For the covariance matrix defined in Eq. 3.114, the two confidence interval values are calculated as $r_1 = 3.44$ and $r_2 = 3.44$ which can be seen in Fig. 3.23, too.

3.6.4.7 Decision Process

After calculation of the matching coefficient \mathbf{c} the resulting information has to be evaluated towards its content. The coefficient comprises how much of the signatures \mathbf{s}_i was found in the signal. Since the signal was processed using a STFT a new value for the coefficient \mathbf{c} is found every $t_d = l/(2f_s)$. Typical values for the acoustic-emission sensor are¹⁸ $f_s = 120$ kHz and a window length of $l = 600$. Consequently, a decision delay of $t_d = 2.5$ ms

¹⁸If calculation power does not play an important role this value can be increased reducing the delay time until a coefficient value is available.

occurs. A new value of \mathbf{c} is calculated every $t_r = p/f_s$. A typical value for $p = 50$ and hence a new value is found every $t_r = 0.42$ ms.

With having the coefficient vector \mathbf{c} and an uncertainty estimator in terms of the covariance matrix Λ_c a decision can be found by different methods. For this thesis a decision limit was calculated using descriptive statistic methods.

Chapter 4

Experiments and Results

In this chapter the performed measurements and obtained results with the acoustic-emission sensor are presented. At first, the performance of the used cavity temperature sensor was evaluated towards the melt front detection response time stated by the manufacturer. The cavity temperature sensors were used to verify the moment of melt front recognition obtained by the acoustic-emission sensor.

The measurement concept of the acoustic-emission sensor was tested on an injection molding machine. Thereby the concept was verified if a distinctive sound is generated when the melt front passes the acoustic actuator.

For multiple implementation of acoustic actuators different resonant structures are needed for signal separation. The used structures were analyzed towards their impulse response. In addition, performance considerations of the acoustic-emission sensor are made, investigating the impact of several influencing factors. Special focus was laid on the movable pin and its time-dependent movement in dependence of the acting pressure, spring rate and pin mass. The time needed to move the pin from its initial position to the impact position is crucial in terms of sensor performance.

For the automatic recognition of the passing melt front, the impact sound of the movable pin has to be identified in the recorded data signal. Three different methods were tested towards their results whereby all methods have a different focus in terms of information content and calculation effort.

4.1 Cavity Wall Temperature Response Characteristic

The performance of the acoustic-emission sensor is compared to well known cavity wall temperature sensors. Cavity wall temperature sensors were chosen as a result of their ability of detecting a passing melt front in a very fast manner. For test purposes two cavity wall temperature sensors of type 4009b, from Priamus System Technologies AG, Switzerland, were used. The sensor has a head diameter of 0.6 mm and is of type N. It is the smallest commercially available cavity wall temperature sensor for injection molding from Priamus [153] in the year 2006 and is believed to be it until 2013. In the fact sheet of the sensor a response time of 3 ms for melt front detection is claimed by the manufacturer [154]. Since the performance measurement of the acoustic-emission sensor is based on the response characteristic of the temperature sensor, the response time of 3 ms was verified within the following measurements.

The response time is defined as the time required for a sensor output to change from its previous state to a final settled value within a tolerance band of the correct new value [146]. However, for the detection of the melt front the response time is defined as the sufficient change in the output signal from a constant state. In this term sufficient comprises a change over the noise level of the sensor to ensure reliable melt front detection.

For the verification measurement of the response time a sufficient hot heat source has to get into perfect contact with the sensor head in infinite short time. The perfect contact is necessary to ensure a fast heat transfer from the heat source into the sensor element. Therefore it is desirable to pressurize the heat source, enhancing heat transfer. This would also reflect conditions appearing within an injection mold. The infinite short time is required to reduce errors originating from other heat transport mechanisms, such as heat radiation. However, these requirements can solely be realized within physical limits.

For response time verification a measurement setup was developed which enables a fast approach of the heat source. A schematic of the setup is shown in Fig. 4.1. The temperature sensor (*A*) is implemented via an adapter (*B*) in the injection mold. As it can be seen, the temperature sensor is not perfectly aligned with the cavity surface which is a result of manufacturing tolerances of the mold components as well as the sensor. During injection molding the melt (*C*) flow direction is approximately orthogonal to the implementation direction of the sensor axis. However, such a setup was not possible to realize and a setup was realized where the heat source approaches inline with the

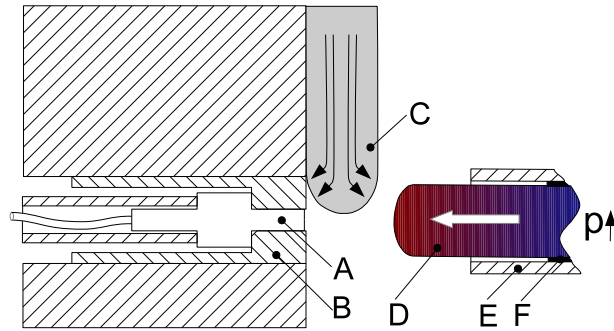


Figure 4.1: Schematic of cavity temperature sensor response time measurement. Cavity temperature sensor (*A*) is placed via an adapter (*B*) within the mold. In injection molding the melt (*C*) passes the sensor orthogonal to sensor axis. To simulate this behavior a polymer rod (*D*) was placed in a pipe (*E*) which was pressurized to accelerate the rod towards the temperature sensor. To enhance acceleration the rod was sealed (*F*) to reduce air leakage. Since the rod was plasticized before the measurement, the rod perfectly casts the sensor in its implementation position enabling good heat transfer.

sensor axis. The resulting influences on the response time measurement are believed to be small.

For the verification measurements a polymer rod (*D*), like it is used in a hot glue gun, was used as a heat source. The rod was placed inside a pipe (*E*) and was plasticized before measurement. The pipe was connected to a valve which closed off a pressurized air circuit with approximately 10 bar pressure. When opening the valve abruptly, the rod gets accelerated and ejects out of the pipe. To enhance acceleration the rod was sealed (sealing is indicated by *F*) to reduce pressure leakage. Since the rod is plasticized it perfectly casts the sensor head in its installed position enabling a good heat transfer. In addition, a portion of the rod still stays in the pipe yielding the possibility to retain pressure on the rod for enhancing heat transfer.

Prior to the measurements the impact velocity was estimated using a high speed camera with a frame rate of 300 frames per second. The rod was ejected and by using a scale the movement was calculated to be 10 m s^{-1} at impact. This velocity was declared as sufficient for the performed tests since injection velocities in injection molding are not greater.

For the estimation of the response time it is necessary to measure the moment the heat source gets into contact with the temperature sensor head. Since the rod impacts on the sensor with high velocity an impact sound is generated

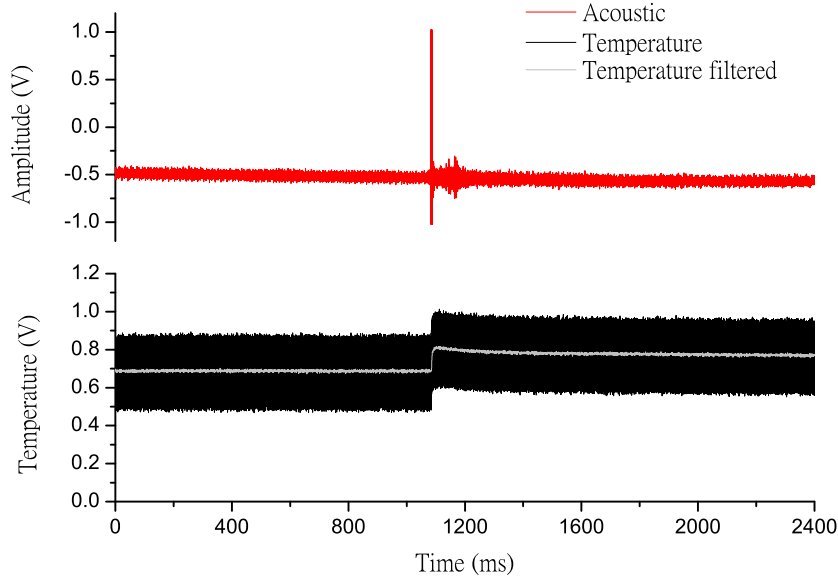


Figure 4.2: Cold mold measurement; *Top*: Recorded acoustic signal using an accelerometer mounted on the outside surface of the mold. At 1.1 s a sharp peak indicates the impact of the plasticized polymer rod; *Bottom*: Synchronously recorded temperature signal with large levels of noise shown as black solid line. The white line represents the low-pass filtered signal of the temperature sensor.

which can be recorded by an accelerometer, in a similar way like it is used for the acoustic-emission sensor. The moment of impact is the start of the response time measurement. The end of the time measurement is defined as the moment where a significant increase in the recorded temperature signal is detected. Both, the cavity temperature sensor as well as the accelerometer signal were sampled using a Data Acquisition System USB-6366 (DAQ) from National Instruments, United States, with $f_s = 25$ kHz sampling rate, resulting in synchronous recorded data. With the used sampling rate a temporal resolution of 0.04 ms is obtained which is sufficient for the estimation of the temperature sensor response time. The measurements were performed at two different mold temperatures, 17 °C (cold ambient temperature mold) and 50 °C (warm mold temperature).

Fig. 4.2 shows the result of an entire measurement at cold mold temperature. In the *Top* diagram the recorded acoustic signal is shown as function of time.

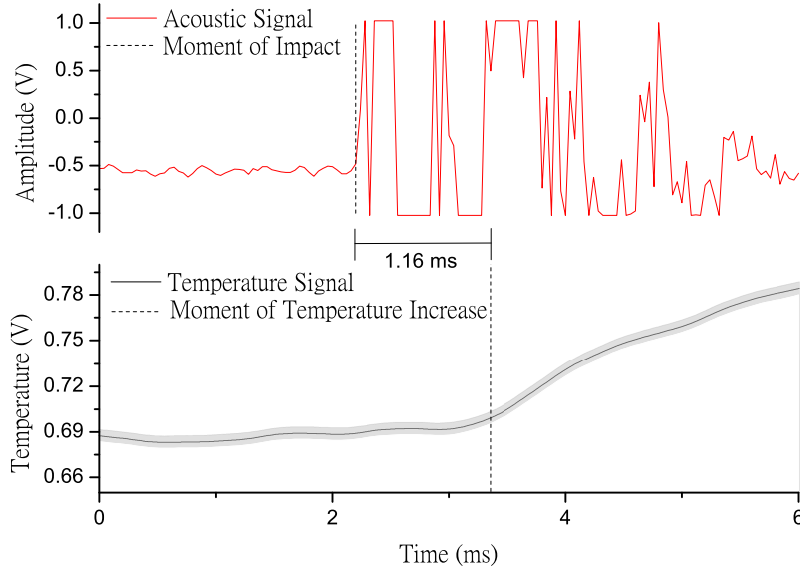


Figure 4.3: Cold mold measurement; *Top*: Zoomed view of the acoustic signal indicating the moment of rod impact through a large deflection; *Bottom*: Temperature signal with indicated standard deviation as a gray patch around the signal. The temperature increase was detected at 1.16 ms after the rod impact. This time is the response time of the cavity temperature sensor at cold mold temperature.

Until about 1.1 s just noise is recorded, which originates mainly from the accelerometer as well as the used amplifier and from the shop environment. The sharp peak at 1.1 s indicates the moment of rod impact. When regarding the temperature signal¹ (Fig. 4.2 *Bottom*) it is found that large levels of noise are present. The original measurement signal is shown as the dark solid line. To obtain useful data the signal was filtered by a low-pass filter with a cut off frequency of 1000 Hz resulting in the signal shown as the white line. Thus, just changes below 1000 Hz remain in the signal. This simplifies detecting the start of temperature increase slope which defines the end point of the response time measurement. The absolute value of the difference of the two temporal moments is the response time.

¹The temperature signal as well as the acceleration are represented in terms of Volt. For both signals the step increase is essential and consequently this representation is sufficient.

In Fig. 4.3 the impact is shown in a millisecond time scale. The beginning of the large deflection can easily be detected and is the starting point of the response time measurement. For the shown measurement the large deflection was found at 2.2 ms. It has to be noted that the DAQ was set to limit the acoustic channel to ± 1 V and consequently not the full deflection is recorded. This, however, does not influence the measurements but results in a signal cut off above and below ± 1 V.

For the temperature sensor signal the start point of the rising temperature signal cannot be detected in that simple way since the slope of the increase is significantly lower. Hence, the start point of the rising temperature was set visually². To improve detection the standard deviation of the signal was evaluated and is shown in form of a gray patch around the filtered signal. For the detection of the start of the rising signal the temperature signal has to increase at least above base level plus the signal's standard deviation. In case of the cold mold, a response time of 1.16 ms was found. Two additional measurements with cold mold temperature were performed and the results are listed in Tab. 4.1. The mean value of the measurements³ performed with cold mold temperature is 1.17 ms.

Table 4.1: Response time of the cavity wall temperature sensor for two different mold temperatures.

| cold mold | response time in ms | warm mold | response time in ms |
|-----------|---------------------|-----------|---------------------|
| c1 | 1.16 | w1 | 1.92 |
| c2 | 1.24 | w2 | 1.36 |
| c3 | 1.12 | w3 | 1.44 |
| average | 1.17 | average | 1.57 |

In Fig. 4.4 a measurement with warm mold temperature is shown. The set temperature of the tempering unit was set to 50 °C. Again the moment of impact was searched in the acoustic signal. 1.92 ms later an increase in the temperature signal is recognized. Again, a value above the indicated standard deviation was searched to ensure a safe detection. This value is slightly higher than the obtained result with a cold mold temperature. This is due to reduced temperature difference which can be denoted as,

²This may not be the most accurate method of finding the start point of the slope but it is sufficient for the statement made in this section.

³Three measurements are not sufficient for a statistical analysis but since all the measurements are below the stated 3 ms of the manufacturer no further measurements were performed at this temperature. Three additional measurements at warm mold temperature were performed leading to a total number of 6 measurements, all staying clearly below 3 ms.

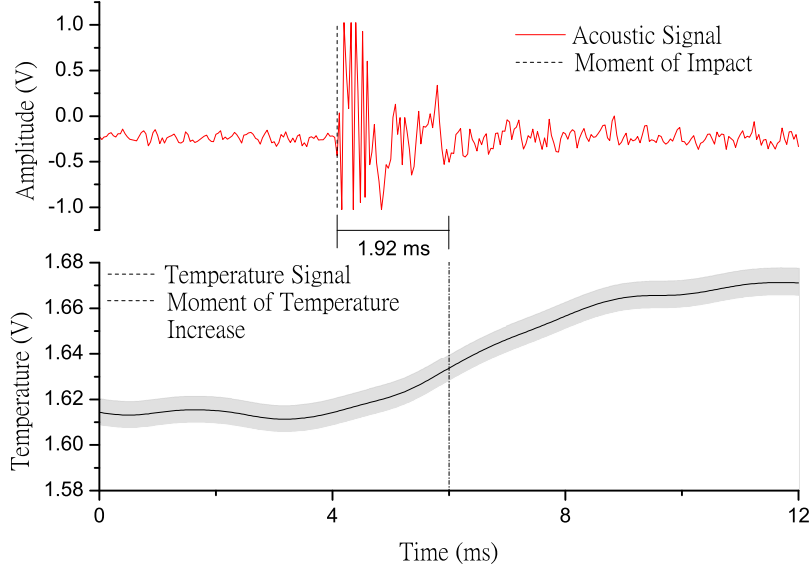


Figure 4.4: Warm mold measurement; *Top:* Zoomed view of the acoustic signal indicating the moment of rod impact through large deflection; *Bottom:* Temperature signal with indicated standard deviation as gray patch around signal. The temperature increase was detected 1.92 ms after rod impact which is the response time of the cavity temperature sensor at warm mold temperature.

$$T_{melt} - T_{moldC} > T_{melt} - T_{moldW}, \quad (4.1)$$

with T_{melt} as the melt temperature, T_{moldC} the cold mold temperature and T_{moldW} the warm mold temperature.

As a result, the driving force of finding an equilibrium between the temperatures is smaller, increasing the response time. Three measurements (shown in Tab. 4.1) were performed resulting in a mean response time for the warm mold of 1.57 ms.

One effect which is not considered in these measurements is the installation situation of the temperature sensor in the mold. Due to the high flexibility of the used mold, the sensor is placed within an adapter which is then screwed into the cavity. This keeps the flexibility to change the sensor for future investigations with little effort. However, tolerances occur due to the manufacturing process of the mold and the adapter which could lead to steps

between the cavity and the sensor as it is sketched in Fig. 4.5. For the used mold a general tolerance manufacturing value of 0.1 mm was defined⁴. During the response time measurements the polymer rod impacts directly onto the mold surface respectively the sensor head and deforms itself due to its plasticity. In addition, the pressure acting on the rod enhances filling up the chamber between sensor head and mold surface. As a result, an immediate good contact between the rod and the sensor can be ensured.

During injection molding the melt flow approaches orthogonally to the sensor axis. As a result, the chamber will not be filled as fast as with the rod which may result in a response time shift towards higher response time values in dependence of the implementation circumstances. To investigate how deep the chamber was manufactured the resulting cast mark from the temperature sensor on an injection molded part was examined. The measurements were performed at the part cast mark since placing the measurement device onto the large mold to measure the depth of the chamber was not possible. The resulting cast mark was investigated on the part surface for both cavities using a FRT MicroProf from FRT, Fries Research & Technology GmbH, Germany [39, 54, 189]. By using this measurement device it was possible to evaluate the cast mark height and consequently refer to the sensor implementation situation. In Fig. 4.6 the results of the mark height measurements are shown. For both temperature sensors a mark height of around 0.1 mm was found. It has to be noted that the height of the mark was not evaluated through the center section of the pin but at a shifted location. Consequently, the measured width of the pin is smaller than the actual sensor head diameter of 0.6 mm.

The measured cast mark height of both temperature cavity sensors is similar for both sensors and within the tolerances. The present pressure inside the melt will fill up the small mark in a fast manner and the found response time values in the test setup will be comparable to them appearing in the injection molding cycle.

An additional effect which needs to be considered derives from the present pressure during response time measurement. In an injection molding cycle the melt front has by definition a pressure level of 1 bar and nearly linear pressure propagation right behind the melt front (confer to Fig. 3.2, on page 49). However, this behavior could not be simulated during the performance measurements since the high approach speed was desired and a high contact pressure was realized right from the beginning of contact. Only in this way a good heat transfer could be ensured. As a result, the response time of the

⁴The value could be set in a tighter range which, however, would increase the mold manufacturing costs.

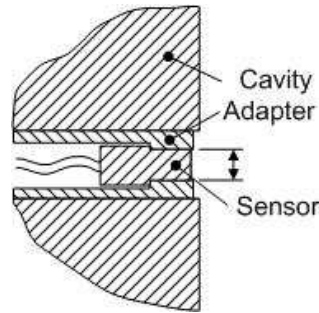


Figure 4.5: Sketch of the cavity wall temperature sensor installation situation within the mold. Manufacturing tolerances as a result of the used adapter lead to a steps between cavity surface and sensor head.

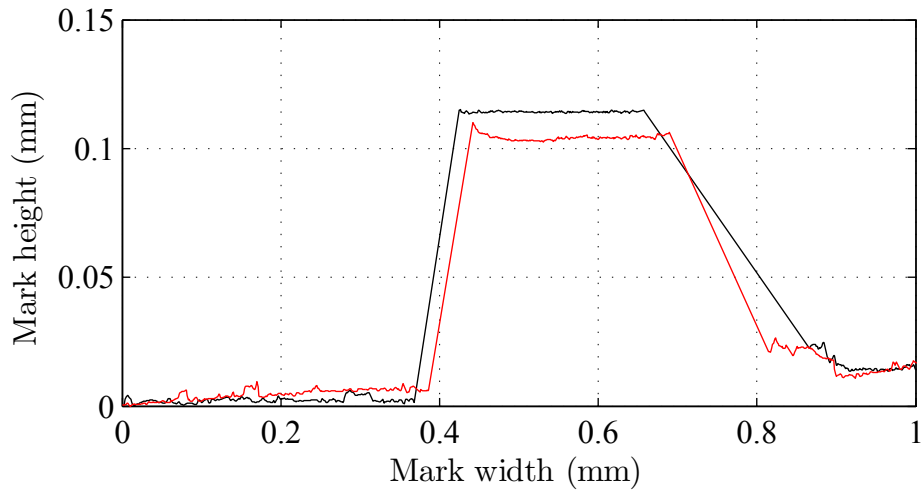


Figure 4.6: Temperature sensor mark height measurement using confocal microscope. Black line indicating Sensor 1, red line Sensor 2. Both sensor marks are of similar height indicating similar installation tolerances.

cavity wall temperature sensor during usage in an injection molding cycle may be slightly higher.

To sum up, the response time from the data sheet of the cavity wall temperature sensor (3 ms) was outperformed for both tested mold temperatures. Measurement influencing factors were investigated and discussed and are believed to be in a small range. Consequently, the sensor type 4009b is suited to be used for fast melt front detection and can be used for comparison with the acoustic-emission sensor.

4.2 Proof of Concept Measurements

The proof of functionality was realized in a series of four different measurement setups each comprising a different number of acoustic actuators:

1. one implemented acoustic actuator;
2. no implemented acoustic actuator;
3. two implemented acoustic actuators and
4. two implemented acoustic actuators with increased injection rate.

The first measurement series was performed with one implemented acoustic actuator. On the outside surface of the mold an accelerometer for structure-borne sound recording was mounted. As soon as the melt front overflows the movable pin the impact sound should be clearly detectable in the recorded acoustic data stream as a large deflection. It is important to note that the amplitude of the deflection is desired to be significantly above the noise level for reliable detection.

For verification if the peak was generated by the acoustic actuator and not by any random source, the signal was compared to the signal of the cavity wall temperature sensor. The cavity temperature sensor is located at the opposite cavity wall side inline with the movable pin's symmetry axis⁵. As a result the same process conditions in terms of melt-pressure, melt-viscosity and melt-temperature are present for both measurement systems. Consequently, identical results regarding the moment of the passing melt front detection are expected by the two independent measurement systems. If so, this would proof functionality of the acoustic-emission sensor.

For additional verification that the recorded large deflection was a result of the impacting movable pin a second measurement series was performed. For this measurement series the acoustic actuator was replaced by a blanked insert. Hence, no deflection should occur at the moment of the passing melt front. However, the cavity wall temperature sensor signal is not affected by this replacement and should still indicate the moment of passing melt front. In a third measurement series one acoustic actuator was placed in each of the two cavities. Both actuators were monitored by installing a cavity temperature sensor on the opposite side of each movable pin. As a result, a recording

⁵A rendered section view of the measurement setup was already shown in Fig. 2.3, on page 36.

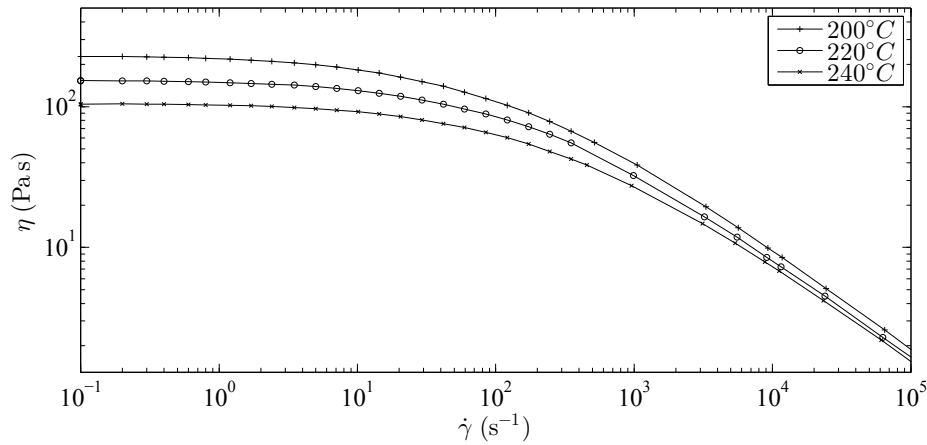


Figure 4.7: Viscosity as a function of shear rate and temperature for Polypropylene (PP) (C7069-100NA) from The DOW Chemical Company, Switzerland.

channel was added for the second implemented temperature sensor. However, still only one channel is required for the accelerometer since it collects all sounds originating from the mold [128].

In a final measurement series, again two acoustic actuators were implemented within the mold. In difference to the measurements before the injection rate was increased expecting both large deflections at an earlier temporal point. Like before the occurring deflections should have a temporal match with the increase of the temperature sensor signals.

The measurements were performed on an Arburg Allrounder 470A 1000-400 alldrive⁶. The used material was a Polypropylene (PP) (C7069-100NA), provided by The DOW Chemical Company, Switzerland. The material is a very easily flowing polymer developed for high speed injection molding of thin wall packaging containers and houseware articles enabling simple processing [182]. In Fig. 4.7 the viscosity plot of the PP as a function of shear rate and temperature is shown. The measurements were performed at the Chair of Polymer Processing at the Montanuniversitaet Leoben, Austria, using a cone-plate rheometer (MCR501) from Anton-Paar GmbH, Austria, for low shear rates and a high-pressure capillary rheometer Rheograph 2002 from Göttfert Werkstoff-Prüfmaschinen GmbH, Germany. The polymer has a rather low zero shear viscosity of around 150 Pa·s at 220 °C and a typical shear thinning behavior.

⁶The machine is an electric injection molding machine with 1000 kN of clamping force and a screw diameter of 40 mm.

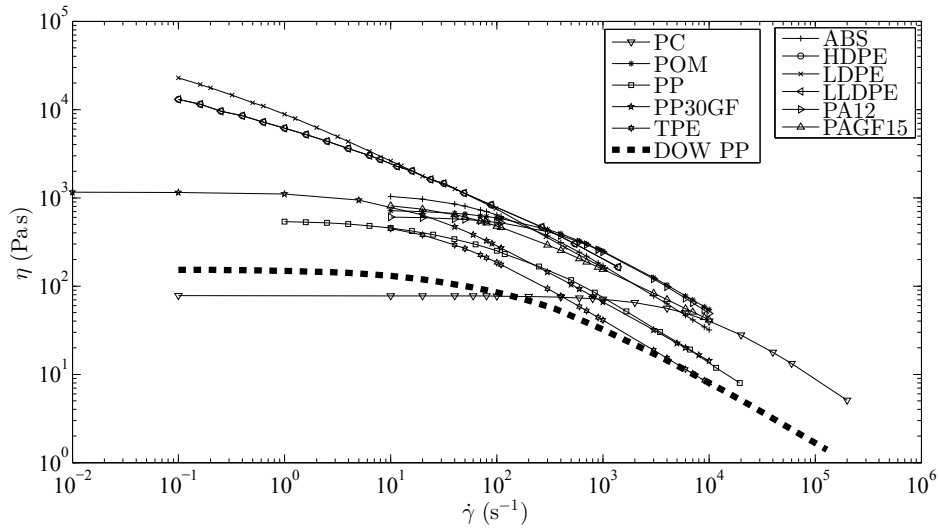


Figure 4.8: Viscosity as a function of shear rate for multiple polymers at their recommended processing temperature in comparison to the used PP (C7069-100NA) indicated by the bold dashed line.

To reinforce the low viscosity level of the used PP, the viscosity of a set of different thermoplastics over a wide shear rate range is shown in Fig. 4.8. The viscosity of all polymers is shown at their recommended processing temperature to have comparable results. As it can be seen, the used PP (bold dashed line) has nearly the lowest viscosity over the complete shear rate range of all the shown materials. The data of the other shown polymers were measured at the Chair of Polymer Processing at the Montanuniversität Leoben, Austria, using the already listed rheometers. As a result, the pressure levels within the cavity are comparably low to other frequently used technical thermoplastics.

For all measurements with the acoustic-emission sensor the melt temperature was set to 230 °C and the mold temperature was set to 45 °C. The injection rate was set to a constant level of $\dot{V} = 60 \text{ cm}^3\text{s}^{-1}$ and to $90 \text{ cm}^3\text{s}^{-1}$ for the fourth measurement series. Additional parameters like holding-pressure and others are not denoted since they do not influence the measurements⁷. The used accelerometer was a J353B01 from PCB Piezotronics Inc, United States, with a sensitivity of 20.88 mV/g and a frequency range ($\pm 3\text{dB}$) from

⁷The acoustic-emission sensor is only capable of detecting the melt front once in the filling phase. After detection the movable pin is pressed against the resonant structure with the acting melt pressure and consequently cannot generate any further sound. Consequently holding-pressure and -time as well as cooling do not influence the acoustic-emission sensor in any way. Hence, no measurement data was recorded after the filling phase.

0.35 to 18000 Hz [145]. Both cavity wall temperature sensors were of type 4009b from Priamus System Technologies AG which were already discussed in Chapter 4.1, on page 98.

All sensors, the accelerometer as well as the temperature sensors, were recorded using a PLC. The used PLC CPU was an X20CP1486 by Bernecker + Rainer Industrie Elektronik Ges.m.b.H., Austria. For sampling of the analog sensor signals two different modules were used, an X20AI4636 for the accelerometer and an X20AI4632 for the temperature signal recording. The module used for the accelerometer signal has the ability to record with a sampling rate of up to 25 kHz. This sampling rate was not necessary for the temperature sensor signal, since temperature is a slow changing magnitude. The temperature sensors were sampled with a sampling frequency of 5 kHz which is a limitation of the fastest task class of the PLC, restricted to 200 μ s. Due to the fact that the PLC is running a real time operating system with critical time slots [15] the recorded channels can easily be synchronized. In addition, the start of the injection molding cycle was detected enabling a synchronization of the recorded signal to the molding cycle. For all four measurement series a plurality of measurements were performed of which only one for each series was picked out and is shown in this thesis.

4.2.1 One Implemented Acoustic Actuator

In Fig. 4.9 one measurement result of the first test series is shown. In this test series one acoustic actuator was placed within the mold. The red solid line represents the signal of the accelerometer sensor in Volt. The obtained signal could be converted into absolute acceleration, due to the fact, that the accelerometer is calibrated. However, since only a peak is searched in the recorded signal this step was not performed. The black dashed line represents the recorded temperature signal. The temperature signal was filtered with a low pass filter to suppress high frequencies disturbing the signal. High frequencies result from the amplifier as well as from the energy source. Furthermore, the signal was smoothed using the well-known Savitzky-Golay-Filter of order 2 and a window width of a 120 samples [166]. The filter is commonly used for increasing signal to noise ratio with the benefit of not distorting the signal to badly.

At about 1 s after start of the injection molding cycle a steep increase in the temperature signal is observed. This increase indicates the melt front passing the temperature sensor head. When analyzing the accelerometer signal it is seen that mainly large levels of noise are continuously present. This noise is generated by different sources, i.e. the injection molding machine, connected

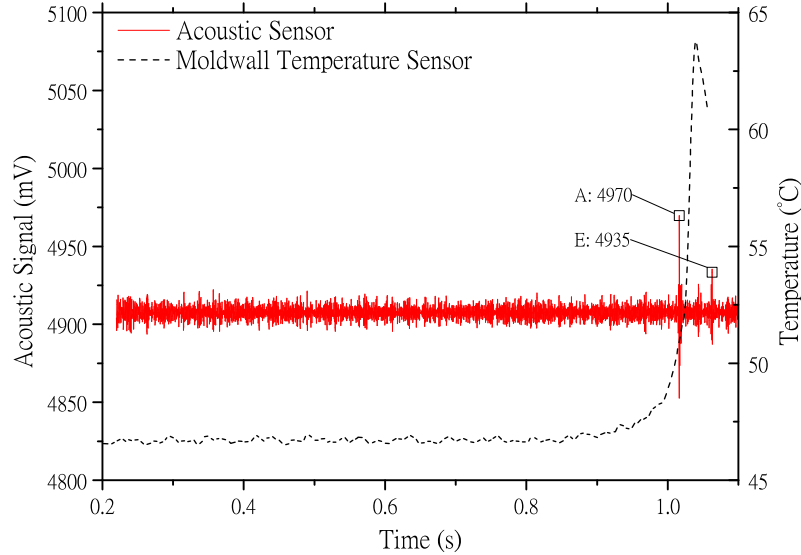


Figure 4.9: One implemented acoustic actuator in the mold at an injection rate of $60 \text{ cm}^3\text{s}^{-1}$, showing the signal of the accelerometer (red solid line) and the one of the cavity wall temperature sensor (black dashed line). Peak *A* originates from the implemented acoustic actuator and peak *E* is from an unknown source and is declared as noise; The occurring peak is in good temporal match with the temperature increase indicating the passing melt front.

cooling units, the mold itself as well as from the environment (human, mold-shop, etc.).

At the moment of the temperature rise a very short intense deflection in the acoustic signal is found (marked with *A*). The amplitude of this peak is about 60 mV. It is expected that this peak was generated by the acoustic actuator triggered by the passing melt front. The proof is given within the next measurement series. Another peak (marked with *E*) is found in the signal which occurs in all the measurement series. Due to the complex mold structure it is not possible to determine the source of the sound but it is believed that either a not tightened ejector pin or a loose mold assembly generated the sound. The amplitude is half the amplitude of the measured peak *A* (*E* has an amplitude of 30 mV) which could be used as a criteria for separation. Furthermore, the occurrence of the peak is at a different moment

and consequently this peak is declared to be noise which occurs but does not influence the measurement negatively.

Comparing the temporal occurrence of the peak *A* and the increase of the temperature signal a good temporal match is found⁸. Consequently, the passing melt front was detected by both independent systems at nearly an identical moment.

4.2.2 No Implemented Acoustic Actuator

In the second measurement series, the acoustic actuator was replaced by a blank, inactive insert. If the measurement concept performs as desired, the peak *A* should not be found in the measured acoustic signal at the position it was before. The former noise peak *E* is still expected to be present in the signal and should be unchanged.

The process parameters are unaltered in comparison to the first series. Fig. 4.10 shows an exemplary result for this measurement series. The temperature signal is identical to that obtained in the first measurement series indicating the passing melt front at around 1.0s after start of the injection molding cycle. The slight variation of the temporal moment of the passing melt front is within typical limits. The only difference can be observed in the acoustic signal. At the temporal moment when the peak *A* was found in the previous measurement series, now only noise is detected although the melt front passed the sensor location indicated by the temperature sensor signal. This verifies that the peak *A* was generated solely by the implemented acoustic actuator. Again the peak *E* can be found in the acoustic signal. Its amplitude is of the same height as before (30 mV). In addition, a peak is found around 0.3s after start of injection molding cycle. This peak occurred early during the filling phase and is believed to be generated by a non tightened ejector pin or a loose mold assembly. Furthermore, it has to be noted, that the signal is not a result of the replacement with the blank insert. However, the peak does not influence the measurement at all, since it is in a different temporal region than the signal generation by the acoustic actuator.

⁸At this point the temporal match is just a visual comparison since no enhanced signal processing is performed at this point. Quantitative results are e.g. shown in Chapter 4.5.3, on page 155.

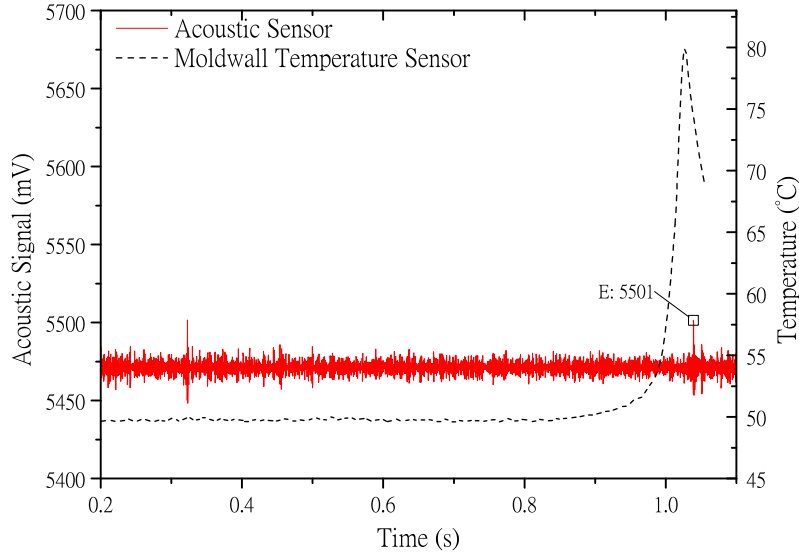


Figure 4.10: Measurement without implemented acoustic actuator in the mold at an injection rate of $60 \text{ cm}^3\text{s}^{-1}$, showing the signal of the accelerometer (red solid line) and the one of the cavity wall temperature sensor (black dashed line). Former Peak *A* disappeared by replacing the actuator by a blank insert; the noise peak *E* is still present.

4.2.3 Two Implemented Acoustic Actuators

A third measurement series with two implemented acoustic actuators was performed. In each cavity of the fully symmetrical mold one acoustic actuator was implemented. Both actuators were located at the identical position in each cavity. Two different measurement results are possible:

1. in the first case, just one peak will be visible because the acoustic actuators were activated at the exact same time. Evidence would be found in the temperature sensor signal which would show up an identical step increase at the coincident moment in both temperature sensor signals. This case, although possible, is unlikely due to the high resolution ($f_s = 120 \text{ kHz}$) of the measurement signal;
2. two separated significant peaks are found in the acoustic sensor signal as a result from unbalanced filling of the multi-cavity mold.

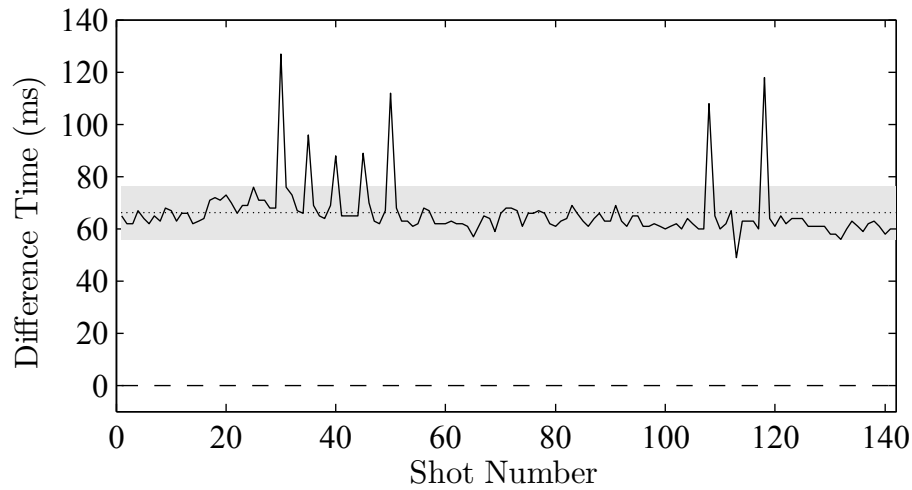


Figure 4.11: Filling time difference of a two cavity mold. The filling time difference was measured using the implemented cavity wall temperature sensors. The measurement data were obtained from 140 shots and the mean value (dotted line) as well as the standard deviation are indicated (gray patch) [41].

Unbalanced filling occurs despite the fully symmetrical construction of the two cavities and having a fully symmetrical hot runner system. Already differences of below 1 K in the hot runner system will lead to an unbalanced filling of the mold [92]. Further influencing factors are manufacturing tolerances as well as debris in the flow paths. The used mold was examined towards unbalanced filling in the Bachelor thesis of Doppelmayer [41]. In Fig. 4.11 the filling time difference between the cavities measured by the installed temperature sensors is shown over a series of 140 shots. A timer was started as soon as one of the temperature sensors detected a passing melt front and was stopped when the second melt front reached the second temperature sensor. As shown in Fig. 4.11, the mean time difference between the two cavities is around 66 ms (dotted line). Additionally, the standard deviation (gray patch around mean value) is indicated with about ± 10 ms. In Doppelmayer [41] possible reasons like production tolerances, temperature inhomogeneity or polymer deposits in the hot runner system for unbalanced filling are stated.

In Fig. 4.12 the results with two installed acoustic actuators are shown. The first temperature signal (black dashed line) rises at about 1.0 s. At the same temporal moment a peak marked with *A* appears in the acoustic signal. The amplitude has a height of about 110 mV. The second temperature signal

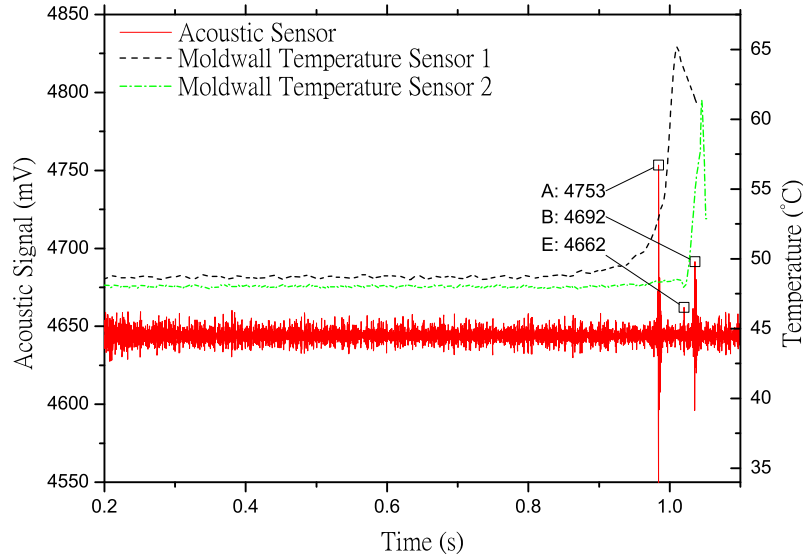


Figure 4.12: Two implemented acoustic actuators in the mold at an injection rate of $60 \text{ cm}^3\text{s}^{-1}$, showing the signal of the accelerometer (red solid line) and the ones of the cavity wall temperature sensors (black and green dashed lines). Two peaks labeled *A* and *B* appear due to the two implemented acoustic actuators; the noise peak *E* is still present; both peaks are in good temporal match with the temperature slope indicating the passing melt front.

(green dashed line) rises slightly later than the first one. At the coincident moment a peak marked with *B* appears with an amplitude of about 50 mV in the acoustic signal. The difference between the two amplitudes of the peak can be described by differences in the production tolerances of the movable pin. Consequently, different friction behavior is present in the two cavities resulting in different impact velocities and in different oscillation amplitudes. Like in the other measurements the peak *E* appears with a relatively low amplitude of about 20 mV. Again the temporal match between the occurrence of the temperature rise and the appearance of the matching acoustic peak is very good for both peaks.

When comparing the rise characteristic of both temperature sensors a difference can be observed. In an additional measurement series this phenomenon was investigated. In Fig. 4.13 the temperature rising is shown in a short

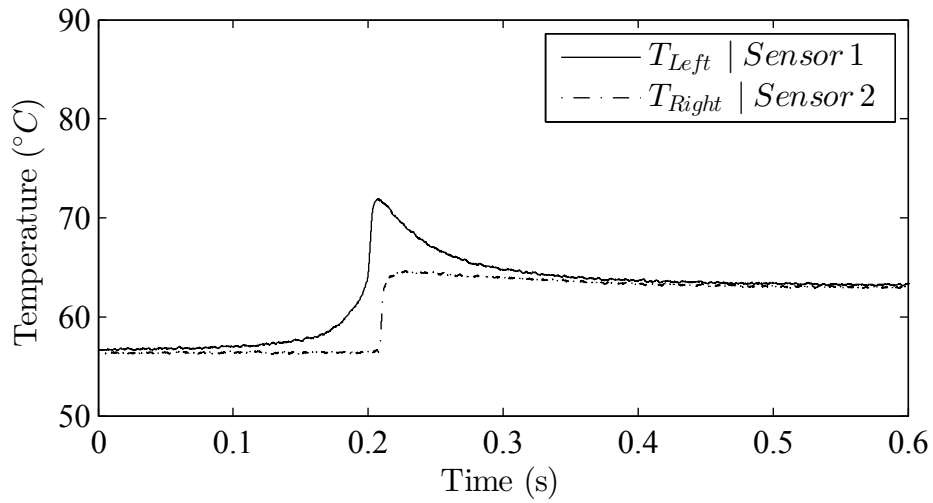


Figure 4.13: Investigation of the rise characteristic of two installed cavity wall temperature sensors. The solid line is dedicated to the sensor placed in the left cavity (Sensor 1); the dash-dotted line shows the measurement result of the temperature sensor located in the right cavity (Sensor 2).

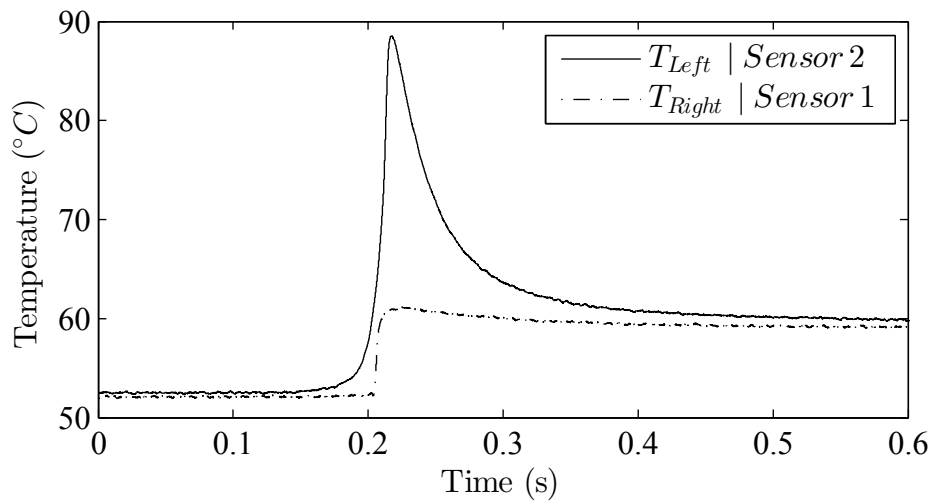


Figure 4.14: Investigation of the rise characteristic of two installed cavity wall temperature sensors in exchanged position as in Fig. 4.13. The solid line is dedicated to the sensor placed in the left cavity (now Sensor 2); the dash-dotted line shows the measurement result of the temperature sensor located in the right cavity (now Sensor 1).

time scale. As it can be observed, the temperature sensor in the left cavity (solid line, Sensor 1), has a creeping rising characteristic. The sensor in the right cavity (dash-dotted line, Sensor 2), however, shows the expected rise characteristic⁹. The temperature rises instantaneously from the mold temperature up to contact temperature and afterwards decreases back to the mold temperature after part ejection (not shown in this time scale).

To verify if the unexpected rise characteristic of the left sensor is a result of a sensor defect or a cavity related problem both sensors were exchanged in position. So Sensor 1 is installed in the location of Sensor 2 and vice versa. In Fig. 4.14 the results are shown in the same time and temperature scale. Again the solid line is dedicated to the left temperature sensor and the right sensor is indicated by dash-dotted line. As it can be seen, the left temperature sensor (now Sensor 2) has again the unexpected rise characteristic and the right temperature sensor (now Sensor 1) has the expected one. Consequently, the unexpected rise characteristic is a cavity related issue and is not referred to a sensor failure. In Chapter 4.1 the installation circumstances of the temperature sensors from both cavities were already investigated indicating no difference. As a result, it is believed that venting in the left cavity seems to be the reason for having an unexpected rise characteristic of the sensor implemented in the left cavity.

⁹In a publication of the sensor manufacturer [8] a similar rise characteristic is stated, too.

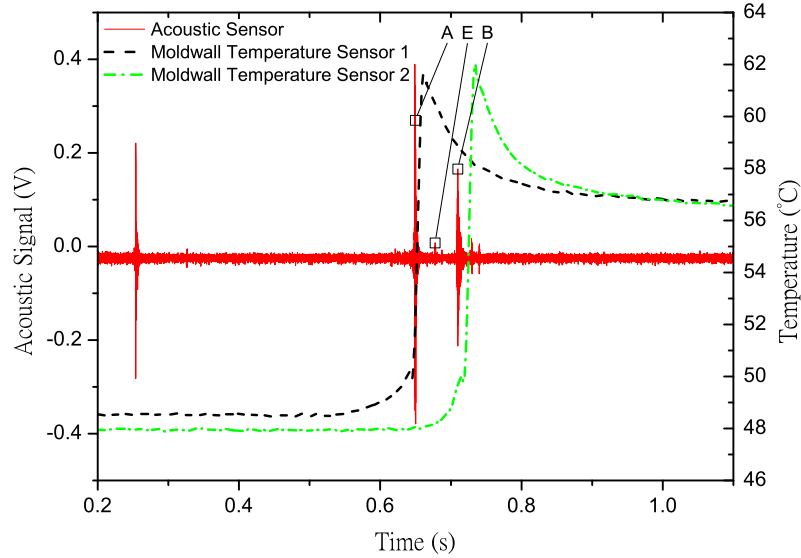


Figure 4.15: Two implemented acoustic actuators in the mold at an injection rate of $90 \text{ cm}^3\text{s}^{-1}$, showing a signal for the accelerometer (red solid line) and two for the cavity wall temperature sensors (black and green dashed lines). Two peaks labeled *A* and *B* appear which are both in good temporal match with temperature increase indicating the passing melt front.

4.2.4 Two Implemented Acoustic Actuators - Increased Injection Rate

In a fourth measurement series the injection rate was increased up to $90 \text{ cm}^3\text{s}^{-1}$ while still having two installed acoustic actuators. It has to be mentioned that this measurement series was performed at a subsequent date in the research. A different accelerometer with higher sensitivity was used for these measurements. The sensor was a 352A60 from PCB Piezotronics. The sensor has a sensitivity range of 5 to 60000 Hz and was calibrated with 10.16 mV/g . For data acquisition a DAQ was used sampling the signals with 120 kHz. To obtain comparable results the data was down-sampled to $f_s = 25 \text{ kHz}$. Therefore a low pass filter with a stop band of 80 dB at $f_s/2$ was applied on the data before down-sampling to prevent aliasing. Using these different components does not affect the basic statement of the measurement series. In Fig. 4.15 the results are shown indicating a passing melt front at 0.64 and 0.70 s indicated by the two temperature slopes. At the coincident

moment two large deflections (labeled with A and B) occur indicating a good temporal match with the results from the temperature sensors. This verifies again that the deflections are generated by the installed actuators which are triggered by the melt front. In addition, this measurement series comprises again the peak labeled with E , which is shifted to early times like the other peaks as a result of increased injection rate. Like in the other measurements before a peak occurs at the beginning of the filling phase as a result of a not tightened ejector pin or a loose assembly. This peak, however, does not affect the measurement at all since it does not appear at the expected moment of the acoustic resonator's sound.

Knowing the part volume¹⁰ V and the injection rate \dot{V} , the expected moments the peaks will occur in the signal are calculable, since the actuators are implemented near flow path end. Both parts have a summed volume of $V = 54 \text{ cm}^3$ which leads to a filling time of $t_f = V/\dot{V}$. In case of an injection rate of $\dot{V} = 90 \text{ cm}^3\text{s}^{-1}$ the moment the peaks are expected is at $t_f = 0.6 \text{ s}$. For the injection rate of $\dot{V} = 60 \text{ cm}^3\text{s}^{-1}$ the peaks are expected at $t_f = 0.9 \text{ s}$. For both injection rates tested this is in accordance to the found results.

In conclusion, it was verified that with the installation of an acoustic actuator additional sound can be generated triggered by the passing melt front. Thereby just one accelerometer mounted outside of the mold is needed for the detection of an independent number of implemented acoustic actuators. The correlation between the moment of large deflection in the acoustic signal due to pin impact and the position of the melt front was verified by using cavity wall temperature sensors. A good temporal match was found between the two different independent measurement systems.

If multiple actuators are implemented in a mold there is no way of separating the two detected peaks and dedicating each peak to an acoustic actuator respectively to the implementation location by just considering the amplitude of the peaks. When using wired sensors it is a simple task to obtain the measurement location since the signal is transmitted via the wires.

In the shown measurements, both peaks were generated by acoustic actuators equipped with differently designed resonant structures. Consequently, the oscillation behavior of each deflection is different to the other one as a result of their structural shape. In Fig. 4.16 *Top* a focus on one peak can be seen¹¹. A good temporal match of the start of the excitation with the temperature rise is given. Comparing the excitation behavior with that of the second peak, which is shown in Fig. 4.16 *Bottom*, differences in the oscillation behavior

¹⁰Just in this case the part volume is sufficient because the acoustic actuator is placed at the flow path end.

¹¹The results were taken from a different measurement series with two implemented resonators (12 kHz and 3.8 kHz resonator).

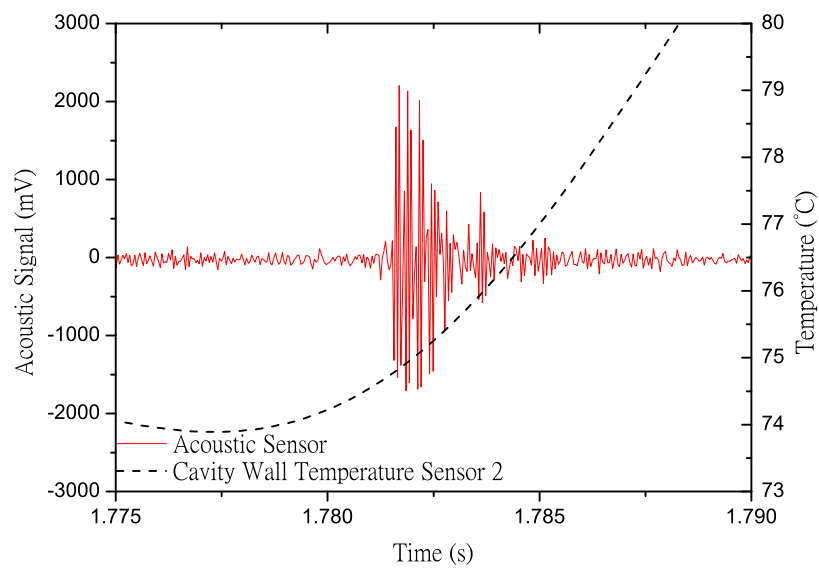
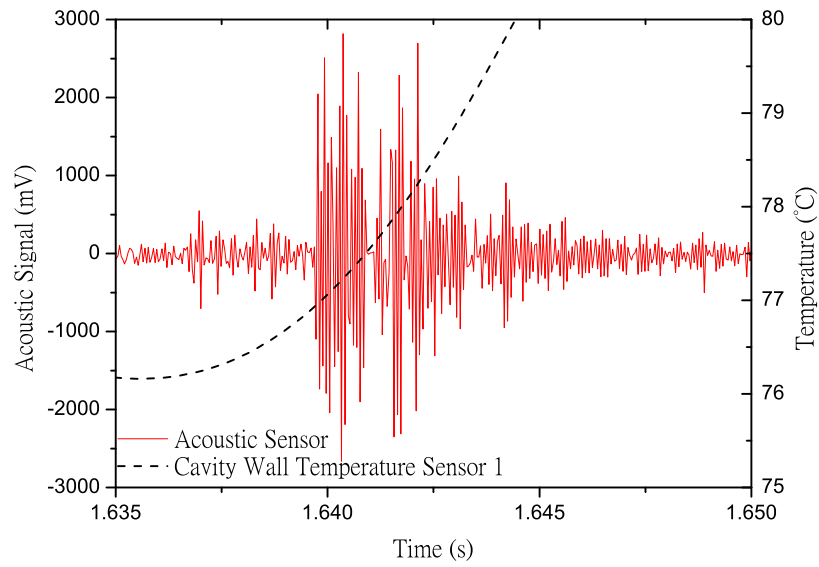


Figure 4.16: Both plots are zoomed on the identical time range during impact. The different oscillation behavior of the resonant structure is used for separation of the two impact events.

appear. Either of the diagrams is showing 15 ms of recorded data. This oscillation differences originate from different frequency components of which the oscillation is composed. These differences are used for separation of the acoustic actuators in the filter analysis, shown in Chapter 4.5.2, starting on page 151, as well as for the resonant frequency pattern recognition method, shown in Chapter 4.5.3, starting on page 155.

4.3 Acoustic-Emission Sensor Performance Evaluation

The overall sensor performance of the acoustic-emission sensor is mainly dependent on the mechanical pin movement. The pin protrudes into the cavity with a certain height, depending on the system mass. The distance the pin moves until impact position is identical to the height so that no other mark than a typical ejector mark can be found on the part's surface. Although the distances are in the few millimeter region the movement time is of special interest since it is the delay time which occurs between the passing melt front and sound generation at impact.

The driving force during the pin movement is the pressure acting on the pin surface. For performance evaluation it is interesting to obtain the time-dependent pin movement in dependence of different melt pressure propagation¹². From the time-dependent pin movement the delay time is derived.

The pressure propagation from the pushing screw to the melt front was already discussed for a Newtonian fluid in Eq. 3.5. However, to receive more accurate results with respect to shear-thinning material behavior the filling of the part was simulated and one result is shown in Fig. 4.17. The simulation was calculated using SigmaSoft v4.8 from Sigma Engineering GmbH, Germany, modeling the complete mold, including hot runner temperature control as well as performing a multi-cycle analysis to receive results from a thermally stationary state¹³. In Fig. 4.17 it can be seen that the pressure propagation is approximately linear over the flow path length from the equidistant distributed isobar lines. In the thicker area of the part (at the

¹²Pressure is the driving force in injection molding. Nearly every process variation, e.g. melt temperature, injection rate or batch-to-batch material variation, results in a change in the melt pressure propagation. Consequently, it is desired to have a sensor concept, which has a response time characteristic that is hardly affected (at maximum a few milliseconds) by pressure variation.

¹³Additional simulation results of the part and mold are presented in the thesis of Doppelmayer [41].

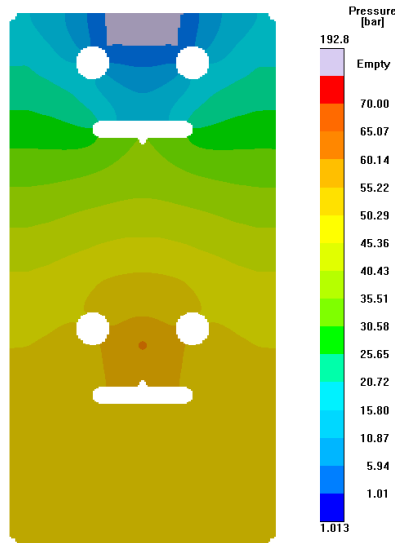


Figure 4.17: Pressure propagation inside the part simulated using Sigma-Soft v4.8. For simulation the complete mold was modeled including hot runner temperature controlling. The result was received after performing a multi-cycle analysis for having thermal steady state conditions.

bottom of the figure) a hydrostatic pressure is present which is a result of already filled up cavity and not solidified material.

The used material, PP C7069, has a very low viscosity over the complete shear range¹⁴. As a result, the overall pressure level is very low for a part of this size. Since a higher viscosity of the polymer¹⁵ would lead to higher pressure propagation, the pin acceleration is increased too, resulting in shorter pin movement time. Consequently, the sensor performance estimation with this particular PP will be conservative.

For the calculation of the time-dependent pin movement three input parameters have to be known (Eq. 3.7):

1. time-dependent pressure $p(t)$ acting on the movable pin;
2. the pin mass m and
3. the spring rate k .

¹⁴Confer to Fig. 4.7, on page 107, for viscosity plot in dependence of shear rate and temperature.

¹⁵Viscosity is typically higher for thermoplastics as it is shown for a variety of polymers in Fig. 4.8, on page 108.

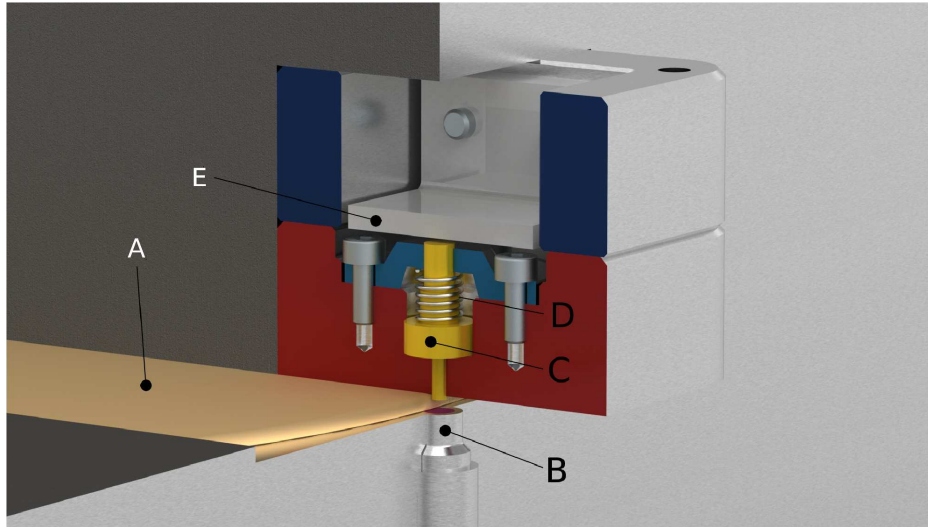


Figure 4.18: Measurement setup to obtain time-dependent cavity pressure during pin movement. The melt front (*A*) passes the pressure transducer (*B*) as well as the movable pin (*C*) simultaneously. Consequently, identical process conditions are present for both measurement systems. Additionally, the spring (*D*) and resonant structure (*E*) are shown.

The easier ones to obtain are the mechanical values, the spring ratio k and the pin mass m . To obtain the pressure value as a function of time $p(t)$ during pin movement a special measurement setup was realized. In Fig. 4.18 a rendered section view of the measurement setup is shown. In one cavity side a pressure transducer *B* of type 6157 from Kistler Instrumente AG, Switzerland, is implemented. The sensor has a head diameter of $d_s = 4$ mm. At the exact opposite cavity side the movable pin of the acoustic actuator is located (*C*). As soon as the melt (*A*) influxes the cavity, both measurement systems are exposed to the same process conditions at the same time. The acoustic actuator comprises the supporting spring (*D*) and the resonant body with (*E*).

For the performed measurements the already introduced PP C7069 was used. The first measurements were performed with an injection rate of $\dot{V} = 60 \text{ cm}^3\text{s}^{-1}$. In Fig. 4.19 a typical measurement result from the implemented pressure transducer is shown with temporal focus on the moment of the passing melt front. At 1.062 s the melt front reaches the pressure transducer which indicates a pressure increase at its output signal. The acoustic signal indicates a sharp peak from the impact of the movable pin at nearly the coincident moment.

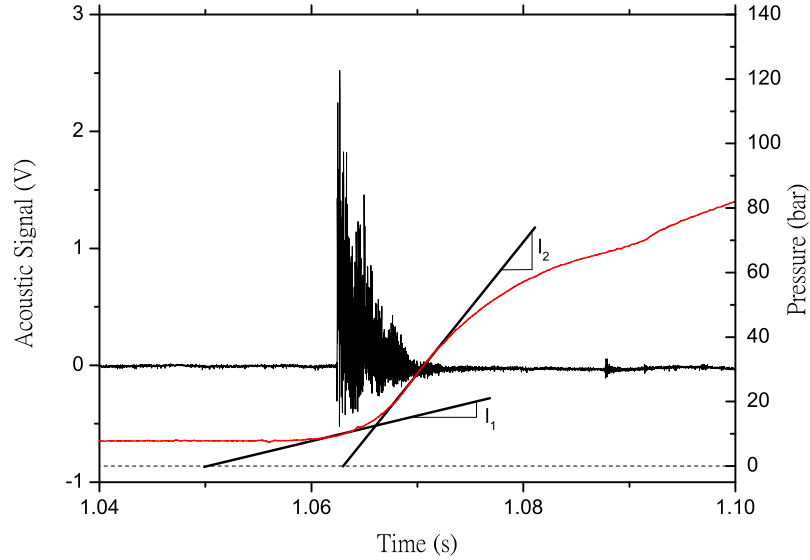


Figure 4.19: Pressure measurement with an injection rate of $60 \text{ cm}^3\text{s}^{-1}$. Red line indicates pressure level and black line indicates acoustic signal. Pressure data were approximated as two straight lines with inclination l_1 and l_2 for estimation of pressure influence on pin movement.

To consider influencing inaccuracies during pressure measurement in short time scale ($< 5 \text{ ms}$), two linear approximations of the pressure trend are introduced with inclination l_1 and l_2 . Thereby the line with inclination l_1 covers the recorded pressure level at the beginning of pin movement. The second line has a steeper inclination l_2 and is introduced to cover possible inaccurate pressure data as a result of a slow response of the pressure transducer in the first few milliseconds.

At this point a parenthesis on possible influencing parameters on the pressure measurement has to be made to help understanding the following results. First, it is **strongly insisted** that in-mold pressure transducers are **not designed** to record low pressure levels in short time scales (millisecond time scale). Instead they are designed to resist high pressures of up to 2000 bar and deliver accurate data over a long measurement time. To compensate this shortage the recorded pressure response behavior was varied by using inclination l_1 and l_2 and investigate the effect on the time-dependent pin

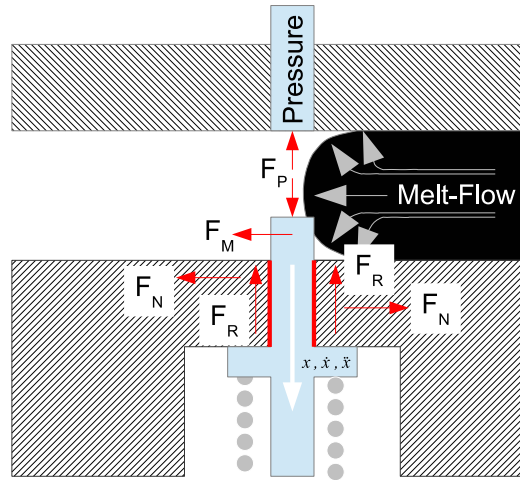


Figure 4.20: Sketch of melt front shape influence on response time of both measurement systems, the acoustic-emission sensor and the pressure transducer. Gray arrows indicate fountain flow. Sketched acting forces by passing melt front on movable pin evoke friction forces before and during movement. F_M denotes the force originating from the melt acting on the pin. As a result F_N is pushing against the surface indicated by the red line. During movement of the pin (white arrow) the force F_R acts in the opposite direction of pin movement, x, \dot{x}, \ddot{x} . The force F_P is acting on both measurement systems resulting in the measurement value.

movement. If the pin movement is hardly effected (a few milliseconds at maximum) by these variations the sensor system can be stated to be robust. An important aspect is the influence of the melt front shape and its propagation velocity on the response time of the two measurement systems. In Fig. 4.20 the implementation situation of the movable pin and the pressure transducer is shown schematically. Due to the shape of the melt front, which results from the fountain flow, the melt front reaches the movable pin before it reaches the pressure transducer sensor head. From this fact an injection rate dependent lag between the two measurement systems will emerge.

In Fig. 4.20 the acting forces during pin movement are shown. The black melt front is in-fluxing the cavity (gray arrows indicate fountain flow), already slightly pushing onto the movable pin, while the pressure transducer is not yet touched by the melt front. Due to the applied pressure within the melt as well as its high viscosity the force F_M is acting on the pin in a deflecting manner. The force F_P is the one responsible for the pin's acceleration. As

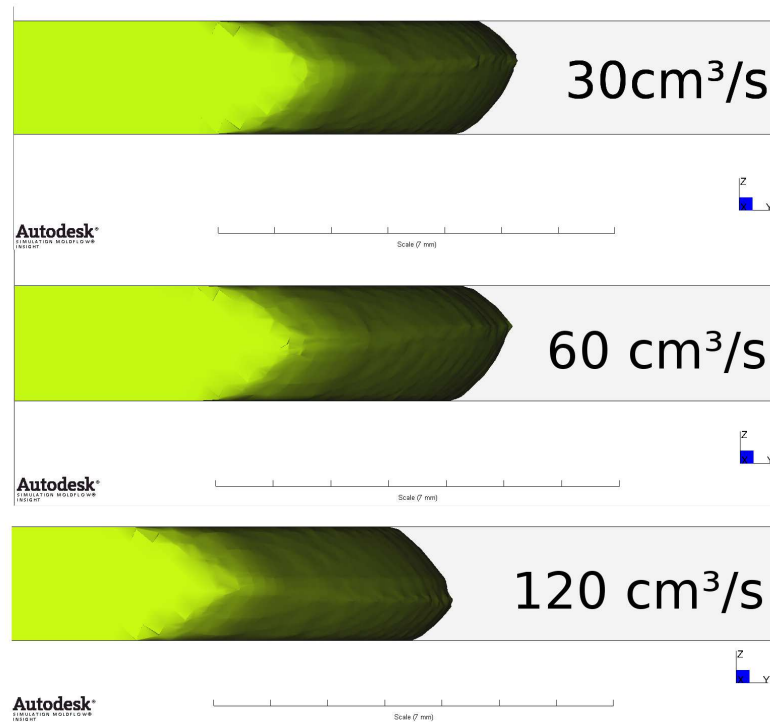


Figure 4.21: Melt front shape over cavity height of a rectangular plate using a PP. Three different injection rates were simulated using Autodesk Moldflow; *Top:* Injection rate $30 \text{ cm}^3\text{s}^{-1}$; *Middle:* Injection rate $60 \text{ cm}^3\text{s}^{-1}$; *Bottom:* Injection rate $120 \text{ cm}^3\text{s}^{-1}$. Inertia is not considered in these results.

a result of F_M the pin pushes onto the surface indicated by the red line. This leads to the force F_N which is the normal component of the friction force F_R . The two forces are proportional to the factor μ_s , the coefficient of static friction. The force F_R is acting in opposite direction of pin movement and consequently reduces or delays pin movement. Hence, some differences between the calculation and experimental consideration of the pin movement appear.

In Fig. 4.21 the melt front was simulated using Autodesk Moldflow Simulation Insight 2013, Autodesk Inc, United States. A simple rectangular plate with a height of 2 mm was meshed with approximately 1 million 3-D tetrahedral elements with 7 elements over part height enabling a fine resolution of the melt front. The melt front was investigated for three different injection rates, 30, 60 and $120 \text{ cm}^3\text{s}^{-1}$ for three different polymers to investigate the influence on the melt front. Since the results of additional calculations with

Table 4.2: Time needed to overflow the pressure transducer head (diameter 4 mm) with melt in dependence of four different injection rates for a cross section of 20 x 2 mm².

| Injection rate in cm ³ s ⁻¹ | Time to overflow pressure-transducer head in ms |
|---|---|
| 15 | 10.6 |
| 30 | 5.3 |
| 60 | 2.6 |
| 120 | 1.3 |

Polyoxymethylene (POM) and Polyamide (PA) are identical to the results of the investigated PP, their results are not shown. It was also investigated if inertia effects influence the melt front shape. A different melt front shape is found when considering inertia but the shape is still similar for the investigated different injection rates. In Fig. 4.21 the results are shown for the used PP indicating that there is no significant influence of the injection rate on the melt front shape. However, it has an influence on the measurements since using a higher injection rate reduces the delay time between the moment the melt front reaches the movable pin and the time the melt front arrives at the pressure transducer.

It is known that pressure transducers may deliver inaccurate results as long as the sensor head is not fully overflowed by melt and is exposed to asymmetric loading. Having an injection rate of 60 cm³s⁻¹ and a cavity width of 20 mm and a height of 2 mm in the region of the sensor implementation, around 2.6 ms are needed to overflow the sensor head diameter of 4 mm. In Tab. 4.2 the overflow times for additional injection rates are listed. However, the time needed to fully overflow the sensor head for a cross section of 20 x 2 mm², i.e. 1.3 to 10.6 ms, is mainly the time at which pin movement will happen, i.e. below 10 ms. Hence, it is important to vary the received pressure data widely to investigate its impact on the calculated pin movement time.

4.3.1 Pressure Influence Investigation

For the acoustic-emission sensor two different distances for pin movement were tested, $d_1 = 0.1$ mm and $d_2 = 0.5$ mm. For both distances pin movement and pin protrusion distances are equal so that no other mark is found on the part's surface than a typical ejector pin mark. The shorter distance d_1 results in quicker response time but the greater distance d_2 results in a better signal to noise ratio since the impact energy is higher.

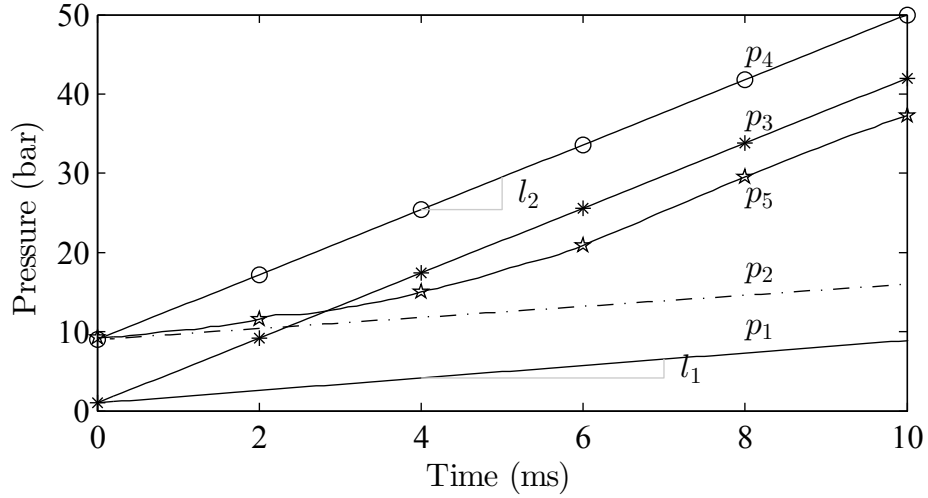


Figure 4.22: Five time-dependent pressures p_i used for calculating the pin movement. p_1 starts at 1 bar with inclination l_1 ; p_2 starts at 9 bar with inclination l_1 ; p_3 starts at 1 bar with inclination l_2 ; p_4 starts at 9 bar with inclination l_2 ; and p_5 is the real measurement data. The inclinations l_1 and l_2 were obtained by measurement data shown in Fig. 4.19.

The first pressure trend line l_1 approximates the pressure trend at the beginning of sensor head overflowing with an inclination of $l_1 = \Delta p / \Delta t = 0.7 \text{ bar} / 1 \text{ ms}$. The second line is in the region of higher pressure increase having an inclination of $l_2 = \Delta p / \Delta t = 4.0 \text{ bar} / 1 \text{ ms}$.

In Fig. 4.19 it can be observed that the pressure level is not at 1 bar level at the moment before the melt front reaches the sensor head but an offset level of around 9 bar is present. This happens although the measurement system is reset at the beginning of an injection molding cycle. To regard this issue the measured offset level as well as a pressure level referenced to 1 bar will be investigated. To cover these uncertainties in terms of pressure measurement, four different pressure trends are set up from the measurement shown in Fig. 4.19, p_1 starting at pressure level 1 bar having inclination l_1 , p_2 starting at the measured level 9 bar having an inclination of l_1 , too. Pressure level p_3 is starting at pressure level 1 bar and p_4 starts from 9 bar. Both pressure levels have inclination l_2 . Finally, a fifth pressure level p_5 is set up using the real measurement data. The five time-dependent pressures are shown in Fig. 4.22 and are plugged into the mathematical model (Eq. 3.24) of the pin movement. The used spring (D-068A-17) has a spring rate $k_1 = 1.179 \text{ N} / \text{mm}$

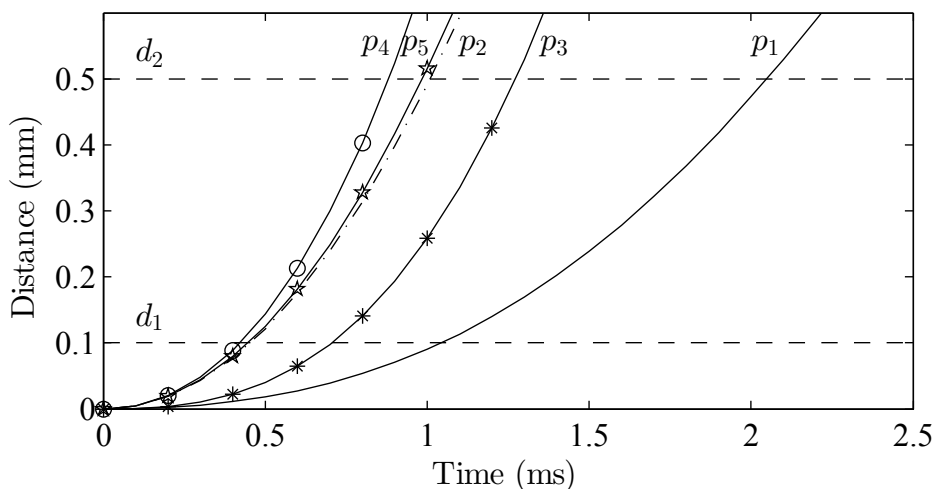


Figure 4.23: Calculated time-dependent pin movement using Eq. 3.24 for five different pressure histories. p_1 starts at 1 bar with inclination l_1 ; p_2 starts at 9 bar with inclination l_1 ; p_3 starts at 1 bar with inclination l_2 ; p_4 starts at 9 bar with inclination l_2 ; and p_5 is the obtained measurement data. Pin mass and spring rate were set constant.

and is from Gutekunst + Co.KG Federnfabriken, Germany. The mass of the movable pin is $m = 3 \cdot 10^{-3}$ kg.

In Fig. 4.23 the pin movement for the five different pressure setups p_i is shown as a function of time. The values to reach distance d_1 and d_2 are listed in Tab. 4.3. Starting with the lowest pressure p_1 , the pin needs about 1.0 ms to overcome a distance of 0.1 mm and 2.0 ms for the distance of 0.5 mm. By using the pressure trend with the higher offset level p_2 , the time needed to reach both distances is reduced by approximately 50 % for each. For the higher pressure gradient l_2 less time is needed when comparing each pressure history with identical offset pressure level, i.e. p_1 and p_2 . When using the recorded values from the pressure measurement p_5 a pin movement similar to p_3 is obtained. The pin needs about 1 ms until impact for a distance of 0.5 mm.

Although a difference in the response time of over 100 % was estimated between pressure level p_1 and p_4 for the distance of $d_2 = 0.5$ mm, the absolute time difference is in a range of just over 1 ms. This value is very low for the used different pressure trends. Conventional in-mold sensing technology for melt front detection is in a similar range concerning response characteristic, e.g. cavity wall temperature sensors (3 to 10 ms) [9].

Table 4.3: Corresponding times to reach distance d_1 and d_2 from data shown in Fig. 4.23.

| Pressure | Time to reach distance d_i in (ms) | |
|----------|--------------------------------------|-------|
| | d_1 | d_2 |
| p_1 | 1.037 | 2.047 |
| p_2 | 0.451 | 1.007 |
| p_3 | 0.702 | 1.273 |
| p_4 | 0.421 | 0.879 |
| p_5 | 0.448 | 0.984 |

The five different pressure levels p_i can also be seen as different polymers having different viscosity η . For a Newtonian fluid in a rectangular channel the viscosity η_N is defined as¹⁶ [142],

$$\eta_N = \frac{\Delta p H^3 B}{12 \dot{V} \Delta L}, \quad (4.2)$$

with H and B the cavity height and width, ΔL the observation length and \dot{V} the volume flow rate. When the cavity and volume flow rate are kept constant a change in the pressure can be seen as a change in the viscosity. The five pressure levels have a maximum difference of about 15 bar in a time span of 2 ms, which is a lot. However, the pin movement time for the distance d_2 changes at maximum around slightly more than 1.0 ms which is very low in comparison to the large pressure changes. From Eq. 4.2 it is known that a pressure change is proportional to a viscosity change. Since pressure has no large impact on the response time characteristic of the acoustic-emission sensor, different polymers with different viscosities will not have an large impact on the response time characteristic either. Hence, the sensor can be used for a wide variety of polymers, especially for those that have a higher viscosity than the used PP, delivering melt front detection in a comparable fast response characteristic.

Furthermore, a response time between the pressure sensor melt front detection and the impact of the movable pin can be estimated. In Fig. 4.24 *Top* the acoustic signal is shown with a temporal focus on the moment of impact. It is easy to determine the moment of impact since the signal to noise ratio is high. In the middle figure, the measured pressure signal is shown as a red line. This signal is perturbed by high levels of noise making it hard to find the moment of rising signal. To overcome this, the signal was smoothed with

¹⁶For simplicity the viscosity is assumed to be Newtonian although thermoplastics have a shear thinning behavior in general.

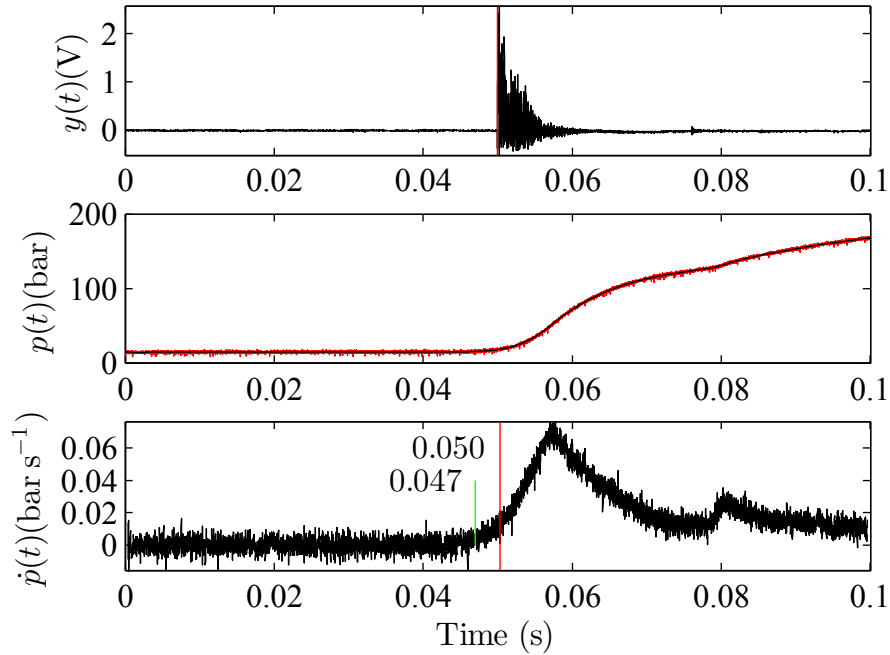


Figure 4.24: *Top:* Acoustic signal with temporal focus on moment of impact, indicated by the vertical red line; *Middle:* Measured pressure signal (red line) at injection rate of $60 \text{ cm}^3\text{s}^{-1}$ and smoothed pressure signal (black line); *Bottom:* First derivative of the smoothed pressure signal with indicated moment of passing melt front (red vertical line).

a moving average filter¹⁷ with a span of 250 samples. The smoothed signal is shown as a black line in Fig. 4.24 *Middle*.

The change in a signal can be estimated at best when calculating its first derivative. The derivative is calculated using a matrix $\dot{\mathbf{S}}$, a global matrix operator which implements the computation of local differentials¹⁸ [134,138]. The first derivative of the pressure signal is calculated by,

$$\dot{\mathbf{p}} = \dot{\mathbf{S}}\mathbf{p}. \quad (4.3)$$

The first derivative of the pressure is shown in Fig. 4.24 *Bottom*, indicating a first signal change at around 0.047 s. To automate the detection a detection level at 0.02 bar s^{-1} was set. The moment of pressure increase is consequently detected at 0.05 s. For the shown measurement a difference time between

¹⁷The command `smooth(y, span)` in MATLAB was used.

¹⁸The same matrix \mathbf{S} was already used for polynomial windowing, although now its first derivative is used; see Eq. 3.93.

the moment of pin impact and pressure increase of -0.3417 ms is measured. The negative sign indicates that the acoustic actuator impact sound had occurred before the pressure signal increased, which is in accordance to the explanations given before.

This kind of delay time evaluation was performed at four different injection speeds. The results are shown in terms of mean value \bar{t}_i , with i the number of total measurement runs, as well as the standard deviation σ in Tab. 4.4. As it can be seen, with increasing injection rate the acoustic actuator detects the melt front earlier than the pressure transducer. Only for the very low injection rate of $15 \text{ cm}^3\text{s}^{-1}$ a larger delay time of the acoustic-emission sensor is present. It is assumed that this delay time results from too low pressure propagation as a result of the low injection rate and consequently low energy level within the melt to accelerate the pin instantaneously. However, the absolute delay time of around 6 ms is still in comparable range in terms of response times for in-mold sensors.

Table 4.4: Injection rate dependent delay time between movable pin impact sound and pressure signal increase. A positive sign indicates pressure increase before movable pin impact sound.

| Injection rate in cm^3s^{-1} | Mean value in ms | Standard deviation in ms |
|--|----------------------|--------------------------|
| 15 | $\bar{t}_8 = 6.27$ | 0.97 |
| 30 | $\bar{t}_8 = 0.19$ | 1.07 |
| 60 | $\bar{t}_8 = -0.397$ | 0.12 |
| 120 | $\bar{t}_4 = -1.53$ | 0.79 |

The obtained pressure results using the different injection rates are plugged into the differential equation Eq. 3.24. The pressure p_6 was obtained via the injection rate of $15 \text{ cm}^3\text{s}^{-1}$, p_7 was obtained via injection rate of $30 \text{ cm}^3\text{s}^{-1}$, p_5 was the already used one at injection rate $60 \text{ cm}^3\text{s}^{-1}$ and finally p_8 obtained via injection rate of $120 \text{ cm}^3\text{s}^{-1}$. In Fig. 4.25 the pressure levels are shown in a short time window of 10 ms. The pressure levels start from approximately 9 bar and with increasing injection rate the pressure gradient becomes steeper.

When plugging these four pressure levels, p_5 to p_8 , into the Eq. 3.24 the results shown in Fig. 4.26 are obtained. Surprisingly, the pin movement seems to be nearly unaffected¹⁹ from the present pressure, respectively from the used injection rate. However, when having a look at the time scale where pin movement happens (below 2 ms) all the pressure levels are nearly identical

¹⁹The maximum difference is below 0.1 ms which is neglectable in terms of sensor response time characteristic.

(confer Fig. 4.25). Consequently, the calculation can only deliver the results obtained. Possible reasons why the pressure levels do not vary in this short time scale are already stated before.

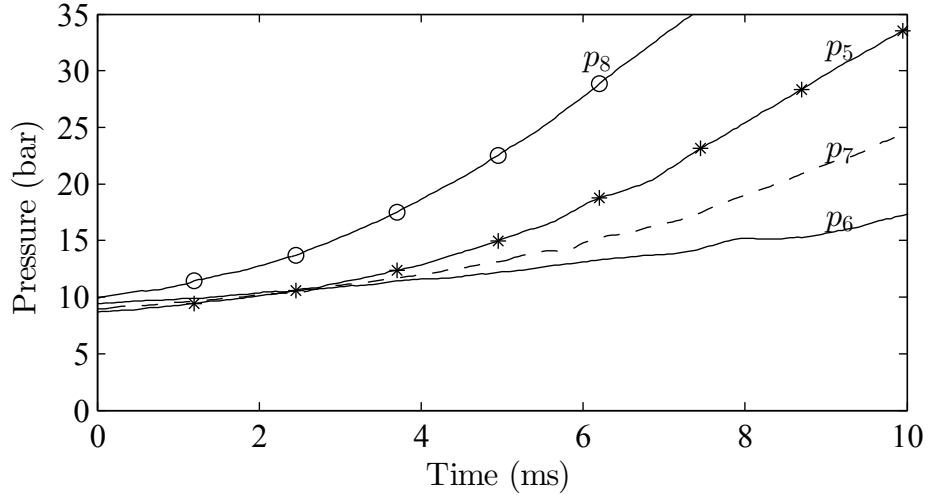


Figure 4.25: Cavity pressure p_i recorded with four different injection rates plotted as a function of time. Pressure level p_6 was obtained with injection rate of $15 \text{ cm}^3\text{s}^{-1}$, p_7 was obtained with injection rate of $30 \text{ cm}^3\text{s}^{-1}$, p_5 is the measurement already shown with injection rate $60 \text{ cm}^3\text{s}^{-1}$ and p_8 was obtained with an injection rate of $120 \text{ cm}^3\text{s}^{-1}$. The pressure levels are shown with the measured offset level of approximately 9 bar.

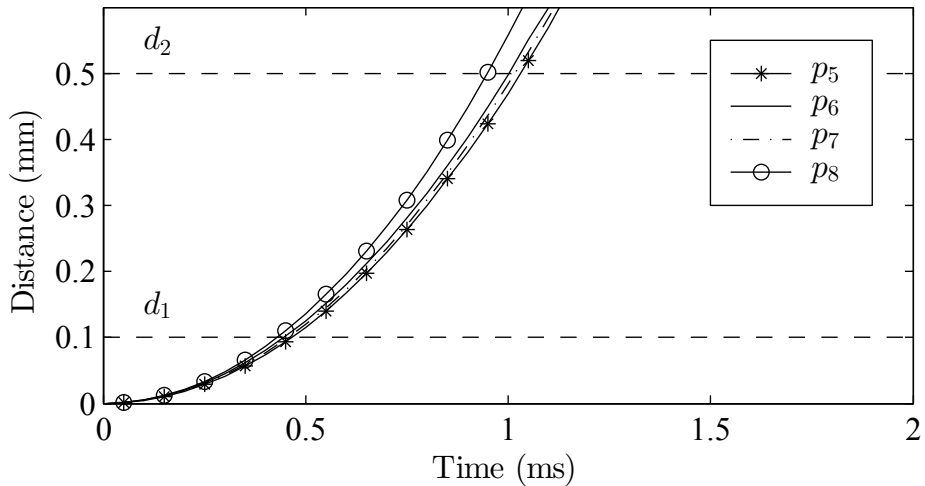


Figure 4.26: Pin movement as a function of time with the pressure levels p_5 to p_8 at an offset level of approximately 9 bar.

Since it is unclear if the obtained offset pressure level of 9 bar is really present in the cavity or it results from a misfeature of the measuring chain, the measurement pressure values are referenced to 1 bar at the beginning of the measurement window. Another four pressure levels are introduced which are the pressure trends p_5 to p_8 but referenced to 1 bar. Pressure level p_9 was obtained with injection rate of $15 \text{ cm}^3\text{s}^{-1}$, p_{10} was obtained with injection rate of $30 \text{ cm}^3\text{s}^{-1}$, p_{11} results from an injection rate of $60 \text{ cm}^3\text{s}^{-1}$ and p_{12} was obtained with an injection rate of $120 \text{ cm}^3\text{s}^{-1}$. In Fig. 4.27 the time-dependent pressures p_9 to p_{12} are shown which are then plugged into Eq. 3.24. The time-dependent pin movement for the pressure offset value of 1 bar is shown in Fig. 4.28. From the first observation it can be seen that the time needed to overcome d_1 and d_2 are approximately doubled to the results with the offset pressure level of 9 bar. For the lowest injection rate, resulting in p_9 , the distance d_2 is reached in only slightly above 2 ms. The maximum delta time between the highest pressure p_{12} and the lowest pressure p_9 for the distance d_2 is below 0.4 ms. This value is again very good for response time characteristic of an in-mold sensor for injection molding.

To sum up the pressure influence investigation on the response time characteristic of the acoustic-emission sensor: from the obtained results it can be safely stated that a large pressure variation has an influence on the pin movement time which, however, is neglectable for in-mold sensors. Hence, the sensor can be used with typically used thermoplastic polymers without having a significant impact on the response time characteristic of the sensor as long as the injection rate is not too low²⁰.

4.3.2 Spring Influence Investigation

Another performance influencing factor is the used spring and its spring rate. Two different springs with spring rates $k_1 = 1.179 \text{ N/mm}$ and $k_2 = 1.013 \text{ N/mm}$ are used²¹. Since the dimensions of the springs are quite small and a certain level of resistance against cavity pressure is needed just few springs are qualified for implementation which are all in similar spring rate region. In Fig. 4.29 pin movement as a function of time and spring rate is plotted. As it can be seen, the two lines are lying nearly on each other indicating low influence of the used springs. For the calculations the measured pressure p_5 was used obtained with injection rate $60 \text{ cm}^3\text{s}^{-1}$.

²⁰For the used test mold the value was found out not to be below $30 \text{ cm}^3\text{s}^{-1}$.

²¹The values are provided from the manufacturer of the springs, Gutekunst + Co.KG Federnfabriken.

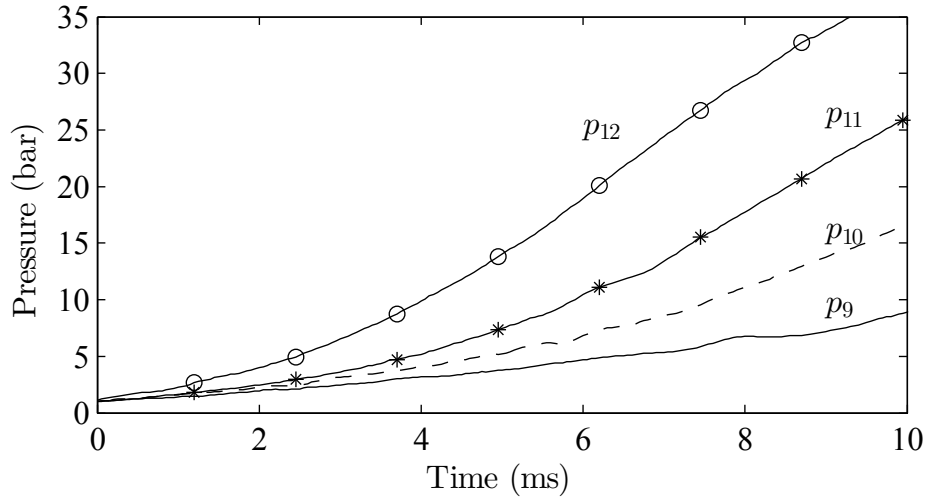


Figure 4.27: Cavity pressure p_i recorded with four different injection rates plotted as function of time. Pressure level p_9 was obtained with injection rate of $15 \text{ cm}^3\text{s}^{-1}$, p_{10} was obtained with injection rate of $30 \text{ cm}^3\text{s}^{-1}$, p_{11} results from an injection rate of $60 \text{ cm}^3\text{s}^{-1}$ and p_{12} was obtained with an injection rate of $120 \text{ cm}^3\text{s}^{-1}$. All the measured pressure levels are referenced to 1 bar at the beginning of the measurement time.

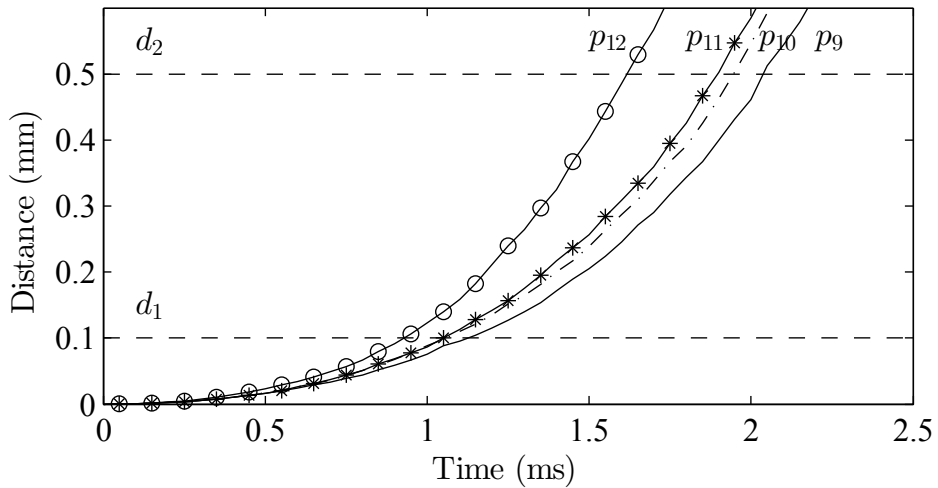


Figure 4.28: Pin movement as function of time with the pressure levels p_9 to p_{12} at an offset level of 1 bar. Pressure level p_9 was obtained with injection rate of $15 \text{ cm}^3\text{s}^{-1}$, p_{10} was obtained with injection rate of $30 \text{ cm}^3\text{s}^{-1}$, p_{11} results from an injection rate of $60 \text{ cm}^3\text{s}^{-1}$ and p_{12} was obtained with an injection rate of $120 \text{ cm}^3\text{s}^{-1}$. All the measured pressure levels are referenced to 1 bar at the beginning of the measurement time.

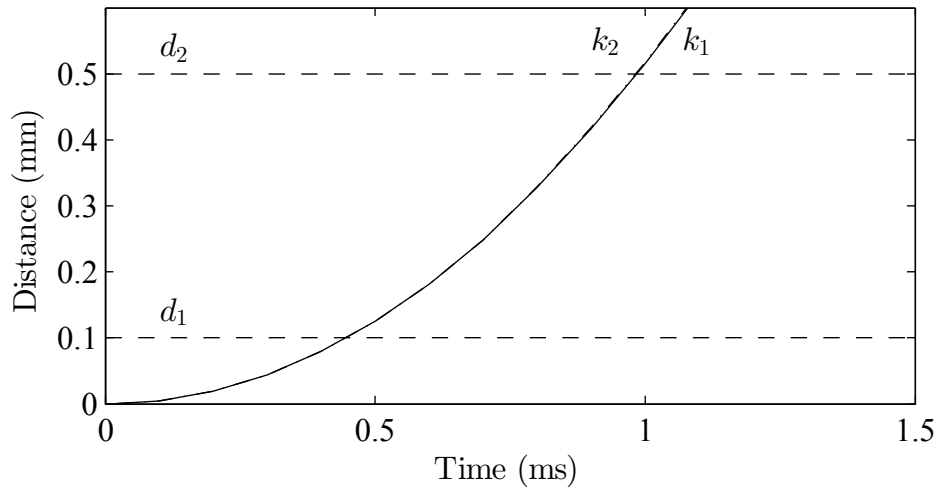


Figure 4.29: Time-dependent pin movement for two different spring types (solid line $k_1 = 1.179 \text{ N/mm}$ and dashed line $k_2 = 1.013 \text{ N/mm}$) with pressure recorded at an injection rate of $60 \text{ cm}^3\text{s}^{-1}$ acting on the pin.

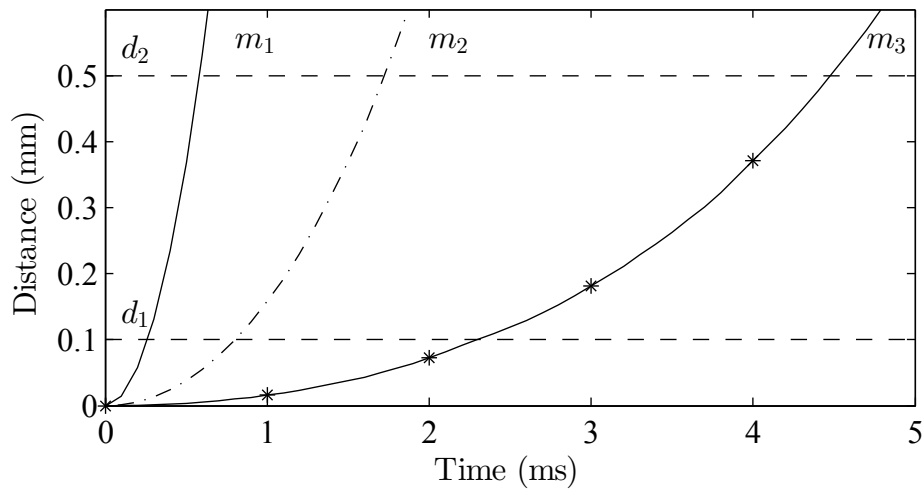


Figure 4.30: Time-dependent pin movement for three differently assumed masses ($m_1 < m_2 < m_3$). The used pressure was recorded at an injection rate of $60 \text{ cm}^3\text{s}^{-1}$.

4.3.3 Pin Mass Investigation

Finally, the influence of the pin mass was investigated. This parameter is of special interest with regard to use ejector pins as the movable pin to excite the

resonant structure²². The currently used pin has a mass of $m = 3 \cdot 10^{-3}$ kg. However, this mass is very low and it was shown that around 0.5 to 2 ms are needed to pass the distances d_1 and d_2 . To investigate the influence of mass three different masses of various orders of magnitude are incorporated in Eq. 3.24, i.e. $m_1 = 10^{-3}$ kg, $m_2 = 10^{-2}$ kg and $m_3 = 10^{-1}$ kg. In Fig. 4.30 the results are shown. As it can be seen, with increasing pin mass the time to overcome the distance d_i is overproportionally increasing. For the highest pin mass m_3 , 4.5 ms are needed to reach distance d_2 . However, the response time values are still in comparable range with those of commonly used cavity wall temperature sensors with a bigger sensor head diameter.

Pin mass has the highest influence of all the investigated parameters and with respect to designing ejector pins with the ability to excite the resonant structure, mass reduction should be considered during the construction phase of the acoustic actuator since a typical ejector pin with a diameter of 6 mm has weight of about 50 to $200 \cdot 10^{-3}$ kg.

4.3.4 Pin Movement Simulation

For additional verification of the pin movement simulations were performed using Abaqus from Dassault Systemes, United States. For the simulations the resonant structure was imported as a full computer-aided design (CAD) geometry whereas the pin was simplified by using a rigid rod having the exact mass of the real pin, i.e. $3 \cdot 10^{-3}$ kg. In the simulation the spring as well as the pressure (obtained via measurements shown in Fig. 4.19) were considered. In Fig. 4.31 pin movement (*Top*) and pin velocity (*Bottom*) are shown as a function of time. From the obtained results it can be observed that the pin impacts on the resonant structure surface and bounces off several times. However, the bouncing is damped since the pressure level increases exponentially and pushing the pin against the resonator surface. The bouncing is a result of converting the pin velocity, which is kinetic energy, into potential energy during impact. The potential energy is stored in form of elastic deformation in the structure material. When the maximum potential energy is reached the process is reverted and the pin lifts off the structure surface as a result of back deformation of the structure. The first impact happens at 1.3 ms which is in good accordance to the results obtained by the governing equation Eq. 3.7. At the first impact the velocity is nearly as high as 0.7 m/s, which can also be calculated via Eq. 3.25.

²²See also Chapter 2.4, starting on page 38.

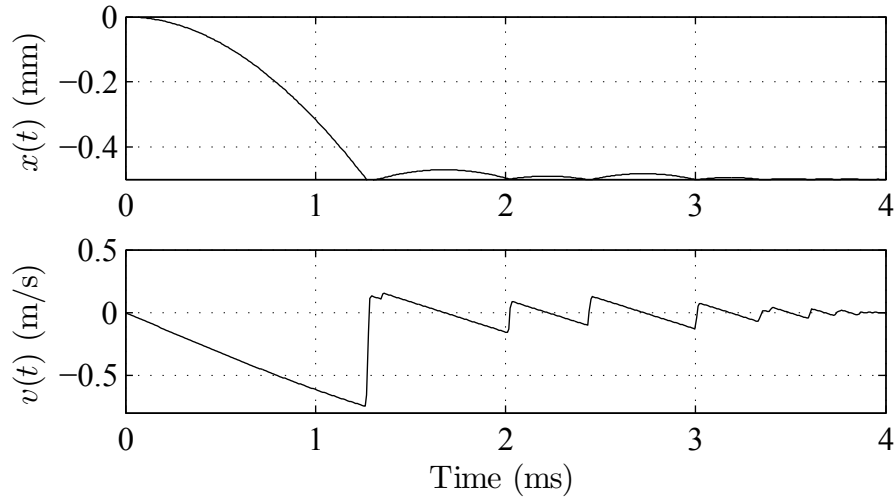


Figure 4.31: *Top:* Pin movement as a function of time simulated by Abaqus from Dassault Systemes. Due to the elastic impact of the pin on the resonant structure the pin bounces off the structure several times; *Bottom:* Simulated velocity of the pin during movement. At first impact the pin has a velocity of nearly 0.7 m/s.

To sum up, the mass of the movable pin is the most critical parameter and should be as low as possible for fast pin movement and consequently for maximum sensor performance in terms of melt front recognition. This is of special interest when using ejector pins as the acoustic actuator since their mass is in general higher than the used movable pin.

Furthermore, it was found that both used springs led to nearly identical sensor performance and had no impact on the gained results. The pressure acting on the pin surface has an influence on the sensor response characteristic. However, the obtained results indicate just low variation in the time-dependent pin movement. For the larger distance d_2 the maximum variation was below 1.5 ms which is very good for in-mold sensors. This enables the usage of the sensor in a wide range of thermoplastic polymers.

4.4 Resonator Frequency Response Analysis

For good sensor performance in terms of separation of multiple implemented actuators different resonant structures with different frequency responses have to be designed. The acoustic actuator housing enables the implementation of u-shaped resonators (see Fig. 2.1, on page 32). The target is to

design them, that each resonant structure oscillates with different frequency components after excitation. During the design process, CAD software supports constructing the resonator designs as well as calculating the modal-frequencies of the structure. Consequently, the effect of a design change can be seen quickly. However, verification measurements were performed, to evaluate the simulated results.

4.4.1 Resonant Structure Design

For separation of multiple implemented acoustic actuators, different resonant structures were designed. Two types of resonant structures were implemented in the actuator housing, plate resonators and tongue resonators. The plate resonator consists of a simple rectangular shaped plate and two perpendicular legs for mounting the structure in the acoustic actuator housing. The plate resonator is not shown but is similar to the tongue resonator presented in Fig. 4.32, solely without the cutouts for the tongue. The shape of the plate is indicated by a black rectangular. The dimensions (labeled A to F) of the plate and tongue resonator are listed in Tab. 4.5. The tongue resonator is a diversification of the plate resonator whereby the tongue is created by a cutout of the plate. A mass is left at the end of the tongue to reduce the oscillation frequency. In Fig. 4.32 the impact area of the pin, which excites the structure, is marked by a green circle. The center of the impact circle is the intersection point of the diagonals of the plate resonator.

Table 4.5: Dimensions A to F of the 3.8 kHz, the 8 kHz and the 12 kHz resonator shown in Fig. 4.32. All units are in millimeters.

| | 3.8 kHz tongue resonator | 8 kHz plate resonator | 12 kHz plate resonator |
|---|-----------------------------|--------------------------|---------------------------|
| A | 3 | 2.4 | 3 |
| B | 33 | 33 | 33 |
| C | 28 | 28 | 28 |
| D | 11 | - | - |
| E | 3.5 | - | - |
| F | 5 | - | - |

In total three resonant structures were designed, all labeled after their primary modal frequency. Two of them are plate resonators varying in the thickness of the plate, the 8 kHz plate resonator with $A = 2.4$ mm and the 12 kHz plate resonator with $A = 3$ mm. The tongue resonator has a thickness of $A = 3$ mm, too, and has its first modal frequency at 3.8 kHz.

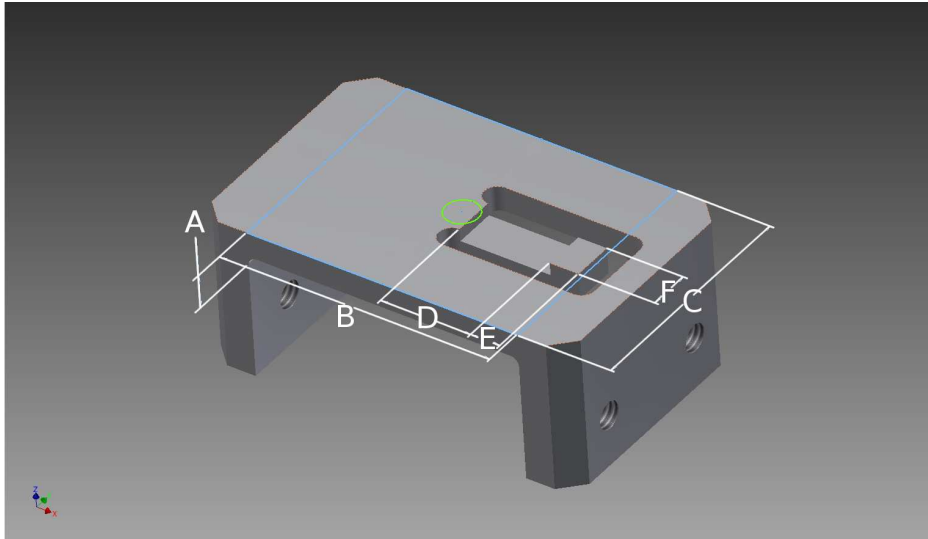


Figure 4.32: 3D-model of tongue resonator with labeled important dimensions (from *A-F*). The black rectangular indicates the plate resonator shape, which is a metal full body. The green circle shows the area where the movable pin impacts.

For additional analysis the plate resonator eigen-frequencies were calculated for variable plate thicknesses. The reason for varying the plate thickness can be found in Eq. 3.37, on page 55, where it is stated, that the thickness of the plate has a significant influence on the oscillation and is one of the parameters that can easily be changed without modifying the housing. The plate thickness was varied from 1.0 mm (which might have not enough stiffness for long-term application and will suffer from fatigue failure) up to 3.0 mm in 0.5 mm steps. The modal frequencies for those plates were calculated using Autodesk Inventor Professional 2011, Autodesk, United States. The results for the first six modal frequencies are shown in Fig. 4.33. It can be seen that with increasing plate thickness the modal frequencies are shifted to higher values. This shifting leads to overlapping frequencies though. For instance, having a 1 mm and a 3 mm resonator, both will have frequency components at about 12 kHz. Consequently, this combination would not be optimal for frequency separation.

In conclusion it will be hard to find resonator combinations that have fully separated resonance frequencies. Hence, the detection algorithm will have to deal with this situation that there are mutual frequency components and still separate them reliable.

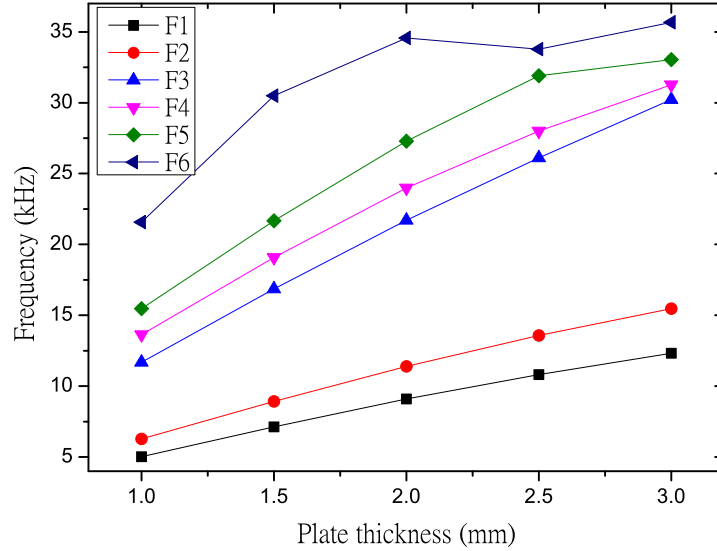


Figure 4.33: Dependence of modal frequencies F1 to F6 of the plate thickness for a plate resonator with dimensions listed in Tab. 4.5 calculated using Autodesk Inventor Professional 2011.

4.4.2 Acoustic Spectrum Analysis

Recording structure-borne sound from an injection mold will result in large levels of noise. By applying a short-time Fourier transform (STFT) on the recorded signal time-dependent frequency components can be made visible. In the following measurement two resonant structures were implemented in the mold, one 3.8 kHz resonator as well as the 12 kHz resonator, each in one of the cavities. In Fig. 4.34 a full measurement with injection rate of $60 \text{ cm}^3\text{s}^{-1}$ in time domain without any data manipulation is shown. Since the measurement start is triggered by hand, data before start of the injection molding cycle is available. This data is shaded with a gray patch. At start of the injection molding cycle both hot runner valves open which results in a large signal deflection. For these measurements a delay time of 0.13 s for the valve opening was set up to ensure nearly balanced filling of both cavities²³ (see Doppelmayer [41]). The green lines limit an area in which statistically significant portions of the signal are searched. The area can be defined by the knowledge of the part volume V and the injection rate \dot{V} which leads to

²³A minor delay for the first valve opening sound can be seen in Fig. 4.34. This delay results from the time needed for the valve to open.

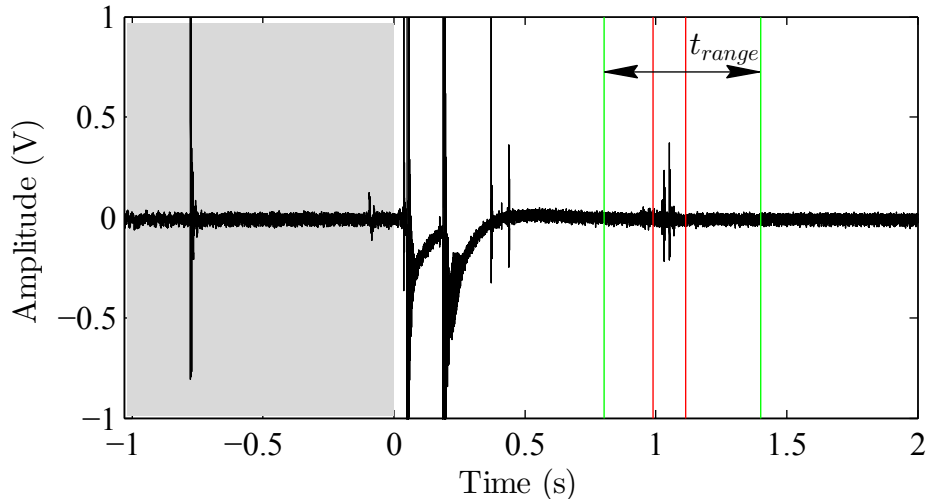


Figure 4.34: Full unmodified measurement in time domain with two implemented acoustic actuators. The gray shaded area indicates the time before injection cycle starts. For this measurement two acoustic resonators were implemented in the mold leading to the two deflections at 1.0s. Green lines limit the area for searching statistically significant portions on which (red lines) the frequency transform in terms of a STFT is performed.

a filling time $t_f = V/\dot{V} \pm t_{range}$ with a search range t_{range} . The identified statistically significant area is indicated by red lines in which the frequency transform in terms of a STFT is performed.

In Fig. 4.35 the magnitude spectrum with the two implemented resonators is shown. The signal was sampled with $f_s = 120$ kHz and for the STFT a window length of $l = 600$ samples was set up. Each run the window was shifted by $p = 50$ samples. Consequently, a resolution of 200 Hz is reached in the range of 0 to 60 kHz. A new value is calculated every $t_r = 0.42$ ms. A blue colored value indicates a small magnitude of a frequency component whereby a red colored value indicates a large magnitude. As it can be seen, most of the time there are just a few frequency components that have a significant magnitude. Especially in the moments of impact dominant frequency components are present. In the spectrum one frequency component at 7.8 kHz is identified as being continuously present over the whole measurement time. Furthermore, it is seen that primarily below around 22 kHz small frequency components appear at various times but in a continuous manner. It is assumed that these frequency components are the resonant frequencies of the mold respectively of assemblies of the mold excited by noise. To verify this

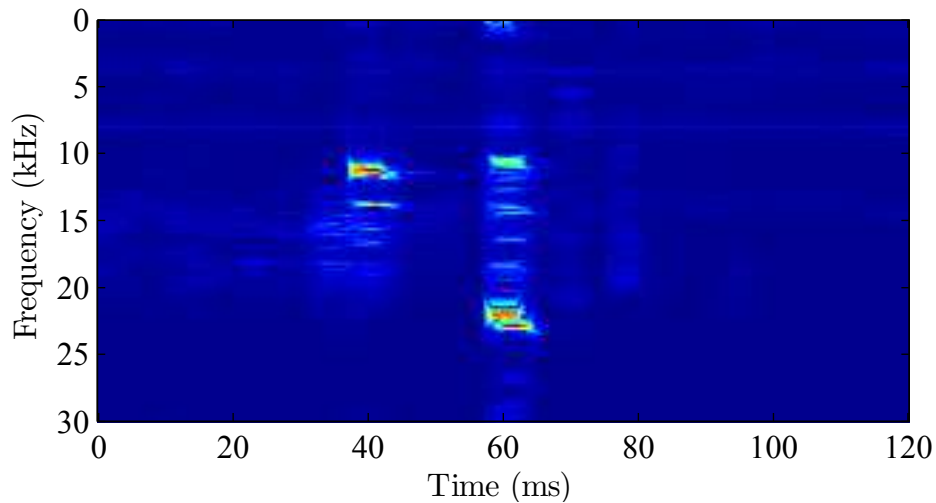


Figure 4.35: Magnitude spectrum as function of time from a measurement with two implemented resonant structures, the 3.8 kHz tongue resonator and the 12 kHz plate resonator. A blue color indicates a low presence of a frequency component and a red color a high presence of a frequency component.

assumption an electro-dynamical exciter (EX 60 S 8 OHM, Visaton, Germany) was mounted on one outside surface of the mold. With this device the mold was excited with white Gaussian noise. By using an accelerometer the response of the mold was measured.

In Fig. 4.36 the response magnitude spectrum of the mold is shown while being excited with white Gaussian noise. Since the excitation is quasi-stationary a magnitude spectrum of the Fourier transform (FT) of the measurement is shown. The used exciter is limited to the acoustic range which will lead to distorted results above approximately 20 kHz. However, it can be seen that the response is more distinctive on some frequencies, i.e. 7.3, 9.9, 13.0, 14.1, 16.0, 18.4 and 21.8 kHz. Comparing them to the spectrum shown in Fig. 4.35, some of the frequency components can be identified matching or matching at slightly shifted frequencies. Since white Gaussian noise is statistical noise spread over all frequency components (with bandwidth limitation of the exciter) the chance is high to excite all possible assemblies which might not be excited in the conventional injection molding process where not all frequency components are present.

Additional measurements were performed where each resonant structure was investigated separately from the mold to obtain their impulse response respectively the frequency response. This knowledge is important for the signal

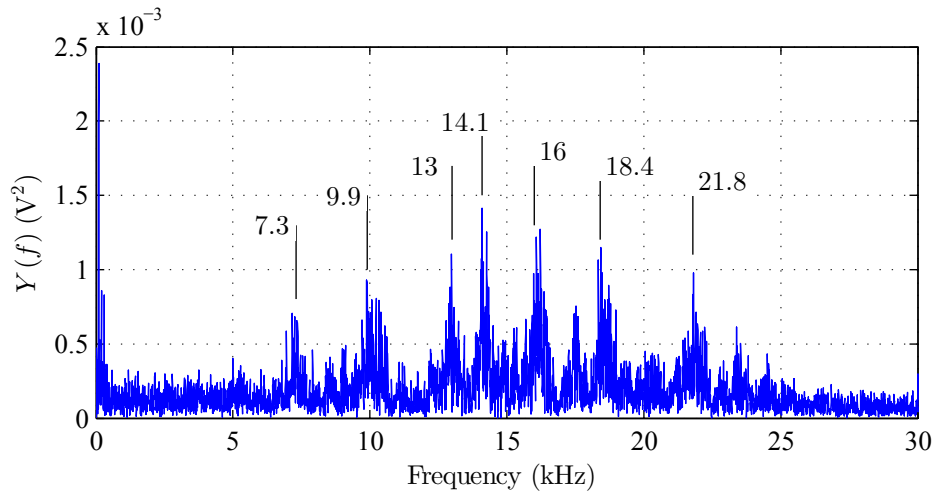


Figure 4.36: Frequency response of the mold which is excited by white Gaussian noise using an electro-dynamical exciter in the acoustic range.

processing part where the characteristic oscillation of each resonator is used for separation. Thereby a special focus was put on the way the resonant structure is excited. In Fig. 4.31 *Top*, page 137, the pin movement during acting pressure was already shown. Due to the impact the pin bounces away from the structure surface several times. Each time the pin impacts again the free oscillation of the plate is influenced until finally the pin is pushed against the structure with cavity pressure, leading to high damping behavior. Hence, it was desired to excite the structures as it gets excited during experimental conditions within the mold. Furthermore, it is necessary to emulate the high damping behavior resulting from the increasing melt pressure level.

A pneumatically moved piston was used for structure excitation enabling the best imitation of the real activation process, especially with a focus on the damping behavior. The oscillations were detected by an accelerometer mounted on the housing frame where the resonant structure is installed. The measured frequencies were compared to the calculated modal frequencies from Autodesk Inventor Professional 2011.

Starting with the 3.8 kHz resonant structure the time-dependent magnitude spectrum while being excited by a pneumatic piston is shown in Fig. 4.37. Since this resonant structure is a tongue resonator two different time-dependent frequency behaviors are expected: the highly damped components with short vibration duration from the plate structure and naturally damped components with long vibration duration, resulting from

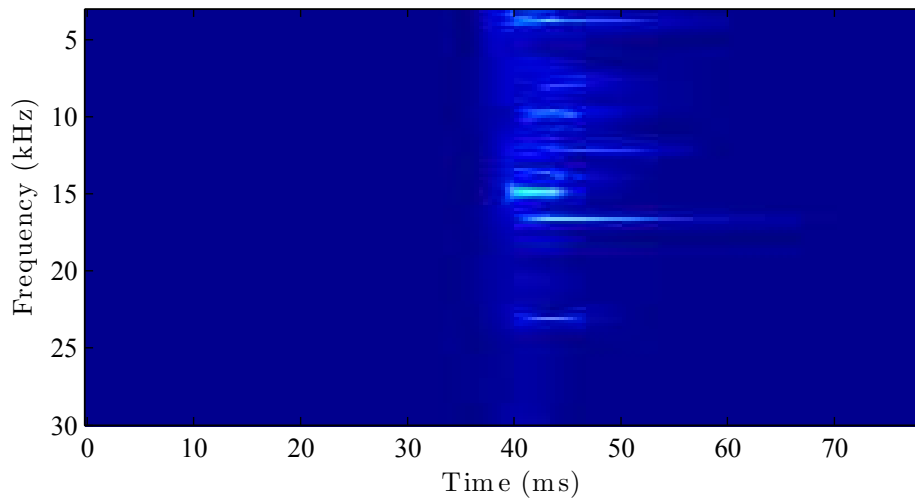


Figure 4.37: Time-dependent magnitude spectrum of the 3.8 kHz resonant structure excited by a pneumatic piston. A blue color indicates a low presence of a frequency component and a red color a high presence of a frequency component.

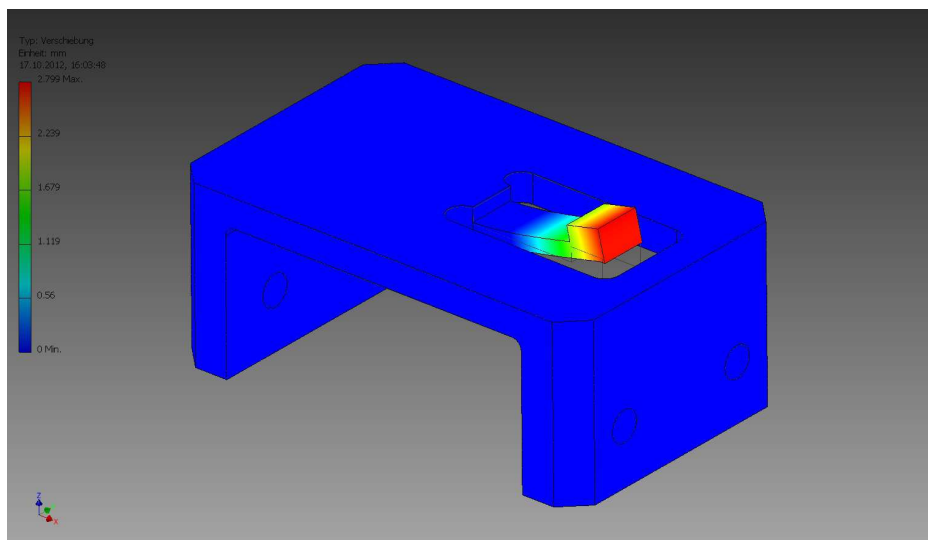


Figure 4.38: Modal frequency analysis in Autodesk Inventor Professional 2011. The displacement of the 3.8 kHz modal frequency is shown.

the free vibrating tongue. In Tab. 4.6 a comparison of the simulated modal frequencies (up to 25 kHz) and measured frequency components of the real resonant structure is given. It has to be mentioned that in the modal fre-

quency simulation just the resonant structure without its frame or additional housing elements like spring, pin, etcetera was simulated whereas they were necessary during the real measurements. Consequently some differences may occurred.

Table 4.6: Comparison of frequency components simulated by the software package Autodesk Inventor Professional 2011 and real measurements for the 3.8 kHz resonant structure.

| | Measurement | Simulation |
|--------------------------------|-------------------------------------|---|
| Frequency components in kHz | 3.8, 9.6, 12.2, 14.8, 16.6, 22.6 | 3.8 ²⁴ , 11.0, 11.3, 14.4, 22.3 |

The first appearing frequency is 3.8 kHz which is present in both, the measurement and the simulation. From the duration of this frequency component (it is present for at least 20 ms) it can be assumed that the tongue vibrates with this frequency since it is not damped by the pushing piston. The simulation supports this assumption. In Fig. 4.38 the simulated displacement for 3.8 kHz component is shown whereby just the tongue is displaced. For all the other frequency components measured and simulated the match is not as exactly as for the primary frequency but still a link can be found.

In Fig. 4.39 the magnitude spectrum of the 12 kHz resonant structure can be seen. The resonant structure is designed as a plate resonator. The measurement procedure was the same as for the 3.8 kHz using the pneumatic position for excitation. In Tab. 4.7 simulated modal frequencies are compared to those of the measurement. A matching frequency opponent is found for some of the listed, especially for both simulated modal frequencies the matching frequency opponent is present in the measurement.

Table 4.7: Comparison of frequency components simulated by the software package Autodesk Inventor Professional 2011 and real measurements for the 12 kHz resonant structure.

| | Measurement | Simulation |
|--------------------------------|---------------------------------|---------------------------|
| Frequency components in kHz | 12.2, 13.6, 15.4, 17.0, 21.0 | 12.0 ²⁴ , 15.2 |

One more component of the acoustic actuator was investigated using the software package: the movable pin. With its small dimensions it is hard to mount any sensor on it to obtain experimental results. In addition, the

²⁴Eponymous modal frequency.

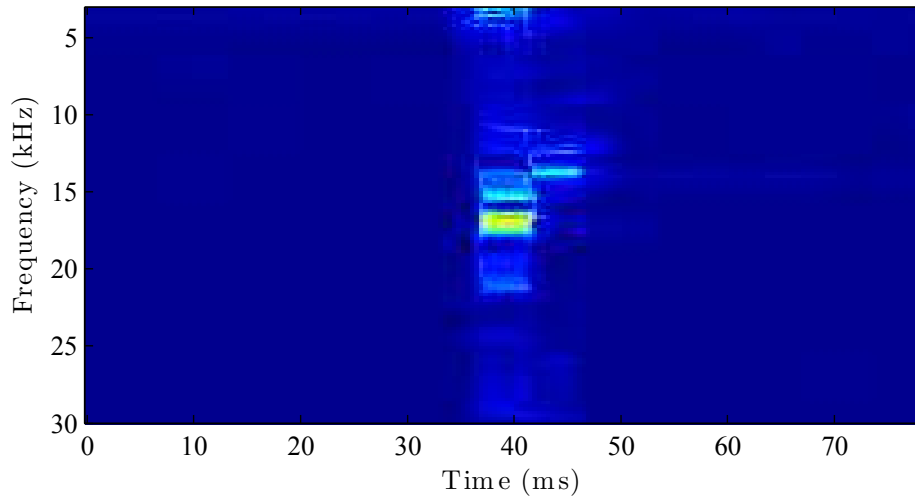


Figure 4.39: Time-dependent magnitude spectrum of the 12 kHz resonant structure excited by a pneumatic piston. A blue color indicates a low presence of a frequency component and a red color a high presence of a frequency component.

mass of the accelerometer would influence the results significantly, since it is clearly greater than the mass of the movable pin. Using the software package nearly no dimensional limitations are given to investigate frequency components. Furthermore, it is possible to set boundary conditions, i.e. the axial guideline of the movable pin, in the direction of which no vibration can arise. It was calculated that the modal frequencies of the movable pin are 10.7 kHz and 22.4 kHz.

To summaries this chapter, many different frequency components appear during a measurement in the mold. Due to the complex structure of an injection mold it is hard to localize the origin of all the components. By analyzing the resonator components as well as the complete mold towards their frequency response, some frequency components' origin was found. This knowledge was used for designing filters for the peak event detection, shown in Chapter. 4.5.2.

4.5 Signal Processing

In Chapter 4.2, on page 106, it was shown that with using an acoustic actuator it is possible to generate distinctive additional structure-borne sound triggered by a passing melt front. In the next three sections results for three different signal processing methods for the automatic detection of the activa-

tion of an acoustic actuator are shown. The three methods differ regarding the gained information and consequently calculation effort. First the envelope method is described which is used at best when just one acoustic actuator is implemented and only little calculation power is available, like on a PLC. The filter bank method as well as the frequency pattern recognition method yield the possibility of separating multiple occurring peaks whereby the frequencies emitted by the resonant bodies are analyzed. Calculation effort is increased in comparison to the envelope method.

4.5.1 Signal Envelope Detection Method

For the measurements with the envelope method a PLC (X20 System - X20CP1486 CPU) from Bernecker + Rainer Industrie-Elektronik, was used. With the module AI4636 in oversampling mode a maximum frequency sampling rate of $f_s = 25$ kHz was achieved. The accelerometer used for the structure-borne sound recording was a transducer (J353B01) from PCB Piezoelectronics Inc, United States, with a sensitivity of 20.88 mV/g. The sensor has a frequency range (± 3 dB) for 0.35 to 18000 Hz [145] but the frequency sampling rate f_s limits the detection to frequencies up to 12.5 kHz. Frequency detection, however, is not performed with this detection method and consequently the data sampling rate is fast enough. The accelerometer was glued to the outside surface of the mold ensuring a good contact.

For the envelope measurements a PP (C7069), was used. In Fig. 4.40 a full measurement is shown. The figure shows the voltage of the envelope over time. At the start a large excitation up to 9.5 V is seen which comes from the nozzle opening event. To switch the position of the nozzles a short electric impulse is sent through the implemented magnets and due to the requirement of high movement forces (up to 1000 N) an intense impact at the end of the movement occurs. The decay from this high level is defined by the constant τ (see Algorithm 3.1, on page 63) which is set to 0.001 for the shown measurements.

At the time 0.4 s the next bigger excitation is detected. This signal occurs in many measurements but the source is unknown. Since the temporal point of occurrence is dependent on the injection velocity, the origin of the sound is probably an ejector pin which is not clamped tightly enough, generating a sound due to the pin movement and following impact during the filling phase. However, this signal does not influence the measurements in any way since it is not appearing in the expected time window which can be calculated from the filling time t_f until melt front reaches the position of acoustic actuator, $t_f = \dot{V}/V$, with \dot{V} the injection rate and V the filling volume up to the position of the acoustic actuator. Hence, the sound can be noticed as noise.

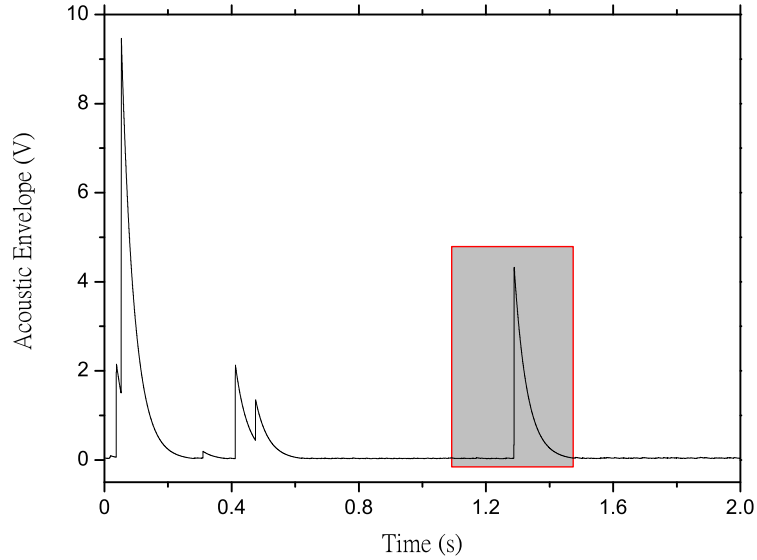


Figure 4.40: Envelope of acoustic signal calculated by Algorithm 3.1, shown on page 63. The peak of interest at 1.3s was generated by the acoustic actuator and is shown in detail in Fig. 4.41.

The temporal point where the signal processing for the automatic detection of the signal from the acoustic actuator starts is set²⁵ to 0.9s, which was calculated from the filling time t_f .

The next deflection of the envelope is seen at 1.3s. At this temporal point the detection algorithm is already searching for peaks. Referring to the three criteria of acoustic actuator detection (see Chapter 3.6.1, on page 64) the first one is fulfilled. The peak appears at a time greater than 0.9s. The second criterion, the detection level, is set to 0.15V. If the envelope excites this level for at least 1.6ms the third criterion is fulfilled, too, and the acoustic actuator impact sound is considered as detected. The 1.6ms period of the third criterion originates from the fact that the envelope has to stay above the detection level for 8 cycles of the detection algorithm which runs on the PLC in a 0.2ms task-class.

In Fig. 4.41 a temporal focus is laid on the marked gray box from Fig. 4.40. Additionally, the detection limit line is indicated by a red horizontal line. As it can be seen, the envelope exceeds this detection line shortly before 1.3s

²⁵For an injection rate of $60 \text{ cm}^3\text{s}^{-1}$.

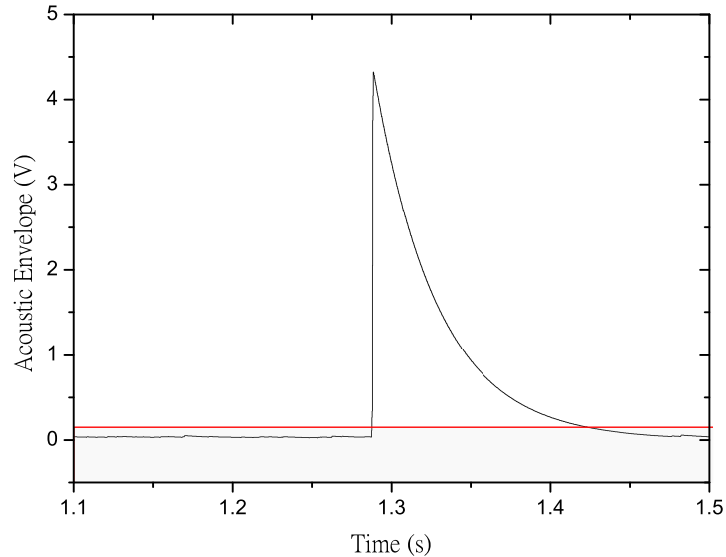


Figure 4.41: Detail of peak detection originating from the sound generated by the acoustic actuator. The red horizontal line indicates the detection threshold which is essential for automatic peak detection.

and stays above the line for at least 100 ms. Hence, this peak is successfully detected by the envelope method.

However, this method yields some disadvantages concerning the automatic detection of the generated sound by the acoustic actuator. In Fig. 4.42 a different measurement is shown, whereby the focus is just laid on the moment of impact. Again, the detection line is indicated by a red horizontal line. As it can be seen, neither the first nor the second peak exceeds the detection line which consequently leads to a non detection of the activated acoustic actuator since the content of the peak is not considered within this signal processing method. This fail detection can be attributed to an adverse defined detection level. However, the reduction of this detection level to smaller values would increase the possibility of fail detection as a result of noise.

The small peak deflection from the fail detected peak originates from a variance in the way the resonant body gets mechanically excited which is general problem of the system. Especially when having a short pin movement distance the chance is high that the pin is not accelerated fast enough to fully excite the resonant structure with full amplitude. One possible reason is

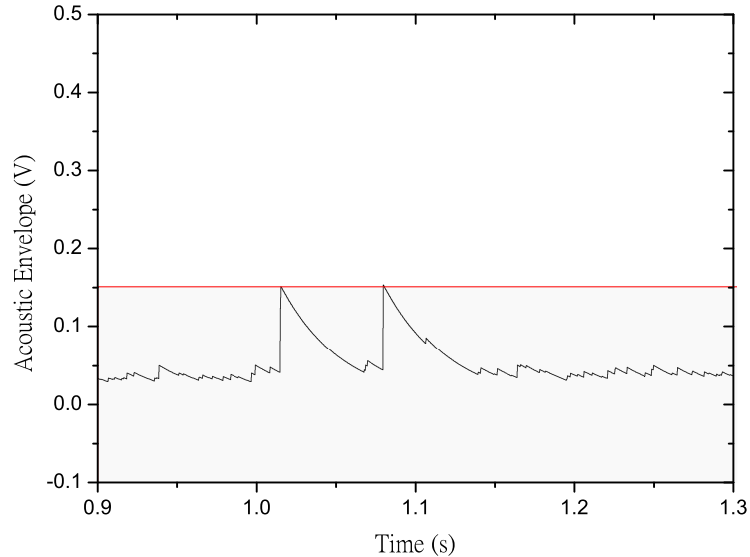


Figure 4.42: Detail of peak detection of another measurement where the deflection has not exceeded the detection line which led to a non-detection of the peak.

tilting of the pin during movement (confer Fig. 4.20, page 124), reducing the amount of available energy on impact. A longer pin movement way is consequently favorable because of having a better signal to noise ratio which enhances peak detection but with the drawback of poorer sensor performance as a result of longer pin movement times.

To summarize, the envelope method is a good way to deal with signals on a system that has limited calculation time. It was shown that the automatic detection is possible for one implemented acoustic actuator. Unfortunately, this method has some limitations. First, the method works best if the mechanical activation of the acoustic actuator is as identical for each run as possible. Since the detection is linked to the amplitude of the envelope a good signal to noise ratio is desired making long pin movement ways favorable.

The method is only applicable for implementation of one acoustic actuator since separation of multiple events is not possible. Assuming that two acoustic actuators are activated coincidentally one of the peaks may disappear within the envelope of the other peak and consequently will not be realized by the detection algorithm.

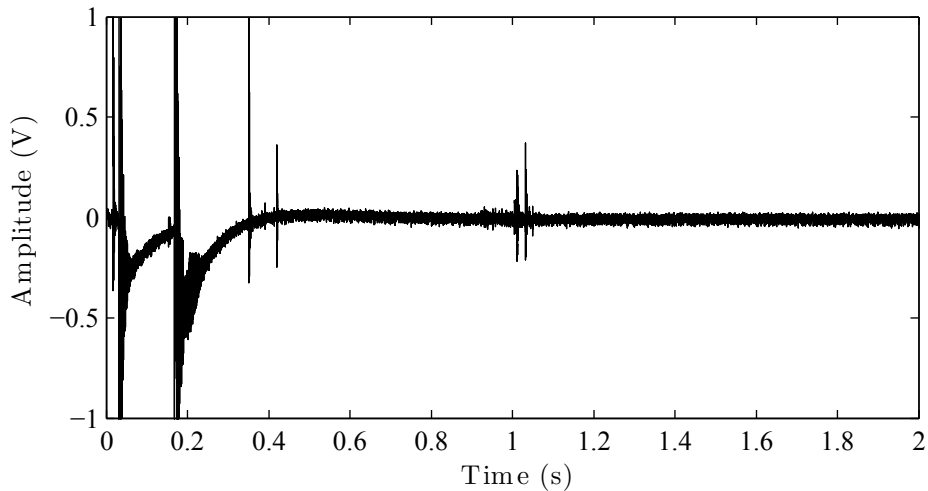


Figure 4.43: Typical measurement result recorded by the accelerometer with two implemented resonant structure types. At the beginning two large noise deflections appear originating from the two valve gate actuators. The melt front passed the movable pins at around 1 s after injection cycle start with an injection rate of $60 \text{ cm}^3\text{s}^{-1}$. The task of the bandpass filters is to separate the two events and assign each deflection to one of the installed structures.

The other presented methods try to overcome these disadvantages by analyzing additional information of the signal, i.e. the frequency components.

4.5.2 Band-Pass Filter Method

On impact, the resonant body starts oscillating with its eigen-frequencies. From Chapter. 4.4, page 137, the frequency response behavior of the used structures is known. This knowledge was used to design band-pass filters for the individual detection of the installed resonators. The presented results were developed in a master thesis by Zhuang [207] at the Montanuniversitaet Leoben using provided measurement data of the acoustic-emission sensor.

In Fig. 4.43 a typical signal recorded by the accelerometer sensor is shown. The sampling rate for the measurement was $f_s = 120 \text{ kHz}$ and the data was sampled with a Data Acquisition System USB-6366 (DAQ). In the test mold two resonant structures were implemented, the 3.8 kHz resonator and the 12 kHz resonator. At the beginning of the measurement a large noise originating from the valve gate actuator opening movement was registered. To achieve a simultaneous filling of both cavities the valves were opened

time delayed as described in the Bachelor thesis of Doppelmayer [41] where the test mold was investigated towards unbalanced filling behavior. This interfering control behavior can be seen in the measurement signal as two delayed peaks at²⁶ 0 and 0.17 s. For the evaluation the peaks have no impact since it is known that both acoustic actuators are placed near the flow path end. The melt reaches both acoustic actuators at around 1 s after start of filling having an injection rate of $\dot{V} = 60 \text{ cm}^3\text{s}^{-1}$. As a result the evaluation of the signal is solely performed around the expected temporal window, i.e. from 0.85 to 1.15 s.

For each resonator a band-pass filter was designed. The filter consists of a lower stop-band, a pass-band, and a higher stop-band. Since no rectangular frequency response shape can be designed, two transition-bands are obligatory. The edge of the lower stop-band is denoted by ν_{sl} , resulting in a stop-band range $0 < \nu < \nu_{sl}$ with an attenuation of δ_s . The first transition-band is in the range $\nu_{sl} < \nu < \nu_{pl}$. The pass-band is in the range of $\nu_{pl} < \nu < \nu_{ph}$ with a pass-band ripple δ_p . The second transition-band is described by the $\nu_{ph} < \nu < \nu_{sh}$ and the second stop-band has the range $\nu_{sh} < \nu < f_s/2$ with an attenuation of δ_s , too. For both pass-band filters the design parameters are listed in Tab. 4.8. For the band-pass filter designed for the 3.8 kHz resonator the frequency response is shown in Fig. 4.44 in the range 0 to 20 kHz. As it can be seen, all frequencies in the stop-band are attenuated by -80 dB and the resulting signal will consist of frequencies between $\nu_{pl} < \nu < \nu_{ph}$ as well as some portions of frequencies within the transition-bands. Both, the stop-band as well as the pass-band show some ripple in the gain which is a result of the filter design process.

Table 4.8: Design parameters for band-pass filter used for the 3.8 kHz and 12 kHz resonator.

| | ν_{sl} | ν_{pl} | ν_{ph} | ν_{sh} | δ_s | δ_p |
|-------------------|------------|------------|------------|------------|------------|------------|
| | kHz | | | | dB | |
| 3.8 kHz resonator | 9.5 | 10.0 | 12.0 | 12.5 | -80 | -24.8 |
| 12 kHz resonator | 20.5 | 21.0 | 23.0 | 23.5 | -80 | -24.8 |

Due to the knowledge, that the peaks of both resonators are expected near the end of the filling phase, the signal was just evaluated in a tight time window. For this case a time period of 0.3 s starting at 0.85 s was evaluated using the designed filters. The portion of the measured signal is shown in Fig. 4.45 in the top diagram. As it can be seen the peaks occur with a

²⁶The first peak is actually slightly shifted since the needle movement takes some time.

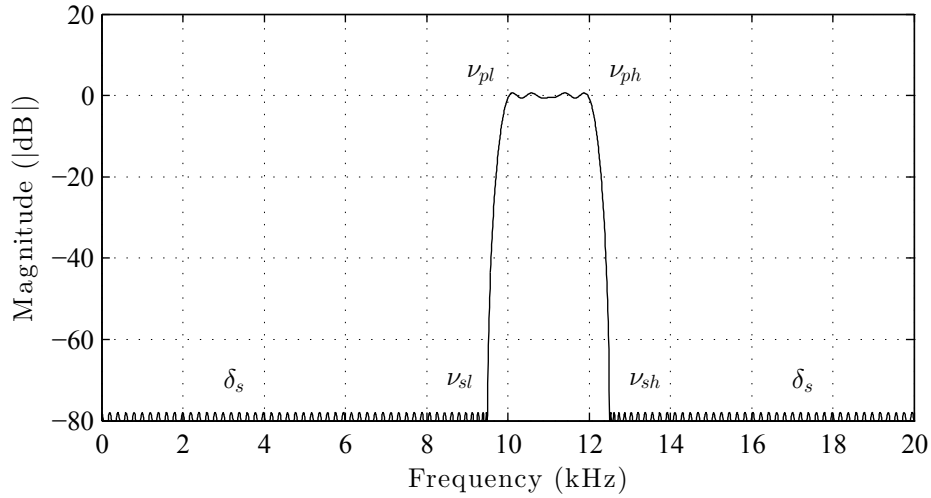


Figure 4.44: Frequency response of the band-pass filter designed for the detection of the 3.8 kHz resonator. The design parameters are listed in Tab. 4.8.

temporal delay to each other. However, just from their optical shape they cannot be separated and consequently cannot be assigned to one resonator type and further be related to a cavity. Fig. 4.45 *Middle* shows the signal after applying the band-pass filters on the signal. Thereby the red line represents the filter dedicated to the 12 kHz resonator and the black line is dedicated to the 3.8 kHz resonator. It can be determined that the filter for the 12 kHz resonator passes frequencies of both occurring peaks. This is a result of the resonator design, both having the same rectangular basic structure with same height. Consequently, both resonators oscillate with the frequencies evoked by the plate design. Hence, it is not possible to differentiate the 12 kHz plate-resonator from the 3.8 kHz tongue-resonator. Though, it is possible to differentiate the 3.8 kHz from the 12 kHz resonator since it has additional eigen-frequencies occurring from the tongue. This can be seen in the filter signal for the 3.8 kHz resonator indicated by the black line. The filtered signal shows a significant portion at the second occurring peak and otherwise consists only of low levels of noise.

For separation of the two peaks a detection logic is formulated. When the filter signal overshoots a critical threshold level a filter storage variable is set to logic 1, otherwise to 0. As soon as the signal drops below the critical level again it is set back to 0. For the detection of the 3.8 kHz resonator both storage variables have to have a logic 1 at the same moment. For the detection of the 12 kHz resonator solely the filter storage variable of the

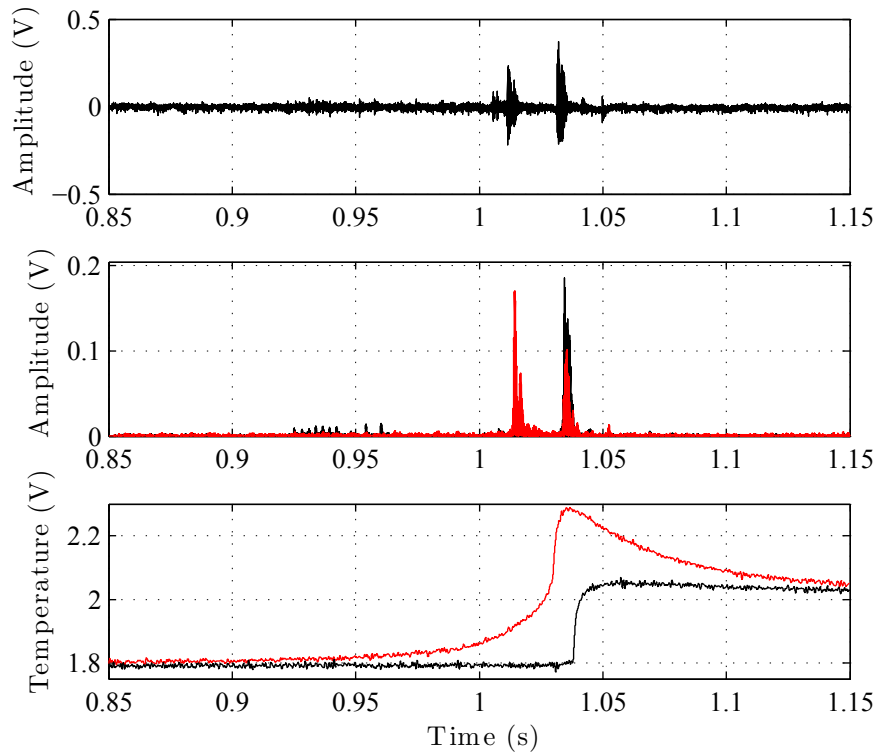


Figure 4.45: *Top:* Accelerometer signal shown in a small time window comprising two peaks from two different resonant structures; *Middle:* Filtered signal for two different band-pass filters. The red filter signal (band-pass at 10 to 12 kHz) is for the 12 kHz resonator filter whereas the black signal (band-pass at 21 to 23 kHz) is for the 3.8 kHz resonator; *Bottom:* Signal from cavity temperature sensors for verification of the obtained signals by the acoustic-emission sensor. The red line indicates the thermocouple located in the cavity where the 12 kHz resonator is located. The black line represents the thermocouple located in the cavity where the 3.8 kHz resonator is located.

12 kHz resonator filter must have a 1 while the other is 0. In Tab. 4.9 the logical conditions for the detection of the resonators are summarized.

Table 4.9: Logic table for the detection of the 12 and 3.8 kHz resonator depending on the peak detection in the filter signals.

| | 12 kHz storage variable | logic operator | 3.8 kHz storage variable |
|-------------------|----------------------------|-------------------|-----------------------------|
| 12 kHz detection | 1 | & | 0 |
| 3.8 kHz detection | 1 | & | 1 |

For verification of the results, cavity wall temperature sensor signal curves are shown in Fig. 4.45 *Bottom*. The passing melt front is indicated by a sharp increase of the temperature signal. For both peaks in the measurement signal a good temporal match is found with the moments of the temperature increase. In addition, it is known that the 12 kHz resonator is implemented in the left cavity where the thermocouple with the red sensor signal line is positioned²⁷. In the right cavity, where the 3.8 kHz resonator is located, the thermocouple with the black line is implemented. From the temporal moments of the temperature increase it is seen, that the detection of the resonators by the filter technique is correct.

4.5.3 Frequency Pattern Recognition Method

The frequency pattern recognition method is introduced to identify an independent number of installed resonators in a fast and efficient manner. The algorithm consists of two separate steps, signature identification and signature matching. During runtime signature matching is performed achieving coefficients and their variances to identify the temporal moment of an excited acoustic actuator.

For the evaluation the recorded signal \mathbf{y}_P is mapped into the frequency domain. To obtain the frequencies as a function of time a STFT is performed using a sliding window. The number of samples in the window l influences the calculation in two ways. A high number for l increases the resolution of the spectrum enabling a more sensible separation but delays the detection since the samples have to be recorded at first. One way to adjust this flaw is to use higher sampling rates so that the window has enough samples but time is short to obtain them. Again this comes with the drawback that calculation effort is increasing since a larger number of samples has to be processed. An additional influencing factor is the shift of the window by p samples. Having a small number for p increases the number of detection coefficients but increases the overall calculation time. So it is desired to find

²⁷The rise characteristic of the left cavity has an unexpected behavior which was already discussed in the Figures 4.13 and 4.14, on page 115.

right parameters to effectively obtain reasonable results for the separation of multiple implemented acoustic actuators.

The measurements were performed on an Arburg allrounder 470A 1000-400 alldrive using the test mold. All the measurements were performed using a PP (C7069). Since this material has a very low viscosity for an injection molding material, results with different materials having higher viscosity are at least as good or better (see also Chapter 4.3).

On the outside surface of the mold the accelerometer 352A60 from PCB Piezotronics was mounted. The sensor is capable to detect frequencies of up to 60 kHz. The measurements were recorded using a Data Acquisition System USB-6366 (DAQ). The DAQ enables to record up to 8 channels simultaneously using an adjustable sampling frequency up to $f_{s,max} = 16$ MHz and directly transfer data to MATLAB. In MATLAB all the signal manipulation was carried out.

4.5.3.1 Experimental Signature Identification

The signature identification process is carried out while neither the injection molding machine nor any other noisy auxiliary unit is running in addition to environmental influences. This reduces spurious presence of noise perturbing the recorded signatures. For test purposes two different resonators were installed in the mold yielding two different signatures. The resonators are those already presented in Chapter 4.4, using the 12 kHz plate resonator as well as the 3.8 kHz tongue resonator. The signatures were recorded in the time domain using a sampling frequency of $f_s = 120$ kHz.

Both resonators were independently artificially excited while measuring their time-dependent impulse response. In Fig. 4.46 the time dependent signatures of the 12 kHz and 3.8 kHz resonators are shown. Both signatures are comprised of $l = 600$ samples and the signal is cut-out in a manner that the beginning is at the moment of excitement. From their response it can be observed that the nominally designed 3.8 kHz resonator has many overtones resulting in high frequency components. As a result, the so called 3.8 kHz resonator has higher frequency components than the 12 kHz resonator. However, this is only a labeling issue but has no effect on the results.

Next, the signatures are mapped into the frequency domain. To suppress spectral leakage the signal \mathbf{y}_P is projected onto the orthogonal compliment of a Gram polynomial \mathbf{G}_d of degree $d = 3$ prior to computing the spectrum. In addition, the signatures are not orthogonal to each other which will lead to cross detection between the signatures. To enhance results, an orthogonalization process as described in Eq. 3.95 is performed. As a result, the orthogonal signatures $\hat{\mathbf{s}}_1$ and $\hat{\mathbf{s}}_2$ are obtained. In Fig. 4.47 *Top* the signa-

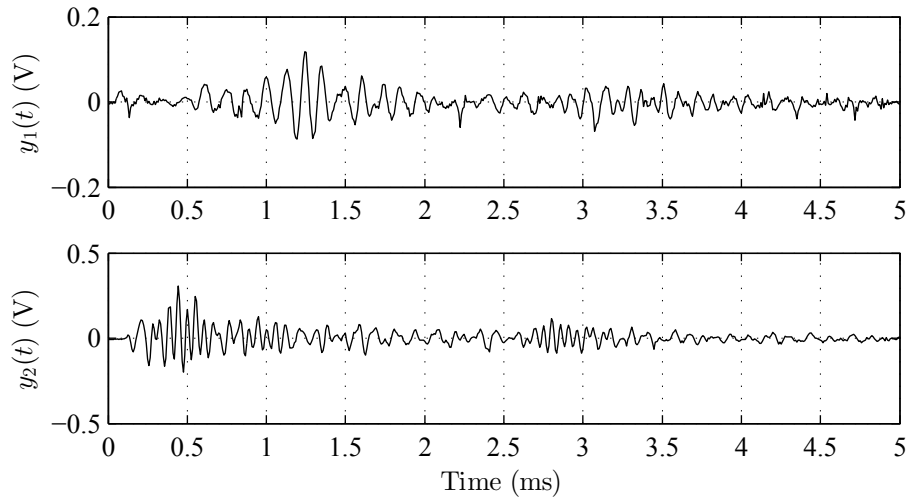


Figure 4.46: *Top:* Impulse response $y_1(t)$ of the 12 kHz resonator; *Bottom:* Impulse response $y_2(t)$ of the 3.8 kHz resonator. From the oscillation behavior of the resonators it can be observed that the nominally designed 3.8 kHz resonator has many overtones. Consequently, its frequency spectrum contains higher components than the resonator designed for 12 kHz. Both signatures are comprised of $l = 600$ samples.

ture of the 12 kHz resonator and in Fig. 4.47 *Bottom* the signature of the 3.8 kHz resonator is shown in the range of 0 to 30 kHz. From the magnitude spectrum it can be seen that for both only significant frequency components appear below 20 kHz. With the given sampling rate of $f_s = 120$ kHz just 50 samples are needed. However, the noise is distributed over all 600 samples of the spectrum leading to a noise gain $g_n = \sqrt{50/600}$. As described before, it can be observed that the 3.8 kHz resonator comprises higher frequency components in comparison to the 12 kHz resonator.

The obtained signatures $\hat{\mathbf{s}}_1$ and $\hat{\mathbf{s}}_2$ build the columns of the signature matrix \mathbf{S} which will be used during signature matching for identification of the resonators.

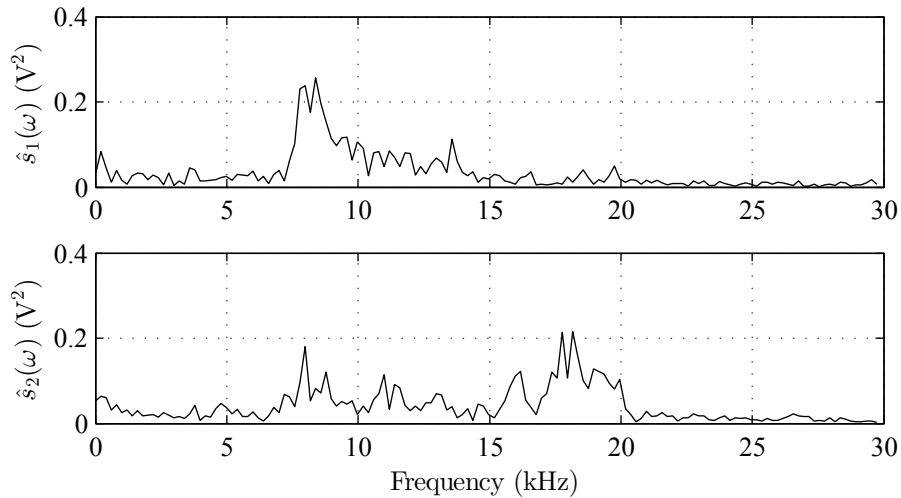


Figure 4.47: *Top:* Spectrum $\hat{s}_1(\omega)$ of the 12 kHz resonator; *Bottom:* Spectrum $\hat{s}_2(\omega)$ of the 3.8 kHz resonator; Both spectra are calculated via projecting $y_P(t)$ onto a low degree Gram polynomial for reducing spectral leakage as well as after orthogonalization.

4.5.3.2 Experimental Signature Matching

The measurements were performed with two implemented acoustic actuators, one equipped with the 12 kHz resonator and the other with the 3.8 kHz resonator. During measurement the accelerometer signal and an additional signal for synchronization with the injection molding process were recorded. Moreover, in each cavity a cavity wall temperature sensor was implemented for comparison of the two independent measurement systems to each other. The sampling rate was set to $f_s = 120$ kHz.

In Fig. 4.48 a typical measurement is shown. The gray shaded area indicates the measurement just before the injection molding cycle started. At the beginning of the injection molding cycle the opening sound of the electromagnetic valves of the nozzle valve system is recorded which happens at²⁸ $t_1 = 0.05$ s and $t_2 = 0.18$ s. The temporal difference between the valve openings was selected to enable balanced filling of the cavities (see Doppelmayr [41]). Afterwards, two larger sounds were recorded (at 0.37 s and 0.43 s). The origin of this sound is unknown but the moment of occurrence is dependent on the melt front within the cavity. This is verified by varying the injection rate. In Fig. 4.49 structure-borne sound measurement

²⁸Actually, just one of the valves opening moment was delayed. However, $t_1 \neq 0$ is a result of the time needed until the valve was fully opened.

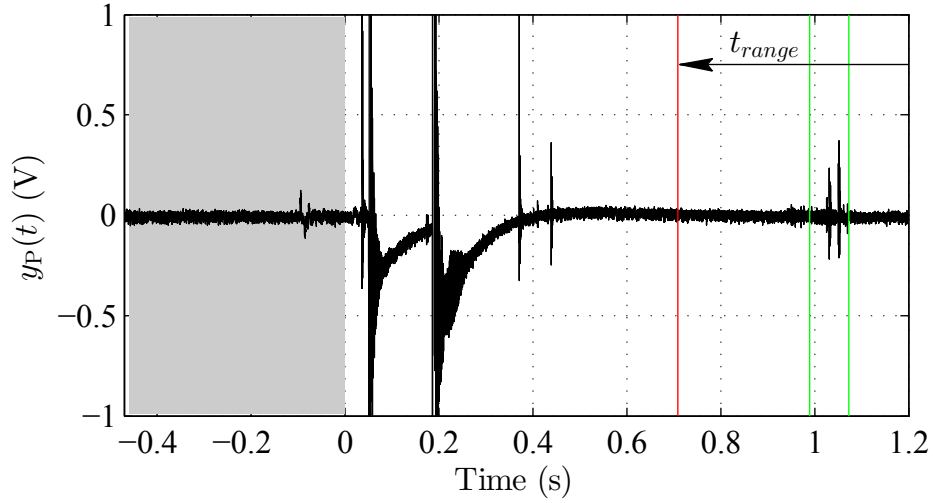


Figure 4.48: Recorded accelerometer signal \mathbf{y}_P as a function of time at injection rate $60 \text{ cm}^3\text{s}^{-1}$. The opening of the valves is delayed to reduce unbalanced filling of the cavities ($t_1 = 0.05 \text{ s}$ and $t_2 = 0.19 \text{ s}$). In the temporal region t_{range} confined by the red lines (the second red line is at $t = 1.5 \text{ s}$) a statistical significant region is searched (identified region is indicated by two green lines) at which frequency pattern matching is performed.

results at injection rates of $\dot{V}_1 = 20 \text{ cm}^3\text{s}^{-1}$ *Top*, $\dot{V}_2 = 35 \text{ cm}^3\text{s}^{-1}$ *Middle* and $\dot{V}_3 = 60 \text{ cm}^3\text{s}^{-1}$ *Bottom* are shown. The noise peak is marked by a black box and the acoustic actuator peak is marked by a red box. With increasing injection rate the moment of appearance tends to earlier times. Consequently, the noise is dependent on the melt front position. A possible origin is a not completely tightly mounted ejector pin which is moved by the passing melt front and generates a sound on impact.

However, this noise does not affect the measurement since it appears at a location where no acoustic actuator is implemented. The noise would cause significant trouble if at the same location an acoustic actuator was implemented. The only way to overcome this problem is by choosing a resonator which frequency response is significantly different from the noise enabling a safe detection.

At the measurement shown in Fig. 4.48 a red line indicates the start point of searching for statistically relevant portions within the signal \mathbf{y} at 0.7 s . This point is defined via the location of the implemented acoustic resonator as well as the injection rate \dot{V}_P . Using this knowledge an expected temporal moment $t_f = V/\dot{V}$ with V the cavity volume needed to reach the acoustic actuator

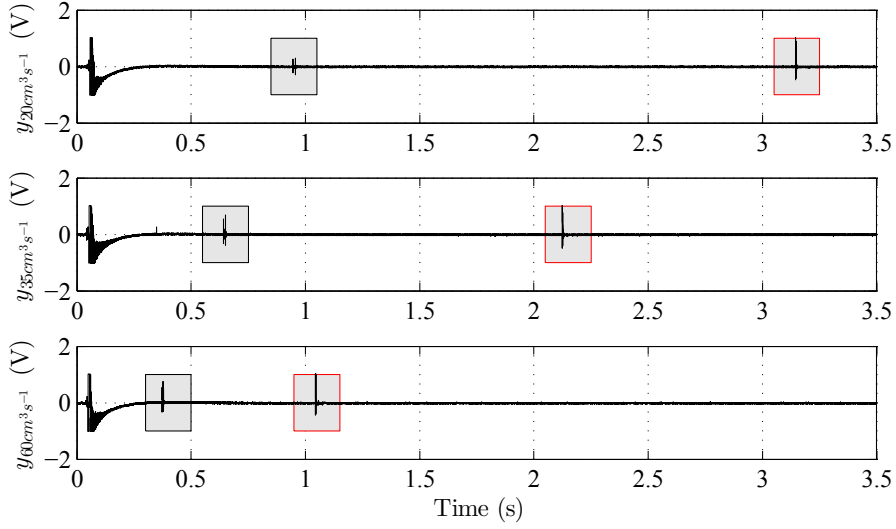


Figure 4.49: Injection rate dependent noise peak indicated by black box and acoustic actuator peak indicated by red box. Injection rate $\dot{V}_1 = 20 \text{ cm}^3\text{s}^{-1}$ *Top*, $\dot{V}_2 = 35 \text{ cm}^3\text{s}^{-1}$ *Middle* and $\dot{V}_3 = 60 \text{ cm}^3\text{s}^{-1}$ *Bottom*.

is calculated. Around this moment t_f a search range t_{range} is set up. The end point of the search region is at 1.5 s (not shown in this plot). A zoomed plot of the recorded signal is shown in Fig. 4.50 *Top*. Using the statistical methods described in Chapter 3.6.3 the normalized time varying standard deviation $|\sigma|(t)$ shown in Fig. 4.50 *Middle* and the time varying skewness $|\mu_3|(t)$ shown in Fig. 4.50 *Bottom* are calculated. The orange line indicates the point where the first statistically significant portion in the signal \mathbf{y}_P was identified. To find this point the signal was split up into bins calculating the cumulative distribution function of the local variance for both the standard deviation as well as for the skewness. This enables defining a detection limit in terms of probability for both criteria. Around the detection point a range is defined at which the frequency pattern matching is performed. This area is indicated by the green lines. The procedure of identifying the statistical relevant data reduces the amount of data needed to be processed by around 90 %²⁹.

After applying statistical signal processing a data subset of \mathbf{y}_P is found starting at 0.98 s and ending at 1.07 s. In Fig. 4.51 the time varying magnitude spectrum \mathbf{s}_t (calculated via Eq. 3.94, on page 89) of this subset is shown

²⁹This value is a rough estimator since it is strongly dependent on both ranges, i.e. the search range and the calculation range, as well as on the length of the completely recorded data stream which is dependent on the injection rate.

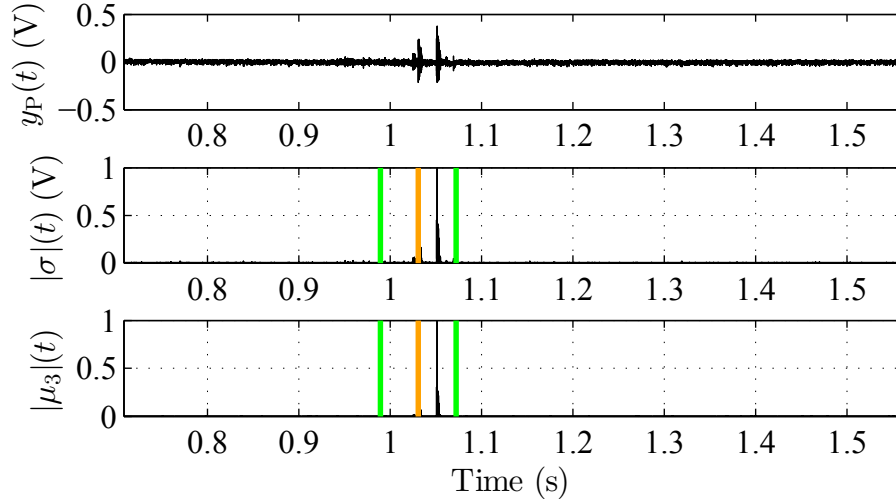


Figure 4.50: *Top:* Measurement signal \mathbf{y}_P in the range of searching statistical significant portions at injection rate $\dot{V} = 60 \text{ cm}^3\text{s}^{-1}$; *Middle:* Time varying normalized standard deviation enabling finding statistical significant portions of the signal. The first appearance of a significant portion is indicated by an orange line around which a calculation interval is set up, indicated by green lines; *Bottom:* Time varying normalized skewness

which does not need to be calculated during processing but supports understanding. The spectrum is calculated using Gram polynomial windowing for suppressing low frequency aperiodic portions of the signal. In this figure a blue color indicates no presence and a red color indicates large presence of a frequency component. As it can be seen, only few frequency components are present over calculation time. At 1.029 s and 1.052 s a prominent amount of frequency components are present which originate from the acoustic resonators. The task of the frequency matching algorithm is to detect those two events and separate them from each other and assign each event to one of the resonators.

On this data subset of \mathbf{y}_P frequency pattern matching is performed resulting in two time varying coefficients \mathbf{c}_i , one for each resonator, as well as their variances. In Fig. 4.52 the two coefficients are shown as a function of time, \mathbf{c}_1 in Fig. 4.52 *Middle* and \mathbf{c}_2 in Fig. 4.52 *Bottom*. The coefficient \mathbf{c}_1 is assigned to the 12 kHz resonator and the coefficient \mathbf{c}_2 is assigned to the 3.8 kHz resonator. The coefficients represent how much of the stored signature, which was stored in the matrix \mathbf{S} , is found in the current frequency spectrum \mathbf{s}_i , where i describes an index for a time step. As it can be seen in Fig. 4.52

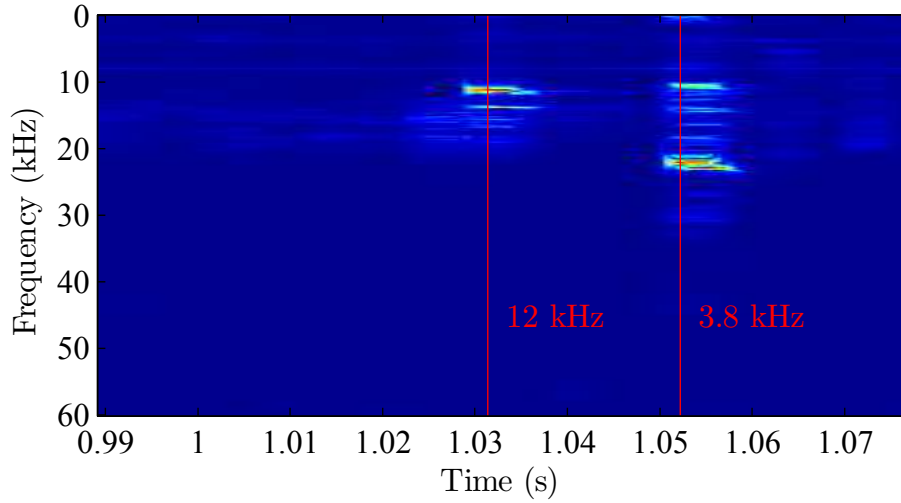


Figure 4.51: Time varying magnitude spectrum s_t of the found subset of \mathbf{y}_P on which frequency matching is performed. A blue color indicates no presence and a red color represents a large presence of a frequency component. Two moments with prominent presence of frequency components are found origination from the acoustic resonators, the 12 kHz and the 3.8 kHz resonator.

at first nearly zero amounts of the signatures are found in the spectrum. At 1.028 s the first coefficient \mathbf{c}_1 rises up indicating a large presence of the 12 kHz signature in the signal. At the temporal moment the detection level³⁰ is overshoot the 12 kHz resonator is declared to be recognized which is indicated by a black line slightly after the first rising at 1.031 s.

After the detection, the coefficient \mathbf{c}_1 is decreasing to a level of nearly zero. During the detection of the first resonator the coefficient \mathbf{c}_2 did not rise³¹. As a result, a clear separation of the first peak is possible.

At 1.05 s the coefficient \mathbf{c}_2 is starting to rise, indicating a significant portion of the 3.8 kHz resonator signature in the signal \mathbf{y}_P . The automatic detection of the resonator happened at 1.052 s. At the coincident moment the value of the coefficient \mathbf{c}_1 stays at a low level. Only minor changes are present which result from a certain amount of cross detection.

Cross detection results from the shape of the two resonators comprising some similar frequency components which were not fully suppressed via the orthog-

³⁰The detection level is not a constant level. It is calculated using descriptive statistics and is from coefficient to coefficient different.

³¹Only a small change in the signal is observed which is discussed later.

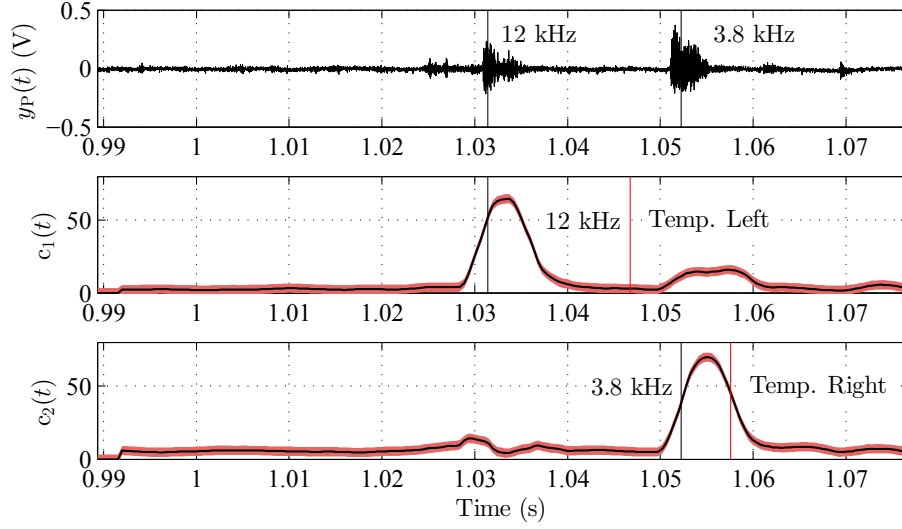


Figure 4.52: *Top:* Acoustic sensor signal \mathbf{y}_P in the time range of statistical significant region indicating two separate peaks; *Middle:* Coefficient \mathbf{c}_1 indicating the amount of 12 kHz resonator signature presence in the measurement signal \mathbf{y}_P ; *Bottom:* Coefficient \mathbf{c}_2 indicating the amount of 3.8 kHz resonator signature presence in the measurement signal \mathbf{y}_P . The red line indicates melt front detection via cavity wall temperature sensors. The red colored patch around the detection signal indicates the 3σ (99.73 %) confidence interval with respect to covariance propagation. The black lines indicate the temporal moment of automatic detection.

onalization process. Similar frequencies are a result of using a plate design as a basis for both resonator types, i.e. plate and tongue resonator. The red colored patch around the detection lines indicates the confidence interval of the coefficient with consideration of the covariance. The covariance matrix Λ_c of this measurement is,

$$\Lambda_c = \begin{bmatrix} 0.8571 & 0.7464 \\ 0.7464 & 0.8574 \end{bmatrix}. \quad (4.4)$$

From the covariance matrix Λ_c the 3σ (99.73 %) confidence interval is derived. As it can be seen the confidence interval is small in comparison to the height of the detection peaks indicating a safe separation between both resonators. For comparison of the acoustic-emission sensor results two cavity wall temperature sensors were placed within the cavity. The melt front recognition is indicated by two red lines at 1.046 and at 1.057 s after start of injection

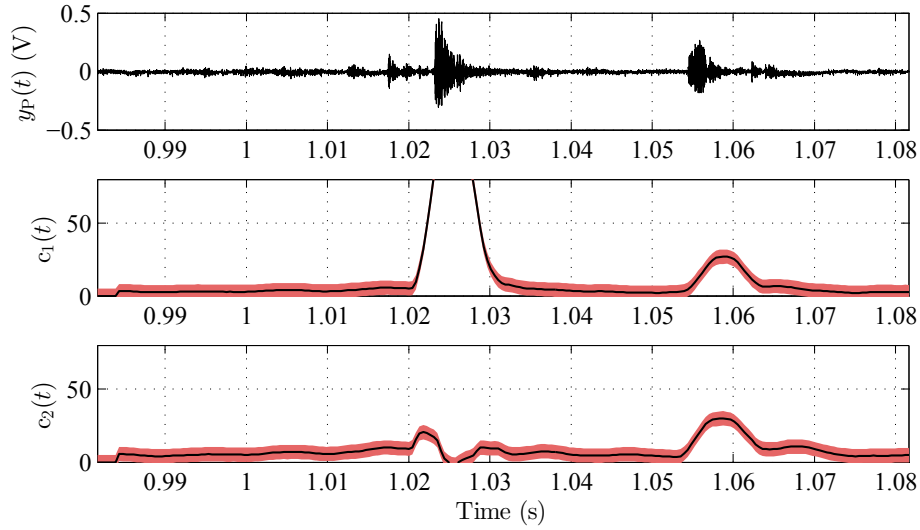


Figure 4.53: *Top:* Accelerometer signal y_P in the time range of statistical significant region indicating two separate peaks; *Middle:* Coefficient c_1 indicating the amount of 12 kHz resonator signature presence in the measurement signal y_P ; *Bottom:* Coefficient c_2 indicating the amount of 3.8 kHz resonator signature presence in the measurement signal y_P .

molding cycle. The moment of detection is calculated by subtracting a low-pass filter from the original signal resulting in a difference as a result of filter delay. If the difference exceeds the limit of 1.5 K the raising edge of the temperature signal is detected and consequently this indicates the moment of passing melt front. Having a wired sensor gives certainty at which cavity the polymer arrived at which temporal moment. As a result, it is possible to verify if the frequency matching algorithm does recognize the resonators correctly. From Fig. 4.52 it can be seen that a matching result between the 12 kHz resonator and the rising edge of the left cavity wall temperature appeared. This is true since this resonator was implemented within of the left cavity. Identical results appear for the right cavity.

Comparing the two independent measurement systems to each other it can be seen that the acoustic-emission sensor detected the melt front earlier than the cavity wall temperature sensors in both cases. However, the time detection delay is different for the cavities. In Fig. 4.13 and Fig. 4.14, on page 115, this effect was already discussed and it was found, that the sensor placed in the left cavity delivers an unexpected sensor signal rise characteristic.

A problem which can occur during the measurements is that the detection of the two resonators fails. This happens in the case one of the resonators does

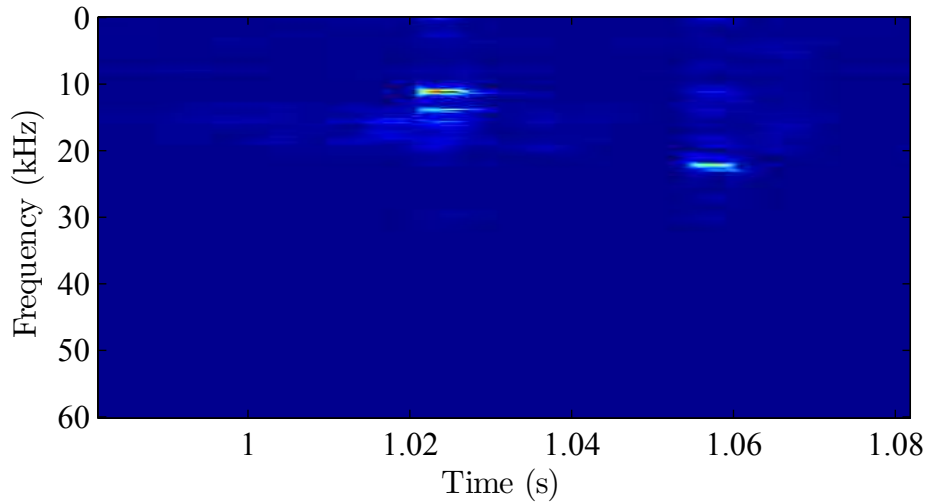


Figure 4.54: Time varying magnitude spectrum \mathbf{s}_t of a measurement with not fully excited 3.8 kHz resonator resulting in bad separation of the installed resonators.

not vibrate with the expected frequency components, resulting from a bad excitement process. In Fig. 4.53 such a bad detection example is shown. The 12 kHz resonator is detected correctly as before. Unfortunately, the 3.8 kHz resonator cannot be detected correctly since the coefficients \mathbf{c}_1 and \mathbf{c}_2 indicate the same amount of signature presence. As a result, no clear separation is possible. When investigating the magnitude spectrum \mathbf{s}_t shown in Fig. 4.54, one can observe that the frequency components of the 3.8 kHz resonator are not fully present as a result of bad resonator excitement. Consequently, the frequency pattern recognition method has to fail since the searched frequency components were never present in the signal.

As a result, it is a must to ensure full excitement of the installed resonant structures which can be achieved for instance by using a longer pin movement distance resulting in higher impact energy.

4.6 Long Term Evaluation of Acoustic-Emission Sensor

In this chapter the evaluation of the automatic detection over a higher number of injection molding cycles was tested to investigate the *long term* performance of the acoustic-emission sensor in combination with the frequency pattern recognition method. In this test long term comprises around 480

injection molding cycles which is a good estimator of the performance evaluation but is not a compensation for a long term test in a series mold.

An important fact to notice is, that the signal processing was not carried out in real time³². The measurement data was recorded and stored using the DAQ. All the signal processing and result evaluation was done afterwards using MATLAB.

4.6.1 One Installed Acoustic Actuator

At first the automatic detection performance with one installed acoustic actuator was tested. For the measurements the already known PP (C7069) was used. For the complete series the injection rate was set to $60 \text{ cm}^3\text{s}^{-1}$ and the experiments were carried out on the injection molding machine 470A-1000 from Arburg. The 12 kHz resonator was installed within the right cavity and for result verification a cavity temperature sensor 4009b was located on the opposite cavity side of the movable pin³³. The recorded results were obtained with a frequency sampling rate of $f_s = 120 \text{ kHz}$. Before measurement results were taken 50 parts for stationary thermal conditions were produced. Then, a series of 225 shots was carried out receiving results as shown exemplarily in Fig. 4.55. Measurement results were evaluated not in real time but afterwards.

In Fig. 4.55 *Top* the acoustic signal \mathbf{y}_P with a temporal focus on the moment of impact is shown. In the Fig. 4.55 *Middle* the correlation coefficient \mathbf{c}_1 is shown which represents the amount of the 12 kHz resonator's signature being present in the signal \mathbf{y}_P . At around 0.975 s an increase of the correlation coefficient \mathbf{c}_1 is recognized. The black vertical line indicates the moment of automatic detection. The correlation coefficient \mathbf{c}_2 is evaluated in addition, although the 3.8 kHz resonator is not used within this series. The coefficient \mathbf{c}_2 can be used for additional verification of separation in a manner that it does stay at a low level over the whole measurement time. If so, this gives additional verification of the algorithm used. At the same moment when \mathbf{c}_1 rises the correlation coefficient \mathbf{c}_2 shows only minor changes in its value enabling separation between the signatures. Consequently, a safe detection of the 12 kHz resonator is possible.

For verification the signal of the cavity temperature sensor was evaluated. The red vertical line indicates the moment of passing melt front detected via the temperature sensor. As it can be seen, the detection happened slightly

³²Real time processing comprises a lot of difficulties which go beyond the scope of this thesis.

³³The same measurement setup was used as for the proof of concept measurements in Chapter 4.2, on page 106.

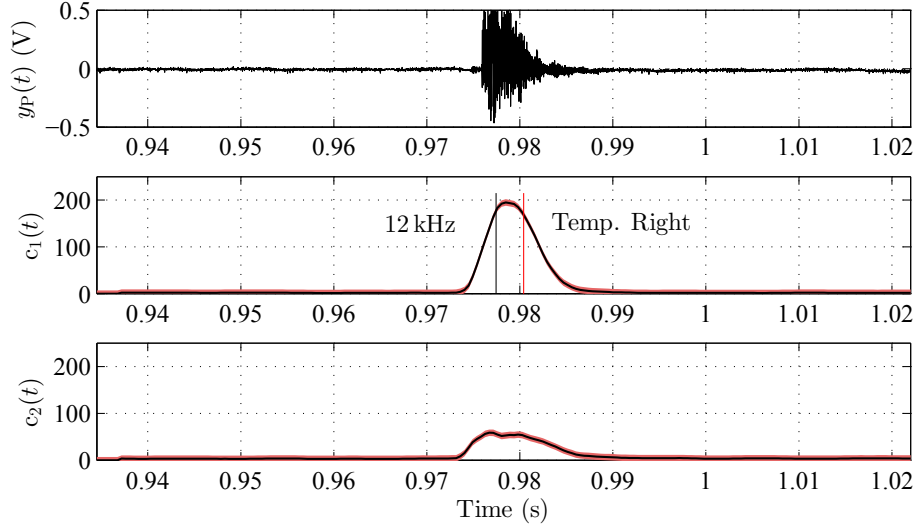


Figure 4.55: *Top:* Acoustic signal y_P in temporal range of pin impact at injection rate $60 \text{ cm}^3\text{s}^{-1}$; *Middle:* Correlation coefficient c_1 representing the 12 kHz resonator. At around 0.975 s the correlation coefficient level rises indicating the detection of the 12 kHz resonator (automatic detection indicated by vertical black line). The red line indicates melt front detection via the cavity wall temperature sensor; *Bottom:* Correlation coefficient c_2 representing the amount of identified signature of the 3.8 kHz resonator which should stay at a low level because the resonator is not installed within this measurement. Separation is successfully performed in the present case.

after the detection of the melt front via the acoustic-emission sensor. For the performance evaluation the temporal difference Δt between the two detection events is calculated as,

$$\Delta t = t_{acoustic} - t_{temperature}, \quad (4.5)$$

with $t_{acoustic}$ the temporal moment the impact of the movable pin was detected and $t_{temperature}$ the moment the passing melt front was recognized via the cavity wall temperature sensor.

In Fig. 4.56 the difference time of the long term performance evaluation is shown for the complete measurement series. The series consists of 225 measurements. As it can be observed from Fig. 4.56 all difference time values are negative values, indicating that the acoustic-emission sensor detected the

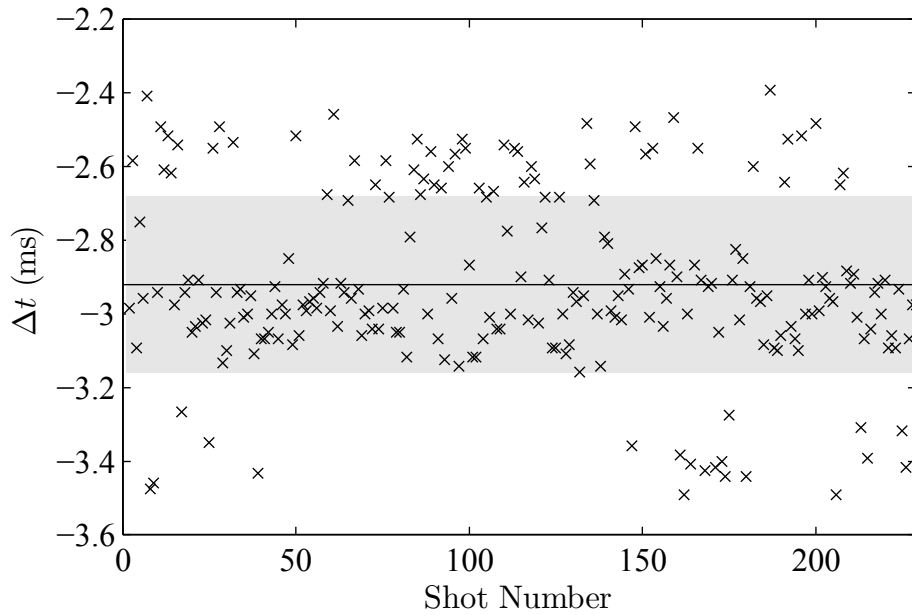


Figure 4.56: Difference time Δt for a measurement series of 225 shots with installed 12 kHz resonator. The mean value $\Delta \bar{t}$ over all shots is indicated by a horizontal black line and the standard deviation σ of the measurement series is represented with the gray patch around the mean value.

melt front in advance of the cavity temperature sensor³⁴. The mean value over all measurements is at $\Delta \bar{t} = -2.92$ ms, indicated by a horizontal black line. The standard deviation of the obtained results is at $\sigma = 0.24$ ms, shown as a gray patch around the mean value. In Fig. 4.57 a histogram of the measurement series is given to support recognizing the deviation in the obtained results. The bins were selected having a width of 0.05 ms. Overall, automatic detection of the 12 kHz resonator for all 225 injection molding cycles was performed successfully. In no case a cross detection appeared yielding a safe detection of the 12 kHz resonator in each cycle.

³⁴This is a result of how the signals were processed. Different evaluation methods to identify the passing melt with the temperature sensor may deliver different temporal moments of detection. However, this measurement series should not evaluate the performance of the temperature sensor but of the acoustic-emission sensor.

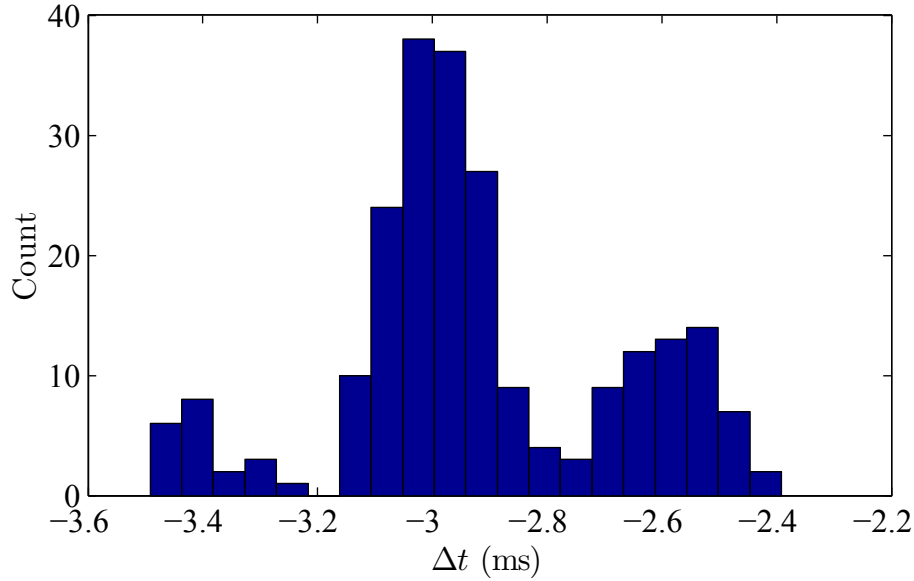


Figure 4.57: Histogram of the difference time Δt while having one actuator installed in the mold. The bins have a width of 0.05 ms.

4.6.2 Two Installed Acoustic Actuators

In another measurement series the automatic detection of two installed actuators in one mold was tested, one in each cavity. Again the frequency pattern recognition method was used to detect and separate the incorporated tongue and plate resonator. In this series 257 shots were carried out, having an injection rate of $90 \text{ cm}^3\text{s}^{-1}$. The measurement was recorded with a frequency sampling rate of $f_s = 120 \text{ kHz}$ using the DAQ. Measurement results were evaluated not in real time but afterwards.

The evaluation of the results was performed in a similar manner to the measurement series with one used resonator. The only difference to the results before is that each resonator is evaluated on its own. The question to be answered is if the separation of the resonators could be achieved for all shots and if the results are in agreement with the results obtained by the cavity wall temperature sensors.

In Fig. 4.58 an exemplary measurement result is shown. In the *Top* figure, the acoustic signal y_P with a temporal focus on the impact of the movable pin is shown. In difference to the results from Fig. 4.55 two separate deflections are observed. In the left cavity the 3.8 kHz resonator is placed whereas in the right cavity the 12 kHz resonator is located. Consequently, a link between the coefficient c_1 and the temperature sensor *Right* is expected and a link

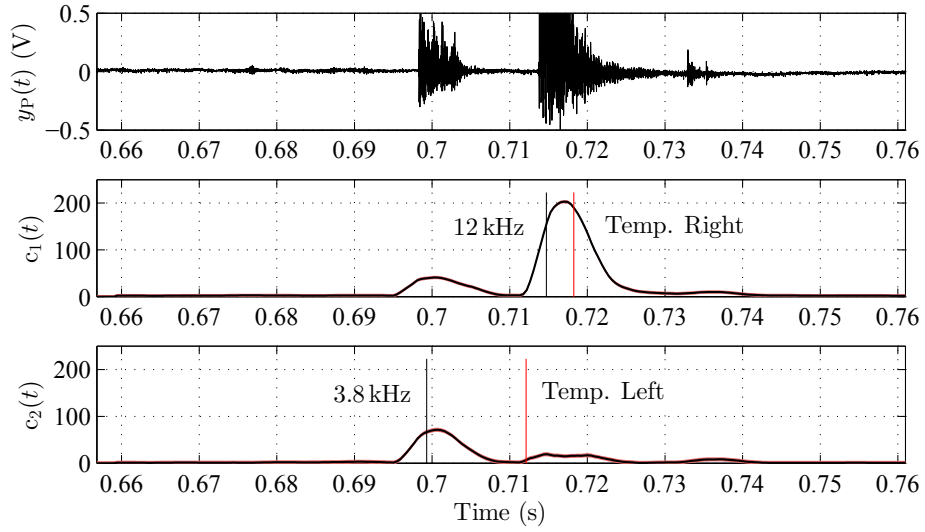


Figure 4.58: *Top:* Acoustic signal y_P in temporal range of pin impact; *Middle:* Correlation coefficient c_1 representing the 12 kHz resonator. At around 0.71 s the correlation coefficient level rises indicating the detection of the 12 kHz resonator (automatic detection indicated by black vertical line). The red line indicates melt front detection via the cavity wall temperature sensor; *Bottom:* Correlation coefficient c_2 representing the 3.8 kHz resonator. At around 0.695 s the correlation coefficient level rises indicating the detection of the 3.8 kHz resonator (automatic detection indicated by black vertical line). The red line indicates melt front detection via the cavity wall temperature sensor.

of the results of the coefficient c_2 is expected to be in match with the signal from temperature sensor *Left*.

In Fig. 4.58 the expected behavior is shown. The value increase of the correlation coefficient c_1 is in good match with the moment of passing melt front detected via the cavity temperature sensor, indicated by a vertical red line. A similar match is found for the increase of the correlation coefficient c_2 with the detection of the passing melt front recognized by the cavity temperature sensor located in the left cavity. It has to be denoted, that as a result of a cavity related issue, the detection of the melt front via the cavity temperature sensor in the left cavity is delayed and will lead to a different mean value $\Delta \bar{t}$ (confer Fig. 4.13 and 4.14, on page 115).

In Fig. 4.58, the correlation coefficients show a different behavior in terms of value height for the detection of the 12 kHz and 3.8 kHz resonator. Start-

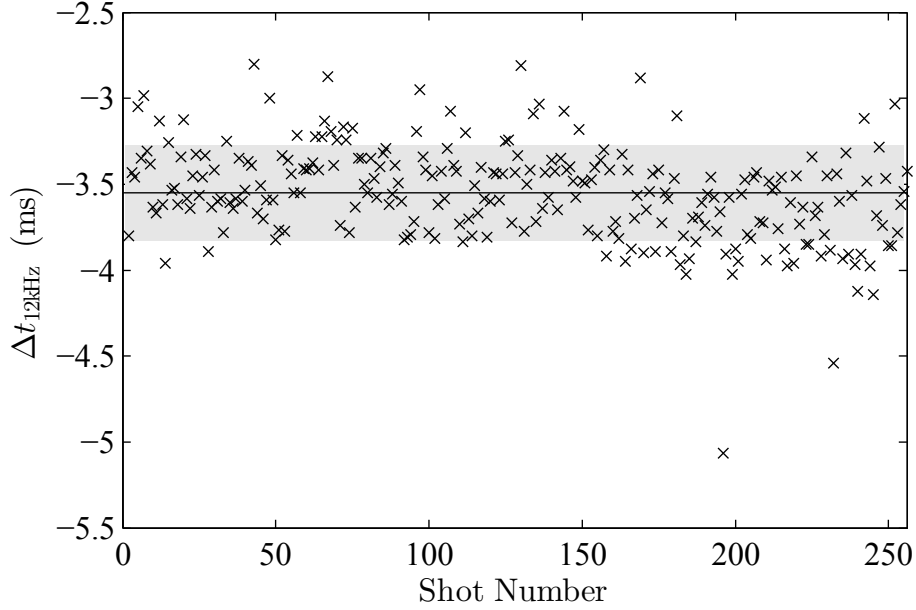


Figure 4.59: Difference time $\Delta t_{12\text{kHz}}$ for a measurement series of 257 cycles comparing detection of 12 kHz resonator with melt front detection via cavity temperature sensor. The mean value $\Delta \bar{t}_{12\text{kHz}}$ over all shots is indicated by a horizontal black line and the standard deviation $\sigma_{12\text{kHz}}$ of the measurement series is represented with the gray patch around the mean value.

ing with the detection of the 12 kHz resonator, the correlation coefficient \mathbf{c}_1 increases significantly at the second occurring deflection in the signal \mathbf{y}_P . Simultaneously, the correlation coefficient \mathbf{c}_2 stays at low level ensuring a safe separation and detection of the resonator. With consideration of the confidence interval for both coefficients, shown as a red patch around the signal, separation is reliable.

For the detection of the 3.8 kHz resonator the correlation coefficient rises not to a similar height as the coefficient \mathbf{c}_1 during detection of the 12 kHz resonator. The coefficient \mathbf{c}_2 increases up to approximately half the value of the detection value from coefficient \mathbf{c}_1 at the detection of the 12 kHz resonator. Still, detection is possible, since the coefficient \mathbf{c}_1 stays at a comparable low value at the detection of the 3.8 kHz resonator. The difference in the peak height is most probably a result of the pin movement behavior which, if different, leads to a difference in the oscillation amplitude of the resonator. The different oscillation amplitude is reflected within the correlation coefficients. Up to now, only the peak values between the both correlation coefficients

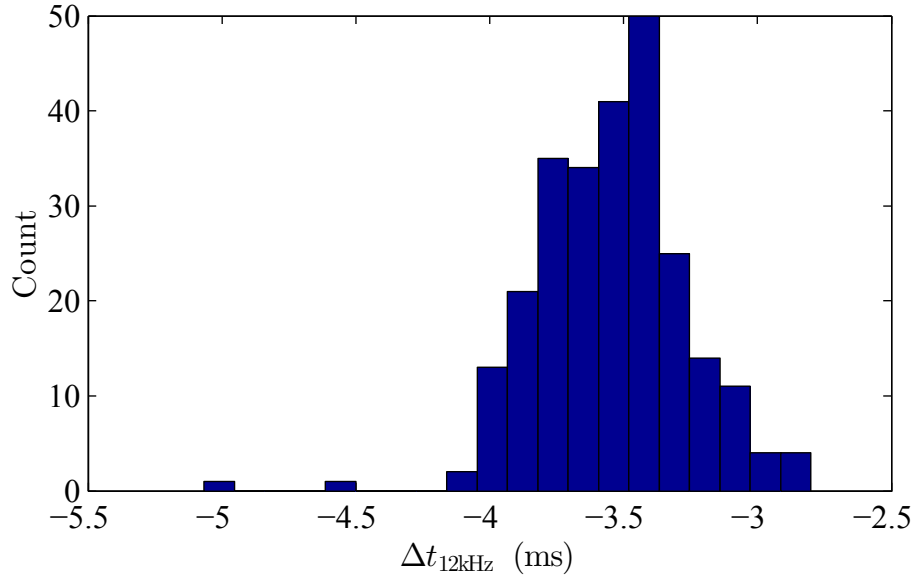


Figure 4.60: Histogram of the difference time of the 12 kHz resonator. The bins have a width of 0.10 ms.

were compared. However, when just having the result of one correlation coefficient still a safe detection is possible. The increase at the point of detection is for both coefficients always more significant than at the point of cross detection.

In Fig. 4.59 the difference time $\Delta t_{12\text{kHz}}$ between the 12 kHz resonator detection moment and the rising signal of the cavity temperature sensor in the right sided cavity is shown. The results are shown for 257 cycles. The mean difference time is at $\Delta \bar{t}_{12\text{kHz}} = -3.55$ ms and the measurement series has a standard deviation of $\sigma_{12\text{kHz}} = 0.28$ ms. The mean value is indicated by a horizontal black line surrounded by a gray patch marking the area of standard deviation. Like in the measurements with only one installed acoustic actuator, the difference time is negative over all measurements. Consequently, the melt front was recognized by the acoustic-emission sensor in advance of the detection via the cavity temperature sensor. In Fig. 4.60 the gained results are shown in a histogram with a bin width of 0.10 ms enabling observation of the distribution of the difference time. Except for a few aberration values the difference time is in a small time window of -4.05 to -2.79 ms as seen in the histogram.

One of the few aberration values in the difference time occurred at shot number 197 which is shown in Fig. 4.61. In this figure the focus is on the correlation coefficient c_1 and the question to be answered is why detection is

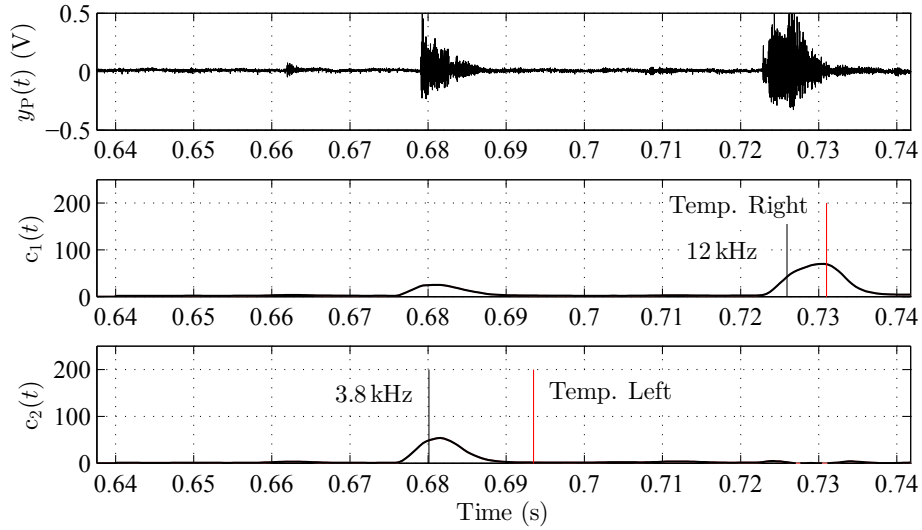


Figure 4.61: Measurement of cycle 197 delivering an aberration value for the difference time $\Delta t_{12\text{kHz}}$. This is a result from differently shaped correlation coefficient c_1 during resonator detection leading to a shifted temporal detection moment.

different to the majority of the measurements. In comparison to the result shown in Fig. 4.58 one can notice that the shape of the correlation value increase in Fig. 4.61 is different. The reason for the differently behaving detection coefficient is not known for sure but is believed that pin movement was different in this shot resulting in lower impact energy and consequently different oscillation amplitude of the resonator. Measurements for verification are not yet performed. As a result of the way the automatic detection is implemented in the algorithm³⁵, the moment of detection of the 12 kHz resonator is shifted to an earlier time.

In Fig. 4.62 difference time results for the 3.8 kHz resonator over all 257 cycles are shown. The difference time $\Delta t_{3.8\text{kHz}}$ is calculated between the moment of melt front detection via the acoustic-emission sensor and the cavity temperature sensor in the left cavity. At first, the clearly lower value of $\Delta \bar{t}_{3.8\text{kHz}} = -13.70\text{ ms}$ is recognizable, indicated by a black horizontal line. Again, this effect can be traced back to a cavity related issue investigated using temperature sensors. The standard deviation for the difference time using the 3.8 kHz resonator is slightly higher than the value obtained for the

³⁵As stated before, the automatic detection is realized using descriptive statistic to detect the peak value in the time-dependent correlation coefficient.

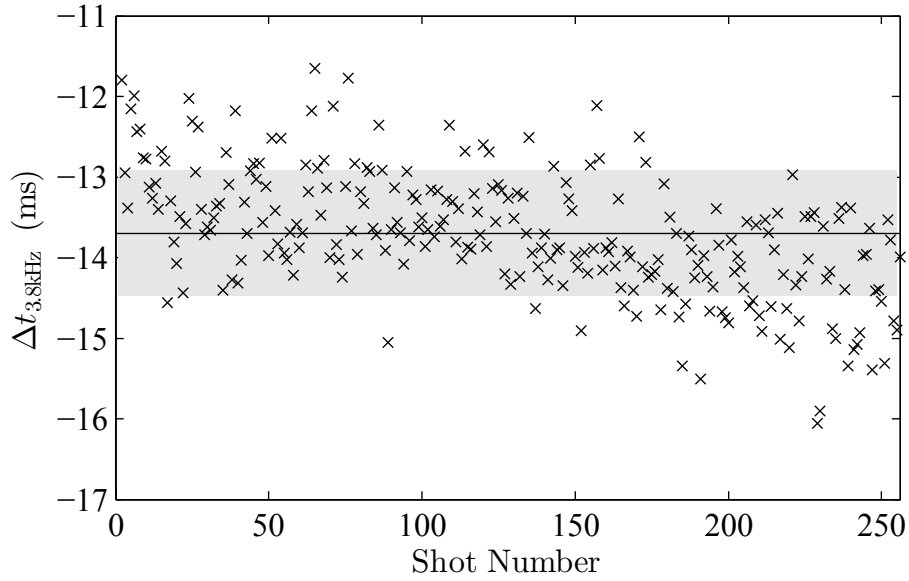


Figure 4.62: Difference time $\Delta t_{3.8\text{kHz}}$ for a measurement series of 257 shots comparing detection of the 3.8 kHz resonator with melt front detection via cavity temperature sensor. The mean value $\bar{\Delta t}_{3.8\text{kHz}}$ over all shots is indicated by a horizontal black line and the standard deviation $\sigma_{3.8\text{kHz}}$ of the measurement series is represented with the gray patch around the mean value.

12 kHz resonator, $\sigma_{3.8\text{kHz}} = 0.78\text{ ms}$, indicated by a gray patch around the mean value.

The obtained values for the $\Delta t_{3.8\text{kHz}}$ are shown in Fig. 4.63 as a histogram. It can be seen that the shape of the distribution is wider than the distribution obtained for the 12 kHz resonator. However, no aberration values are present. To summarize long term evaluation, it is stated that the acoustic-emission sensor in combination with the frequency pattern matching algorithm worked for the tested 482 measurements. For both tests with one installed actuator and with two incorporated actuators, very good results in terms of reliability were achieved. The standard deviation of both measurement series was small indicating only slight variation in the melt front detection using the acoustic-emission sensor. Since melt front detection is reliable using cavity temperature sensors it is deduced, that melt front detection is reliable with the acoustic-emission sensor. Otherwise, aberration values would be present in the shown results.

Still, the sensor has to stand a test in a series mold delivering good results

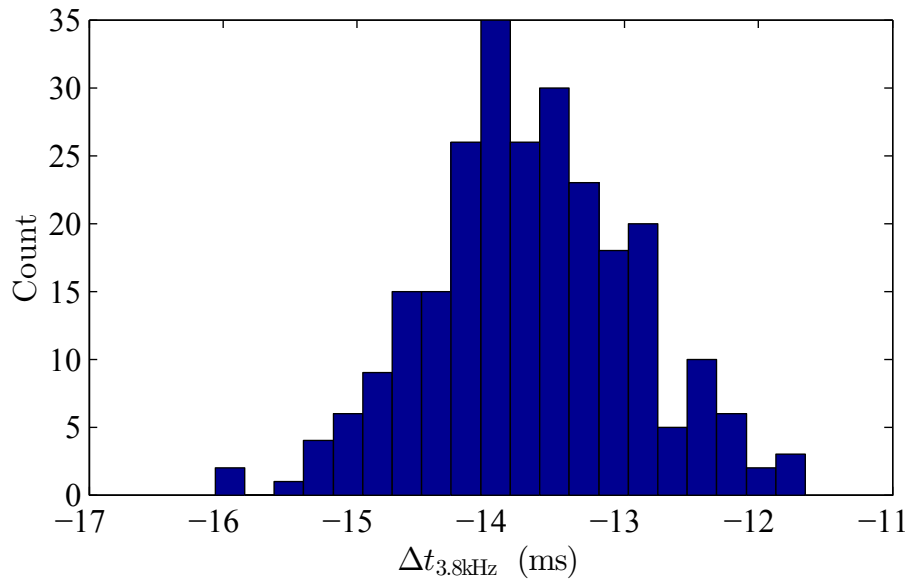


Figure 4.63: Histogram of the difference time of the 3.8 kHz resonator. The bins have a width of 0.25 ms.

over a duration of several tens of thousands of cycles. This proof, however, cannot be given from tests in a laboratory scale.

Chapter 5

Conclusion and Outlook

Within this thesis a new purely mechanical wireless in-mold sensor for injection molding is introduced which is capable of detecting the passing melt front at multiple locations. Wireless sensors yield the advantages of avoiding energizing and data transmitting wires, i.e. simplifying mold design. For data transmission the acoustic-emission sensor uses structure-borne sound enabling the installation of a multiple number of transmitters by using only one receiver in form of an accelerometer. The passing melt front excites the incorporated resonant structure of the transmitter. The energy to trigger the excitement is gained from the pressurized passing melt front. For separation of multiple transmitters different resonator designs are introduced enabling differentiation via their eigen-frequencies.

The introduced design approach, however, poses challenges in terms of automatic melt front detection. Since the used accelerometer detects a plurality of upcoming sounds from the inside of the mold, signal processing is necessary to gain the information comprised in the recorded signal. Two classical signal processing approaches were tested. The envelope method was verified to be functionally when having solely one transmitter installed. The method was tested on a programmable logic controller with limited calculation time. The second signal processing technique tested uses pass-band filters. The pass-band filters were designed to detect the oscillating frequencies originating from the used resonators. By applying a logic algorithm, separation of the installed resonators was verified.

A third signal processing technique was introduced, named frequency pattern recognition algorithm. It uses Fourier transformation in combination with polynomials for a least squares approximation for the instant of time when the resonator was excited. The algorithm turns out to be very efficient calculating correlation coefficients between stored frequency signatures

and searched frequency components in the recorded signal. In addition, the covariance propagation is calculated yielding the possibility to estimate a confidence interval of the correlation coefficients.

The frequency pattern matching algorithm was tested for the automatic detection of single and multiple incorporated resonators over a *long-term* measurement series. The results state that the algorithm is capable of detecting and separating the installed resonators reliable for all tested cycles.

Furthermore, it was verified by investigating the time-dependent pin movement of the transmitter that the acoustic-emission sensor response characteristic is influenced below 1.5 ms when varying acting melt pressure. Since the melt pressure is proportional to the polymer's viscosity, polymers with different viscosity than the one of the tested PP will not influence the response time characteristic of the sensor either. In addition, the sensor response time for melt front detection is in comparable range with conventional used in-mold sensors for melt front detection, i.e. melt front detection faster than 2.5 ms for injection rates higher or equal than $30 \text{ cm}^3\text{s}^{-1}$ using the described test mold.

Throughout the thesis, the acoustic-emission sensor was compared against commercially available in-mold sensors, capable of detecting a passing melt front. It was found that the novel measurement concept is at least in comparable temporal range at melt front recognition.

For the verification of concept's functionality the transmitter was designed bigger than essentially necessary. For a series mold a design concept was introduced, using ejector pins to overtake the task of the transmitter used in the test mold. In this manner, ejector pins gain an additional task without losing their original purpose of part demolding. This implementation approach saves valuable space near the cavity surface while gaining important process conditions from the inside of the mold.

For future work it is proposed to design additional differently shaped resonators delivering independent signals when being excited. The new resonators will ensure better detection and separation while reducing the high requirements for signal processing since the input data quality is enhanced. Using the acoustic-emission sensor for controlling the injection molding process in a series mold it is desirable to implement the proposed frequency pattern recognition algorithm in a real time calculation environment. This enables the direct interference with the process, e.g. controlling the switch-over point.

Another major aspect is the pin movement behavior. For continuous automatic detection of the frequency components it is a must to ensure reproducible excitement of the resonant structures. This can only be ensured if the

excitement process is as reproducible as possible which demands reliable pin movement. The pin movement can be improved by using plain bearings or friction reducing coatings as well as using tighter manufacturing tolerances. Another possible usage of the acoustic-emission sensor is to use it for pressure sensing. By applying a spring with appropriate spring ratio, the concept is capable of detecting if a certain pressure level was overshoot at a certain time during the injection molding cycle.

The proposed design study using ejector pins as the transmitter needs to be verified on practicability as well as on reliability. Only if the sensor concept stays simple while delivering trustworthy results it may have a chance to be incorporated within a multiple number of series injection molds in future.

List of Abbreviations

| | |
|--------|---|
| ADC | analog-to-digital converter |
| ANN | artificial neural network |
| CAD | computer-aided design |
| CPU | central processing unit |
| DC | direct current |
| DFT | discrete Fourier transform |
| FEM | finite element method |
| FIR | finite-impulse response |
| FT | Fourier transform |
| FFT | fast Fourier transform |
| GPC | generalized predictive control |
| i.i.d. | independent and identically distributed |
| IIR | infinite-impulse response |
| IR | infra-red |
| LTI | linear time-invariant system |
| MTTF | mean time to failure |
| DAQ | Data Acquisition System USB-6366 |
| ODEs | ordinary differential equations |

| | |
|------|----------------------------------|
| PID | proportional–integral–derivative |
| PLC | programmable logic controller |
| PA | Polyamide |
| POM | Polyoxymethylene |
| PP | Polypropylene |
| RF | radio-frequency |
| SAW | surface acoustic wave |
| SIM | sequential injection molding |
| SDOF | single-degree-of-freedom |
| STFT | short-time Fourier transform |

Bibliography

- [1] J.-F. Agassant. *Injection molding: Technology and fundamentals*. Progress in polymer processing. Hanser, Munich and Cincinnati and Ohio, 2009.
- [2] A. R. Agrawal, I. O. Pandelidis and M. Pecht. Injection-molding process control - A review. *Polymer Engineering and Science*, 27(18):1345–1357, 1987.
- [3] N. Angelova and D. Hunkeler. Rationalizing the design of polymeric biomaterials. *Trends in biotechnology*, 17(10):409–421, 1999.
- [4] K. I. Arshak, D. Morris, A. Arshak, O. Korostynska and E. Jafer. Development of a wireless pressure measurement system using interdigitated capacitors. *IEEE Sensors Journal*, 7:122–129, 2007.
- [5] N. Asadizanjani, R. X. Gao, Z. Fan and D. O. Kazmer. Viscosity Measurement in Polymer Injection Molding using a Multivarite Sensor. In *Proceedings of ANTEC 2012*, St. Louis, 2012.
- [6] L. F. Bachman. *Statistical analyses for language assessment*. Cambridge University Press, Cambridge, 2004.
- [7] C. Bader. Das kleine Einmaleins der Werkzeug-Sensorik. *Kunststoffe International*, (6):114–117, 2006.
- [8] C. Bader and H. Derkx. The Time is Ripe: Hot-runner Control. *Kunststoffe International*, 2009(6):8–12, 2009.
- [9] C. Bader and S. C. Zeller. Die Entdeckung der Schmelzefront: Sensortechnik. *Kunststoff Magazin Online*, (6):2–6, 2010.
- [10] G. Bechtold, K. Gaffney, J. Botsis and K. Friedrich. Fibre orientation in an injection moulded specimen by ultrasonic backscattering. *Composites Part A: Applied Science and Manufacturing*, 29(7):743–748, 1998.
- [11] H.-H. Behrens. Technisches und fachliches Niveau im Gleichschritt. *Kunststoffberater*, (05):31–32, 2012.
- [12] A. Bendada, A. Derdouri, M. Lamontagne and Y. Simard. Analysis of thermal contact resistance between polymer and mold in injection molding. *Applied Thermal Engineering*, 24(14-15):2029–2040, 2004.

- [13] Bernecker + Rainer Industrie-Elektronik Ges.m.b.H. B&R Help Explorer Ver: 2.1.1.18824: Automation Studio 3.0.81.22, 2011.
- [14] J. E. Betters and M. Smith. Method of using a sequential fill valve gated injection molding system. US Patent 5762855, 1998.
- [15] W. Bolton. *Programmable logic controllers*. Newnes, Amsterdam and Boston, 5th edition, 2009.
- [16] S. Brandt. *Data Analysis: Statistical and Computational Methods for Scientists and Engineers*. Springer, 1999.
- [17] H. A. Broadbent, S. Z. Ivanov and D. P. Fries. PCB-MEMS Environmental Sensors in the Field. In *2007 IEEE International Symposium on Industrial Electronics*, pages 3282–3286. IEEE, 2007.
- [18] F. Buja. Apparatus for data acquisition and application in an injection molding process. US Patent 4904172, 1990.
- [19] T. Bulgrin and T. Richards. Application of advanced control theory to enhance molding machine performance. *IEEE Transactions on Industry Applications*, 31(6):1350–1357, 1995.
- [20] W.-E. Bulst, G. Fischerauer and L. Reindl. State of the art in wireless sensing with surface acoustic waves. *IEEE Transactions on Industrial Electronics*, 48(2):265–271, 2001.
- [21] P. Bürgisser, M. Clausen and M. A. Shokrollahi. *Algebraic complexity theory*, volume 315 of *Grundlehren der mathematischen Wissenschaften*. Springer, Berlin and London, 2011.
- [22] M. Burgsteiner. *Entformungskräfte beim Spritzgießen in Abhängigkeit von Oberflächenrauigkeit, Stahlwerkstoff, Vorzugsrichtung der Oberflächenstruktur, Beschichtung und Kunststofftyp*. Master Thesis, Montanuniversität Leoben, Leoben, 2009.
- [23] M. Capiński and P. E. Kopp. *Measure, integral and probability*. Springer, London and New York, 2nd edition, 2004.
- [24] P. J. Carreau. Rheological Equations from Molecular Network Theories. *Journal of Rheology*, 16(1):99, 1972.
- [25] P. J. Carreau, Carreau-DeKee-Chhabra, R. P. Chhabra and D. C. R. DeKee. *Rheology of polymeric systems: Principles and applications*. Hanser [u.a.], Munich [u.a.], 1997.
- [26] P. J. Carreau, D. D. Kee and M. Daroux. An analysis of the viscous behaviour of polymeric solutions. *The Canadian Journal of Chemical Engineering*, 57(2):135–140, 1979.
- [27] X. Chen, G. Chen and F. Gao. Capacitive transducer for in-mold monitoring of injection molding. *Polymer Engineering and Science*, 44(8):1571–1578, 2004.

- [28] X. Chen and F. Gao. An On-Line Measurement Scheme of Melt-Front-Area during Injection Filling via a Soft-Sensor Implementation. SPE ANTEC Tech Papers, 2000.
- [29] X. Chen, F. Gao and G. Chen. A soft-sensor development for melt-flow-length measurement during injection mold filling. *Materials Science and Engineering: A*, 384(1-2):245–254, 2004.
- [30] X. Chen, L. Zhang, X. Kong, J. Lu and F. Gao. Automatic velocity profile determination for uniform filling in injection molding. *Polymer Engineering & Science*, 50(7):1358–1371, 2010.
- [31] Z. Chen and L.-S. Turng. A review of current developments in process and quality control for injection molding. *Advances in Polymer Technology*, 24(3):165–182, 2005.
- [32] J. J.-W. Cheng, T.-C. Chao, L.-H. Chang and B.-F. Huang. A model-based virtual sensing approach for the injection molding process. *Polymer Engineering and Science*, 44(9):1605–1614, 2004.
- [33] J. J.-W. Cheng, Y.-W. Lin and F.-S. Liao. Design and Analysis of Model-based Iterative Learning Control of Injection Molding Process. In *Proceedings of ANTEC 2003*, pages 556–560, Nashville, 2003.
- [34] D. Clarke. *Advances in model-based predictive control*. Oxford University Press, Oxford and New York, 1994.
- [35] P. D. Coates and R. Speight. Towards intelligent process control of injection moulding of polymers. *Proceedings of the Institution of Mechanical Engineers, Part B: Journal of Engineering Manufacture 1989-1996 (vols 203-210)*, 209(52):357–367, 1995.
- [36] C. Collins. Monitoring cavity pressure perfects injection molding. *Assembly Automation*, 19(3):197–202, 1999.
- [37] J. W. Cooley and J. W. Tukey. An Algorithm for the Machine Calculation of Complex Fourier Series. *Mathematics of Computation*, 19(90):297, 1965.
- [38] L. Cremer, M. Heckl and B. A. T. Petersson. *Structure-borne sound: Structural vibrations and sound radiation at audio frequencies*. Springer, Berlin and New York, 3rd edition, 2005.
- [39] P. Davidovits and M. D. Egger. Scanning Laser Microscope for Biological Investigations. *Applied Optics*, 10(7):1615, 1971.
- [40] Debounce Logic Circuit. <http://eewiki.net/x/FgBM>, 23.10.2012.
- [41] N. T. Doppelmayr. *Untersuchung eines Regelkonzepts zum automatischen Füllausgleich bei Mehrkavitäten-Spritzgießwerkzeugen*. Bachelor Thesis, Montanuniversitaet Leoben, Leoben, 2012.

- [42] R. Dubay. Predictive Control of Cavity Pressure during Injection Filling. In *Proceedings of ANTEC 2001*, Dallas, 2001.
- [43] R. Dubay, A. C. Bell and Y. P. Gupta. Control of plastic melt temperature: A multiple input multiple output model predictive approach. *Polymer Engineering & Science*, 37(9):1550–1563, 1997.
- [44] O. R. Dumitrescu, D. C. Baker, G. M. Foster and K. E. Evans. Near infrared spectroscopy for in-line monitoring during injection moulding. *Polymer Testing*, 24(3):367–375, 2005.
- [45] R. Edwards and C. Thomas. On-line measurement of polymer orientation using ultrasonic technology. *Polymer Engineering & Science*, 41(9):1644–1653, 2001.
- [46] L. Euler. Découverte d’un nouveau principe de mécanique. *Memoires de l’Academie royal des sciences*, 6:185, 1752.
- [47] S. O. Fahey and J. Pratt. FREQUENCY DOMAIN MODAL ESTIMATION TECHNIQUES. *Experimental Techniques*, 22(5):33–37, 1998.
- [48] Z. Fan, R. X. Gao and D. O. Kazmer. Design of a self-energized wireless sensor for simultaneous pressure and temperature measurement. *Advanced Intelligent Mechatronics (AIM)*, 2010.
- [49] R. M. Fano. *Signal-to-noise ratio in correlation detectors*. Massachusetts Institute of Technology, Research Laboratory of Electronics, Cambridge and Massachusetts, 1951.
- [50] Y. Farouq, C. Nicolazo, A. Sarda and R. Deterre. Temperature measurements in the depth and at the surface of injected thermoplastic parts. *Measurement*, 38(1):1–14, 2005.
- [51] A. Flammini, D. Marioli, E. Sisinni and A. Taroni. Design and Implementation of a Wireless Fieldbus for Plastic Machineries. *IEEE Transactions on Industrial Electronics*, 56(3):747–755, 2009.
- [52] J. Frey. Method for automatically balancing the volumetric filling of cavities. US Patent 2004/0113303 A1, 2009.
- [53] Friedrich, W. Friedrich and G. Homborg. *Friedrich Tabellenbuch Metall- und Maschinentechnik: Nach der Neuordnung der Metallberufe*, volume 5103 of *Dümmmlerbuch*. Dümmmler, Bonn, 1993.
- [54] Fries Research & Technology GmbH. Data Sheet: FRT CWL - Chromatic White Light Sensor, 2012.
- [55] L.-A. Gäng. *Präzisionsspritzteile durch rechnerunterstütztes Optimieren der Prozessparameter: Basierend auf der gleichzeitigen Temperatur- und Druckmessung im Werkzeug*. Inst. f. Konstruktion u. Fertigung in d. Feinwerktechnik d. Univ. Stuttgart, Stuttgart, 1986.

- [56] F. Gao, W. I. Patterson and M. R. Kamal. Self-tuning cavity pressure control of injection molding filling. *Advances in Polymer Technology*, 13(2):111–120, 1994.
- [57] F. Gao, W. I. Patterson and M. R. Kamal. Cavity pressure control during the cooling stage in thermoplastic injection molding. *Polymer Engineering & Science*, 36(19):2467–2476, 1996.
- [58] R. X. Gao, Z. Fan, N. Asadizanjani and D. O. Kazmer. A New Method for Determining Melt Front Velocity Through Temperature Measurement. In *ASME 2011 Dynamic Systems and Control Conference and Bath/ASME Symposium on Fluid Power and Motion Control, Volume 2*, pages 167–172. ASME, 2011.
- [59] R. X. Gao, Z. Fan and D. O. Kazmer. Injection molding process monitoring using a self-energized dual-parameter sensor. *CIRP Annals - Manufacturing Technology*, 57(1):389–393, 2008.
- [60] R. X. Gao, Z. Fan and D. O. Kazmer. METHOD AND SYSTEM FOR MULTIVARIATE REMOTE MONITORING OF POLYMER PROCESSING. US Patent 2013/0030723 A1, 2012.
- [61] R. X. Gao, D. O. Kazmer and Z. Fan. Design and Performance Evaluation of a Modulator Circuit for an Acoustic Dual-Parameter Sensor. *IEEE Transactions on Industrial Electronics*, 2010.
- [62] B. Geissler, J. Macher, S. Laske, C. Holzer and G. R. Langecker. INFLUENCE OF THE SHEAR RATE AND THE NUCLEATING AGENT ON THE DEGASSING PRESSURE IN FOAM EXTRUSION. In *SPE Foams 2013*, Toronto, 2013.
- [63] O. R. Ghita, D. C. Baker and K. E. Evans. An in-line near-infrared process control tool for monitoring the effects of speed, temperature, and polymer colour in injection moulding. *Polymer Testing*, 27(4):459–469, 2008.
- [64] J. Giboz, T. Copponnex and P. Mélé. Microinjection molding of thermoplastic polymers: a review. *Journal of Micromechanics and Microengineering*, 17(6):96–109, 2007.
- [65] G. H. Golub and C. F. van Loan. *Matrix computations*. Johns Hopkins studies in the mathematical sciences. Johns Hopkins Univ. Press, Baltimore, 3rd edition, 2007.
- [66] V. G. Gomes, W. I. Patterson and M. K. Kamal. An injection molding study. Part II: Evaluation of alternative control strategies for melt temperature. *Polymer Engineering and Science*, 26(12):867–876, 1986.
- [67] I. J. Good. The interaction algorithm and practical Fourier analysis. *Journal of the Royal Statistical Society*, 20 (1958):361–372, 1958.

- [68] M. J. Gordon. *Total quality process control for injection molding*. Hanser Publishers, Munich and New York, 1993.
- [69] J. Gram. Über die Entwicklung realer Funktionen in Reihen mittelst der Methode der kleinsten Quadrate. *Journal für die reine und angewandte Mathematik*, pages 150–157, 1883.
- [70] R. M. Gray and L. D. Davisson. *An introduction to statistical signal processing*. Cambridge University Press, Cambridge, 2004.
- [71] R. J. Groleau. Best Practices with In-Mold Sensors. Society of Plastics Engineering Regional Technical Conference, 2004.
- [72] M. P. Groover. *Automation, production systems, and computer-integrated manufacturing*. Prentice Hall, Upper Saddle River, 3rd edition, 2008.
- [73] D. C. v. Grünigen. *Digitale Signalverarbeitung: Mit einer Einführung in die kontinuierlichen Signale und Systeme ; mit 91 Beispielen, 80 Aufgaben sowie einer CD-ROM mit Lösungen sowie Entwurfs- und Simulationsprogrammen*. Fachbuchverl. Leipzig im Carl-Hanser-Verl., München, 4th edition, 2008.
- [74] S. Haase. *Spectral and statistical methods for vibration analysis in steel rolling*. PhD Thesis, Montanuniversitaet Leoben, Leoben, 2002.
- [75] M. Harker and P. O’Leary. First order geometric distance (The myth of Sampsonus). *Proc. 17th Brit. Mach. Vision Conf*, pages 87–96, 2006.
- [76] M. Harker and P. O’Leary. Least-Squares Polynomial Approximation for the Reduction of Frequency Spreading and Gibbs Error in Fourier Analysis, 2012.
- [77] H. Havlicsek and A. Alleyne. Nonlinear control of an electrohydraulic injection molding machine via iterative adaptive learning. *IEEE/ASME Transactions on Mechatronics*, 4(3):312–323, 1999.
- [78] B. He, X. Yuan, H. Yang, H. Tan, L. Qian, Q. Zhang and Q. Fu. Ultrasonic measurement of orientation in HDPE/iPP blends obtained by dynamic packing injection molding. *Polymer*, 47(7):2448–2454, 2006.
- [79] B. He, X. Zhang, Q. Zhang and Q. Fu. Real-time ultrasonic monitoring of the injection-molding process. *Journal of Applied Polymer Science*, 107(1):94–101, 2008.
- [80] M. T. Heideman, D. H. Johnson and C. S. Burrus. Gauss and the History of the Fast Fourier-Transform. *Archive for History of Exact Sciences*, 34(3):265–277, 1985.
- [81] B. Heiing. *Fahrwerkhandbuch*. Springer Fachmedien, Wiesbaden, 2008.
- [82] H. v. Helmholtz and A. Wangerin. *Theorie der Luftschwingungen in Rhren mit offenen Enden*. W. Engelmann, 1896.

- [83] R. C. Helps, B. A. Strong, R. Al-Zubi, B. M. Lunt and K. E. Kohkonen. Generalization of a Method Using Neural Networks to Predict Part Quality Control During Injection Molding. *Journal of Injection Molding Technology*, 3(4):212–225, 1999.
- [84] T. Hirano. Automated Switchover in Injection Molding. *Journal of the Japan Society of Polymer Processing*, 9(11):843, 1997.
- [85] W. Homes and R. Kabus. Spritzgießprozesse in Echtzeit regeln: Eine neue Technik zur aktiven Angussbalancierung. *KU Kunststoffe*, 91(01):68–70, 2001.
- [86] M.-S. Huang. Cavity pressure based grey prediction of the filling-to-packing switchover point for injection molding. *Journal of Materials Processing Technology*, 183(2-3):419–424, 2007.
- [87] R. E. Hummel. *Electronic properties of materials*. Springer, New York, 4th edition, 2011.
- [88] A. Ionescu, S. Mahapatra and V. Pott. Hybrid SETMOS Architecture With Coulomb Blockade Oscillations and High Current Drive. *IEEE Electron Device Letters*, 25(6):411–413, 2004.
- [89] L. B. Jackson. *Digital filters and signal processing: With MATLAB exercises*. Kluwer Academic, Boston, 3rd edition, 1996.
- [90] A. Jaeger. Process Technology: No More Incomplete Parts. *Kunststoffe International*, (4), 2012.
- [91] F. Johannaber. *Injection molding machines: A user's guide*. Hanser, München, 4th edition, 2008.
- [92] F. Johannaber and W. Michaeli. *Handbuch Spritzgiessen*. Hanser, München, 2nd edition, 2004.
- [93] M. R. Kamal, W. I. Patterson, N. Conley, D. A. Fara and G. Lohfink. Dynamics and control of pressure in the injection molding of thermoplastics. *Polymer Engineering and Science*, 27(18):1403–1410, 1987.
- [94] M. R. Kamal, W. I. Patterson and V. G. Gomes. An injection molding study. Part I: Melt and barrel temperature dynamics. *Polymer Engineering and Science*, 26(12):854–866, 1986.
- [95] S. M. Kay. *Fundamentals of statistical signal processing*. Prentice Hall PTR, Upper Saddle River, 1993.
- [96] D. O. Kazmer. *Injection mold design engineering*. Hanser and Hanser Gardner, Munich and Cincinnati, 2007.
- [97] D. O. Kazmer. *Plastics manufacturing systems engineering: [a systems approach]*. Hanser Verlag, München, 2009.

- [98] D. O. Kazmer, S. P. Johnston, R. X. Gao and Z. Fan. Feasibility Analysis of an In-mold Multivariate Sensor. *International Polymer Processing The Journal of the Polymer Processing Society*, XXVI(01):63–72, 2011.
- [99] D. O. Kazmer, S. Velusamy, S. Westerdale, S. Johnston and R. X. Gao. A comparison of seven filling to packing switchover methods for injection molding. *Polymer Engineering and Science*, 50(10):2031–2043, 2010.
- [100] A. Kelly, M. Woodhead and P. D. Coates. Comparison of injection molding machine performance. *Polymer Engineering & Science*, 45(6):857–865, 2005.
- [101] F. Kohlrausch, H. Ebert and F. Henning. *Praktische Physik: Zum Gebrauch für Unterricht, Forschung und Technik*. Teubner, Stuttgart, 24th edition, 1996.
- [102] J. Kolerus and J. Wassermann. *Zustandsüberwachung von Maschinen: Ein Lehr- und Arbeitsbuch für den Praktiker ; mit 7 Tabellen und DVD-ROM Lab VIEW 8.6, Studentenedition ; virtueller Analysator VIISA*, volume 79 of *Edition expertsoft*. Expert-Verl., Renningen, 4 edition, 2008.
- [103] M. Kutz, editor. *Applied plastics engineering handbook: Processing and materials*. PDL handbook series. William Andrew, Amsterdam and Boston, 2011.
- [104] G.-Y. Lai and J. X. Rietveld. Role of polymer transparency and temperature gradients in the quantitative measurement of process stream temperatures during injection molding via IR pyrometry. *Polymer Engineering & Science*, 36(13):1755–1768, 1996.
- [105] I.-W. Lee and G.-H. Jung. An efficient algebraic method for the computation of natural frequency and mode shape sensitivities—Part I. Distinct natural frequencies. *Computers & Structures*, 62(3):429–435, 1997.
- [106] A. W. Leissa. *Vibration of plates*, volume 160 of *NASA special publications*. Scientific and Technical Information Div. Off. of Technology Utilization National Aeronautics and Space Administration, Washington, 1969.
- [107] Y.-W. Lin and J. J.-W. Cheng. Model-based melt flow virtual sensors for filling process of injection molding. *Polymer Engineering and Science*, 48(3):543–555, 2008.
- [108] C. S. Lindquist. *Adaptive & digital signal processing: With digital filtering applications*, volume 2 of *International series in signal processing and filtering*. Steward, Miami, 1989.
- [109] O. Lingk. *Einsatz von Ultraschall zur Prozessanalyse beim Spritzgießen von Thermoplasten*. PhD Thesis, Rheinisch-Westfälische Technische Hochschule Aachen, Aachen, 2010.

- [110] S. D. Lipshitz, R. Lavie and Z. Tadmor. A melting model for reciprocating screw injection-molding machines. *Polymer Engineering and Science*, 14(8):553–559, 1974.
- [111] C. Liu and L. T. Manzione. Process studies in precision injection molding. I: Process parameters and precision. *Polymer Engineering & Science*, 36(1):1–9, 1996.
- [112] S. Liu, K. Lin and S. Tsai. Improving weldline strengths of injection moulded parts by ultrasonic oscillation. *Plastics, Rubber and Composites*, 37(1):23–28, 2008.
- [113] C. H. Lu and C. C. Tsai. Adaptive decoupling predictive temperature control for an extrusion barrel in a plastic injection molding process. *IEEE Transactions on Industrial Electronics*, 48:968–975, 2001.
- [114] T. Lucyshyn. *Messung von pvT-Daten bei prozessnahen Abkühlraten und deren Einfluss auf die Simulation von Schwindung und Verzug mit Moldflow Plastics Insight*. PhD Thesis, Montanuniversitaet Leoben, Leoben, 2010.
- [115] C. Y. W. Ma. A design approach to a computer-controlled injection-molding machine. *Polymer Engineering and Science*, 14(11):768–772, 1974.
- [116] C. Maier. Infrared temperature measurement of polymers. *Polymer Engineering & Science*, 36(11):1502–1512, 1996.
- [117] A. I. Malkin and A. I. Isayev. *Rheology: Concepts, methods, and applications*. ChemTec Pub., Toronto, 2nd edition, 2012.
- [118] A. Mamat, T. F. Trochu and B. Sanschagrín. Analysis of shrinkage by dual kriging for filled and unfilled polypropylene molded parts. *Polymer Engineering and Science*, 35(19):1511–1520, 1995.
- [119] P. S. Mann. *Introductory statistics*. Wiley, New York, 2nd edition, 1995.
- [120] R. Mäusl. *Hochfrequenzmesstechnik: Messverfahren u. Messgeräte*. Uni-Taschenbücher. Hüthig, Heidelberg, 2nd edition, 1978.
- [121] G. Menges, W. Michaeli and P. Mohren. *How to make injection molds*. Hanser and Distributed in USA by Hanser Gardner Publications, Munich and Cincinnati, 3rd edition, 2001.
- [122] G. Menges, W. Michaeli and P. Mohren. *Spritzgiesswerkzeuge: Auslegung, Bau, Anwendung*. Hanser, München, 6th edition, 2007.
- [123] W. Michaeli and A. Schreiber. ONLINE CAVITY PRESSURE CONTROL IN INJECTION MOULDING. *Journal of Polymer Engineering*, 27(6-7):429–446, 2007.
- [124] W. Michaeli and C. Starke. Ultrasonic investigations of the thermoplastics injection moulding process. *Polymer Testing*, 24(2):205–209, 2005.
- [125] K. Mörwald. *Einblick in die Konstruktion von Spritzgußwerkzeugen*. Brunke Garrels, 1965.

- [126] M. Möser. *Technische Akustik*. Springer Vieweg, Berlin, 9th edition, 2012.
- [127] F. Müller, P. O’Leary, G. Rath, C. Kukla, M. Harker, T. Lucyshyn and C. Holzer. Resonant Acoustic Sensor System for the Wireless Monitoring of Injection Moulding. In *Sensornets 2013, 2nd International Conference on Sensor Networks*, Barcelona, 2013.
- [128] F. Müller, G. Rath, T. Lucyshyn, C. Kukla, M. Burgsteiner and C. Holzer. Presentation of a novel sensor based on acoustic emission in injection molding. *Journal of Applied Polymer Science*, 127(6):4744–4749, 2013.
- [129] R. Nelson. Simplified calculation of eigenvector derivatives. *AIAA Journal*, 14(9):1201–1205, 1976.
- [130] I. Newton. *The principia: Mathematical principles of natural philosophy*. Snowball Pub., 2010.
- [131] N.N. Aktive Qualitätssicherung bei der Produktion von TPE-Teilen: Boida Kunststofftechnik. *Sonderdruck aus Österreichische Kunststoffzeitschrift*, (7/8):151–153, 2010.
- [132] W. Obendrauf. Erfahrungen bei der Temperaturmessung mit Infrarot-Sensoren. *Tagungsband zum 13. Leobener Kunststoff-Kolloquium*, pages 15–24, 1994.
- [133] W. Obendrauf. *Neue Methoden zur Temperatur- und Dehnviskositätsmessung für die Simulation von Kunststoffverarbeitungsprozessen*. Dissertation, Montanuniversitaet Leoben, Leoben, 1996.
- [134] P. O’Leary and M. Harker. An Algebraic Framework for Discrete Basis Functions in Computer Vision. *Computer Vision, Graphics & Image Processing, 2008*, pages 150–157, 2008.
- [135] P. O’Leary and M. Harker. Discrete Polynomial Moments and Savitzky-Golay Smoothing. *World Academy of Science, Engineering and Technology*, 48:440–444, 2010.
- [136] P. O’Leary and M. Harker. Polynomial approximation: An alternative to windowing in Fourier analysis. In *Instrumentation and Measurement Technology Conference (I2MTC), 2011 IEEE*, Hangzhou, China, 2011.
- [137] P. O’Leary and M. Harker. *3-D Surface Geometry and Reconstruction: Developing Concepts and Applications Surface: Modelling Using Discrete Basis Functions for Real-Time Automatic Inspection*. IGI Global, 2012.
- [138] P. O’Leary and M. Harker. A Framework for the Evaluation of Inclinometer Data in the Measurement of Structures. *IEEE Transactions on Instrumentation and Measurement*, 61(5):1237–1251, 2012.
- [139] A. V. Oppenheim and R. W. Schaffer. *Discrete-time signal processing*. Pearson, Upper Saddle River, 3rd edition, 2010.

- [140] S. A. Orroth. *Infrared Melt Temperature Measurements in Injection Molding of Thermoplastics*. Master Thesis, University of Massachusetts Lowell, Lowell, 1974.
- [141] G. Pacher, G. R. Berger, W. Friesenbichler, D. Gruber and J. Macher. IN-MOLD SENSOR CONCEPT TO CALCULATE PROCESS-SPECIFIC RHEOLOGICAL PROPERTIES. In *The 29th International Conference of The Polymer Processing Society*, Nürnberg, 2013.
- [142] M. Pahl, W. Gleissle and H.-M. Laun. *Praktische Rheologie der Kunststoffe und Elastomere*. VDI-Verl., Düsseldorf, 4th edition, 1995.
- [143] R. R. Panchal and D. O. Kazmer. In-mold Shrinkage Monitoring Sensor for Injection Molding. SPE ANTEC Technical Papers, 2009.
- [144] S. J. Park and T. H. Kwon. Optimal cooling system design for the injection molding process. *Polymer Engineering & Science*, 38(9):1450–1462, 1998.
- [145] PCB Piezotronics. Model J353B01: General purpose, quartz shear ICP® accelerometer: Installation and Operating Manual, 2012.
- [146] R. Pethig and S. Smith. *Introductory bioelectronics: For engineers and physical scientists*. John Wiley & Sons, Chichester, 2013.
- [147] L. Piche, A. Hamel, R. Gendron, M. Dumoulin and J. Tatibouet. Ultrasonic characterization of polymer melts under processing conditions. US Patent 5433112, 1995.
- [148] PlasticsEurope.org. *Plastics – the Facts 2012: An analysis of European plastics production, demand and waste data for 2011, 2012*.
- [149] Po-Jui Chen, D. Rodger, S. Saati, M. Humayun and Yu-Chong Tai. Micro-fabricated Implantable Parylene-Based Wireless Passive Intraocular Pressure Sensors. *Journal of Microelectromechanical Systems*, 17(6):1342–1351, 2008.
- [150] H. Potente, J. Natrop and D. Hanning. Konzepte zur Qualitätssicherung. *Kunststoffe*, 11(82):1078–1083, 1992.
- [151] B. Pramujati and R. Dubay. A Novel Tuning Method for Predictive Control of Melt Temperature and Plastication Screw Speed in Injection Molding. *Journal of Injection Molding Technology*, 6(4):247–258, 2002.
- [152] W. H. Press, S. A. Teukolsky, W. T. Vetterling and B. P. Flannery. *Numerical Recipes in C: The Art of Scientific Computing: Second Edition*. Cambridge Univ. Pr., Cambridge, 2nd edition, 1992.
- [153] Priamus System Technologies AG. Datasheet 4009B / 4010B, 2006.
- [154] Priamus System Technologies AG. Der kleinste Werkzeugwandtemperatur-Sensor der Welt, 2006.
- [155] Priamus System Technologies AG. Priamus Pass Monitor Type 7203A, 2010.

- [156] G. P. Quinn and M. J. Keough. *Experimental design and data analysis for biologists*. Cambridge University Press, Cambridge, 2002.
- [157] F. Raschke, J. Gießauf and G. Steinbichler. *Potentiale moderner Temperierverteilsysteme: Neue Möglichkeiten zur Prozessoptimierung: Spritzgießen 2013*, volume 4327 of *VDI-Berichte*. VDI-Verl., Düsseldorf, 2013.
- [158] I. Rawabdeh and P. Petersen. In-Line Monitoring of Injection Molding Operations: A Literature Review. *Injection Molding Technology*, (3):47–53, 1999.
- [159] J. Rayleigh. *The theory of sound*, volume 1. Macmillan and co, 1877.
- [160] D. V. Rosato, D. V. Rosato and M. G. Rosato. *Injection molding handbook*. Kluwer Academic Publishers, Boston, 3 edition, 2000.
- [161] C. S. Rudisill and Y.-Y. Chu. Numerical Methods for Evaluating the Derivatives of Eigenvalues and Eigenvectors. *AIAA Journal*, 13(6):834–837, 1975.
- [162] E. Sachs, E. Wylonis, S. Allen, M. Cima and H. Guo. Production of injection molding tooling with conformal cooling channels using the three dimensional printing process. *Polymer Engineering & Science*, 40(5):1232–1247, 2000.
- [163] L. Sachs. *Angewandte Statistik: Anwendung statistischer Methoden*. Springer, Berlin, 6th edition, 1997.
- [164] H. Saechtling and E. Baur. *Saechtling-Kunststoff-Taschenbuch*. Hanser, München, 30th edition, 2007.
- [165] S. Sato, Y. Nakano, A. Sato and T. Nomura. Effect of Y-Doping on Resistance Degradation of Multilayer Ceramic Capacitors with Ni Electrodes under the Highly Accelerated Life Test. *Japanese Journal of Applied Physics*, 36(Part 1, No. 9B):6016–6020, 1997.
- [166] A. Savitzky and M. J. E. Golay. Smoothing and Differentiation of Data by Simplified Least Squares Procedures. *Analytical Chemistry*, 36(8):1627–1639, 1964.
- [167] E. Schmidt. Zur Theorie der linearen und nichtlinearen Integralgleichungen. I. Teil: Entwicklung willkürlicher Funktionen nach Systemen vorgeschriebener. *Mathematische Annalen*, 63:433–476, 1907.
- [168] Schoppe, Zimmermann, Stöckeler and Zinkler. Verfahren zum überwachen der Verarbeitung von Polymerwerkstoffen. DE Patent 102008047002, 2010.
- [169] U. Seuthe. Method and Device for Monitoring and Optimizing Injection Molding Process. WO Patent 2011/154123 A1, 2011.
- [170] U. Seuthe. Vorrichtung und Verfahren zum überprüfen eines Bauteils auf Schäden. EP Patent 2 317 308 A2, 2011.
- [171] L. Sevgi. Numerical Fourier transforms: DFT and FFT. *IEEE Antennas and Propagation Magazine*, 49(3):238–243, 2007.

- [172] B. Sheth, C. M. Barry, N. R. Scott, R. D. Higdon and B. Davison. Improved part quality using cavity pressure switchover. In *Proceedings of ANTEC 2001*, Dallas, 2001.
- [173] R. Speight, F. Costa, P. K. Kennedy and C. Friedl. Best practice for benchmarking injection moulding simulation. *Plastics, Rubber and Composites*, 37(2):124–130, 2008.
- [174] R. Speight, J. Hull and P. D. Coates. Control of Polymer Melt Flow Front Position During the Injection Molding Process. SPE ANTEC Tech Papers, 1996.
- [175] R. Speight, A. J. Monro and A. Khassapov. Velocity-phase profiles boost quality in injection molding. *Modern Plastics*, 76(8):79–81, 1999.
- [176] R. Spina. Injection moulding of automotive components: comparison between hot runner systems for a case study. *Journal of Materials Processing Technology*, 155-156:1497–1504, 2004.
- [177] M. St. Jacques. An analysis of thermal warpage in injection molded flat parts due to unbalanced cooling. *Polymer Engineering and Science*, 22(4):241–247, 1982.
- [178] D. S. Stevens, J. C. Andle, S. Sabah, S. J. Jumani, B. W. Wall, M. Bauer, T. Martens and R. Gruenwald. Applications of Wireless Temperature Measurement Using SAW Resonators. In *Fourth International Symposium on Acoustic Wave Devices for Future Mobile Communication Systems*, Chiba University, Chiba, 2010.
- [179] V. Strassen. Gaussian elimination is not optimal. *Numerische Mathematik*, 13(4):354–356, 1969.
- [180] Z. Tadmor and C. G. Gogos. *Principles of polymer processing*. Wiley-Interscience, Hoboken and N.J, 2 edition, 2006.
- [181] T. J. Terrell and L.-K. Shark. *Digital signal processing: A student guide*. Macmillan, Basingstoke, 1996.
- [182] The Dow Chemical Company. Datasheet Polypropylene C7069-100NA: Impact Copolymer Resin, 2010.
- [183] The MathWorks Inc. Matlab - Primer: R2012a, 2012.
- [184] The Society of the Plastics Industry Website. About the Industry, 2005.
- [185] C. Theurer, Li Zhang, D. O. Kazmer, R. X. Gao and R. Jackson. Passive charge modulation for a wireless pressure sensor. *IEEE Sensors Journal*, 6(1):47–54, 2006.
- [186] C. Thomas, E. Russell and L. Diao. Continuous Wave Ultrasonic Process Monitor for Polymer Processing. WO Patent 03/089214 A2, 2003.
- [187] U. Tietze, E. Gamm and C. Schenk. *Halbleiter-Schaltungstechnik*. Springer, Heidelberg, 13th edition, 2010.

- [188] P. A. Tipler and G. Mosca. *Physik für Wissenschaftler und Ingenieure*. Spektrum Akademische Verlag, Heidelberg, 2nd edition, 2004.
- [189] H. J. Tiziani and H.-M. Uhde. Three-dimensional image sensing by chromatic confocal microscopy. *APPLIED OPTICS*, 33(10):1838–1843, 1994.
- [190] H.-P. Tsoi and F. Gao. Control of injection velocity using a fuzzy logic rule-based controller for thermoplastics injection molding. *Polymer Engineering & Science*, 39(1):3–17, 1999.
- [191] A. Ujma and B. Walder. Werkzeugwartung zur rechten Zeit. *Kunststoffe*, (2):18–20, 2013.
- [192] T. C. Urdan. *Statistics in plain English*. Lawrence Erlbaum Associates, Mahwah, 2nd edition, 2005.
- [193] H. Wang, B. Cao, C. K. Jen, K. T. Nguyen and M. Viens. On-line ultrasonic monitoring of the injection molding process. *Polymer Engineering & Science*, 37(2):363–376, 1997.
- [194] K. K. Wang, J. Zhou and Y. Sakurai. An Integrated Adaptive Control for Injection Molding. In *Proceedings of ANTEC 1999*, New York City, 1999.
- [195] B. Watkins. Five myths about sensing mold pressure. *Sensors Magazine*, 14:73–78, 1997.
- [196] A. Witschnigg, S. Laske, M. Kracalik, M. Feuchter, G. Pinter, G. Maier, W. Märzinger, M. Haberkorn, G. R. Langecker and C. Holzer. In-line characterization of polypropylene nanocomposites using FT-NIR. *Journal of Applied Polymer Science*, pages 3047–3053, 2010.
- [197] H. Wobbe and J. Gießauf. Total-Quality-Prinzip beim Spritzgießen immer wichtiger: Ein Statusbericht aus der Sicht von Engel Austria / Qualitätsicherung neu definiert. *Kunststoffberater*, 2007.
- [198] S. L. B. Woll and D. J. Cooper. Pattern-based closed-loop quality control for the injection molding process. *Polymer Engineering & Science*, 37(5):801–812, 1997.
- [199] S. L. B. Woll, D. J. Cooper and B. V. Souder. Online pattern-based part quality monitoring of the injection molding process. *Polymer Engineering & Science*, 36(11):1477–1488, 1996.
- [200] X. Xu, E. Sachs and S. Allen. The design of conformal cooling channels in injection molding tooling. *Polymer Engineering & Science*, 41(7):1265–1279, 2001.
- [201] Y. Yang and F. Gao. Injection Velocity Control Using A Self-tuning Adaptive Controller. *International Polymer Processing*, 14(2):196–204, 1999.
- [202] Y. Yang and F. Gao. Adaptive control of the filling velocity of thermoplastics injection molding. *Control Engineering Practice*, 8(11):1285–1296, 2000.

- [203] L. Zhang, C. Theurer, R. X. Gao and D. O. Kazmer. Design of ultrasonic transmitters with defined frequency characteristics for wireless pressure sensing in injection molding. *IEEE Transactions on Ultrasonics Ferroelectrics and Frequency Control*, 52(8):1360–1371, 2005.
- [204] L. Zhang, C. B. Theurer and R. X. Gao. A SELF-ENERGIZED SENSOR FOR WIRELESS INJECTION MOLD CAVITY PRESSURE MEASUREMENT: DESIGN AND EVALUATION. *Journal of dynamic systems, measurement, and control*, 126(2):309–318, 2004.
- [205] L. Zhang, C. B. Theurer, R. X. Gao and D. O. Kazmer. DEVELOPMENT OF A WIRELESS PRESSURE SENSOR WITH REMOTE ACOUSTIC TRANSMISSION. *Transaction North American Manufacturing Research Institute*, 30:573–580, 2002.
- [206] C. Zhao and F. Gao. Melt temperature profile prediction for thermoplastic injection molding. *Polymer Engineering & Science*, 39(9):1787–1801, 1999.
- [207] Y. Zhuang. *Cross Development for Real-Time Systems and Embedded Automation*. Master Thesis, Montanuniversitaet Leoben, Leoben, 2012.